La Rivista del Nuovo Cimento (2025) 48:315–434
https://doi.org/10.1007/s40766-025-00070-7

REVIEW PAPER

Advanced X-ray techniques to study the alteration of pigments in paintings

Letizia Monico[1,2,3] · Koen Janssens[3,4,5] · Marine Cotte[6,7] · Samuel M. Webb[8] · Frederik Vanmeert[3,4] · Victor Gonzalez[9] · Geert Van der Snickt[3,5] · Katrien Keune[4,10] · Brunetto Giovanni Brunetti[1,2] · Gerald Falkenberg[11] · Jan Garrevoet[11] · Annelies van Loon[4,12] · Marc Vermeulen[13] · Maite Maguregui[14] · Steven De Meyer[3,15] · Ermanno Avranovich Clerici[3] · Fréderique T. H. Broers[3,4,10,16] · Laura Cartechini[1] · Nouchka De Keyser[3,4,5,10] · Francesco d'Acapito[17] · Florian Meirer[16] · Aldo Romani[1,2] · Francesca Rosi[1] · Sara Carboni Marri[1,2] · Daniela Comelli[18] · Nina Deleu[3,5] · Ida Fazlic[4,6,10] · Marta Ghirardello[18] · Clément Holé[6] · Silvia Pérez-Diez[19,20] · Mathieu Thoury[21] · Costanza Miliani[22]

Received: 30 November 2024 / Accepted: 10 April 2025 / Published online: 2 September 2025

Abstract

The application of X-ray methods (using conventional sources or synchrotron radiation) for investigating degradation phenomena in paintings has significantly increased in the last two decades. This rise is due to their ability to provide spatially resolved elemental, molecular, and structural information from the macroscopic to the nanoscopic levels. This review will focus on the application of latest-generation X-ray techniques, including X-ray fluorescence (XRF), X-ray absorption spectroscopy (XAS), and X-ray diffraction (XRD), to study the alteration processes of pigments in paintings. The first part outlines the fundamentals of XRF, XAS, and XRD techniques and then describes the corresponding instrumental set-ups used for non-invasive macro-scale mapping of paintings and synchrotron radiation-based X-ray analysis of paint micro-samples. Subsequent sections will cover advancements in X-ray data analysis software, workflow management systems, Open Science and FAIR data initiatives, alongside practical aspects of sample preparation and issues concerning X-ray-induced damage to paints. The final section will review degradation phenomena resulting from chemical changes of selected classes of pigments. This will involve describing key findings obtained from paintings, related micro-samples, and artificially aged paint mock-ups. The outcomes discussed in this review highlight their crucial role in developing effective monitoring and preventive conservation strategies for artworks highly susceptible to degradation within heritage sites and museums.

Keywords X-rays · Heritage science · X-ray imaging · Synchrotron · Art conservation

Extended author information available on the last page of the article

1 Introduction

1.1 Alteration phenomena in paintings

Within heritage science, the understanding and prevention of the alteration of paintings is a challenge. Degradation in paint layers can manifest itself as losses of stability and cohesion, and/or as modifications of optical properties such as color. The occurrence of these phenomena, which may compromise the perception of the artwork and its transmission to next generations, depends on the nature of the materials used, the way they were applied, possible past restorations and the environmental conditions to which the painting has been exposed over time.

Since ancient times, intellectuals and artists were already aware of the fugitive nature of many artists' materials, such as pigments. For example, the first century author Pliny the Elder, in the *Naturalis Historia* (33, 40), mentioned that *"a surface painted with cinnabar is damaged by the action of sunlight and moonlight"* [1]. The Italian painters and essay writers Cennino Cennini (fourteenth-fifteenth century) [2] and Giovanni Paolo Lomazzo (1538–1592) [3] recommended to use minium, lead white (or *biacca*), orpiment, and cinnabar with caution in frescos, even avoiding mixing these materials with other pigments, due to their propensity to change color over time. In 1887, Camille Pissarro, in a letter to his son Lucien [4], described the quick tendency of emerald green to darken when mixed with cadmium, white, and red pigments. One year later, Vincent van Gogh wrote to his brother Theo (letter nr. 595) that *"all the colors that Impressionism has made fashionable are unstable"*, including among them chrome yellows, emerald green, and Prussian blue [5].

Degradation issues affect many paintings in heritage sites and museums nowadays. Among numerous examples, the darkening of cinnabar or vermilion red (α-HgS) threatens several Roman wall paintings of the first century BCE-first century CE period in different archaeological sites of the Vesuvian area [6–8] and in a series of fourteenth–seventeenth century tempera and oil paintings [9–12]. Color changes and/or losses of structural integrity of blueish copper-based areas and of dark lead-containing paints were observed in thirteenth century wall paintings by Maestro di San Francesco, Cimabue, and Giotto in the Basilica di San Francesco in Assisi [13–16] and in several seventeenth–nineteenth century paintings, including those by Rembrandt van Rijn [17], Johannes Vermeer [18], and Vincent van Gogh [19]. "Sickness" of ultramarine blue [$(Na,Ca)_8(AlSiO_4)_6(SO_4,OH,S,Cl)_2$)] was noticed in Flemish and Dutch artworks from fourteenth to seventeenth century [20–24] and in twentieth century paintings [23, 24]. A translucent brown or grayish-green appearance, accompanied by crack formation and surface blanching, was observed in the areas painted with smalt (a cobalt-containing potash glass) of several sixteenth–nineteenth century paintings [20, 25–29]. In a series of eighteenth century Danish Golden age masterpieces, a significant fading of Prussian blue ($MFe^{3+}[Fe^{2+}(CN)_6]\cdot xH_2O$, with $M = K^+$, NH_4^+ or Na^+) has been found only in the paints exposed to ambient illumination, while below their frame, the color of the artworks is still intact (Fig. 1a) [30]. The discoloration of orpiment (α-As_2S_3) and cadmium yellows ($CdS/Cd_{1-x}Zn_xS$), sometimes occurring along with flaking of the paint, is a frequently observed phenomenon in several artworks

Fig. 1 Some examples of degradation in paintings. **a** *View of Lake Sortedam from Dosseringen Looking Towards the Suburb Nørrebro outside Copenhagen* by Christen Købke oil on canvas, 1838; Statens Museum for Kunst, Copenaghen, DK, inv. nr. KMS359; Copenhagen, DK): details of the bottom edge of the water and of the right-hand edge of the sky showing a less significant fading of the Prussian blue painted areas protected from light by the frame. **b** *Maestà di Santa Maria dei Servi* attributed to Cimabue (tempera and gold on panel painting, ca. 1280–1285; Basilica di Santa Maria dei Servi, Bologna, IT): photographic detail of a darkened "fake-gilded" decoration of the throne as indicated by the white rectangle in the painting. **c** *Company of District II under the Command of Captain Frans Banninck Cocq*, the official title of *The Night Watch* by Rembrandt van Rijn (oil on canvas, 1642; Rijksmuseum, Amsterdam, NL, inv. nr. SK-C-5) (insert): stereomicroscope detail of a lead soap protrusion found on the surface of *The Night Watch*. Adapted with permission from [30, 46, 95]

from thirteenth to seventeenth century by Italian, Flemish, and Dutch masters (Fig. 1b) [31–33, 46] and in late nineteenth–early twentieth century masterpieces, such as those by James Ensor [34], Edvard Munch [35], and Henri Matisse [36]. The darkening of zinc yellows ($K_2O{\cdot}4ZnCrO_4{\cdot}3H_2O$) and chrome yellows ($PbCrO_4/PbCr_{1-x}S_xO_4$) affects several artworks by Georges Seurat [37] and Vincent van Gogh [38–40]. Darkening, taking place along with the formation of cracks and flaking of the paint, was also observed in areas painted with either organo-copper green pigments (i.e., copper acetate or resinate) or emerald green [$Cu(CH_3COO)_2{\cdot}3Cu(AsO_2)_2$] of a number of fifteenth–sixteenth century masterpieces [9, 41–43] and of nineteenth century paintings by Théodore Rousseau and Vincent van Gogh [44, 45].

The spreading of alteration phenomena in paintings has undeniably called upon museums and scholars from different domains (i.e., chemists, physics, art conservators, restorers, art historians, etc.) to work synergistically for a common purpose: to contribute to the development of efficient and sustainable preventive strategies for the long-term conservation of unique masterpieces. A leap forward has been made since

2–3 decades, when a systematic action was launched to seek answers to the following questions: what are the causes and factors that govern specific paint alteration processes? Are transformations reversible? How can state-of-the-art diagnostic techniques contribute to assessing, monitoring, and optimizing the conservation conditions and treatments of artworks subject to degradation?

1.2 A multi-technique approach at multiple length scales

Paint films, when observed either under a microscope or, in some cases, simply with the naked eye, appear as multi-layered and heterogeneous systems made up of organic polymers (binders and varnish layers) and inorganic and/or organic pigments, that are subject to complex physico-chemical transformations over time. These processes usually depend on both internal factors (i.e., the chemical nature of the paint components) and on external environmental factors, such as light, humidity, temperature, and air pollutants.

It has been extensively documented that amorphous or crystalline carboxylates of metal ions (soaps) [47–49] and newly formed compounds arising from changes in the oxidation state of one or more elements constituting some pigments [50–52] are common alteration products of paint components. From the analytical point of view, the study of such complex processes is rendered more complicated by the fact that amorphous and/or crystalline secondary compounds may form as layers and/or aggregates of limited size (generally below 100 μm) within heterogeneous paint matrixes. Thus, the combination of complementary and spatially resolved analytical methods is usually required, exploiting their ability to visualize chemical changes at multiple length scales (i.e., from the millimetric to the nanometric scale) both directly throughout the painting surface and across the stratigraphy of minute paint samples.

The past two decades have witnessed a significant rise in the application of synchrotron radiation (SR)-based X-ray methods (including 2D/3D mapping/imaging and point analysis) for analyzing micro-fragments from historical paintings and paint mock-ups. This increase is attributed to their ability to provide elemental, molecular, and structural information down to the (sub)micrometer length scale [53–56] and has been further enabled by developments in other research fields, such as materials science and health and life sciences [57–62].

Considering both 2D mapping and single-point techniques, the combination of micro-X-ray fluorescence (μ-XRF) with X-ray absorption spectroscopy (XAS) (utilizing energies above 2.1–2.2 keV) has proven effective for characterizing pigments in both amorphous and crystalline forms. This approach provides specific information on changes of the oxidation state and coordination geometry of the absorbing element, as demonstrated by studies on sulfur (2−) in CdS and HgS [7, 34], chromium (6+) in chromate-based yellows [63, 64], arsenic (3+)/sulfur (2−) in orpiment and emerald green [31, 44, 46, 65], cobalt (2+) in smalt [28, 66, 67], and iron (2+)/iron (3+) in Prussian blue [68–70]. Complementary information on the nature and distribution of crystalline secondary compounds of some of these pigments were obtained by integrating XAS with 2D micro-X-ray diffraction (μ-XRD) data [12, 46, 71, 72]. In selected cases, 2D μ-XRD was combined with micro-X-ray diffraction computed tomography

(μ-XRD-CT) to visualize the inner distribution of crystalline components in minute historical lead-based paint samples, without physically cross-sectioning the material under investigation [19, 73]. SR high-resolution X-ray diffraction (HR-XRD) was used to obtain bulk information on the nature of crystalline alteration compounds of silver foils and paints in a series of fifteenth century artworks [74–76]. The same technique was also applied to study the chemical composition and micro-structural properties of a wide range of artists' pigments and materials, including lead white [77–79], zinc white [80], cadmium reds [55, 81, 82], and lead-hydroxyapatite compounds [83], thus providing new insights into their manufacturing processes and artists/workshops practices. As more recently described by Dalecky et al. [84], further knowledge about the optical and dielectric properties of a series of pigments was obtained by SR-based non-resonant inelastic X-ray scattering (IXS) spectroscopy. Changes in the luminescence properties of zinc oxide [85, 86] and cadmium sulfide oil paints [87], associated with the oxidative degradation of the paint, were detected via SR deep-UV photoluminescence. X-ray excited optical luminescence (XEOL), a suitable technique for studying the radiative recombination properties of materials through their emission in the UV, visible, or near IR range [88–90], has also been used in combination with XAS to correlate the optical properties of differently produced zinc oxide powders at the nano-scale length, using an optical detection system equipped with a scanning transmission X-ray microscope (STXM) [91].

Concerning 3D imaging methods, SR-based computed X-ray tomography, sometimes combined with SR high-resolution computed laminography, enables non-destructive 3D visualization of paint stratigraphy, thus providing detailed information on the local microstructure of paint layers, ground, and support [92–94]. More recently, SR-based correlated X-ray ptychography and XRF nano-tomography have allowed for the acquisition of 3D morphological and chemical information on a minute sample taken from the ground layer of the *Night Watch* by Rembrandt van Rijn. This analysis helped explain the presence of lead soap protrusions in areas of the painting where lead-based pigments were absent from the ground layer (Fig. 1c) [95].

Further insights into the chemical nature and stratigraphic distribution of secondary compounds arising from pigment-binder interactions (such as oxalates and soaps) were often achieved by combining the wide range of the above-described SR X-ray methods with micro-Raman and SR-based or conventional micro-IR spectroscopies [43, 46, 65, 74–76, 96–102]. Electron energy loss spectroscopy (EELS) mapping [37, 103] and electron paramagnetic resonance (EPR) spectroscopy [41, 104–107] were sometimes employed in a complementary fashion to XAS, allowing Cr and Cu speciation information to be obtained, at the nano-scale and bulk levels, in altered chromate- and green copper-based paint samples.

At the macro-scale level, complementary knowledge into some of the above-described paint alteration phenomena was obtained by integrating the micro-analytical data obtained from paint samples with non-invasive measurements (from the IR to the X-ray range) gathered with portable devices [17, 32, 33, 102, 108]. Such investigations, performed in situ, directly on paintings, have opened the possibility to visualize and to map areas where paint components at major risk of degradation are present or alteration processes might still be ongoing [18, 109]. Recent developments about such

range of techniques and their applications on paintings have been widely reviewed over the last 10 years [110–119].

In what follows, this review will focus on the application of X-ray methods for studying alteration processes of pigments in paintings. In the first part (Sect. 2), an overview of fundamentals of XRF, XAS, and XRD techniques, along with a description of the corresponding instrumental set-ups used for non-invasive mapping analysis of paintings at the macro-scale and for SR-based X-ray investigations of altered paint samples at the micro-scale will be provided. X-ray software developments, workflow management systems, Open Science and FAIR data initiatives, and practical aspects of sample preparation will also be presented (Sects. 3, 4). Considering the two published reviews by Bertrand et al. [120, 121], issues related to potential radiation damage induced by the exposure of different types of pigments and paint materials to X-ray beams will be then described (Sect. 5). In the last part (Sect. 6), degradation phenomena due to chemical changes of selected classes of pigments will be reviewed, via the description of the most significant X-ray results obtained from historical paintings, related micro-samples and artificially aged paint mock-ups.

2 Analytical methods

2.1 Nano-/micro-scale SR X-ray methods

Among the various SR X-ray methods, XRF, XAS, and XRD are the ones that have been most frequently employed for the study of painting degradation phenomena over the last years. The complementarity of these methods, along with their non-destructive nature, low detection limits (in the case of XRF and fluorescence mode XAS), high-lateral resolution, and high chemical specificity (in the case of μ-XAS and μ-XRD), are all characteristics that are extremely desirable for the characterization of precious, heterogeneous, and complex materials, such as paint micro-samples.

In the field of pigments/paintings degradation, the growing use of SR-based XRF, XANES, and XRD, by themselves or in various combinations, is evidenced in Table 1. Between 2014 and 2024, more than 25 beamlines internationally offered the possibility to investigate pigments, paints, and corresponding alterations at the (sub)micrometer scale using different XRF, XANES, and XRD experimental set-ups. These configurations, including single-spectrum/diffractogram acquisition, 2D mapping/imaging, and tomographic analyses, have resulted in numerous publications.

Fundamentals and features of such SR-based micro/nano-analytical techniques are reviewed in the following paragraphs, with an overview of the most used experimental configurations for pigment and paint degradation studies at different synchrotron beamlines.

2.1.1 SR XRF and XAS: elemental characterization and speciation down to the nano-scale

XRF spectroscopy is commonly used for the determination of the elemental composition of many materials, including alloys, ceramics, glasses, geologic materials, as well

Table 1 Overview and characteristics of several beamlines that offer XRF, XANES, and XRD in different experimental configurations and that have been used for paints/pigments-related studies between 2014 and 2024

Beamline, facility, country	Experimental configurations	Energy range (keV)	Range or minimum beam size (v × h)	References by topics (2014–2024)
P06 (micro-hutch), PETRA III-DESY, Germany [122]	XRF mapping, XRF-CT, XRD imaging (transmission), XRD-CT, XANES imaging (XRF)	5–23 (KB) 15–90 (CRL)	Down to ~ 0.35 × 0.35 μm^2 (KB) 1.5 × 0.5 μm^2 (CRL)	Composition [95, 128–131], Degradation [14, 17–19, 32, 33, 46, 47, 71, 97, 101, 102, 108, 123–127], Radiation damage [120, 132]
ID13 (micro-branch), ESRF, France [133]	XRF mapping, XRD imaging (transmission)	12.7–20	2 × 2 μm^2	Composition [83, 138–140], Degradation [17, 27, 28, 55, 87, 97, 127, 134–138], Radiation damage [55, 95]
ID21, ESRF, France [141][a]	XRF mapping (single or multiple energies), XRD imaging (transmission), XANES point and imaging (transmission and XRF)	2.1–10	Down to ~ 0.3 × 0.7 μm^2 (microscope) Down to ~ < 0.2 × 0.2 μm^2 (new nanoscope)	Composition [22, 78, 83, 138, 139, 148–151], Degradation [46, 63, 65, 87, 101, 102, 106–108, 123–126, 135, 137, 142–146], Radiation damage [55, 132]
ID16B, ESRF, France [152]	XRF mapping (single or multiple energies), XRD imaging (transmission), XANES point (transmission and XRF)	4–30	0.05 × 0.05 μm^2–0.1 × 0.1 μm^2	Degradation [31, 46, 153]
BM01, ESRF, France	HR-XRD	10–22	500 × 500 μm^2	Composition [154]
ID22, ESRF, France [155]	HR-XRD	6–75	50 × 150 μm^2–1 × 1 mm^2	Composition/microstructure [55, 78–80, 82, 83, 139, 156–158]

Table 1 (continued)

Beamline, facility, country	Experimental configurations	Energy range (keV)	Range or minimum beam size (v × h)	References by topics (2014–2024)
BM02-D2AM, ESRF, France [159]	HR-XRD, XRD-CT	6–45	30 × 30 μm^2–5 × 5 mm^2	Composition [75, 76], Structure determination [5]
BM25-SpLine, ESRF, France	HR-XRD	5–45 (3–39.5)	0.4 × 0.5 mm^2–10 × 15 mm^2 (50 × 40 μm^2–5 × 5 mm^2)	Composition [160], Structure determination [161]
ID26, ESRF, France	XANES/EXAFS point (transmission, XRF, HERFD)	2.4–27.0	100 × 50 μm^2–500 × 100 μm^2	Radiation damage [132]
BM08-LISA, ESRF, France [162]	XANES/EXAFS point (transmission, XRF, TEY)	4–90	~ 100 × 50 μm^2	Local atomic structure determination [149], Degradation [145]
I18, DLS, UK [163]	XRF mapping (single or multiple energies), XRD imaging (transmission), XRD-CT, XANES point (transmission and XRF)	5–15	~ 2 × 2 μm^2	Degradation [72, 73, 164]
I11, DLS, UK [165]	HR-XRD	6–25 (typically 15)	0.8 × 2.5 mm^2	Structure determination [166, 167]
B18, DLS, UK [168]	ED-XRD	2.05–35	0.25 × 0.2 mm^2–1 × 1 mm^2	Composition [81]
XALOC, ALBA, Spain [169]	XRD point and imaging (transmission)	4.6–23 keV	Down to ~ 6 × 50 μm^2	Degradation [170]

Table 1 (continued)

Beamline, facility, country	Experimental configurations	Energy range (keV)	Range or minimum beam size (v × h)	References by topics (2014–2024)
MCX, Elettra, Italy [171]	XRD point (reflection)	6–21	0.3 × 0.3 mm^2–1 × 5 mm^2	Composition [56, 172]
PUMA, SOLEIL, France [173, 174]	XRF mapping (single or multiple energies), XRD imaging (transmission and reflection), XANES/EXAFS point (transmission and XRF)	4–20	1.5 × 3 μm^2	Composition [56], Degradation [14, 27, 175], Radiation damage [176]
DiffAbs, SOLEIL, France	XRD point and imaging (transmission and reflection), XANES/EXAFS point (transmission and XRF)	3–23	10 × 10 μm^2 (KB) – ~ 340 × 340 μm^2	Composition [178], Degradation [178] Radiation damage [179]
ODE, SOLEIL, France [180]	ED-XANES/EXAFS	3.5–25	Down to ~10 × 10 μm^2	Radiation damage [181]
MicroXAS, SLS[b], Switzerland	XRD imaging (transmission)	3–23	1 × 1 μm^2	Degradation [146]
PHOENIX X07MA/B, SLS, Switzerland	XANES/EXAFS point (transmission, XRF, HERFD, TEY)	0.4–8.0	~2.5 × 2.5 μm^2	Composition [83], Degradation [71, 99]

Table 1 (continued)

Beamline, facility, country	Experimental configurations	Energy range (keV)	Range or minimum beam size (v × h)	References by topics (2014–2024)
BL 2–3, SSRL, USA [182]	XRF mapping (single or multiple energies), XANES point and imaging (transmission and XRF)	5–24	~5 × 5 μm^2 – ~1 × 1 μm^2	Degradation [44, 65, 183, 184]
BL 6-2c, SSRL, USA [182]	Full-field X-ray transmission tomography (multiple energies)	2.4–17.5	0.2 × 0.4 mm^2	Degradation [183]
BL 7–2, SSRL, USA [182]	XRF mapping (single or multiple energies), XANES point (transmission and XRF)	5–16	25 × 25 μm^2 –250 × 250 μm^2	Degradation [184]
BL 14-3b, SSRL, USA [182]	XRF mapping (single or multiple energies), XANES point (transmission and XRF),	2.1–5	~5 × 5 μm^2 – ~1 × 1 μm^2	Composition [147], Radiation damage [185]
4-BM (XFM), NSLS-II, USA [186]	XRF mapping (single or multiple energies), XANES/EXAFS point (transmission, XRF)	2.1—21	Down to ~ 1 × 1 μm^2	Degradation [187]
BL15U1, SSRF, China [188]	XRF mapping, XANES/EXAFS point (transmission, XRF)	5–20	~2.5 × 2.5 μm^2	Degradation [189]
XFM, Australian Synchrotron, Australia [190]	XRF mapping, XRF-CT, XANES point (transmission, XRF), XANES imaging (XRF)	4.1–27	Down to ~5 × 5 μm^2 – ~1 × 1 μm^2	Degradation [123]

[a]The FT-IR, XRD, and transmission XANES imaging (full-field) end-stations of ID21 were discontinued after the ESRF-EBS upgrade
[b]Beamline characteristics before the SLS 2.0 upgrade

as paintings. In heritage science, such measurements are carried out non-invasively in situ with compact and easy-to-handle instruments, but also on fragments or samples by exploiting both laboratory set-ups and synchrotrons. XRF is characterized by the fact that the incident X-rays in general are more penetrating than other modes of ionization, so that this method is sensitive to the bulk of the material and not just the upper surface. SR-based XRF has the added benefit over traditional tube sources of using monochromatic X-rays that can be tuned to either ensure that a particular element is efficiently excited or to avoid potential interference. Furthermore, XRF generally is the first diagnostic measurement made in an X-ray experiment, particularly when micro-focusing is involved. Preliminary XRF measurements ensure that the areas of the materials being analyzed further (e.g., with XAS or XRD) contain the expected elements of interest.

XAS techniques have been used for the study of pigments and paintings for more than 2 decades, resulting in hundreds of publications (see [191–193] and references therein). The modification of the color of a pigment is related to a change of its composition and/or structure. Since XAS techniques probe the oxidation state, coordination geometry, and chemical environment of elements, it follows that they are very efficient in interpreting chromatic changes. This explains the success of XAS in heritage science, especially for the study of paintings. Figure 2 reports the number of publications in which XAS has been exploited to understand degradation phenomena (panel a) or to retrieve information about manufacturing processes (panel b). The publications are ordered as a function of elements of interest and relative pigments. Figure 2a shows that XAS has been extensively used for the study of the degradation of chrome and cadmium yellows, of arsenic-based yellows as well as of cinnabar/vermilion (see Sect. 6 for details). Sulfur is the most studied element, and this can be explained by two main reasons. First, it is present in many synthetic and natural sulfide pigments

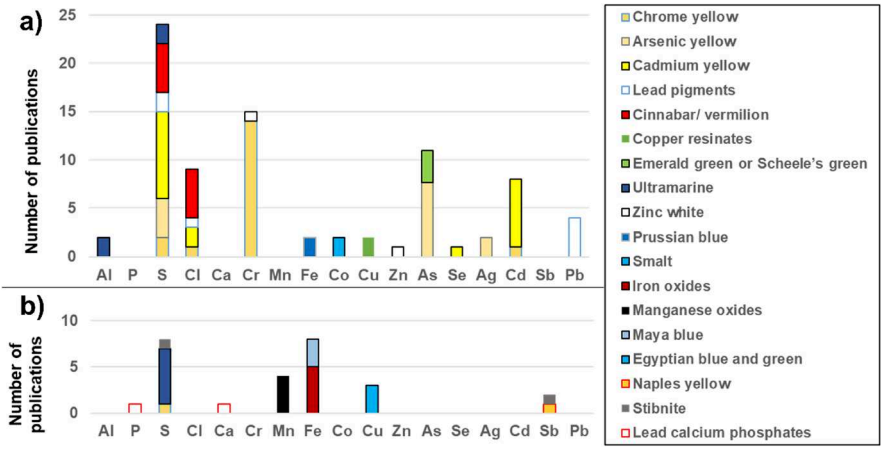

Fig. 2 Distribution of the articles (n. 104 in total) published on the XAS analysis of paintings over the last 30 years as a function of pigments (color), element of interest (x-axis), and main objective: **a** degradation of the pigment; **b** influence of the geographical sources and/or of the heat treatment on the composition and optical properties of the pigment

(e.g., $Cd_{1-x}Zn_xS$, $CdS_{1-x}Se_x$, HgS, and As_xS_y), in some chrome yellow pigments ($PbCr_{1-x}S_xO_4$) and in ultramarine, where its speciation (notably the polysulfide radical anion S_3^-) has a major influence on the blue hue [194]. Second, sulfur is also involved in some degradation processes as an external reactant, in the form of SO_2 (see for example the formation of lead sulfate crusts in par. 6.1) [195]. Similarly, many XAS analyses have probed the chemical environment of the element chlorine as it is regularly involved in alteration reactions (cf. Section 6). Figure 2b shows that, among the most studied pigments, there are iron and manganese oxides and lapis lazuli. This group of publications includes research about the influence of the geographical sources and/or of the heat treatment on the composition and optical properties of these materials.

General principles of XRF. The principle of XRF involves recording the X-rays emitted from a material after it has been excited by irradiation with (more energetic) X-rays. This process typically involves the absorption of X-rays, which leads to the ionization of a core-shell electron. The resulting electronically excited state of the material then returns to its ground state through radiative decay, producing characteristic X-ray emissions (Fig. 3).

The intensity of the X-ray fluorescence emission is dependent on several factors. First, there is the fluorescence yield of the element, which is the statistical probability that the decay of an excited state will lead to the emission of a characteristic X-ray photon. Other possibilities include the non-radiative decay that results in the emission of an Auger electron. Additionally, the decay of the excited state may involve one

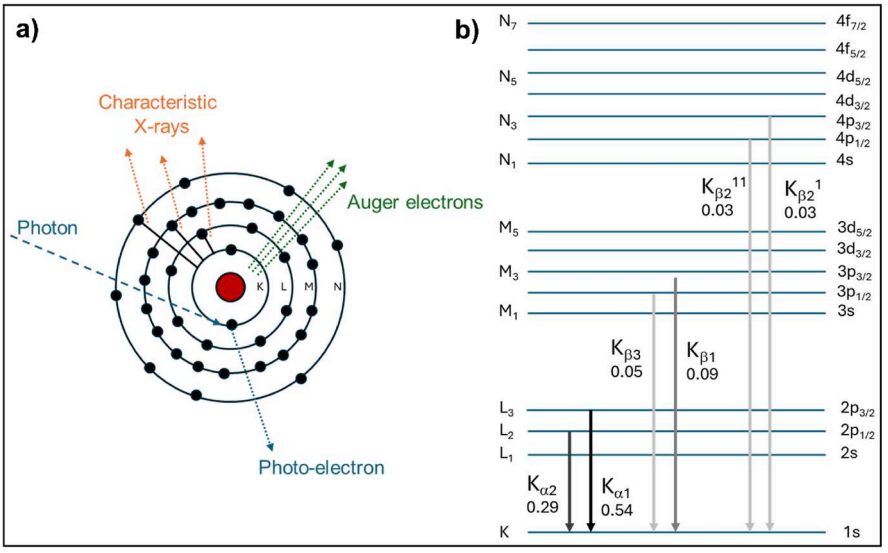

Fig. 3 **a** Excitation of an atom by an X-ray via the photoelectric effect. The ionization of the atom leads to the decay from the excited state by an electron from a higher energy level, leading to the emission of either a fluorescent X-ray or Auger electron. **b** Diagram of K shell radiative decays and their respective X-ray emission lines and rate

of many higher (i.e., less strongly bound) electron levels in the element, which leads to a statistical weighting of the production of various characteristic X-ray emission lines. Finally, the matrix in which the element is present may reabsorb a portion of the emitted X-ray photons, leading to a decrease in the measured signals. This last effect can be more prominent with lower energy X-ray photons and in thick samples where the emitted X-rays must travel through larger distances in the matrix.

The nomenclature of characteristic lines typically refers to the X-ray levels, or electron configuration, of the initial and final states of the radiative process. Commonly, Siegbahn notation [196] is often used to label X-ray lines based on the relative intensities of the emissions (e.g., Cu-Kα_1), although the IUPAC recommendation is naming the X-ray transitions by referring to the initial and final X-ray levels separated by a hyphen (e.g., Cu K-L_3). More details on specifics of X-ray levels and naming can be found in the International Tables of Crystallography, Volume C [197].

Several sources of tabulated X-ray data exist, and the compilation of Elam et al. [198] provides a comprehensive tabulation of values and critical parameters that can be used to determine most X-ray properties, including the excitation edge energies, X-ray emission lines, and fluorescence yields. These parameters and compilations are the foundation for many computer codes that are used in the calculation of X-ray properties [199–201].

As micro-XRF data typically consist of full fluorescence emission spectra at each location on the sample, the data can be roughly "binned" into XRF regions of interest (ROI) for rapid examination of the fluorescence intensity of a characteristic line (Fig. 4a,b). While this can be done rapidly for quick viewing, it fails to account for background contributions or overlapping peak artifacts. A more thorough data analysis involves integrating the spectrum using knowledge of the elements to be analyzed and their characteristic lines and taking the absorption of the incident and emissions X-rays by the sample matrix into account.

General principles of XAS. The family of XAS techniques is based on measuring the sample absorption coefficient $\mu(E)$ as a function of the energy of the incoming X-ray beam. It provides information on the local structure around a chosen element of

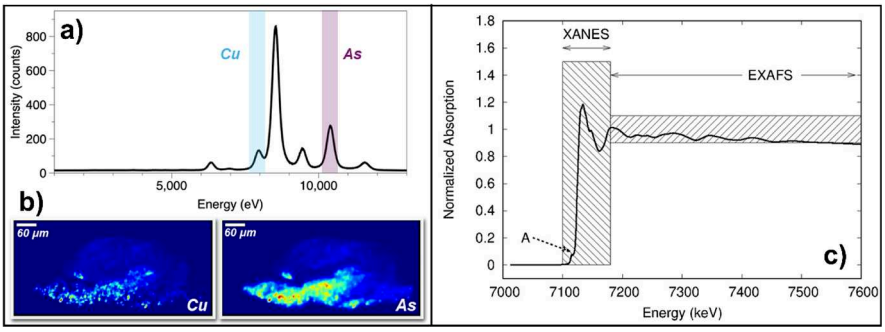

Fig. 4 Examples of **a** XRF spectrum, **b** 2D µ-XRF maps (here the Cu and As maps of a paint cross-section), and **c** the EXAFS and XANES regions in a Fe_2O_3 (hematite) XAS spectrum collected at ESRF-BM08-LISA beamline with a Si (111) monochromator

interest from the features appearing on the absorption spectrum at and above a given absorption edge. The XAS spectrum can be divided into two zones corresponding to different energy regions: the X-ray Absorption Near Edge Structure (XANES) part is that around the absorption edge up to about 150 eV, whereas the Extended X-ray Absorption Fine Structure (EXAFS) part extends up to 1–2 keV (Fig. 4c). Different types of information can be retrieved from these two zones, as discussed below.

The features present in the XAS spectrum can be explained as follows: after the absorption of a photon from a core state |i> of a given atom, an electron from that state is emitted in the continuum of conduction band states. This photoelectron can be viewed as a spherical wave outgoing from the atom and this wave will interact with the electronic charge density of the surrounding atoms by being partially backscattered. The final electron state <f| will then be the sum of the original outgoing wave and the partially scattered waves. In this vision, the absorption cross-section of photons can be derived from Fermi's Golden Rule (Eq. 1) [202–204]

$$\mu(E) \propto \sum_{f}^{E_f > E_F} |\langle f|\hat{\epsilon}\cdot r|i\rangle|^2 \delta\left(E_i - E_f - \hbar\omega\right). \tag{1}$$

The |i> state is a deep core state (e.g., 1s, 2s, $2p_{1/2}$, and $2p_{3/2}$) and it will be nonzero only in a small spatial region around the nucleus. Consequently, the integral in Eq. 1 will be proportional to the amplitude of <f| near the nucleus depending on how the partial waves (scattered by the various neighbors) will sum in phase or in antiphase. An oscillatory behavior will be observed, that is the origin of the features above the edge. The absorption coefficient μ(E) can be found either with the Multiple Scattering (MS) approximation [202, 204] or, in an exact way, via the Full Multiple Scattering approach (FMS) [205]. The former method is used for the calculation of EXAFS spectra, whereas the FMS method is used for the analysis of the XANES region.

XANES spectra can also be analyzed in more direct ways. As an example, the valence state of the atom can be derived from the position of the edge, as it has been shown that positively charged ions exhibit a shift of several eV toward higher energies compared to the metallic state [206]. This property has been regularly used to differentiate, for example, sulfur in sulfide (2−) and sulfate (6+) compounds in degraded pigments [191]. Moreover, in cases involving 3d metals such as Cr or Fe, the local site symmetry (either tetrahedral or octahedral) can be derived by considering the peaks appearing just before the absorption edge (noted A in Fig. 4c). In the case of iron, it is possible in this way to obtain a complete description of both valence state and local symmetry [207]. Similarly, the pre-edge peak intensity in Cr K-edge XANES spectra is a highly effective diagnostic parameter for monitoring the degradation of chromate-based pigments (see par. 6.7).

XRF and XAS experimental configurations. From a practical point of view, there are many options to be considered in the acquisition of XRF and XAS spectra, from the source to the detector (Fig. 5a). The text below focuses on the most used configurations for the study of painting degradation, but the list is not exhaustive. Depending on the information needed (e.g., element of interest, sample composition, sample heterogeneity, etc.), the choice of set-up and of beamline needs to be refined.

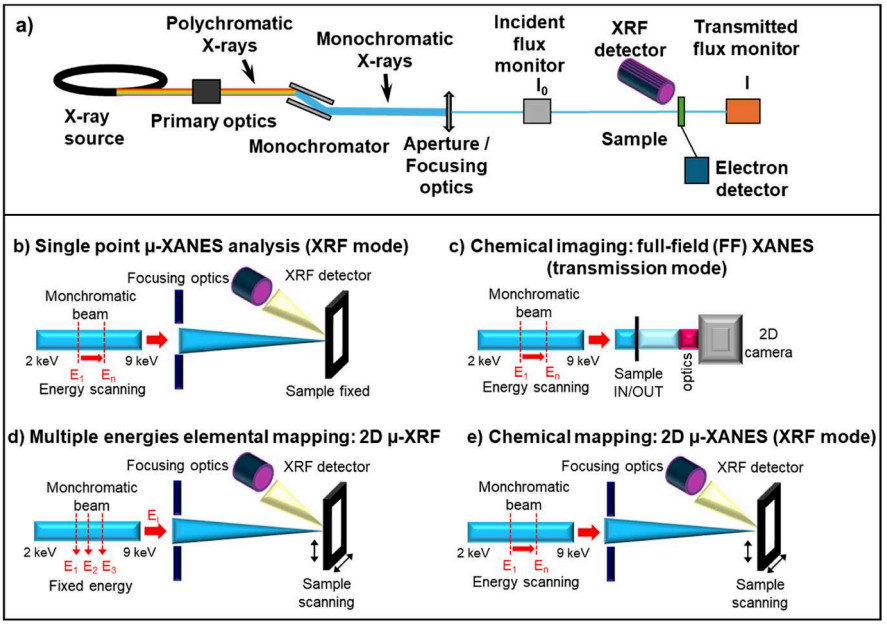

Fig. 5 Experimental configurations for XRF and XAS analysis. **a** Main instrumental components needed to record μ-XRF maps and μ-XAS data. **b–e** Four main instrumental set-ups for the acquisition of XAS single-point spectra or 2D maps

Regarding X-ray sources, conventionally, synchrotron facilities offer an intense X-ray source with an extended spectral range. In a standard XRF/XAS set-up, a double-crystal monochromator is used for the precise selection of the X-ray energy. The most commonly used crystal is Si(111) (d ~ 3.135 Å, $\Delta E/E \sim 2\ 10^{-4}$).

The beam size is also a factor to be considered in relation to the heterogeneity of the samples. Depending on the beamline and on the use of focusing optics, the beam size can vary from a few millimeters to less than 100 nm. For the study of reference materials (powders) or mock-up samples that can be considered homogeneous at the scale of some 0.1 mm, it is better to use a large unfocussed beam, the size of which is defined by slits or pinholes. However, for the study of heterogeneous samples (historical samples or artificially aged mock-ups samples studied along their stratigraphy), the use of a focused beam is usually required. Different focusing optics exist, either based on total reflection (e.g., polycapillaries or mirrors) [208–210], diffraction (e.g., zone plates) [211, 212], or refraction [compact refractive lenses (CRL)] [213]. The choice of optics often depends on the parameters desired for the experiment, including overall flux, beam size, achromaticity of the focusing, and working distance of the optic to the sample. For X-ray spectroscopy, the achromatic Kirkpatrick–Baez (KB) mirrors are usually preferred. Large beams can also be used for the study of heterogeneous samples when their heterogeneity is probed thanks to 2D detectors in the "full-field" (FF) mode, as an alternative to the more common micro/nanobeam scanning mode. In the ~ 100 publications reporting the XAS analysis of paintings, about 2/3 have been carried

out with a (sub)-micrometric beam. This proportion increases to ¾ if the corpus is restricted to experiments tackling paint degradation. Indeed, the degradation layers are usually only a few micrometers in thickness on top of the non-degraded layers, and their precise analysis requires the use of (sub-)micrometric X-ray probes. So far, there have been only few nano-XANES analyses of degraded pigments (with a beam of ~ 100 × 100 nm^2 at ID16B, cf. Table 1) [31, 46, 153]. However, with the increasing number of nano-XAS beamlines worldwide, especially with the implementation of an X-ray nano-scope at ESRF-ID21, it is highly probable that nano-XAS will should soon be regularly exploited to analyze painting degradation processes.

The sample stage is usually designed in relation to the beam size. Beamlines dedicated to bulk-XAS/XRF often provide the possibility to mount large objects, while micro- and nano-beamlines, which require accurate scanning capabilities with precisions down to ~ 10 nm, usually restrict the maximum size to ~ < 1 cm and are well suited for the detailed analysis of paint fragments. As the focused X-ray beam is static for photons (i.e., its position cannot be easily changed unlike electrostatic focusing of electron beams), the sample must be raster-scanned spatially in front of the focused beam to create an image. This contrasts with portable macro-XRF (MA-XRF) imaging devices, in which X-rays are produced by an X-ray tube and the X-ray source, focusing, and detection equipment is mounted on a gantry that can be spatially rastered in front of the object under study (see below, par. 2.2). An X-ray emission spectrum is collected at each location of interest on the sample. A data collection modality that involves stopping sample motion to collect spectra at each location repeatedly over many thousands to millions of pixels would take a prohibitively long amount of experimental time. With the large incident flux at third- and fourth-generation light sources, the sample can be moved continuously in front of the X-ray beam and data collected "on the fly" in a continuous scanning mode [214]. This reduces data collection to several/tens of milliseconds per pixel with little overhead from the motors stopping and starting.

Most XRF measurements have been performed on some type of 2D projections, typically on small, extracted samples from historical paintings, mock-ups, a simple pigment powders, or full works of art. In such cases, samples are scanned along a plane. Although samples are inherently 3D, the penetrating nature of the X-ray beam projects the volume onto a 2D dataset. However, if a series of 2D XRF maps is successively recorded while rotating the sample (i.e., changing the angle between the incident beam and the 2D plane), a 3D XRF tomographic dataset can be obtained. Furthermore, a combination of X-ray ptychography with hard XRF tomography has been used to examine the 3D microstructure and composition of a specimen. This has recently been applied to a historical paint sample from Rembrandt's *The Night Watch*, where the analysis has led to the discovery of a "hidden" Pb layer, located between the canvas and the quartz-clay ground layer [95]. This approach was particularly useful because ptychography enabled the visualization of components not readily visible with traditional XRF, such as the quartz and organic fractions of the paint. Correlating the sample volume with tomographic XRF then allowed for the superposition of these layers onto the XRF volume data of the major elements constituting the paint, such as Pb.

Regarding the samples themselves, most are paint fragments (from historical works of art or from paint mock-ups). However, XRF and XAS data are occasionally acquired directly from entire objects, as done recently on book covers [184] or daguerreotypes [215]. For the study of low Z elements (< Ca), it is recommended to operate under vacuum to avoid air absorption and scattering. Advice regarding sample preparation is given in Sect. 4. Concerning the sample environment, X-ray penetration is a strong asset making it possible for XAS data to be recorded in various in situ conditions (such as high pressure, high temperature, gas reactions, etc.). This capability is rarely exploited for the studies of painting degradation, which often are limited to analyzing samples in static and ambient conditions. In this respect, it is relevant to point out that cryo-preservation aids in slowing down radiation damage phenomena, as quantified in a study of degradation of chrome yellow pigments during XANES analyses [132].

Regarding detectors, XAS data can be recorded directly or indirectly using different detection modalities (Fig. 5b–e). In its most basic configuration, XAS spectra are measured directly in transmission mode. Two detectors are placed upstream and downstream of the sample, to record the incident (I_0) and transmitted (I) beam intensities, respectively. The linear absorption coefficient $\mu(E)$ is defined according to Eqs. 2 and 3 as

$$I = I_0 e^{-\mu(E)t} \tag{2}$$

$$\mu(E)t = -\ln(I/I_0), \tag{3}$$

where t is the thickness of the sample. This configuration imposes constraints on sample preparation and composition. If the element of interest is too concentrated or the sample too thick, the attenuation is too high and XAS features may be flattened. Conversely, if the element of interest is too diluted or the sample too thin, the edge structures may be lost in the noise on the background signal.

The following conditions are given to estimate the appropriate absorption conditions:

(i) The total absorption above the edge must not be too high: $\mu_{\text{above edge}} \times t \sim 2$–$5$, meaning that $I/I_0 \sim 0.14$–0.007. Ideally $\mu_{\text{above edge}} \times t \sim 2$–$3$. Note that this criterion should be considered in the zones of high absorption (the so-called white lines).

(ii) The contrast at edge must be as large as possible: $[\mu_{\text{above edge}} - \mu_{\text{below edge}}] \times t > 0.1$. Ideally, $[\mu_{\text{above edge}} - \mu_{\text{below edge}}] \times t = 1$.

In the context of cultural heritage materials, transmission mode is typically used for the acquisition of XAS spectra of reference materials (usually powders spread on tape or prepared as pellets). In a few cases, thin sections of paint can be prepared with appropriate thickness suitable for transmission.

Generally, the intensity of the transmitted beam is measured with a photodiode or with a gas detector. Occasionally, it is recorded with a pixelated detector, providing 2D information about the heterogeneity of the sample and the spatial distribution of the different species. In the past, the ID21 beamline at the ESRF was equipped with an FF mode XANES set-up (Fig. 5c), allowing to obtain spectral images in a large

field of view (~ 2 × 2 mm^2) via the acquisition of hundreds of X-ray radiographs [216, 217]. This set-up has been notably used to study the degradation of cadmium yellows in Henri Matisse paintings [218], as well as for the identification of spectral markers in heat-treated lapis lazuli rocks used to extract ultramarine blue [148]. More generally, some beamlines offer the possibility to combine spectroscopy and 3D imaging, through repeated acquisitions of X-ray tomographic datasets at different energies. This approach has recently been exploited to image the distribution of different arsenic species in a degraded orpiment pigment [183]. While it can be extended to spectro-ptychography by acquiring high-resolution ptychography images or tomographic volumes at several energies [219], this method has not yet been applied to the study of paint degradation phenomena.

Alternatively to transmission, XAS data can be recorded indirectly in XRF mode, which is the most frequent detection mode for the study of paint degradation (Fig. 5b,d,e). X-ray detection is typically performed using a solid-state Si or Ge detector that measures both the number of incident photons and their individual energies. This type of detection is crucial, as the XRF experiment relies on its ability to distinguish the difference between the various characteristic XRF emission lines. Si detectors typically exhibit an energy resolution of ~ 120 eV at 5 keV, while Ge detectors achieve around 200 eV resolution [220, 221] at the typical count rates used in XAS analyses. Si detectors are more commonly used, due to their slightly better resolution. However, Ge detectors may be preferred for the detection of higher energy photons (typically > 15 keV) owing to their enhanced absorption of hard X-rays compared to Si at these energies. Recent advancements in Si detector technology also include thicker Si detector elements, which further improve sensitivity [222]. Over the last decade, significant efforts have been dedicated to improving the XRF detector solid angle and acquisition speed, enabling to reach millisecond acquisition times per XRF spectrum, (i.e., per XAS energy increment) [123]. Such short collection times can be realized via the use of multi-element detectors, i.e., a detector that has several Si or Ge sensors integrated into the same system. As a broader extension of this, arrays of small-sized Si elements have been created [223, 224], although their energy resolution is generally worse (> 250 eV) [225]. To increase the sensitivity of XAS, the XRF intensity is cumulated within a specific range of detector channels around the emission of the element of interest, excluding emissions at lower energies as well as scattering signals (cf. Figure 4a). By placing a collecting X-ray objective (usually a polycapillary) between the sample and the XRF detector, it is also possible to perform μ-XANES in confocal-mode, which provides in-depth information about the distribution of species. A clear illustration of this is its application to the study of copper colorant in ancient lead-silica glassy systems [188].

More recently, the implementation of crystal analyzer spectrometers with a ~ 1 eV energy resolution at XAS beamlines has led to the development of High-Energy Resolution Fluorescence Detected XAS (HERFD-XAS). This technique outperforms traditional XAS, acquired with standard XRF detectors, in terms of: (i) sensitivity (especially when the XRF of an element from the matrix overlaps with the emission of the element of interest) and (ii) the sharpness of the XANES spectra, enabling more accurate species differentiation [226]. It is expected that such HERFD-XAS set-ups

will soon offer unprecedented results in the field of pigment degradation, notably for the study of Hg and Pb L-edge XANES.

When information on the sample at its surface is sought, an appropriate XAS data collection mode is Total Electron Yield (TEY). This technique is based on the detection of the secondary electrons produced by the XAS process (photoelectrons and Auger electrons) via a collecting anode polarized at a positive potential placed in front of the sample. Due to the high interaction cross-section of electrons within materials, it is possible to detect only electrons coming from about 50–200 nm below the surface [192, 227]. This capability has been particularly effective studying the surface layer of ceramics [228] and of paintings, as shown in the case of chrome yellows [145].

Finally, while XRF imaging can display the distribution of a set of relevant elements, for the degradation of paints, it is often the combination of distribution and chemical speciation data that is of the most importance. This can be done by selecting individual, localized points of interest from an initial XRF map and recording full XAS spectra at these locations. Alternatively, a XANES mapping/imaging experiment can be performed via tuning of the energy of the incident X-ray beam to values that show maximum contrast in the different species of the element of interest and acquiring a set of μ-XRF maps from the same region of interest. From these maps, either a set of multi-variate analysis techniques, i.e., principal component analysis (PCA), non-negative matrix factorization (NNMF), or linear combination fitting (LCF), can be employed to create speciation maps (cf. Section 3).

2.1.2 SR XRD: identification of crystalline phases at the micro-scale

XRD methods are used for advanced structural analyses of cultural heritage materials [229]. Compared to what was discussed above for XRF, which is limited to elemental information, XRD gives access to specific structural information. The high brightness and continuous range of X-ray energies available at synchrotron facilities, together with advances in fast XRD detectors, have made XRD beamlines increasingly popular for cultural heritage studies over the past 10 years (see Table 1 and [230]). Using various focusing optics, SR μ-XRD in imaging mode permits the characterization of the distribution of phases within heterogeneous paint materials at the micro-scale length. This makes the technique particularly suited to investigate the (often very superficial) degradation processes occurring within paint samples [231]. Beyond imaging, HR-XRD is increasingly used for accurate pigment composition quantification, microstructure analysis (crystallite size and strain), and comprehensive determination of unknown or incomplete crystal structures [55].

General principles and structural information. XRD exploits the constructive interference of elastically scattered X-rays (of wavelength λ) by the atoms composing a crystalline structure. When an X-ray interacts with an ensemble of randomly oriented crystallites, a sufficient number of those crystallites should have a suitable orientation for the diffraction phenomenon to take place along the reflection angle 2θ. If the beam size is (much) larger than the size of the randomly oriented crystals, so-called Debye–Scherrer rings (Fig. 6, step 1) with a uniform intensity distribution are observed in the diffraction pattern. For this reason, SR HR-XRD experiments are performed using larger beams (> 100 μm; cf. Table 1). In the opposite case, when the

beam is small (< few μm) and only a small number of crystallites are irradiated, the pattern is limited to several bright diffraction spots resulting in an erratic intensity profile (Fig. 6, step 2). For studies related to pigment and paint degradation, most SR μ-XRD experiments assume the first case, while for the second one, many diffraction patterns with comparable composition can be averaged to obtain a more 'powder-like' pattern.

Different information can be derived from a diffraction pattern by examining the intensity variation, either along the scattering (2θ) or the azimuthal (γ) angles. Through integration of the 2D diffraction image over the azimuth, the obtained 1D diffraction pattern shows an intensity variation of the diffracted radiation as a function of 2θ, where each peak corresponds to a specific interplanar distance (d). The position of these peaks follows Bragg's law: $n\lambda = 2d\sin(\theta)$, where n is a positive integer indicating the diffraction order. This information is used to identify the crystalline phases (either

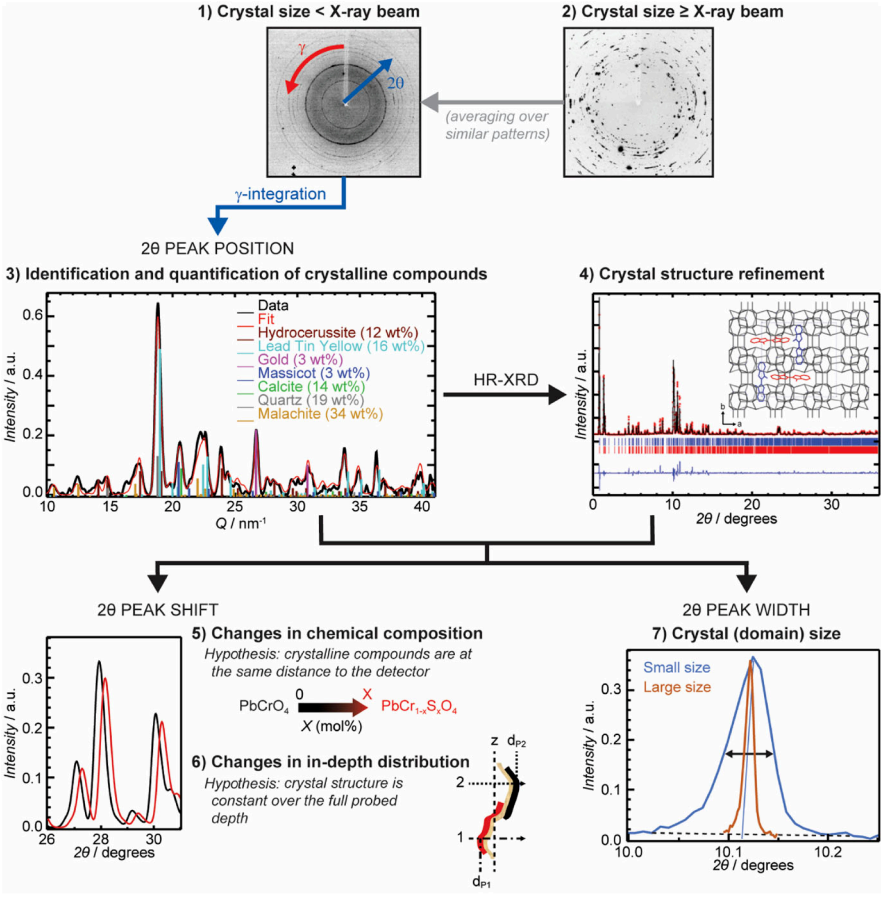

Fig. 6 Schematic illustration of structural information commonly extracted from SR XRD within paint (degradation) studies. Adapted with permission from [231, 232]

original compounds or degradation products) present in a material (Fig. 6, step 3) by comparing the peak positions and relative intensities with databases of reference compounds, such as the ICDD (International Centre for Diffraction Data) or COD (Crystallography Open Database). Using SR HR-XRD, the improved data quality in terms of LOD and the reduction of instrumental broadening further enables crystal structure refinement/determination (Fig. 6, step 4).

Qualitative identification by XRD allows secondary compounds of paint layers to be distinguished. New insights into the degradation pathways of historical pigments in paint matrixes were therefore often obtained using XRD, as shown for example for lead whites [14, 73, 134], red lead [19], chrome yellows [108, 233], cadmium yellows [87, 97, 101, 102, 124, 125, 135], cinnabar or vermilion [12, 234], and orpiment [32, 33, 46].

While crystalline phase identification is usually the first step in any compositional analysis of paint, more subtle chemical differences can be derived from slight variations in the position of the diffraction peaks. For example, these variations can be caused by a slight modification of the lattice parameters of a crystalline phase, such as, through substitution of CrO_4^{2-} ions with SO_4^{2-} ions within the crystal structure of chrome yellow (Fig. 6, step 5). For this pigment, with the general formula $PbCr_{1-x}S_xO_4$, the substitution degree x not only affects the shade of yellow but also determines its stability to light and its tendency to form a green–brown superficial degradation layer. This has been demonstrated in several paintings by Vincent van Gogh, including the Amsterdam *Sunflowers* (see par. 6.7 for details and [10, 11]). On the other hand, the peak position is also influenced by slight variations in the distance between the diffracting material and the XRD detector. This effect can be exploited to obtain stratigraphic information of the crystalline phases (Fig. 6, step 6). So far, only a few studies have employed this for differentiating pigments in various paint layers [128, 235–237]; nevertheless, this could similarly be useful when investigating the stratigraphic distribution of degradation products within the paint.

The width of the XRD signals also contains information about the material under investigation. Diffraction peaks can be broadened by several physical effects, such as crystallite size and strain. The amount of broadening can be quantified using the Full-Width-at-Half-Maximum (FWHM) of the diffraction peaks. The FWHM of a diffraction peak increases with decreasing dimensions of crystallites (Scherrer broadening). This information can be used to estimate the size of crystalline domains, and sometimes provide clues about crystal formation (e.g., natural minerals versus synthetic compounds, crystals formed through precipitation, etc.) (Fig. 6, step 7). Gonzalez et al. [17] carried out an investigation on the paint formulations employed by Rembrandt van Rijn in *The Night Watch*, showing that, in a single paint sample, two subtypes of hydrocerussite [$Pb_3(CO_3)_2(OH)_2$], a phase component of the lead white pigment, were present: (i) the original lead-white pigment showing narrow diffraction signals, thus corresponding to a large (> 1 μm) crystal size; (ii) neo-formed hydrocerussite with nanosized crystals, that was thought to be the result of chemical transformations within the paint layers.

XRD experimental configurations. Based on the overview provided by Table 1, it becomes clear that different XRD experimental configurations are being used for paint-related studies. In the past 10 years, XRD imaging modes are increasingly being

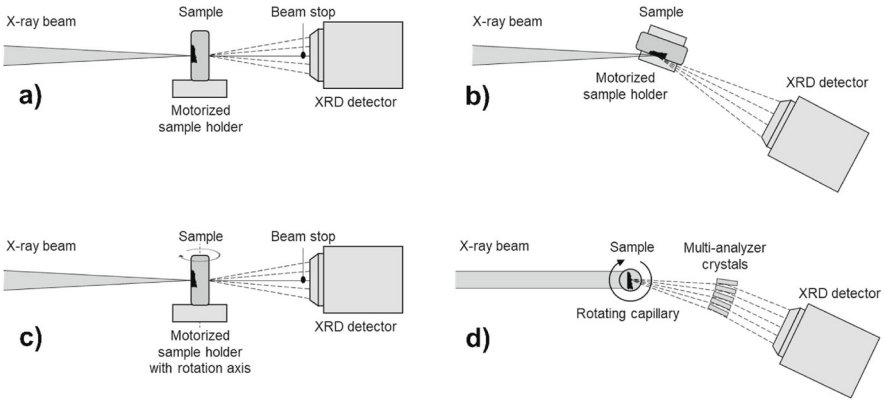

Fig. 7 Schematic view of different XRD data collection modes: **a** XRD imaging in transmission, **b** XRD imaging in reflection, **c** XRD tomography, and **d** HR-XRD using a rotating capillary and several multi-analyzer crystals

used to directly visualize degradation products within paint layers with a thickness of a few micrometers. In what follows, different XRD data collection modes along with their advantages and limitations are shortly summarized. Less frequently used methods, such as energy-dispersive XRD, will not be discussed, although these are also suitable for the study of paints in back-reflection geometry, as described by Hiley et al. [81].

For SR μ-XRD imaging in transmission geometry, the sample is placed perpendicular to the incident beam, while the XRD detector is positioned on the opposite side (Fig. 7a). As such, transmission SR μ-XRD requires a sufficiently high energy to reduce attenuation and penetrate the entire sample. This effect can also be achieved using an energy that is slightly lower than the X-ray absorption edge of the main (heavy) elemental constituent of the paint. Such types of experiments have been carried out on lead-containing paint cross-sections, using an incident beam at 13 keV, i.e., just below the Pb L_3-edge [55]. Furthermore, for compounds with a high d-spacing (e.g., metal soaps), a lower energy is preferred, as the detection of signals at small 2θ angles is often hampered by primary beam scatter or by the extent/position of the beam stop. The use of fast X-ray sensitive area detectors brings additional benefits, since they permit to reduce dwell times and minimize the effect of crystals with a size larger than the beam size (> few μm). In transmission mode, the detector is often centered on the beam axis (downstream a beam stop), but it can be of interest to place it out of axis, for example to extend the detected angular range. For transmission mode analysis, samples are often prepared as embedded cross-sections or thin sections, so that the paint stratigraphy is visible. When possible, thin sections are preferred to better control homogeneity along the path of the beam as poorly oriented cross-sections can cause two spatially resolved layers to become undistinguishable within the XRD data. According to Table 1, transmission mode SR μ-XRD imaging has been often used to investigate the pigment composition and to shed light on degradation phenomena in paint cross-sections.

Even if less commonly applied, XRD imaging experiments in reflection mode might be a valuable alternative to those carried out in transmission mode. In this geometry, the detector and X-ray beam are positioned on the same side of the sample (Fig. 7b). Samples or fragments too thick for transmission XRD can thus still be analyzed, although reflection XRD will only probe their superficial layers (several tens of microns in depth). Due to the elliptical footprint of the beam, it is recommended to scan with the smaller beam dimension (usually vertical) along the sample dimension with the highest heterogeneity. A lower energy is typically preferable to probe more superficial layers and to increase the angle of the diffracted X-rays, as diffraction angles smaller than the incident angle are absorbed by the sample. Reflection SR μ-XRD was recently used to study the discoloration processes in large (several cm^2) heterogeneous mural paint fragments from the upper Basilica di of San Francesco in Assisi [14].

While most SR μ-XRD imaging experiments are carried out in 2D, the third dimension can be accessed through computed tomography (CT) by rotating the sample around an axis perpendicular to the incident beam (Fig. 7c) [238, 239]. At every rotation angle, a 1D XRD line is acquired. The intensity of a particular phase for each translational and rotational position is represented in a sinogram. After reconstruction, 2D compound-specific virtual slices are obtained. Some data pre-processing can be performed before or during azimuthal integration to remove intense diffraction spots from the powder data as they create artifacts in the tomographic reconstruction. SR XRD-CT is well suited for locating crystalline phases within a non-flat 3D structure and has been used to identify and localize degradation products within paint fragments for red lead and lead white [9, 64]. As SR XRD-CT is usually very time-intensive, care must be taken to reach a compromise between parameters, such as the spatial and angular resolution, dwell time, and size of the imaged cross-sectional area. While SR XRD-CT in 3D is now possible (e.g., for studying consolidation treatments in stone monuments [240]), its application to the study of paint degradation has so far been rare [164]. To reduce computing time and automate parts of the data processing, the usefulness of multi-variate analysis methods for these large datasets is being explored [241].

Contrary to the previously discussed techniques, SR HR-XRD is not an imaging modality, but it contributes to add knowledge about paint degradation phenomena by accurately quantifying the composition of paints/pigments and by gaining insights into their microstructure. Diffraction patterns from paint fragments and powders are collected with an excellent angular resolution and a strong reduction of preferred orientation effects. To achieve the highest angular resolution, analyzer crystals (e.g., Si 111) on a multi-analyzer stage can be used in combination with an area detector or with scintillator counters (Fig. 7d). The high-quality XRD datasets, for example, have been used to elucidate the structure of various lead soaps [161], to accurately quantify the relative abundance of different crystalline phases in a sample through Rietveld refinement and to estimate the size of crystallites based on the width of the diffraction signals using the Williamson–Hall plot. While powders are most frequently measured, also data from historical paint fragments can be obtained, as shown for the pigment lead white used by Old Masters for which the composition and microstructure was investigated [78, 79, 156].

2.2 Macro-scale X-ray imaging methods

2.2.1 2D imaging

Next to various SR-based X-ray methods that are used to examine minuscule paint samples at the (sub)micrometer scale, in the last two decades, different X-ray based methods have been developed to examine works of art in a non-invasive manner, i.e., without any sampling. Both macroscopic XRF (MA-XRF) and macroscopic XRD (MA-XRD) find their origin in the microscopic equipment exploited at SR facilities However, they differ in several key aspects: (i) They employ scan areas that typically are at the 0.1–1 m^2 rather than the 0.1–1 mm^2 scale; (ii) they yield images with a lateral resolution/pixel size generally around 0.5–1 mm rather than of 0.5–1 μm; (iii) they make use of micro-focus X-ray tubes instead of synchrotron facilities as a source of X-rays, allowing the scanning equipment to be moved inside museums and picture galleries for in situ examination of the works of art [242–244]. The working principle of MA-XRF and MA-XRD is shown in Fig. 8; these methods usually operate in reflection mode, so that the artworks under study can remain stationary, while the scanner is responsible for moving its measuring head in an XY fashion relative to the painting. In the case of MA-XRF, the high penetrating power of X-rays not only allows for the mapping of elements on the paint surface but also enables the detection of materials deeper within the paint stratigraphy. This capability can, in some cases, reveals paint

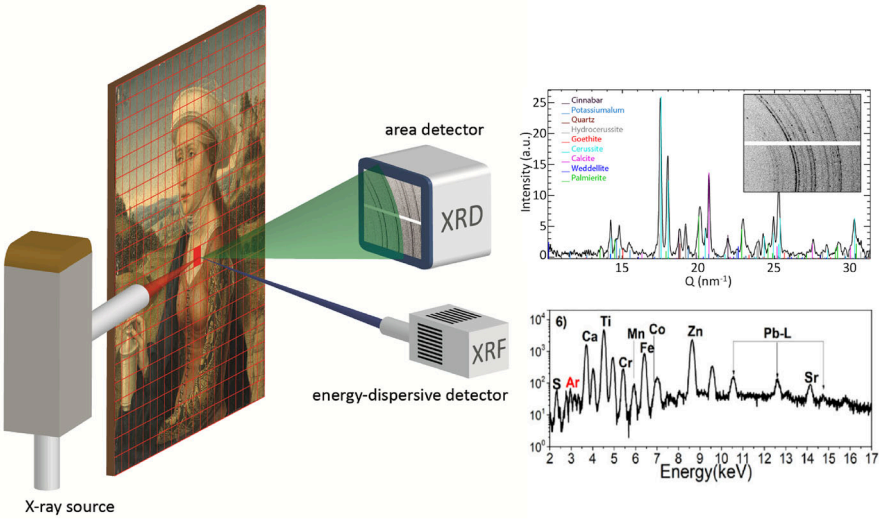

Fig. 8 Principle of MA-XRF and MA-XRD scanning. A primary X-ray beam (red) is sequentially scanned over a work of art, while at each irradiated position, XRF (blue) and XRD (green) signals are recorded by means of suitable detectors. Either the work of art is moved in an XY fashion, while the X-ray source and detectors remain stationary, or the X-ray components are moved relative to a stationary artwork. Next to each detector, a typical example of the resulting spectral distributions per pixel is shown. Adapted with permission from [112]

layers invisible to the naked eye. In this way, completely hidden compositions can be made visible again in a non-invasive manner [245, 246].

MA-XRF was first introduced in 2008 [242, 245, 247–250] during a pioneering experiment at the synchrotron facility DORIS-III (DESY, Hamburg). Now, it is a mature, mainstream technique, employed in many museums and cultural heritage institutions worldwide. Mobile MA-XRF instruments were developed that allow scanning experiments to be performed inside museums or art galleries, where the works of art are normally on display or conserved. MA-XRF involves the (moderately fast) scanning of an X-ray source and XRF detector assembly relative to a work of art or vice versa. The X-ray source is equipped with a collimator or focusing system that produces a polychromatic X-ray millibeam, generally of 200–500 μm diameter.

With typical dwell times of 50–200 ms per point, a (very) large number of XRF spectra (of the order of one to several million spectra/artwork) are recorded, yielding (after appropriate spectrum evaluation) large-scale elemental maps [251]. Thanks to MA-XRF scanners, it has become possible to examine a great variety of artworks by well-known artists, including Peter Paul Rubens [252, 253], Rembrandt van Rijn [254–256], Johannes Vermeer [257], Francisco Goya [258], Paul Gauguin [259], Vincent van Gogh [108, 247, 260], René Magritte [261, 262], Paul Delvaux [263], Piet Mondrian [264], Jackson Pollock [265], and others. The aim of these investigations is usually to discover new information on their history and/or on their current state of conservation [33, 52, 102, 266]. Next to oil paintings on panel or canvas, also other types of cultural heritage objects can be examined, including illuminated manuscripts and scrolls [267–270], printed and hand-colored books [271, 272], stained-glass windows [273, 274], ceramic tile tableaus, heritage textiles, shrouds and leather wall coverings [267, 275, 276], bronze statues, and silver coins [277, 278].

Several X-ray instrumentation manufacturers and research institutions have described MA-XRF scanners of their own making [279–282]. A recent trend both in the commercial as in the self-built instruments is to employ more than one (for example 2, 4, 6) XRF detectors for signal collection in a close coupled geometry to speed up the entire scanning process accordingly [281]. Since 2015, a bi-annual MA-XRF conference has been organized [in Antwerp (2015), Trieste (2017) [283], Catania (2019) [284], Delft (2022), and Washington D.C. (2024) [285]], with a typical number of 100–150 participants. A consultation of the Web of Science performed in August 2024 revealed that since 2021, annually about 50 papers explicitly mentioning MA-XRF are being published, collecting ca. 600 citations per year. Several reviews about the various applications of MA-XRF illustrate the wide use of this technique within heritage science [116, 286–288]. In some articles, chemometric methods and machine learning techniques have been used to extract relevant information from raw MA-XRF data blocks, making the approach more friendly for non-expert users [289–295].

However, MA-XRF can only provide information on the distribution of elements and, for example, cannot distinguish between lead white [usually mainly $2PbCO_3 \cdot Pb(OH)_2$], red lead (Pb_3O_4), and other lead-based pigments. MA-XRD was developed during the last decade to complement MA-XRF, providing information on the crystal structure rather than the elemental composition of solid materials. As opposed to XRF, where the secondary radiation has a (much) lower energy than the X-rays employed, XRD originates from the constructive interference of elastically

scattered X-rays (of wavelength λ) by the atoms composing a crystalline structure. Thus, the diffracted signals emerging from an irradiated sample/objects have the same energy as that of the primary, monochromatic radiation (cf. par. 2.1.2). Similar to MA-XRF, MA-XRD mapping generally consists of acquiring (often several tens of thousands) XRD patterns at each pixel in a 2D area. In addition, like SR μ-XRD, it is capable of directly identifying crystalline phases in complex mixtures and has the specific advantage of allowing the relative abundance of these components to be quantitatively determined. On the other hand, mainly because of the irradiation/detection geometry, reflection mode MA-XRD is a method that is fairly surface-specific, i.e., probing only a few micrometers below the irradiated paint surface. In this way, information related to chemical changes that occurred at the paint surface in the collected XRD data is maximized. In heritage science, XRD point analysis or micro-scale mapping is currently applied to many types of artifacts of different shapes and materials, while MA-XRD mapping has been limited to the investigation of quasi-flat artifacts, such as paintings and manuscripts. Next to its obvious advantage of yielding highly specific images of crystalline painter's materials and in situ formed degradation products, MA-XRD suffers from a coarse resolution and extended acquisition times. This is illustrated in Fig. 9, showing MA-XRF and MA-XRD data derived from a twentieth century "fake" painting, rendered in the style of seventeenth century flower piece [289]. In Fig. 9a, fourteen MA-XRF maps and ten MA-XRD maps derived from this canvas are shown, enabling for a comprehensive understanding of the pigment types employed to create this painting, and to (indirectly) date it. In Fig. 9b, the result of fusing the higher-resolution but less-specific MA-XRF maps with the lower-resolution but more pigment-specific MA-XRD maps is shown for a few pigments: highly specific compound distributions that also show a high-lateral resolution are the result.

Both MA-XRF and MA-XRD may be combined to support or refute subjective art-expert opinions on the authenticity of specific artworks. This approach can also help detect fake paintings and allow art restorers to distinguish between original and non-original parts of a large work of art. For heritage researchers, using MA-XRF and/or MA-XRD in the initial stages of examining a work of art allows them to select in a better optimized, more representative, and more problem-targeted manner the sampling locations of paint micro-flakes. Often the maps recorded by MA-XRF and MA-XRD are among the most convincing and objective arguments that persuade artworks curators to permit such sampling. After this initial, completely non-destructive macro-imaging phase, SR-based and other microscopic methods can be used for the characterization of the samples. Two reviews were recently published focusing on μ-XRF/MA-XRF [51] and μ-XRD/MA-XRD [231].

2.2.2 Accessing the third dimension

Cultural heritage objects are very often multi-layered systems, either because the artist used a specific sequence of layers to obtain a desired visual effect, or because the original materials have evolved over time, leading to the formation of non-original layers. The location of different materials in 3D is therefore important. MA-XRF has been occasionally combined with confocal XRF (CXRF) on painted works of art; CXRF is a variant of μ-XRF that features depth selectivity [296–299]. While XRD mapping

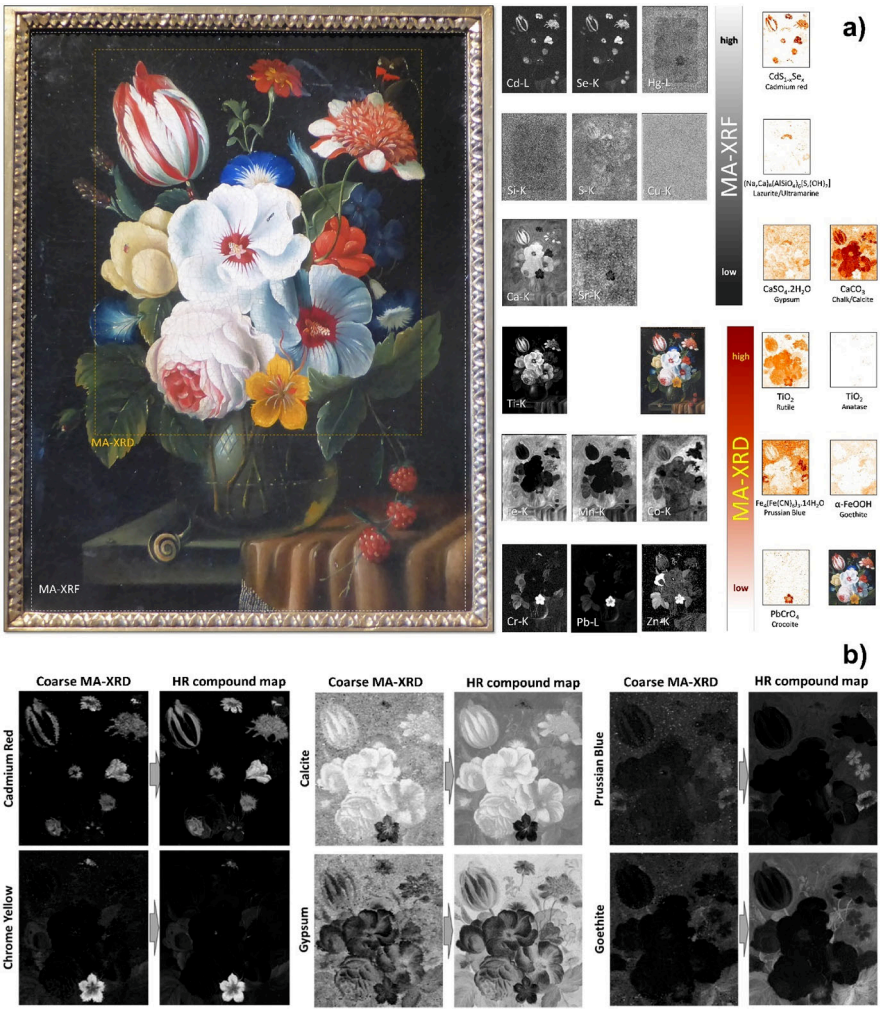

Fig. 9 a Flower piece canvas, painted in a seventeenth century Netherlandish style and associated MA-XRF and MA-XRD maps; **b** comparison of coarse (as collected) MA-XRD maps of some compounds in the painting and the corresponding fused high-resolution (HR) "MA-XRF + MA-XRD" compound maps, showing higher resolution and less noise than the original MA-XRD distributions. Adapted with permission from [289]

is mostly carried out over 2D regions and in reflection mode, in transmission mode, the extension to 3D is sometimes possible, by exploiting one of two quite different experimental strategies. The first strategy relies mainly on a software approach (information obtained by analyzing the XRD peak shifts), while the second one is a hardware (tomographic) approach (involving rotation of the sample or object) and is limited for practical reasons to paint micro-samples [73, 164].

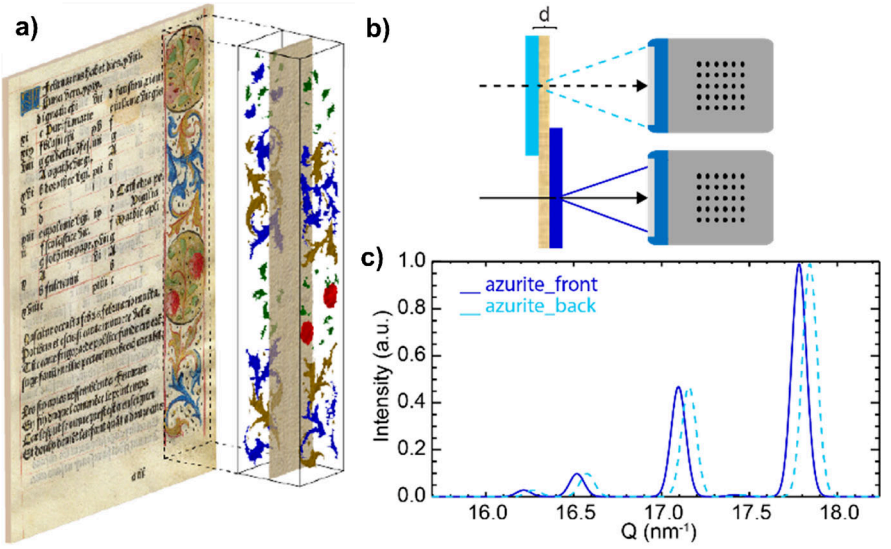

Fig. 10 **a** Fifteenth century illuminated manuscript, painted on two sides with a decorative vegetal pattern in which different pigments were employed, one of them being azurite. The (slightly) different distance of the azurite layers on the recto and verso side of the manuscript relative to **b** the XRD detector results in a (slight) shift of the **c** XRD pattern, and this can be exploited to separate both contributions and reconstruct the azurite pigment distributions on both sides of the folio. Adapted with permission from [231]

The complex build-up of artistic materials (with layers often of micrometric thickness) results in small shifts in diffraction peak position, as only a single layer of the stratigraphic system is positioned at the calibrated distance of the instrument. In the case of a painting, if all inorganic compounds are identified and their structures known, stratigraphic information can be derived from the shift between the measured and reference peak positions. This approach has been used to simultaneously identify and map pigments present on both sides of a fifteenth–sixteenth century illuminated sheet of parchment (Fig. 10) [236]. The same approach was recently exploited, together with MA-XRF, to non-invasively obtain stratigraphic information, from of *Exit from the Theater*, a painting attributed to Honoré Daumier and produced over an earlier landscape [235]. It was also applied to the iconic painting by Vermeer, *Girl with revealing a Pearl Earring*, a cerussite-rich lead-white paint on top of a hydrocerussite-rich underlayer [128].

3 X-ray analysis software, workflow management systems, open science, and FAIR data

Many X-ray-based techniques can be collected across a variety of experimental "dimensions". This can be either a single point (1D), where there is a single spectrum/diffractogram to interpret, or over a specimen's spatial variations (2D), or using depth sensitive techniques, e.g., tomography (3D). These can further be extended in

a time-series sense to examine how properties change over time, as in reactions with different environmental factors (i.e., light, humidity, temperature, and pollutants) or even photoreactions with the X-ray beam itself.

Paragraphs 3.1–3.3 are organized in this dimensional thinking, where the various types of data analysis codes for 1D technique specifics are discussed first, with the extensions to extra-dimensional data following. The following is not intended to be completely exhaustive but rather will point to sources that discuss the current state-of-the-art and a few codes that have been commonly utilized by those studying paint materials. An overview of the most used X-ray analysis software suites that are involved in the processing and displaying XRF, XRD, and XAS datasets obtained from the analysis of paintings is provided in Table 2.

3.1 Single point data (1D)

1D datasets for X-ray analysis are typically the simplest reduced form of data. These could be single-point analysis of a specimen, or standard materials that are to be used as references for comparison or fitting to unknown samples. While data are recorded in terms of an abscissa axis (X-ray energy, diffraction angle, etc.) and an ordinate axis (such as the intensity of photon counts), the 1D in this sense is that it is a single spectrum/diffractogram measured at a single location (or averaged over an area).

3.1.1 XRF

XRF spectra arise from the X-ray emissions that are detected from the sample when core electrons are excited by ionizing radiation (cf. par. 2.1.1). Typically, several diagnostic X-ray emission lines can be detected for an element, depending on the X-ray excitation level. While each line could be considered effectively unique for an element, in practicality, the line broadening due to the X-ray detector often leads to overlapping lines, which requires some type of spectral fitting analysis to deconvolve. This can be done simply by fitting a polynomial, smoothly varying background, superimposed with Gaussian-like peak shapes for each XRF line. However, several other factors, such as detector pile-up, detector escape peaks, elastic and inelastic scatter from the sample, and peak asymmetries often require that more specialized software be implemented.

A typical standard code for XRF fitting often utilized is PyMca [300, 301], which can fit XRF spectra using first principles and tabulated atomic X-ray emission lines. The code is written in Python (Python Software Foundation) and its core functionality can be easily accessed in several other computer codes as well. Elemental composition in the spectrum can be determined via the sum of detector counts, evaluating the area of each peak present in the spectrum as this is, in the ideal case, directly proportional to the concentration of a specific element within the sampling volume. Absolute quantification either requires calibration of the spectrometer or using an internal standard, i.e., an element with known concentration in the sample. Challenges in quantification include the so-called matrix effects, that is, the potentially unknown absorption and scattering of X-ray intensity by the sample itself caused by elements that are not in the

Table 2 List of selected X-ray analysis software suites used in the study of cultural heritage materials, in particular pigments and paints

Software name (URL)*	Dataset type	Interpretation methodologies	References
PyMca (https://www.silx.org/doc/PyMca/dev/index.html)	XRF, XAS, XRD, FT-IR, Raman	Pre-processing (background, XAS, derivative, etc.), processing (XRF fitting, peak mapping, quantification, multi-variate analysis, etc.)	[300, 301]
MicroAnalysis Toolkit (https://www.sams-xrays.com/smak)	XRF, XAS, FT-IR, Raman, Mass Spec Imaging	Mapping, quantification, XAS imaging, FT-IR/Raman background remove, multi-variate analysis, multi-modal analysis	[302]
XRDUA (https://sourceforge.net/projects/xrdua)	XRD	Azimuthal integration, whole pattern fitting, Rietveld refinement, tomographic reconstruction, mapping, quantification	[131]
aXis2000 (http://unicorn.mcmaster.ca/aXis2000.html)	STXM data, XAS	Mapping, XAS imaging, multi-variate analysis	[303]
TXM Wizard (https://sourceforge.net/projects/txm-wizard/)	TXM (2D and 3D), XAS	Tomographic reconstruction, XAS imaging, multi-variate analysis	[304]
ATHENA and ARTEMIS (https://bruceravel.github.io/demeter/)	1D XAS	Processing and fitting of XAS data to theory	[305]
Larch (https://xraypy.github.io/xraylarch/)	XAS, XRD, XRF	Processing and fitting of XAS data to theory. Interpreter language to more complex functions. Includes XRD area detector analysis and XRF image viewing tools	[201]
SIXPACK (https://www.sams-xrays.com/sixpack)	1D XAS	Processing and fitting of XAS data to theory with multi-variate analysis	[306]
FEFF (https://feff.phys.washington.edu/feffproject-feff-xafsdataanalysis.html)	1D XAS	experimental fit of XAFS spectra to theoretical calculations from FEFF	[307]
DL EXCURV (https://software.pan-data.eu/software/85/dl-excurv-formerly-excurve)	1D XAS	Data analysis of EXAFS spectra using the fast spherical wave method	[308]
GNXAS (http://gnxas.unicam.it/pag_gnxas.html)	1D XAS	XAFS data analysis based on multiple-scattering (MS) calculations; fitting of raw experimental data	[309]

*URLs were accessed in June 2025

spectral range of the spectrometer or as a function of sample depth. Note that the information depth of emitted X-rays depends on their energy, making depth corrections for quantification rather complex.

While PyMca is commonly used in heritage science, several other notable programs exist, including XRFitProc [310], Peakaboo [311], PyXRF [312], MAPS [313], GeoPIXE [314, 315], Larch [201], as well as several proprietary programs that are distributed by companies of traditional tube source XRF analytical instruments.

3.1.2 XAS

XAS is a technique that generally probes the oxidation state and coordination environment of an element of interest. Since it is element specific, it is useful for analyzing the local structure of both crystalline and non-crystalline materials (cf. par 2.1.1).

XAS data analysis can generally be separated into steps of pre-processing (background subtraction and normalization) and analysis (comparison/fitting to standards, comparison/fitting to theory, and/or statistical analysis). Pre-processing steps are nearly always required to put XAS data into a mode that is useful for continued analysis. When the compound measured is of a nearly pure phase, or has a coordination environment that can be modeled, comparison and fitting the theory can be executed, and a detailed picture of the local structure can be determined. This requires high-quality data in the EXAFS region or theory to describe the electronic transitions in the XANES range.

In general, the analysis of EXAFS portion of the spectrum provides quantitative determination of local structural parameters such as the number of neighbors in a given shell (accuracy about 10%), distance (accuracy about 1%), and mean square displacements of atoms in the given shell (accuracy about 20%) [202]. The data treatment is carried out by extraction of the oscillating part above the edge, Fourier filtering, and fit to a given model. The theoretical EXAFS signals necessary for the fitting procedures can be calculated ab initio using one of the several codes available for this purpose (Table 2). The XANES part provides useful information on both electronic and atomic structures. In a basic approach, the experimental spectrum can be compared with those calculated for candidate structures with subsequent choice of those exhibiting the best agreement. Frequently used codes are FEFF [307] and FDMNES [316].

Fitting of experimental data to a set of standards, either in EXAFS or XANES data, can be used to quantify the phase compositions of the mixtures, but does require a modest expectation of what is present in the sample to be accurate. Statistical analysis, using various multi-variate techniques, is most often used in the reduction and interpretation of large numbers of spectra, either in the form of multi-dimensional datasets (i.e., spatial or temporal). Most software packages are either dedicated to the calculation and theory of various aspects of the XAS spectrum, or the pre-processing, fitting, and/or statistical analysis of the data.

In addition to the XAS analysis packages of Table 2, a more exhaustive list can be found in the International Tables for Crystallography, Volume I [317], which has several sections dedicated to the salient features of many software packages.

3.1.3 XRD

XRD is a technique used for the characterization of the long-range structure of crystalline materials and is typically used to identify and quantify the major phases present (cf. par. 2.1.2). Analysis can also determine the texture of materials and, when combined with micro-beam facilities, the spatial variation of phase composition within a sample.

Nowadays, XRD is mostly performed using 2D X-ray sensitive area detectors. Therefore, a first pre-processing step is required in the form of 2θ- or γ-integration to reduce the collected 2D diffraction images to 1D diffraction patterns (diffractograms). Various software and in-house written routines exist for this purpose; however, pyFAI is currently frequently used due to its high performance and its ability to work with complex detector geometries (i.e., not limited to flat area detectors) [318]. The functionality of pyFAI can be integrated into other software, such as a Python library, or can be used stand-alone with or without a graphical user interface (GUI).

In a second step, phase identification can be performed. Analysis for phase identification typically consists of using a search-match type procedure to look for the appropriate reference pattern that matches with the experimental data using a large reference data base (i.e., ICDD [319]; Inorganic Crystal Structure Database (ICSD) [320]; Cambridge Structural Database (CSD) [321]), some of which are freely available (i.e., American Mineralogist Crystal Structure Database [322]; Crystallography Open Database [323]), or with the use of model standard references. Different software solutions are available to automate the identification of the crystalline phases, but are often commercial products, such as Match! [324]; however, QualX2 [325] is available as a free alternative.

For relatively single-phase composition samples or for those with a minor or poorly crystalline impurity, Rietveld refinement can be used to determine a crystalline structure refinement of the atomic lattice positions. This can be useful to investigate subtle changes in the crystalline structure of samples with different conservation conditions, or to study variations in the chemical composition of materials that were synthesized using different methods compared to database compounds. The typical standard for Rietveld analysis in use is GSAS [326], developed from the original algorithmic refinement and first published by Rietveld in 1969 [327]. However, many more alternatives are available.

A comprehensive review of diffraction-based software is beyond the scope of this review, but a useful survey list is provided in the International Tables for Crystallography, Volume H [328], which summarizes active software, its primary use, references, URLs, and license availability.

3.2 Laterally resolved data (2D) and tomography (3D)

Laterally resolved data (2D datasets) can be considered an extension of the 1D case in most situations. The same types of pre-processing are generally still performed but extended onto a larger number of sampling points. 2D datasets are commonly displayed to show a feature of the collected dataset (i.e., a particular XRF peak, a

particular XAS species, a particular XRD peak or crystalline phase) in an image, where the x- and y-dimensions are the spatial locations on the specimen, and the color of each pixel is the mapped intensity of the feature of interest. As the data are viewed as an image, in addition to the typical pre-processing and fitting of the specific analytical technique, the experimenter may also invoke image processing steps. These can be used to enhance signal-to-noise using adjacent pixel averaging, or multi-variate methods to look for related characteristics in the image dataset. Since a particular pixel may have several spectral features, the data are in fact a "cube" of information that can viewed or "sliced" along one of the dimensions.

A common issue in examining works of art in this manner is the large number of spectra (either XRF, XRD, or XAS) that may need to be analyzed, with some datasets consisting of millions of pixels (i.e., datasets where every pixel is a spectrum). Analysis of this type requires accurate determination on low signal data, in a timely manner; several codes have been compared to examine the different strategies that can be employed [251].

As mentioned above, the non-proprietary software package PyMca was initially developed for the analysis of XRF data but has been progressively extended to many other techniques. More particularly, the package ROI Imaging offers various tools to display and explore many types of hyperspectral data (XRF, XAS, XRD, FT-IR, Raman, etc.) [301]. The easy-to-use interface provides different options to process both images and spectra. Regarding pre-processing, spectra can be batch background-corrected, normalized, derivated, and specific options (such as peak deglitching, EXAFS extraction, and Fourier Transform) have been added to analyze XAS spectra. Regarding processing, spectra can be batch-fitted (using simple fitting model and advanced XRF fitting model); images can be generated based on peak intensity, peak fitting or on statistical analyses, such as PCA or non-negative matrix approximation (NNMA). The software package also allows the parallel analysis of different datasets (e.g., if XRF and XRD have been collected simultaneously over 2D maps). PyMca offers additional tools to display and compare images (through the RGB widget) and to extract easily data, such as 1D profiles, scatter plots, and average spectra. Its user-friendliness, multi-support, and a very wide range of options (Fig. 11) make this software package a reference for the analysis of datasets related to painting degradation phenomena and, more generally, for the study of cultural heritage with SR micro-probes or with macro-XRF scanners as well [251].

XRDUA [131] is an open-source project dedicated to the visualization of crystalline phase distributions from 2D scanning XRD or XRD tomography. It was developed to integrate the complete sequence of data reduction and interpretation steps required to convert large datasets of powder diffraction patterns into a limited set of crystalline phase maps within a single software package. It accepts images from flat area detectors in various formats and allows for: (1) correction of the collected 2D diffraction images and calibration of the diffraction geometry; (2) azimuthal integration; (3) phase identification; (4) modeling (Rietveld, Pawley, Pattern Decomposition) of the entire set of diffractograms in an autonomous way. In step 1, different options are available to mask unwanted artifacts, remove background and/or dark current, and perform spatial distortion and flat field corrections. Various options are available for azimuthal integration in step 2, including the use of average and median (or other percentiles),

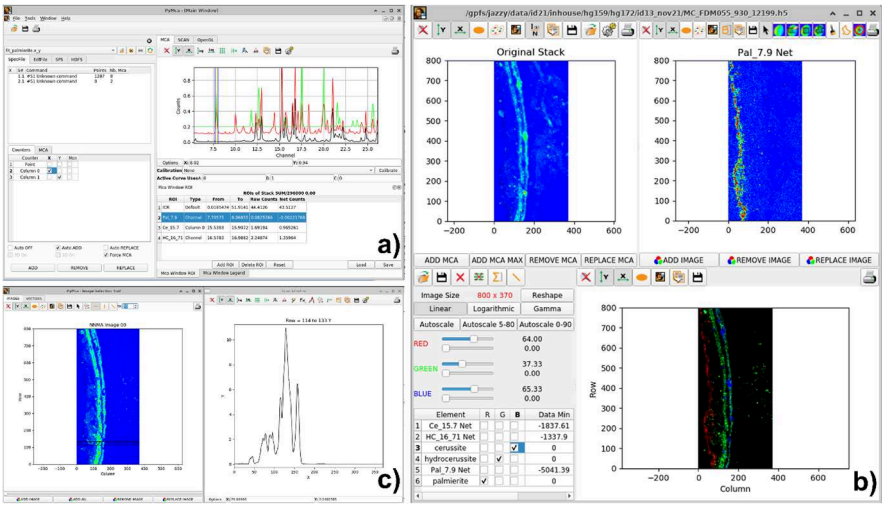

Fig. 11 Some capabilities of PyMca illustrated with a μ-XRD map acquired on a painting thin section. **a** Main panel for spectra/pattern retrieval, display, processing. The black pattern is the average of the full XRD map (after background subtraction), and the green pattern is a reference pattern from palmierite. A ROI has been selected around the XRD peak at $2\Theta = 7.9°$ to map palmierite (named "Pal_7.9"). **b** ROI imaging panel for manipulation of maps: complete original stack (top left corner); ROI image of the net XRD intensity map over the ROI Pal_7.9 (top right corner), where some pixels were automatically selected to extract an average pattern of palmerite (shown in red in **a**); RGB composite image of ROI maps of palmierite (red)/hydrocerussite (green)/cerussite (blue) (bottom). **c** Multi-variate analysis done through NNMA. The left panel shows the first NNMA image, which highlights the distribution of hydrocerussite. A horizontal line has been drawn (with a vertical width of 20 pixels) to extract a 1D profile (right). Adapted from [55]

which help to remove single diffraction spots commonly present in diffraction patterns from (historical) paint samples that distort the expected relative Bragg peak intensities. To assist phase identification in step 3 and provide immediate feedback on the data collected, XRDUA offers a mode called "explorative processing". This processing mode automatically converts 2D diffraction patterns to 1D diffractograms, while regions of interest can be selected in 2θ to map their intensity as a distribution map. Selected 1D diffractograms or averaged diffractograms based on their intensity can be directly compared to imported reference patterns for identification. Following identification, models can be constructed to automate the fitting of the entire dataset in step 4. Depending on the available crystallographic information, Rietveld refinement, Pawley groups, and/or peak groups without structural information can be integrated into the model. The main limitations of the software package are the limited options for phase identification (i.e., no search-match algorithm) and the lack in performance when dealing with increased XRD data collection rates achievable at contemporary SR facilities.

TXM-Wizard is a software package [304] that was originally designed for processing FF mode X-ray microscopy, which, by definition, can create very large hyperspectral datasets as typical FF detectors have at least 1 k × 1 k pixels. The package consists of two parts, one for 3D reconstruction of tomography data (one of

the main applications of FF-TXM) and one for processing data from XANES imaging. In the following, we only discuss the XANES imaging part, which is denoted TXM XANES Wizard [304]. This package can load and process many different file formats and is specifically designed to handle very large XANES imaging datasets. However, while the pre-processing steps are specific to XAS, externally pre-processed (e.g., background correction, normalization, etc.) image datasets from different methods (e.g., chemical force microscopy, IR, Raman, XRF [329]) can also be processed in the exploratory analysis step explained below. Showcases even include time-series of spectra, as these can easily be rearranged into an indexed matrix that can be processed as an "image", offering advantages for visual inspection [330].

TXM XANES Wizard provides options for XANES image analysis following a four-step workflow: (1) determination of the edge-jump and noise filtering; (2) batch normalization and determination of edge energy; (3) exploring the data; (4) batch fitting the data. Step 1 is used to filter pixels with spectra with a too low S/N ratio and in turn produces a so-called edge-jump map, which corresponds to the concentration of the studied atom species of interest. This first step also allows the normalization parameters for step 2 to be optimized, during which a second filter can be applied, filtering pixels where the batch normalization fails. These two steps are important, because in FF XANES imaging, often involves spectra with very low S/N ratios (e.g., in pixels with no or very little sample). In the second step, the edge energy position is also determined because of the batch normalization, thus producing a map that gives first information on the oxidation state of the element of interest. Step 3 offers the option to perform PCA and clustering. Finally, step 4 allows for a batch least squares linear combination fitting of each pixel using a model consisting of XANES spectra of reference compounds, thus producing weight maps for each reference. After fitting, the quality-of-fit parameters can be inspected as maps and used for further data exploration. For instance, analyzing the edge-jump versus R-factor offers a powerful approach to test the quality of the fitting model and detect unexpected (minority) species present in different kind of cultural heritage materials, including Roman ceramics [331], consolidated lime-stones [332], and altered paints [123, 183].

3.3 Time-dependent measurements

The dimension of time is a crucial addition to spatial dimensions in X-ray data analysis, allowing for the extension of analysis at: (i) single locations—extending 1D to 2D, (ii) across spatially resolved data—extending 2D to 3D, and (iii) occasionally on tomographic data—extending 3D to 4D.

Often, an analysis is done in a "before" and "after" sense, where the measurements are performed before a reaction starts, and again at the end of the reaction, and often on multiple samples. However, a truly additional source of information can be exploited by tracking the same sample over time. There are several cases in which laboratory sources have been used with XRD to track chemical changes in pigments as well as to record information related to the kinetics [333–335], as an extension of 1D data to 2D data. In the heritage analysis of paint using SR, time studies typically fall into the first or second category above, similar to the laboratory studies noted below, where

the examination of potential radiation damage by the X-ray beam (cf. Section 5) or the analysis studies the reaction over long time scales or simulated time exposures. At this time, no 4D SR X-ray studies have been performed that we are aware of in the study of degradation of pigments and paints.

As SR sources achieve higher brightnesses, many of these types of time-series experiments become more reasonable, as measurements can be conducted quickly, and the time-domain becomes more accessible, either with the same sample, or with a large series of parallel samples. Although higher dimensional datasets do not necessarily have a rich history, new capabilities of synchrotrons will likely bring more emphasis on these modalities in the future.

3.4 Workflows

To deal with the increasing size of datasets and following the objectives of making data processing more Findable, Accessible, Interoperable and Reusable (FAIR), workflow management systems are being developed and increasingly used. They allow different steps of processing to be gathered in a unique system, which makes the whole processing more reproducible and easily shareable between groups. The increasing interest of such systems is illustrated for instance with the development of Ewoks (ESRF Workflow System), which is not a workflow management system itself, but allows similar tasks and graphs in different workflow management systems to be used. Its aim is to execute and automate data processing during and after experiments at large-scale facilities to deal with the large datasets generated there in a systematic and traceable way [336].

As an example, Orange Data Mining is an open-source workflow management system software, based on Python [337]. Its interactive interface allows for visual programming by placing and linking pre-coded widgets to accomplish specific tasks (fitting a peak, plotting a result, etc.) on a canvas to build step-by-step a flow of actions to open, manage, process, display, and save data. Being open source, it also enables coders to develop their own widgets if the processing action they desire is not present in the widget library. Additional libraries of widgets are also downloadable as add-on, such as one dedicated to spectroscopy (pre-included in Quasar, a variant of Orange dedicated to scientific data analysis).

Figure 12 shows a fairly simple but representative Orange workflow dedicated to implement multi-variate statistical analysis (PCA) and to pre-process (average and normalize) XANES spectra. It is used in this instance on a sub-dataset of 40 measurements, assessing beam damage of chrome yellow paints during repeated Cr K-edge XANES measurements [132]. The sample corpus covers lead chromates-based pigments of two stoichiometries, $PbCrO_4$ and $PbCr_{0.2}S_{0.8}O_4$, pure or mixed with oil, measured both at room temperature (RT) and in cryogenic condition (Cryo).

In brief, after opening the dataset (step 1), the metadata management widgets (step 2) allow each measurement to be efficiently categorized depending on the sample chemistry (stoichiometry of the chrome yellow pigment and dispersion or not in oil), acquisition conditions (Cryo or RT), and measurement repetition. The spectra are then normalized or derived (step 3) and the metadata previously managed can immediately

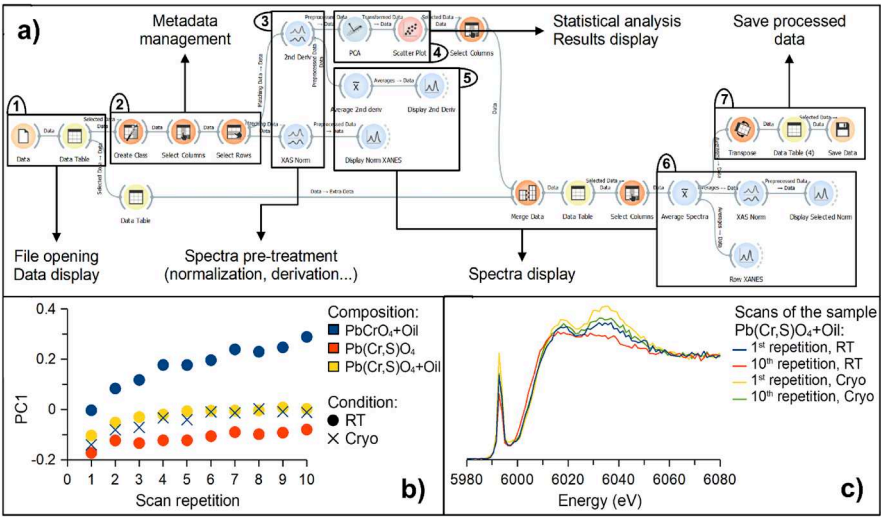

Fig. 12 **a** Example of workflow developed to pre-process XANES datasets at the ESRF-ID21 beamline. **b** Reproduction of the display generated by the statistical analysis and results display widgets. **c** Reproduction of the display generated by the spectral display widgets

be used in the displays of the PCA results (step 4) and spectral processing (5) to color or shape sub-datasets. As an example, Fig. 12b shows the contribution of the first PCA component as a function of the measurement repetition. Here, the color of the point represents the "composition" metadata and the shape (either circle or cross) of the "acquisition conditions" metadata. On this display, relevant points or groups of points can be easily selected to extract and compare their corresponding averaged and normalized XANES spectra (Fig. 12a, step 6), as shown in Fig. 12c. These spectra can finally be saved for further processing if relevant (Fig. 12a, step 7).

Beyond this simple case study applied to a relatively small point XANES dataset, there is a general increasing use of workflow management systems, notably Orange/Quasar, in the field of heritage science. Besides spectroscopy and statistical analysis, such workflows can provide efficient tools, for instance, to manage reference datasets for identifying unknown data or to process spectroscopy mapping.

This concept can also be expanded in 2D XRF image processing, where a consistent workflow pattern is desired to ensure that the treatment of data is the same across samples or regions of interest. This can include various image processing steps, including background removals and normalization, fitting of XRF spectra over the image with PyMca routines, quantitative concentration measurement through analytical standardization, fitting of XAS image data when multiple excitation energies are collected over an image, as well as many other processing and analysis steps. The MicroAnalysis Toolkit [302], for instance, supports a list macro-concept to set up a series of data processing and analysis steps that can be applied sequentially. Results can be integrated across open files, so that statistical processing can be directly compared.

3.5 Open science and FAIR data

Beyond improvements in data collection and the establishment of reproducible processing and analysis using workflows, it is crucial to highlight the global efforts advancing Open Science and FAIR data practices. Given the precious and unique nature of materials analyzed in heritage science, this topic is particularly critical.

For instance, in 2015, the ESRF implemented a data policy for publicly funded research, committing to making raw data openly available under a CC-BY license after a 3-year embargo and to archiving high-value data (e.g., from rare and significant samples) for at least 10 years. In 2023, the ESRF updated its data policy to incorporate recommendations from the Photon and Neutron Open Science Cluster (PaNOSC) FAIR Research Data Policy Framework [338], which was a deliverable of the European H2020 European Open Science Cloud (EOSC) project PaNOSC. The update led to the inclusion of the FAIR principles, the extension of the policy to processed data, and the allowance for data triage to manage increasing data volumes. The implementation of the ESRF data policy includes: (i) the use of a standard data format (HDF5) to ensure that data are easily accessible in the future; (ii) the adoption of the NeXus metadata standard and following the PaNET ontology of techniques; (iii) the deployment of a data portal (ICAT) giving direct access to raw (and increasingly processed) data and electronic logbooks; (iv) the ability to easily reserve and mint Digital Object Identifier (DOIs) for publication of datasets.

The case of the ESRF exemplifies the growing global movement toward Open Science and FAIR data. Another initiative directly relevant to Cultural Heritage is the Synchrotron X-ray analysis of Heritage Accessible to and Reusable by Everyone (SHARE). SHARE, funded by the European Commission's Horizon Europe Research and Innovation Program under the OSCARS call (Grant Agreement nr. 101129751), will extend the standard FAIR practices at the ESRF to defining and implementing richer metadata (regarding samples and techniques). This enhancement aims to ensure that data are more easily Found, Accessed, Interoperable, and Reused. Ultimately, these efforts seek to maximize the impact of data and foster new scientific discoveries.

4 Sample preparation

4.1 General considerations

Sample preparation is a fundamental step in the analytical chain, that can dramatically impact the success of experiments. It must be optimized according to the analytical techniques that will be applied to the sample. Several techniques (based or not on the use of X-rays) are usually combined for the study of painting degradation phenomena and they may impose, sometimes, different incompatible constraints in terms of sample preparation. In what follows the procedures related to SR-based X-ray analyses are described in detail. An extended discussion about sample preparation for combined FT-IR and X-rays micro-analyses can be found elsewhere [218].

The two major questions to be addressed to optimize sample preparation are the following:

– Does the analysis aim at a bulk measurement or is it based on X-ray microscopy (2D or 3D)?
– Are the X-rays collected upstream or downstream the sample?

Regarding the first question, if no microscopic information is required, the sample preparation is usually straightforward. When data can be collected with a relatively large (few tens to few hundred microns) beam, the surface quality of the sample is not critical. Instead, if experiments are carried out with a micrometric beam, sample preparation is often more delicate. If X-rays are measured upstream the sample in 2D mode, it is important to have a flat surface, to prevent reflected or fluoresced X-rays from being intercepted by a rough surface.

Regarding the second question, if X-rays are measured through the sample, then the sample thickness must be cautiously considered. X-ray penetration depth will depend on the sample composition, density, and X-ray energies. Many software packages, such as PyMca (cf. Section 3), allow calculating X-ray absorption through a given material. The X-ray transmission of a series of pigments and fillers calculated in the 1–30 keV range has been described by Pouyet et al. [218]. X-ray transmission increases with the energy, so working above ~ 30 keV allows analyzing paint fragments of thickness above ca. 100 μm. However, when performing XAS analyses, the energy of incoming X-ray beam is imposed by the edge of the element of interest. In this case, the sample thickness needs to be adjusted to allow a proper transmission. Typically, for the study of 3d transition metals, at their K-edge (~ 5–10 keV), thickness of ~ 10–20 μm is usually adequate, and a microtome is often suitable to obtain such thicknesses. Conversely, transmission X-ray microscope at the carbon K-edge or the L-edges of metals requires much lower thickness (~ 100 nm) that necessitate an ultra-microtome or a focused ion beam (FIB).

If X-rays are collected upstream the sample, then the sample thickness is usually not critical, and thus, analyses can be carried out on thick (~ 1 mm) painting fragments. However, it may still be relevant to prepare thin sections for measurements in reflection or fluorescence mode, since this will permit to control the volume probed by X-rays. This is particularly important to reduce self-absorption effects [218] and when the sample is heterogeneous through its thickness and/or when the stratigraphy is not well orthogonal to the section surface.

4.2 Some practical aspects

Some advice is given below, for each main SR-based X-ray technique described in Sect. 2, and with a particular focus on degraded paint samples.

4.2.1 XRF/XAS

The acquisition of reference spectra is usually carried out with a millimetric beam on powders. Powders can be spread on tape (which must not contain the element of interest), or mixed with an inert filler (boron nitride, cellulose, etc.) and prepared as pellets.

Bulk XRF- and TEY-XANES spectra can be acquired on powders and paint fragments without complex sample preparation. TEY requires the samples to be glued on a conductive substrate (such as carbon adhesive tape) [145].

μ-XANES are commonly acquired in XRF mode on paint cross-sections. The preparation of thin sections (e.g., with a microtome) allows for control of the probed volume and limits self-absorption effects; similar considerations apply to 2D μ-XRF maps. This is usually relatively easy for paint mock-ups and may be more challenging for historical paintings, for which corresponding paint fragments have been often embedded in hard resin blocks decades ago. In such a case, a protocol has been implemented, which consists in slicing the cross-section on one of its sides, rather than along its main polished surface. If the thin section is fragile and breaks, it can be collected on a piece of tape, applied on the resin block just before slicing. The details of this protocol can be found in the supporting information of a previous work by Gonzalez et al. [78]. As an alternative to the microtome, thin sections down to ~ 30 μm thickness can be obtained by polishing samples from both sides. A protocol has been proposed for the case of ceramics [339, 340]. The use of a microtome is still highly recommended, since, conversely to polishing, it preserves the sliced material.

When μ-XANES is performed in transmission (e.g., in 2D FF mode, or 3D transmission X-ray microscopy), then sample thickness should be carefully considered, even more so the X-ray energy is imposed by the edge of the element of interest. As an example, sections of less than 20 μm were prepared to analyze Cd, Cl, and S speciation in degraded cadmium yellow pigments from two paintings by Matisse [97]. FIB was applied to resin-embedded degraded orpiment to perform multi-energy TXM [95]. However, this procedure must be considered carefully, since it may damage the (analyzed) sample.

4.2.2 XRD

The most standard set-up for XRD measurement is in transmission mode.

For HR-XRD measurements, powders and liquids are usually contained in a glass capillary. The diameter of the capillary can be adjusted according to the X-ray energy and the sample composition. Painting fragments (mock-up or historical) can be placed in capillaries as well. Two strategies are usually adopted to ensure that the fragment will fall inside the capillary: (i) resizing the fragment; (ii) increasing the capillary diameter. A second thinner capillary is sometimes added, to push the sample and guarantee that it will not move too much along the capillary axis upon X-ray analyses.

Concerning μ-XRD mapping, samples are ideally prepared as thin sections using a microtome as mentioned above. A similar sample preparation procedure has been developed by the TS Lab & Geoservices (Pisa, IT) to obtain polished thin sections suitable for μ-XRD/μ-XRF mapping. This protocol is particularly relevant for the preparation of sections from mural paintings, that usually break in small parts when sectioned with a microtome [341].

For small or precious embedded historical fragments, especially when using incident X-ray beams above 20 keV and where thin-section preparation is impractical, transmitted XRD signals can be measured through the cross-section with minimal interference from the embedding resin. In such cases, drilling a small cone behind the

sample is advised to further reduce beam absorption by the resin. Alternatively, SR μ-XRD data can be collected in reflection mode, where the sample thickness is not critical. This approach, however, reduces the intensity of collected signal by approximately half (as half of the diffraction rings are hidden by the sample) and requires a larger beam footprint along the grazing direction. In such a case, the stratigraphy is usually oriented, such that the smaller beam dimension probes the different paint layers, selectively. In this regard, a combination of reflection/transmission mode MA-XRD and SR μ-XRD measurements has been used by Avranovich Clerici et al. [14] for successfully studying a series of altered wall painting fragments and corresponding thin sections from the upper Basilica di San Francesco in Assisi (cf. Section 6).

For 3D μ-XRD investigations, the paint fragments are usually mounted on a pin, as such or with preliminary embedding in resin. The sample and the embedding material should be reduced to the minimum to selectively probe the layer of interest and to avoid having a too high absorption of incoming and diffracted beam. A detailed protocol is provided in the supporting information of [164].

4.3 Choice of materials for sample preparation and mounting

Besides the sample itself, attention must be paid to the materials used to prepare and mount the samples. These materials should not (i) modify the sample (for example lead to the dissolution of part of the painting) and (ii) contribute too much to the measured signal. For instance, if one is interested in studying the role of Cl in painting degradation, it is very important to choose a Cl-free embedding resin for the preparation of sections. Most standard embedding resins are suitable for X-ray analyses. This is not the case for FT-IR analyses, where different protocols have been developed, notably for combined FT-IR/X-ray analyses [342]. It should be pointed out that for the study of mock-up paint films, applying the film on a soft, thin ($\leq$ 1 mm) and inert substrate (e.g., polycarbonate, Teflon) rather than on glass slides facilitates its further manipulation: the substrate can be cut to obtain pieces of paint films, which can be easily manipulated without the need to prepare resin-embedded blocks, and can be mounted as such in the microtome.

If tape is used to glue thin sections for μXRD measurements, it is advised to use a tape with low diffraction signal (such as Magic tape by Scotch).

Finally, efforts are also made to reduce the time spent mounting samples at the beamlines. For this purpose, some beamlines are equipped with robots that take care of dismounting and mounting samples automatically. This is notably the case at the HR-XRD ESRF-ID22 beamline (Fig. 13a–c). Alternatively, sample holders are developed to mount many samples together, thus contributing to minimizing the time lost in installing samples (venting/pumping, entering the hutch, configuration of the instruments, etc.). As an example, sample holders with up to 54 holes have been designed for the μ-XRD ESRF-ID13 beamline (Fig. 13d–f). Bearing in mind the increase of the speed of data collection, such developments contribute to optimizing high throughput.

In summary, thanks to their high penetration depth, many X-ray analyses can be carried out with limited sample preparation, either directly on painting fragments or on resin-embedded cross-section, as commonly performed for optical light and

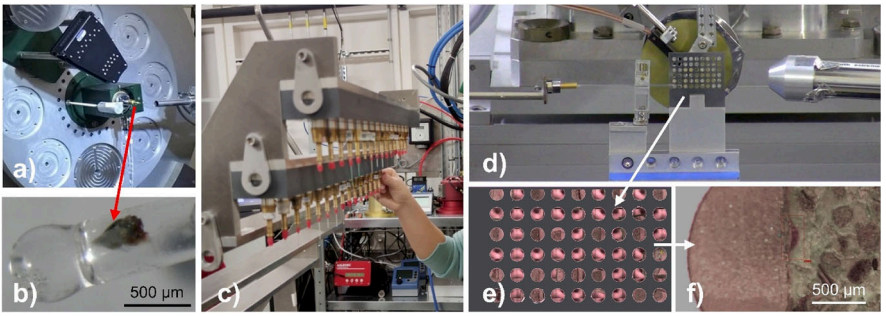

Fig. 13 Examples of sample preparation and mounting. At ESRF-ID22 beamline: **a** the sample stage and detector, **b** a raw fragment of painting placed in a capillary, **c** tens of capillaries are mounted on racks, and a robot automatically dismount and mount them. At ESRF-ID13 beamline: **d** a 54-hole sample holder mounted on the micro-branch sample stage, with the beam stop (left) and the XRF detector (right), **e** close-up on the 54-hole sample holder, and **f** one mural painting fragment prepared by double-side polishing

electron microscopies. This allows analyzing a large corpus of fragments, as kept in sample collections. Noteworthy, the preparation of thin sections (either using a microtome or by polishing the sample) offers a series of advantages: (i) better control of the probed volume; (ii) improvement of data quality; (iii) reduction of re-absorption effects in XRF mode; (iv) minimization of the absorption of incoming X-ray beam during transmission mode μ-XRD measurements; (v) increasing of the chance to have a homogeneous composition along the probed depth. Notably, considering that the degraded layers are usually a few micrometers thick, the preparation of thin sections reduces the risk to mix degraded and safe materials along the beam direction.

5 Radiation damage

As previously discussed, SR-based techniques employing intense X-ray beams are valuable analytical tools providing extensive chemical and structural information. However, the extreme intensity and brilliance of SR as a probe can also induce changes in analyzed materials, a problem observed in diverse samples, including cultural heritage and biological specimens [55, 120, 121, 343, 344]. The extent of damage, as widely reported [120, 121], is influenced by factors such as the absorbed dose, sample composition, analysis environment, sample preparation protocols, and the energy of the incident X-ray beam. Non-destructive methods, like Atomic Force Microscopy (AFM) and VIS/IR spectroscopy, are preferred for evaluating potential damage [55, 343]. However, when these methods are insufficient, X-ray techniques can still provide valuable information, even though some X-ray induced changes occur on ultrafast timescales (e.g., picoseconds) and may remain undetected.

In heritage science, awareness of potential risks has grown, particularly in recent years. Literature now reviews strategies to mitigate unwanted radiation-induced side-effects and discusses damage risks [120], as well as summarizing active trends in

damage analysis and the application of new tools for damage mitigation during measurements [121]. A critical aspect of this topic is addressing the taboo surrounding radiation damage [120]. Often, it is entirely omitted. While more recent studies briefly mention the absence of observed damage during data analysis [147] or state that "only the undamaged data" are presented (e.g., [345]), reports of negatively impacted results have historically been scarce. However, this trend is shifting, with more recent publications including side-effect damages in supplemental materials [148, 346] or discussing it within the main data analysis [185]. These newer works are increasingly raising awareness of radiation-induced side-effects and focusing on mitigation strategies.

5.1 What is damage?

For paints and pigments, initial assessments of damage often rely on visual perception, evaluating alterations in appearance or potentially weakening the mechanical properties through methods like naked-eye inspection or microscopy and under various types of illumination [55, 120, 121]. However, visible observations are intrinsically qualitative and subjective to the eye of the beholder. Changes at the atomic or molecular level may not be readily visible. Bertrand et al. [120] recommend reserving "damage" for changes that can be visibly assessed and using "radiation-induced side-effects" for all alteration phenomena that can be characterized.

The concept of damage should not be limited to that which is observable by eye or considered as the physical qualities of the object. One can also consider damage to the analysis data itself, where the analysis prompt modifications to the material in a manner that changes the results and/or data quality, including changes to the oxidation state of the element of interest [132, 179, 181] or alterations in the pigment's structure [132, 164, 176]. These changes can be transient and reversible or permanently alter the object. Beyond affecting data in the current experiment, long-lasting effects can degrade or impact future scientific analyses. Furthermore, the consequences of such side-effects may not be immediately apparent and could lead to delayed and physically noticeable damage in the future [120].

In SR-based X-ray experiments, the initial measurement with the primary probe often first reveals radiation damage. Subsequent scans or secondary measurements on the same sample area may show changes in the datasets compared to this initial measurement. Therefore, the measurement timescale is crucial when using the experiment itself as the primary indicator for damage, side-effects, or change. For example, a typical EXAFS experiment can take over 20 min per measurement, representing a significant dose exposure (depending on beamline flux) for many materials that could saturate damage before the first measurement concludes. In such cases, analysis might misleadingly suggest no change between subsequent measurements or in the sample itself. Development of rapid X-ray spectroscopy techniques, like quick-XAS [347] or energy-dispersive XAS [348], enabled time-resolved data collection on a much faster timescale than EXAFS, or traditional XANES. Consequently, changes in data quality or chemical state are often only noticed during post-experiment data analysis, which can be some time after the radiation exposure.

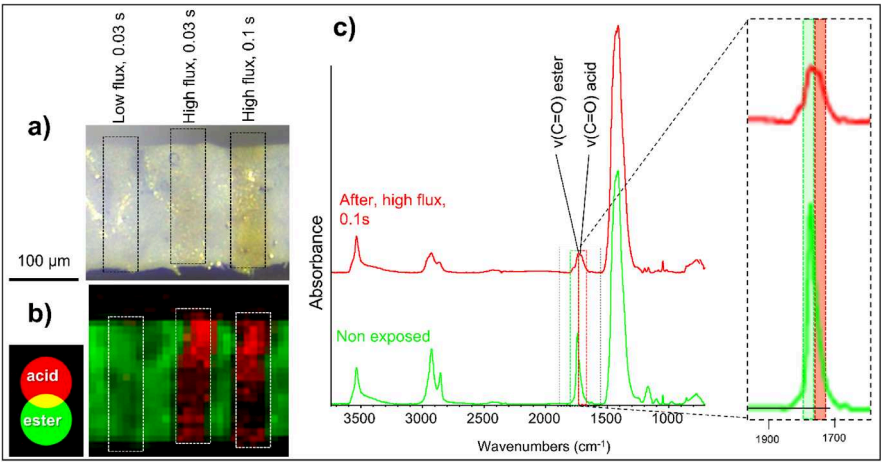

Fig. 14 **a** Micrographs of a thin section of a lead white (hydrocerussite) oil paint mock-up showing the effect of a SR X-ray micro-focused beam and corresponding **b** RG composite μ-FT-IR maps displaying the integrated intensity over the ν(CO) acid band (1683–1724 cm^{-1}) (red) and ν(CO) ester peak (1726–1759 cm^{-1}) (green). Three SR μ-XRD maps were acquired at ESRF-ID13 beamline, under different dwell time and flux conditions (high flux: ~ 10^{12} ph/s; low flux: ~ 10^{11} ph/s; beam size: 2 × 2 μm^2). **c** Average FT-IR spectra of the non-exposed sample (green) and over the map acquired with high flux at 0.1 s (red). The inset shows the strong modification of the C = O signal, with decreasing ester contribution and increasing acid contribution, as well as the ester and acid wavenumber ranges. Adapted from [55]

Diffraction experiments at third- and fourth-generation synchrotrons are often much faster than full spectroscopy measurements, taking advantage of large fluxes and sensitive area detectors. A recent study [55] demonstrates that X-ray dose induces the broadening of diffraction peaks, shifts in position, and decreases in total intensities, associated with the increased amorphization of the sample during the irradiation. For example, a series of lead-white oil paint mock-ups were analyzed using an X-ray micro-beam (energy: 13 keV; size: ~ 2 × 2 μm^2) under varying flux and dwell times [55]. Figure 14a shows some of the resulting data. Visible-light microscopy revealed increased darkening with increasing flux and/or dwell time. μ-FT-IR mapping allowed for the assessment of X-ray induced damage by detecting a relative decrease in ester group signals and an increase in acids' group signals, indicating the oil binder alteration (Fig. 14b,c). The result suggests that minimizing both visible and molecular modifications in such experiments is best achieved with low flux (~ 10^{11} ph/s) and short dwell times (< 0.3 ms).

FT-IR studies also investigated the effects of SR X-ray beams (ca. 7.7–13 keV) on mixtures of Zn white with rabbit glue, showing that: (i) X-ray irradiation altered the secondary structure of the proteinaceous glue, inducing a transition α-helices to β-turns and random coils; (ii) this effect was most significant at excitation energies near the Zn K-edge (9695 eV) [348].

In many experiments analyzing paintings and pigments, complementary measurements are often conducted to assess potential damage from X-rays' exposure. VIS–NIR sources are commonly used for this purpose, enabling semi-quantitative evaluation

of colorimetric changes beyond simple visual inspection (e.g., [136]). Raman spectroscopy is another method that can be used for characterizing X-ray induced damage, although the impact of the incident laser wavelength warrants consideration [136, 349–354].

5.2 Determining safe measurements

While a first step in the issue of radiation-induced side-effects and damage in synchrotron experiments is to acknowledge be aware of the problems, the second step is to define how to determine what is "safe". This involves considering both the visible and mechanical properties of the specimen and the threshold at which collected data collected remain "useful" or above detection limits. An experiment employing extremely low X-ray power and flux might prevent visible changes but could compromise the ability to obtain meaningful data. Therefore, a balance must be found between these two aspects. It is important to note that the thresholds for "low" and "useful" above are inherently vague, as they are highly sample dependent, in terms of the dose that a sample can tolerate, the X-ray method employed, and the detectable analyte concentrations.

The ALARA principle—"as low as reasonably achievable"—is central to this discussion and has originated from the radiological protection field. Synchrotron experimenters will have been introduced to some versions of ALARA during radiation awareness training. This principle states that: (i) no practice shall be adopted unless its introduction produces a net positive benefit; (ii) all radiation exposures shall be kept as low as reasonably achievable, taking economic and social factors into account [355]. When applied to a synchrotron experiment and radiation damage, this implies that the measurement must be useful, and that any risk associated with the measurement should be offset by the knowledge gained from the measurement [121].

Recent studies have directly addressed the issue of beam-induced damage by quantifying it using data from the technique itself. For example, Ganio et al. [185] used both micro-beam and bulk-beam XANES measurements at the sulfur K-edge to expose in lapis lazuli pigments to a range of X-ray doses (Fig. 15). Their findings showed that the alteration followed a pseudo-first-order kinetic rate law dependent on the absorbed dose by the sample. The parameters of the kinetics relied on only the dose and the "grade" of the sample, or how much of the chromophore was initially present.

Similarly, research on chromium-based paint and pigments investigated the influence of photon flux, binding medium, vacuum conditions, and cryogenic temperatures on the rate of alteration (cf. Figure 12) [132]. This comprehensive examination showed the alteration rate (change in the oxidation state of chromium) as a function of the absorbed dose across all these parameter spaces. Both works [132, 185] establish kinetic models that future researchers can use to predict what level of beam-induced damage may occur during their measurement and establish a safe level of measurement.

Documenting the radiation exposure history of cultural heritage objects during analysis is therefore crucial. Unlike many X-ray experiments where purpose-built or

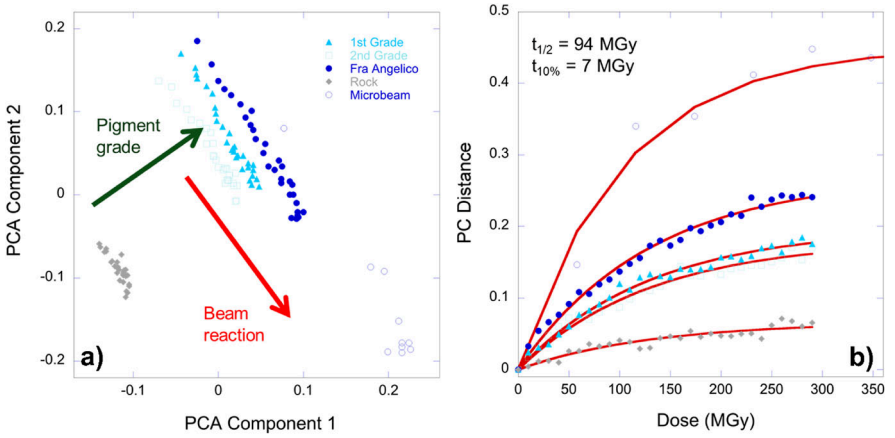

Fig. 15 **a** Principal component analysis (PCA) of time-resolved XANES spectra collected in the first 60 min of beam exposure at the S K-edge excitation energy. PCA resolves two components, one of which resolves difference in the pigment grade, and a second that follows the time-series of dose from the X-ray beam. Note the increased reaction rate of the Fra Angelico grade with exposure to micro-beam vs bulk-beam conditions. **b** Kinetics of the beam-induced radiation damage, showing the extent of reaction as the distance of each time point from the initial sample on the PCA plot as a function of the calculated absorbed dose. All kinetics can be solved as a pseudo-first-order reaction with the same rate constant, with the only variable being the amount of reactive lapis radical in the beam. Calculated values for the "half-dose" amount and an arbitrary threshold of "10% change" as 95 MGy and 7 MGy, respectively. Adapted with permission from [185]

synthesized samples are often discarded, heritage samples are returned to the host institution for future use and potential display in the case of entire paintings. Thus, detailed records of analysis types and extent are essential for recognition and awareness of any potential side-effects of the measurements. Following the IAEA technical meeting held in Amsterdam in 2017 [356], an Irradiation Passport for Art (IPA) initiative was developed as an online tool [357] to track the radiation exposure history of cultural heritage objects. This has been released, which documents the types of measurements, radiation, parameters used, and any observations or notes on the occurrence of damage or side-effects, either in the present or in future observations.

5.3 Next steps

Recognizing the potential for X-ray induced side-effects, the heritage science community is increasingly focusing on characterizing these effects and their underlying chemical and physical mechanisms. Recently, Godet et al. [176] successfully employed EPR spectroscopy to examine defect formation in Egyptian blue and green pigments caused by SR X-ray micro-probes. Furthermore, studies have also shown the complex behavior of historical paint materials, emphasizing that the interaction between pigments, binders, and varnishes cannot be ignored [132]. As paints and pigments are complex heterogeneous materials, continued study and documentation of damage and side-effects (as well as the mechanisms behind alterations) are needed to encompass

the whole breadth of open possibilities. A recent review that examined the practice of safe heritage analysis [121] proposed a paradigm shift from data-driven approaches at the synchrotron, where effects are only noticed secondarily after collection, to object-driven experimental approaches, where the preservation of the sample is put first, and data quality is second issue. This change in approach also requires less-intensive data collection strategies, achieved through either more efficient beam utilization, improved detection hardware, or enhanced collection efficiency (e.g., larger solid angle detectors). Additionally, employing parallel detection methods (UV–VIS–IR) concurrent with synchrotron data collection would enhance safe analysis. A multi-modal approach would give the experimenter several data avenues to examine for changes in the sample that occur during the data collection. To further mitigate damaging effects, a "real-time" assessment mode, where data from primary and secondary analysis modes are continuously monitored to detect and halt exposure at the first signs of undesirable behavior, could be highly effective. These recommendations broadly apply to both ion beams and X-ray analysis, and to the wider field of experimental examinations of paintings and paint materials.

6 Applications and case studies

6.1 Lead-based pigments

For several decades now, the examination of historical paintings revealed various manifestations of paint layers alteration linked with lead-based compounds, that can affect the optical and mechanical integrity of artworks. Several phenomena have been identified: the formation of whitish crusts at the surface of paintings, an increased transparency of superficial layers, color changes, and the formation of (re-mineralized) aggregates of lead soaps, often referred to as protrusions, that can break the paint surface and result in a loss of cohesion of the paint build-up. These phenomena can be linked to different classes of non-original lead salts, formed within the paint layers following chemical transformations. The lead source is often a lead-containing pigment or drier, including lead white, lead–tin yellow, red lead, litharge, massicot, or lead acetate, present across the paint stratigraphy.

The triggering and the kinetics of these transformations (sometimes harmful, sometimes harmless) are multifactorial. Depending on the observed cases, they are ascribable to both intrinsic (i.e., the combination of dissimilar materials by artist, their implementation in paint formulations following specific recipes) and extrinsic (environmental parameters, application of conservation treatments) conditions. In what follows, an overview of the main classes of lead-based alteration compounds reported until now will be provided, along with the description of selected examples presenting results obtained from historical paintings and/or laboratory model samples.

6.1.1 Lead soaps

An intense work aimed at assessing and understanding the roles of lead soaps in paintings has been carried out over the last two decades [137]. These compounds,

resulting from a reaction between lead-containing pigments or driers and the fatty acids of the oily binder, have been associated with several visible degradation phenomena, namely: protrusions with a white or orange core, efflorescence, exudates, drips, and darkening of the paint accompanied by increased transparency. Metal soaps are hybrid materials (long organic hydrocarbon chains terminating with carboxylate groups complexed to metal cations). Thus, vibrational spectroscopies, such as FT-IR and Raman, are very efficient techniques to detect and distinguish this class of compounds in paint, according to the type of cation and their degree of crystallinity [47, 48, 358–360]. More recently, NMR of both ^{207}Pb and ^{13}C has proven relevant in the present context [361]. Morphological studies were also performed on lead soaps via SEM–EDX [362]. X-ray techniques have also occasionally been used to detect lead soaps in historical and paint mock-ups. In the present case, XRF is not an ideal technique, since lead soaps are usually mixed with other lead compounds. μ-XANES spectroscopy, both at Pb $M_{5,4}$- edges [363] and Pb L_3-edge [364], has also been used to detect lead soaps in paint fragments. While this technique allows differentiating Pb soaps from some Pb pigments (such as lead white, lead-tin yellow, and red lead), it fails at distinguishing different lead carboxylates [e.g., azelate ($C_9H_{14}O_4Pb$) and palmitate ($(C_{16}H_{31}O_2)_2Pb$)]. When lead soaps are crystallized, XRD techniques are instead very efficient in their detection and identification. More particularly, the exact location of Bragg peaks can be exploited to determine the length of the fatty chains [e.g., palmitate and stearate ($(C_{18}H_{35}O_2)_2Pb$)], when pure [365] but also when mixed as $Pb(C_{16})_{2-x}(C_{18})_x$ [366].

Several experiments have been carried out to study oil saponification by PbO (used over centuries as a drier in oil paintings), mimicking the recipe of *huile de litharge*, proposed by Sir Théodore Turquet de Mayerne in 1633 [137, 367]. The main reaction leads to a mixture of unsaponified oil (liquid at room temperature) and lead soaps (solid) [367]. However, careful analyses by combining μ-XRD and μ-FT-IR mapping, around unreacted PbO particles, have revealed the presence of other lead carboxylates, such as lead formate [$Pb(HCOO)_2$] and sometimes lead (2+) formate hydroxide [Pb(HCOO)(OH)], which crystallize over oil drying [17]. As detailed below in Sect. 6.1.2, different unusual lead carbonates, such as shannonite (Pb_2OCO_3) and plumbonacrite [$Pb_5(CO_3)_3O(OH)_2$] (hereinafter denoted as "PN"), were also found along with neo-formed hydrocerussite [$Pb_3(CO_3)_2(OH)_2$] [139].

As more comprehensively described in the next paragraph, some of these uncommon phases have been recently reported in selected iconic sixteenth–seventeenth century masterpieces by Leonardo da Vinci and Rembrandt, leading to the hypothesis that these two artists used processes close to *huile de litharge* to prepare their paintings and that these phases are side products of the reaction of oil with PbO or Pb_3O_4 (red lead/minium). It should be noted that, except in the case of protrusions, which can effectively affect the esthetical rendering of the paintings by spotting over the painting surface, the presence of lead formates and unusual lead carbonates does not necessarily denote dramatic effects on the visual appearance and overall integrity of the painting. Besides, lead soaps can be present in painting without being involved in any degradation [137].

6.1.2 Lead carbonates

Lead carbonates are omnipresent in historical paintings, as they are the components of lead white, a pigment often encountered in the palettes of painters from Antiquity to the twentieth century. Lead white is commonly composed of a mixture of cerussite ($PbCO_3$) and hydrocerussite in different proportions [368]. Nevertheless, there are also several occurrences of the in situ formation of lead carbonates in paintings. An important point for the study of lead white and the understanding of its in situ formation is that the stability of this class of materials is governed by pH, which provides important chemical clues on the conditions of their formation [77]. Among the non-original lead carbonate compounds, PN is perhaps the most detected recently, thanks to technical advances in structural analysis at multiple length scales. This compound, only stable in strong alkaline conditions (pH > 12), was first reported by Vanmeert et al. [19], following the SR μ-XRD-CT analysis of a micro-sample from a painting by Van Gogh. Its formation was then linked to the photo-degradation process of the original red lead pigment. Gonzalez et al. [140] then reported the detection of plumbonacrite in the *impasto* (three-dimensional paint formulations to add texture and dimension to the painting) layers of several Rembrandt's paintings, among them the *Portrait of Marten Soolmans*, *Susanna*, and *Bathsheba*.

This study was conducted by combining SR HR-XRD and high-lateral 2D SR μ-XRD mapping. It highlighted that the distribution of PN (only present in *impastos* and not in other lead-white-based layers) and its microstructure (homogeneously distributed as nanometric crystallites much smaller than the lead-white pigment crystallites) pointed to the use by Rembrandt of a specific recipe, that would have created the chemical conditions of PN formation and crystallization. It was hypothesized that the use of alkaline lead (2+) oxide driers [i.e., litharge (α-PbO) and massicot (β-PbO)] could result in a chemical environment favoring the formation of PN. PN was further detected at the macro-scale via non-invasive MA-XRD mapping of selected areas of *The Night Watch* by Rembrandt (Fig. 16a) [17] and, in parallel, in several sixteenth–seventeenth century artworks [139, 140], thus suggesting that its presence in historical paintings is more common than initially expected. Gonzalez et al. [78] noted that while PN seemed relatively common in paintings from the north of Europe, it was absent in a corpus of Renaissance Italian paintings studied via SR HR-XRD. This was, however, before its detection in the ground layer of Leonardo da Vinci's *Mona Lisa*, again via SR HR-XRD [139]. In both *The Night Watch* and *Mona Lisa*, the spatial distribution of PN was correlated with different lead-based compounds, such as lead (2+) formates and lead soaps (Fig. 16a). These results, integrated with also those of model samples, support again the hypothesis that the formation of PN was linked with the use of lead oxide driers (Fig. 16b).

It is important to mention that while cerussite and hydrocerussite are generally identified as coming directly from the painters' palettes, chemical clues suggest that some hydrocerussite could also originate from chemical transformations active within paint layers. Notably, a precise analysis of SR μ-XRD patterns collected on a paint sample from *The Night Watch* allowed two subtypes of hydrocerussite to be distinguished according to their XRD peak widths: the crystalline phase coming from the original lead-white pigment, characterized by narrow peaks, and a non-original variety

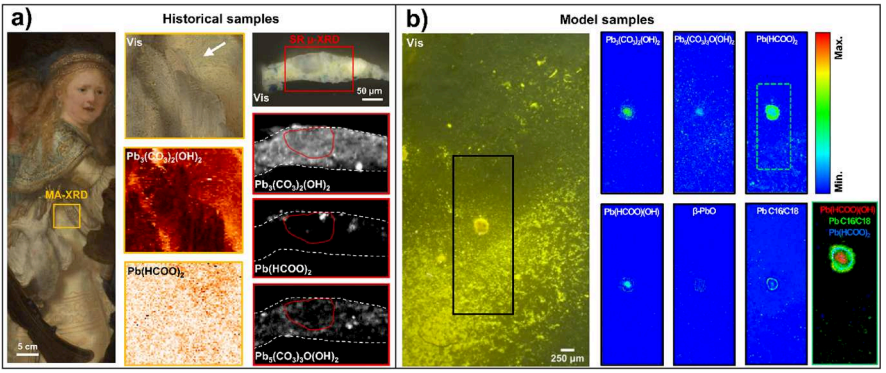

Fig. 16 a Multi-scale structural mapping of historical samples (from left): MA-XRD maps collected at the surface of *The Night Watch* (1642) by Rembrandt (Rijksmuseum, Amsterdam, NL) and SR μ-XRD maps collected on micrometric fragments taken from the painting. **b** SR μ-XRD crystalline phases distribution and RGB maps of Pb(HCOO)(OH)/PbC16/C18 soaps/$Pb(HCOO)_2$ of model samples designed to investigate compounds formed in linseed oil containing dissolved (and/or partially dissolved) β-PbO particles. Adapted from [17]

identified via wider peaks, indicating a specific nano-scale microstructure typical of an in situ crystallization [17].

Finally, more uncommon lead-carbonate compounds have recently been reported in historical paint layers. As mentioned earlier, shannonite was recently reported in Leonardo da Vinci's *Last Supper*, directly associated with non-dissolved grains of β-PbO [139], while leadhillite [$Pb_4SO_4(CO_3)_2(OH)_2$] was found in a sample of Rembrandt's *Homer* via SR μ-XRD-CT, as well as in a sixteenth century portrait of a monk and a eighteenth–nineteenth century copy of a self-portrait by Rembrandt [164].

More generally, these studies call for a wider and more systematic study of uncommon lead-based compounds in paintings. It is particularly interesting to further investigate the micro-scale organization of these newly formed compounds, as it provides valuable information on the transport mechanisms active in historical paint formulations based on lead-based siccatives, as well as on the kinetics of non-original products.

6.1.3 Lead chlorides

Lead chlorides are a class of compounds that can be identified by SR-based X-ray techniques in different pigment-containing materials, such as paintings and inks on papyri and cosmetics. Often, but not always, Pb–Cl compounds result from degradation reactions of original lead-based pigment(s). For example, laurionite [Pb(OH)Cl] and phosgenite ($PbCO_3 \cdot PbCl_2$) were identified as original synthetic components of Egyptian cosmetic containers (dated between 2000 and 1200 BCE) preserved in the Louvre Museum by SR HR-XRD [369, 370].

In the superficial white crust of a red ink of an Ancient Egyptian papyrus (dated back to first–second century CE), a combination of SR μ-XRF and SR μ-XRD mapping revealed the presence of another lead chloride compound (XPb_2Cl_5, with X =

K^+ and/or NH^{4+}), considered as secondary products developed by lead-containing driers used to prepare the ink [371]. In the same ink fragments, measurements also suggest the presence of an apatitic-like structure compound of general composition $(Ca, Pb)_5(PO_4, AsO_4)_3(Cl,OH)$. Their very peculiar distribution did not permit their origin (original compound or degradation product) to be defined, thus calling for a wider study of lead–calcium phosphates, as recently initiated by Costantino et al. [83]. SR μ-XRF/μ-XRD mapping were also exploited to identify challacolloite (KPb_2Cl_5) in a series of micro-samples from *Tebtunis portraits* excavated in the Fayum region of Egypt (ca. first-to-third century CE) [126]. The complementary distribution of this compound with respect to that of hydrocerussite led to the conclusion that challacolloite is a secondary compound of the originally applied pigment.

More recently, SR μ-XRF/μ-XRD mapping of a series of fragments and micro-samples from thirteenth century wall paintings by Cimabue and Giotto in the upper Basilica di San Francesco in Assisi (Italy) enabled to visualize the distribution of different chlorinated lead and copper compounds [14], namely: lead hydroxychloride, laurionite, the rare mineral cumengeite $[Pb_{21}Cu_{20}Cl_{42}(OH)_{40}{\cdot}6H_2O]$, and the copper hydroxychlorides atacamite $[Cu_2Cl(OH)_3]$ and clinoatacamite $[Cu_2(OH)_3Cl]$. All these components were identified and interpreted as degradation products of the original lead- and copper-containing pigments, thus pointing out the key role played by Cl-containing species.

Lead chlorides were also identified as weathering products in a series of oil paintings, such as *Anatomy Lesson of Dr. Nicolaes Tulp* (1632) by Rembrandt. Here, fiedlerite $[Pb_3Cl_4(OH)_2]$ was identified in lead soap protrusions by XRD measurements [372]. Sources of Cl compounds can be multiple (e.g., impurities of the matrix, environment, etc.), but, in most cases, the origin of these species is uncertain. The number of laboratory studies aimed at investigating the susceptibility of lead-based pigments under effects of chlorinated compounds is quite scarce [373–375]. The formation of laurionite was observed by XRD, when lead white is put in contact with a sodium chloride (NaCl) containing solution [373]. Electrochemical methods and XRD permitted the identification of the same compound along with phosgenite, when lead (2+) oxides were treated with solutions of NaCl or ammonium chloride (NH_4Cl) at fixed pH [374, 375].

More recently, the oxidative effect of hypochlorous acid (HOCl) on the alteration of lead white was also assessed. In situ laboratory XRD measurements allowed the monitoring of the oxidation process of cerussite and hydrocerussite with increasing exposure time to HOCl, revealing the gradual formation of whitish phosgenite and cotunnite ($PbCl_2$), along with black plattnerite (β-PbO_2) (Fig. 17). The latter compound, arising from the oxidative degradation of Pb^{2+}-containing pigments to Pb^{4+} and sometimes occurring with its polymorph scrutinyite (α-PbO_2) [14, 376], is often responsible of serious blackening phenomena, especially in mural paintings [13, 369, 377–379]. In contrast, due to its high solubility in water, $PbCl_2$ is hardly observed in historical paint samples.

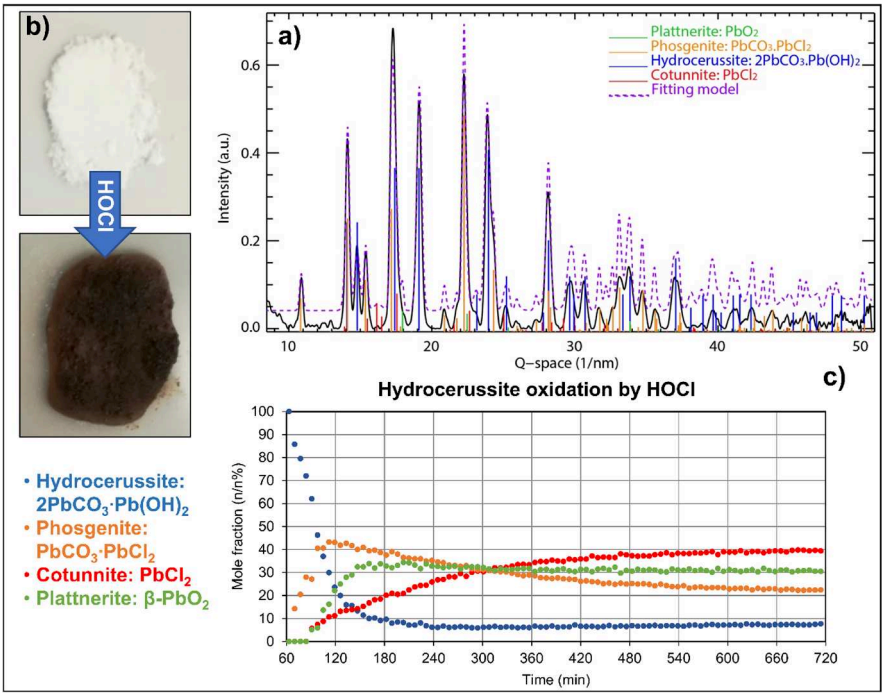

Fig. 17 **a** Photographs of hydrocerussite before (top) and after (bottom) prolonged exposure to HOCl. **b** 1D XRD pattern recorded after more than 1 h exposure of hydrocerussite to HOCl, illustrating the formation of phosgenite, cotunnite, and plattnerite. **c** Plot of the molar fraction of hydrocerussite *vs* exposure time to HOCl, showing the gradual decreasing of relative amount of hydrocerussite and the corresponding increasing of relative abundance of phosgenite, cotunnite, and plattnerite

6.1.4 Lead sulfates

Anglesite ($PbSO_4$) and palmierite [$K_2Pb(SO_4)_2$] have been first reported in weathering crusts on medieval glass windows and stone sculptures (quartz sandstones), along with gypsum ($CaSO_4{\cdot}2H_2O$) and syngenite [$K_2Ca(SO_4)_2{\cdot}(H_2O)$] [380, 381]. These compounds can form when lead in the glass or polychromy is exposed to SO_2 (air pollutants) and potassium from cleaning agents such as K-soaps or KOH. The same lead sulfate compounds have been found in wall and mural paintings or fragments, both on the surface of the paint and deeper within the layer structure, as identified using SR μ-XRD [14, 55, 379, 382]. The identification of anglesite and palmierite as degradation products in easel paintings has been progressively increased over the last years. In these cases, SO_2 and potassium may also originate from an internal source, such as smalt or an organic lake pigment, that might be present as original paint components. Portable XRD and MA-XRD non-invasively identified lead sulfates in *Girl with a Pearl Earring* by Vermeer, Rembrandt's *The Jewish Bride* and several seventeenth century still life paintings [18, 33, 383, 384]. Micro-sample analysis is often needed to further elucidate where and how the new lead phases form in the paint.

The combination of SEM–EDX and μ-FT-IR or μ-Raman has proven effective in indicating the formation of lead and lead potassium sulfates in whitish surface crusts on paints rich in smalt, such as on Rembrandt's *Homer* [385, 386]. SR XRD-CT of a paint sample from this painting identified anglesite and palmierite as the dominant sulfate phases, with minor contributions from lanarkite [$Pb_2(O)SO_4$] and leadhillite [164]. In this case, it was suggested that lead (Pb^{2+}) came mainly from the saponified lead white-containing ground, potassium (K^+) from the smalt pigment in the paint, and sulfur/sulfate from environmental SO_2. Depending on the availability of potassium, either anglesite or palmierite forms or dominates [47]. Lanarkite, in addition to anglesite and palmierite, was identified using SR μ-XRD and SR XRD-CT in an inclusion formed in a smalt and ultramarine paint in a painting by Philips Wouwerman [73]. Palmierite is also found associated with potash alum [$KAl(SO_4)_2{\cdot}12H_2O$]. Alum was commonly used in making organic lake pigments as a substrate for the dyestuff. Palmierite can form in and around organic lake pigment particles if the lake substrate contains excess K_2SO_4, which acts as a direct reaction site for mobile Pb^{2+} ions (often from lead white) [129, 387]. In Vermeer's *The Art of Painting*, palmierite was analyzed in several cross-sections using SEM–EDX and SR μ-XRD where alum was thought to have been added during a nineteenth century lining treatment [388, 389]. Anglesite and lanarkite found in an oil canvas painting by Friedrich Amerling, along with Naples yellow (lead–tin antimonate Pb–Sb–Sn), were assumed to be byproducts of the synthesis of Naples yellow pigment, which involves alum [390].

As the ions involved in the in situ formation of lead sulfate compounds in historical paintings can come from various sources, internal or external to the paint layers, their distribution within paint stratigraphies varies considerably. This is, for example, exemplified when comparing the spatial distribution of palmierite, present as crystalline aggregates in the Wouwerman sample studied by Gonzalez et al. [73] and as thin layers at interfaces in the Vermeer sample [18, 47]. The schematic diagram proposed by Price et al. [164] to explain the chemical pathways possibly active in Rembrandt's *Homer* highlights the variability of Pb-SO_4 products, depending on the local chemical environment such as alkalinity/acidity and availability of SO_4^{2-} and CO_3^{2-} and other ions, which can vary from layer to layer within heterogeneous paint systems (Fig. 18). This can justify the formation of some rare minerals, including lanarkite and leadhillite, deeper in the paint. Research is today ongoing to precise the kinetics of these reactions, by implementing in-operando structural measurements via micro-beams on model samples.

6.2 Cobalt smalt pigments

6.2.1 Occurrence, manufacture, and composition

The pigment smalt, a blue cobalt glass, was extensively used in European oil painting from the late fifteenth to the eighteenth century as a valid alternative to the costly ultramarine or azurite [9]. The earliest instances of smalt in European paintings date back to around 1400 [391]. However, long before that, the coloring potential of cobalt had been exploited when humans began making glass in antiquity. Apart from easel

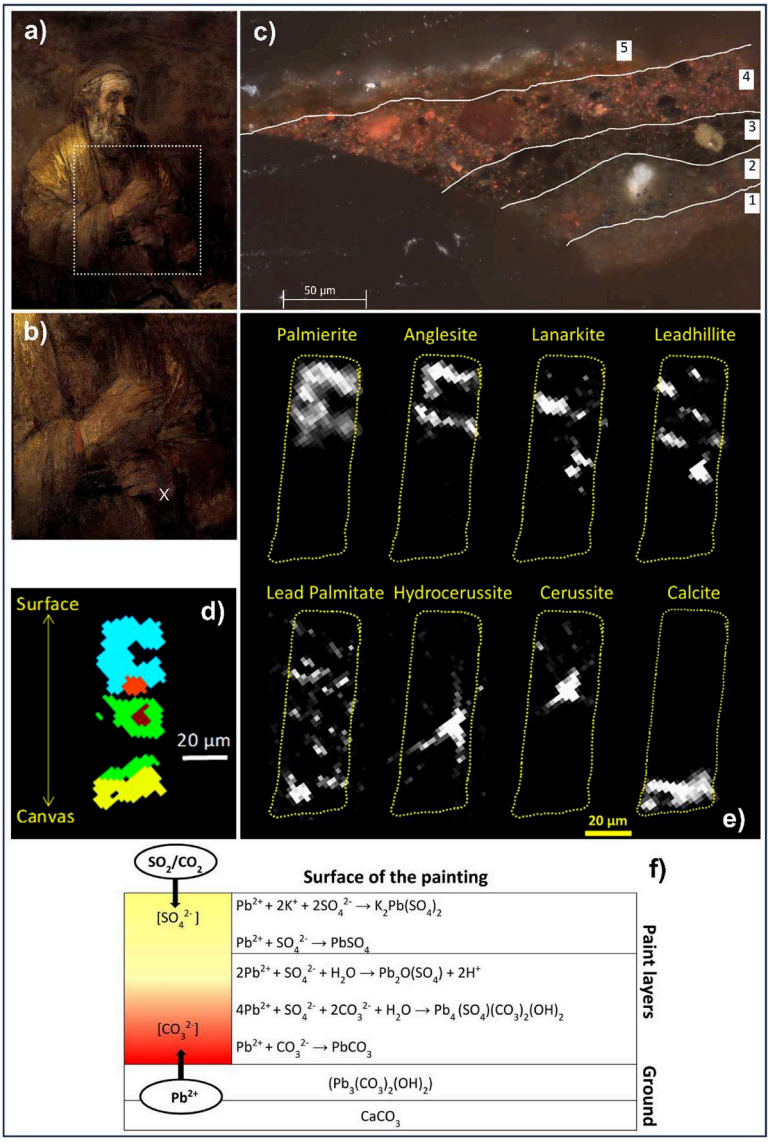

Fig. 18 SR-based XRD-CT analysis of Pb–S degradation products in a paint cross-section from Rembrandt van Rijn's *Homer* (1663, oil on canvas; Mauritshuis, The Hague, NL). **a** Photograph of the painting and corresponding **b** detail indicating the sampling spot. **c** Optical microscope image of the cross-section (MH584 × 35) taken from Homer's left hand (shown in **b**), revealing distinct layers: chalk/red earth ground (1), lead-white ground (2), dark brown undermodeling (3), reddish paint (4), and surface paint with discolored smalt and Pb-rich deposits (5). **d** Cluster analysis of XRD-CT showing a virtual (Slice 1) that is perpendicular to the cross-section plane. Each cluster corresponds to regions with similar diffraction patterns. **e** Maps showing the location of each major Pb-containing phase for Slice 1. **f** Schematic diagram illustrating the formation and localization of various Pb phases within the painting. Adapted with permission from [164]

painting, smalt was also important as a pigment in wall paintings, polychrome sculptures, enamels, and ceramic glazes, across a wide range of dates and regions [392, 393].

Smalt was made by melting a source of silica, such as pebbles or sand, along with potash as the flux, and roasted 'zaffre'—a mixture of roasted cobalt ore and varying amounts of quartz or sand— at temperatures around 1200 °C [394–396]. Cobalt (2+) gives smalt its blue color. The cobalt content in paintings typically ranges from 3 to 7 wt% CoO [29, 397]. In addition to SO_2, K_2O, and CoO, significant amounts of arsenic are usually present in the formulation of historical pigments, as well as smaller concentrations of iron, nickel, and bismuth. These elements are introduced with the cobalt ore and are associated with its geological source and preparation method. The elemental composition of the smalt can also be influenced by the composition of silica or potash source, or other additives introduced during manufacturing, which may account for small percentages of calcium, aluminum, manganese, copper, sodium, and/or barium [9]. Variation in the content of elements affects the properties of the smalt such as color, translucency, and stability.

Smalt is a glass; thus, it is not possible to identify this pigment using XRD. However, other elemental spectroscopic analyses have proven useful in characterizing smalt, including SEM–EDX/-WDX, PIXE, and XRF [29, 391, 397]. Laser ablation ICP-MS can be further explored for spatially resolved studied of degradation phenomena of smalt, as it has the potential to visualize variations in elemental content at trace amounts (< ppm) within a paint sample [398]. The recent development of mobile MA-XRF scanners has enabled the non-invasive identification and mapping of smalt in historical paintings [256]. The combined presence of cobalt, nickel, arsenic, and possibly potassium and bismuth is considered a reliable marker for the characterization of smalt, even when the pigment is degraded [399–401]. This method complements the previous investigations of paintings using neutron activation autoradiography, which can also map cobalt in the inner layers of a painting [402, 403].

The relative concentrations of the various elements as well as variations in particle-size distribution can provide information about the type of smalt used and be diagnostic for a particular artist, region, or period. For instance, Spring et al. [397] noted a significant change in the quality of smalt at the end of the sixteenth century. The cobalt content of smalt, indicating its intensity of color, decreased from up to approx. 9 wt% CoO to up to approx. 4 wt% CoO. In Italian paintings, smalts made of soda glass instead of potash glass have been occasionally found [29].

There can also be considerable differences in the levels of arsenic, nickel, and bismuth, resulting from variations in the cobalt ore preparation, which has proven useful in distinguishing different smalt pigments in the same painting [255, 397]. For example, the combination of quantitative SEM–EDX analysis of cross-sections and MA-XRF scanning of the painting was used to reveal that three types of Co-containing materials are present in the original parts of the *Saul and David* by Rembrandt, while a fourth Co-material was used in the non-original canvas insert (Fig. 19a). From the Fe and Co distribution maps (Fig. 19b,c), it is immediately clear that the upper right canvas piece (part γ), painted in a monochrome dark tone, does not show the same origin as the other canvas sections (parts α and β, respectively). Throughout the γ area, both Co and Fe appear to be present at high abundance; the joins between the various

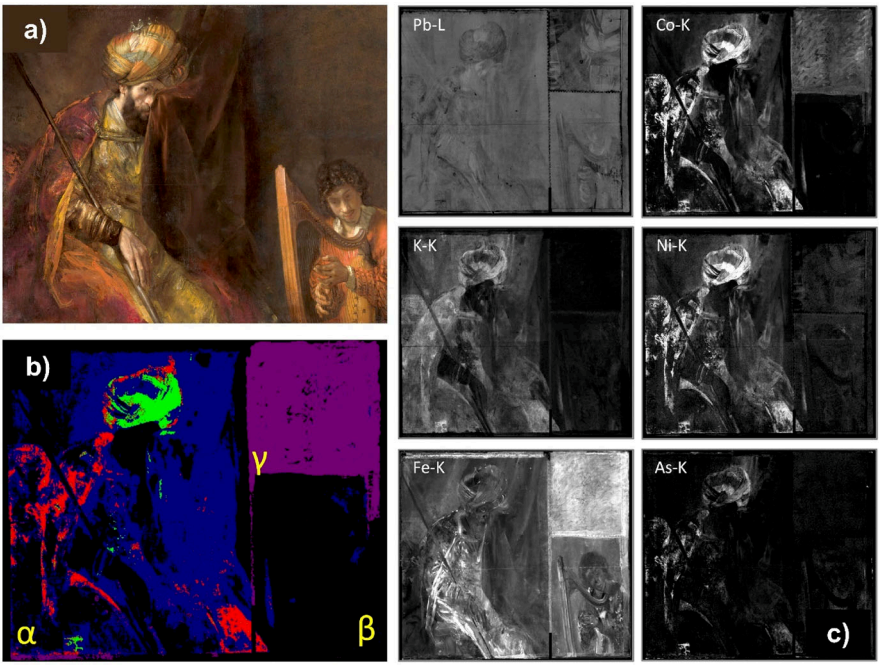

Fig. 19 **a** Photograph of *Saul and David* by Rembrandt, (ca. 1652, oil on canvas, inv. MH621; Mauritshuis, The Hague, NL). **b** Pixel cluster map showing locations of different Co/Ni ratio values [color codes: green: "high Ni", red: "medium Ni", magenta: "low Co/Ni", blue: "rest (Co/Ni ratio undetermined due to low Co and Ni abundance)"; black: "No smalt present"]. **c** MA-XRF maps (1656 × 1311 pixels) of various elements present in the painting. Adapted with permission from [255]

sub-parts as well as the entire γ-section were uniformly covered with a Fe and Co-containing paint to dissimulate the differences with sections α and β. The Co map of the α-section demonstrates that smalt was extensively used in the areas of the turban, the curtain, Saul's garments, and his chair. K is associated with smalt but also with red lake (likely from alum or KOH added during its production). The Fe distribution in the α-section is quite different from the other elements, since it is dominated by the earth pigment-containing areas, where the Fe concentration is much higher than in smalt (where it is of the order of a few wt%). By considering the Ni–K:Co–K XRF intensity ratios throughout the painting, four groups of pixels can be distinguished (Fig. 19b).

6.2.2 Alteration processes

Smalt is highly unstable in oil media (in media other than oil, it tends to be better preserved). Historical smalt paints have often become discolored and degraded, resulting in a patchy, translucent brown or grayish-green appearance, accompanied by crack formation and surface blanching [400, 404–408]. Smalt usually contains only potassium as the alkali. It follows that the pigment is particularly prone to deterioration due

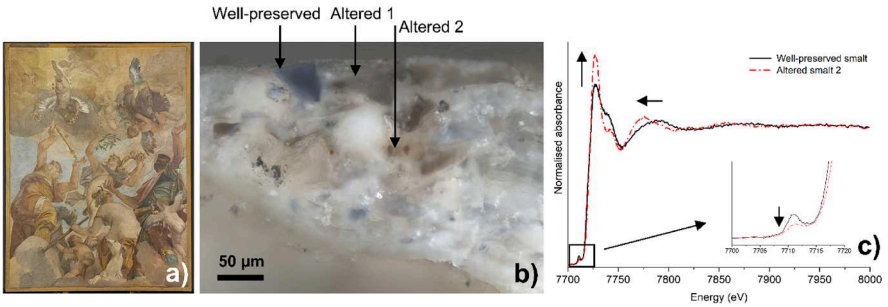

Fig. 20 **a** Photograph of *Les Dieux de l'Olympe* by Paolo Veronese (1557, fresco transferred to canvas, Louvre Museum, Paris, FR). **b** Optical microscope image of the cross-section (L2925) from (**a**) showing well-preserved and altered smalt. **c** Co K-edge XAS spectra collected from well-preserved (black) and altered smalt (red) in the cross-section from (**b**), showing changes in the profile on alteration: the pre-edge intensity centered at 7711 eV decreases and the white line centered at 7727 eV becomes sharper and increases in intensity, suggesting an increase in the cobalt coordination number. Panels **b** and **c** are reprinted with permission from [66]

to the very low amount of alkaline-earth elements, such as calcium, that can act as stabilizers.

After investigating paint cross-sections from discolored smalt paints using SEM–EDX, secondary-ion mass spectrometry (SIMS), and UV–VIS spectroscopy, Boon et al. [409] noted a significant depletion of potassium in the rims of discolored smalt particles compared to the well-preserved core along with an increase of potassium in the oil paint matrix around the particles. They also observed only minor changes for cobalt and other elements, proposing that, after the depletion of potassium out of the glass, water molecules were incorporated in the glass itself, thus lowering its basicity. This would have affected the structural coordination of Co^{2+}, transitioning from tetrahedral coordination—where the pigment is blue—to octahedral coordination—where the pigment is a very weak pink, almost colorless. This theory was later proved in a series of SR experiments by Robinet et al. (Fig. 20) [66] and Cianchetta et al. [67]. XANES/EXAFS spectroscopy at the Co K-edge on cross-sections and macroscopical samples was instrumental in demonstrating that the oxidation state of cobalt is not modified, and that the Co–O distance is increased in discolored smalt [66, 67]. This is the consequence of the formation of higher coordinated Co–O polyhedra and these structures have been shown to possess a modified optical absorption leading to the weak pink hue [67]. Additional ATR mode FT-IR and Raman spectroscopy measurements also revealed changes in the silica structure of the glass, showing that the alteration of the pigment is even more complex [410].

Apart from loss of color and degradation of smalt itself, the leached potassium can cause a yellowing or darkening of the oil binder. This occurs as it reacts with fatty acids from the oil to form potassium soaps [29]. The latter are soluble in water and can migrate to the paint surface or further react with atmospheric pollutants, such as sulfates or carbonates, to form complex potassium salts.

Calcium oxalates are usually associated with potassium crusts. Potassium sulfates are soluble in water, but upon contact with lead ions (from lead white or another

lead source in the paint), they form insoluble deposits of potassium lead sulfates [385, 386]. SR μ-XRD conducted on paint cross-sections was able to identify them as predominantly palmierite [$K_2Pb(SO_4)_2$] [73, 164], a compound that may have different manifestations in smalt paints: in surface crusts, around smalt particles, and, occasionally, also in inclusions in the smalt paint (cf. Figure 18).

The influence of various oily-based binding media on alteration rates of smalt was recently proved by de Mecquenem et al. [28]. K and Co K-edges μ-XANES measurements, combined with SEM–EDX and μ-XRF techniques, of a series of smalt paint mock-ups and cross-sections from a series of sixteenth–nineteenth century paintings showed that smalt degraded more rapidly in samples prepared using cooked walnut oil and PbO siccative linseed oil compared to those obtained employing cooked linseed oil and walnut oil siccative with PbO.

6.3 Copper-based pigments

Copper-based pigments encompass a wide variety of compounds of Cu^{2+}, having both natural and synthetic origins and displaying a range of green-to-blue colors [411]. A general classification of these pigments defines two major groups: (i) mineral copper pigments, i.e., inorganic salts that may have mineralogical analogs, and (ii) organometallic compounds derived from copper complexation with organic ligands [412, 413].

In general, copper pigments were known and used for artistic purposes from Antiquity. Indeed, Egyptian blue was first manufactured in Egypt during the Early Bronze Age (late fourth-to-third millennia BCE) as a by-product from metallurgic or glass workshops and is considered the earliest, synthetic pigment [414]. The pigment is composed of a calcium copper silicate ($CaSi_2O_5{\cdot}CuSi_2O_5$), i.e., the synthetic analog of the rare mineral cuprorivaite. These types of silicates were recently extensively reviewed by Nicola et al. [415] together with Egyptian green and the closely related Chinese Blue ($BaCuSi_4O_{10}$) and Chinese Purple ($BaCuSi_2O_6$), which differ only by the presence of Ba^{2+} instead of Ca^{2+}. Authors highlight that alkaline-earth copper tetrasilicates are stable over time, as attested by the many archeological objects containing these pigments in good condition. As a result, SR-based X-ray investigations mainly focused on understanding the chemical structure of these pigments [416, 417], their history of use [418, 419], or their manufacturing methods [150, 420], rather than alteration mechanisms. One notable exception is the study by Godet et al. [176] who warn for damages induced by exposure to SR X-ray micro-probes of Egyptian blue and green (cf. Section 5). By employing EPR spectroscopy, authors defined the irradiation thresholds below which the occurrence of unwanted phenomena in these pigments (i.e., discoloration, creation of radicals, loss of crystallinity, and redox changes) are mitigated.

According to the Pigment compendium [411], Egyptian blue remained the standard blue pigment for several millennia, but its use gradually declined in the late Roman period and Early Middle Ages. Although occasionally reported on works of art until the sixteenth century [176, 421], including its exceptional discovery in some of the wall paintings by Raffaello in Villa Farnesina (Roma, Italy) [422, 423], calcium copper

silicates were diffusely replaced by other Cu-based pigments, such as copper carbonate hydroxides (i.e., blue azurite and green malachite) or green copper halides, or copper acetates (i.e., verdigris), or derivative organo-copper complexes (commonly referred to as 'copper resinates' as umbrella name), which will be discussed in the next paragraphs. While the historical occurrence of copper resinates is less clear due to difficulties in its identification [424–426], verdigris was commonly used in Europe from Middle Ages to the Baroque period [424].

6.3.1 Copper hydroxycarbonate and halides

Malachite [$Cu_2CO_3(OH)_2$] and azurite [$Cu_3(CO_3)_2(OH)_2$] are isomorphous secondary minerals that are formed by the interaction of carbonated solutions with the copper-bearing rocks in the uppermost oxidized areas of ore deposits [9, 411]. Both pigments are basic copper carbonate minerals with a monoclinic crystal structure, that have a relationship of intergrowth with cuprite (Cu_2O), tenorite (CuO) and chrysocolla [$(Cu,Al)_2H_2Si_2O_5(OH)_4 \cdot n(H_2O)$], which often retain as impurities [427].

Numerous investigations established that European painters achieved a wide variety of shades with azurite, ranging from light and deep blue, over green, to deep purple, by a resourceful combination with the other pigments [428]. Salvadò et al. [154] employed SR μ-XRD and SR μ-FT-IR spectroscopy to conclude that azurite, sometimes glazed with precious lapis lazuli, is the dominant blue pigment in fifteenth century altarpieces made in Catalonia and Crown of Aragon. In addition to azurite, a few small $BaSO_4$ particles were also detected as a material of paragenesis, thus indicating the mineral origin of the pigment. This specification is relevant as azurite and malachite were also synthesized from the fifteenth century onwards and commonly called blue and green verditer, respectively. The synthetic variants of both pigments retain the chemical composition and crystalline structure of the corresponding mineral forms, but the particles display a spherulitic shape [406]. Smieska et al. [429] exploited a combination of SR XRF and SR XRD analysis to investigate impurities in azurite in thirteenth-to-sixteenth century illuminated manuscripts, thus attesting differences in preparation or geological provenance.

In easel paintings and illuminations, azurite is relatively stable. In the aforementioned fifteenth century altarpieces, Salvadò et al. [154] attributed the darkening of azurite paint to aging of the binding media and retention of dust and pollution by the surface rather than to chemical changes of the pigment itself. However, in wall paintings, humidity and alkaline conditions can give rise to blackening with the conversion of azurite into tenorite, as discussed by Scott [413] and, more recently, by Mattei et al. [430]. As shown by Cudennec and Lecerf [431], the OH^- ions, released by the plaster, react with Cu^{2+} ions of the pigment, thus giving rise to copper hydroxide, which in turn transforms into water and the more stable CuO. Rickerby et al. [432] demonstrated that, in the solid state, the thermal decomposition of both malachite and azurite into tenorite occurs at 300 °C and 400 °C, respectively, which is relevant for buildings affected by fires.

The degradation of copper-containing pigments into copper halides and basic halide compounds is also usually found in the context of mural paintings where salts and

chlorides are prevalent in an alkaline environment [433, 434]. Upon studying this phenomenon, that often causes a strong chromatic alteration of azurite from blue to green, researchers frequently identified the presence of nantokite (CuCl) or polymorphs of copper hydroxychloride [$Cu_2Cl(OH)_3$], such as atacamite, clinoatacamite, and paratacamite, as reason for alteration. Botallackite, another copper hydroxychloride with the same chemical formula, is mentioned less often in the literature [435].

The question whether copper halides in paint, especially atacamite, were applied as a pigment or have formed as secondary reaction products has been prone to debate [436]. Nevertheless, their intentional application as pigments has been reasonably suggested for several Asian ancient wall paintings. For example, the use of copper hydroxychlorides as pigments was observed in Cave 256 of Mogao Grottoes (960–1279; China) by Shui et al. [437]. Cotte et al. [382] used SR μ-XRD and SR μ-FT-IR to identify atacamite as an original pigment in eighth century painted mural fragments coming from the Bamiyan valley (Afghanistan).

In Europe, the first written trace concerning the production of copper chlorides as pigments is dated back to twelfth century, as described by Theophilus in the *De Diversis Artibus* [438]. In this regard, Bidaud et al. [439] studied a thirteenth century wall painting in Krems (Austria), revealing the intentional use of copper salts, corresponding mainly to clinoatacamite, via SR μ-XRD. In the green layer of a paint cross-section collected from *The Issenheim* Altarpiece (1512–1516) by Matthias Grünewald, a mixture of atacamite and paratacamite was identified by time-of-flight secondary (TOF)-SIMS, SR μ-FT-IR, and SR μ-XRD analyses and interpreted as an original application of the painter [440].

Nevertheless, in other cases, experiments at synchrotron end-stations recognized copper halides in paint samples together with the remains of the original pigment applied, clarifying their presence as secondary products. This is the case of the work by Lluveras et al. [433], who employed SR μ-FT-IR spectroscopy in combination with mass spectrometry methods to conclude that the greenish appearance of some mural paintings in the Monastery of Santes Creus (Catalonia, Spain) is due to the conversion of original blue azurite to greenish copper hydroxychlorides. Valadas et al. [441] performed SR μ-XRF and XRD measurements to ascertain malachite alteration to copper chlorides in seventeenth century frescoes from the Misericordia Church in Odemira (Portugal). SR μ-FT-IR and SR μ-XRD analysis allowed Salvadò et al. [43] to identify different copper hydroxychlorides, including atacamite, paratacamite, and calumetite [$CaCu_4(OH)_8Cl_2 \cdot 3.5H_2O$], in samples from several fifteenth century Catalan altarpieces. Depending on the analyzed painting, authors ascribed the presence of copper chlorides either as secondary products or as original pigments. More recently, Avranovich et al. [14] performed an X-ray study at multiple length scales of a series of thirteenth century painted fragments obtained from one of the discolored vault of the upper Basilica di San Francesco in Assisi (Italy) (Fig. 21a,b,e). A combination of reflection/transmission mode XRD and XRF mapping measurements (with traditional and SR X-ray sources) revealed the distribution of primary compounds and secondary products, including atacamite and clinoatacamite, both across the surface (Fig. 21c,d: top) and throughout the stratigraphy (Fig. 21c,d: bottom) of the paint.

The chemistry of formation of copper chloride and copper hydroxychlorides has been a cause of concern for the conservation of bronzes as well, due to the "bronze

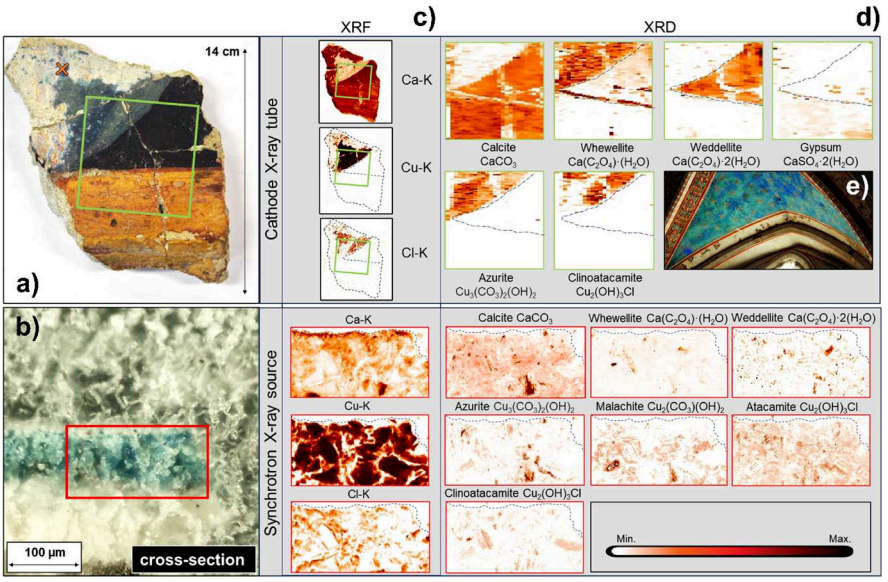

Fig. 21 **a** Painted fragment CA26 from the one of the discolored vault of the upper Basilica di San Francesco in Assisi (late thirteenth century, Italy) shown in (**e**). The orange cross indicates the spot of the sample used to obtain the paint cross-section illustrated from the photomicrograph of (**b**). **c** XRF maps of selected key elements. Top, MA-XRF: area (h × v) = 50 × 50 mm^2, step size (h × v) = 0.3 × 0.3 mm^2, exposure time = 0.3 s/pt, reflection geometry, energy = 20.04 keV. Bottom, SR µ-XRF: area (h × v) = 290 × 100 μm^2, step size (h × v) = 1 × 1 μm^2, exposure time = 1 s/pt reflection geometry, energy = 21 keV. **d** XRD maps of selected primary compounds and secondary products (weddellite, whewellite, atacamite, clinoatacamite). Top, MA-XRD: area (h × v) = 25 × 24 mm^2, step size = 1 × 0.3 mm^2, exposure time = 10 s/pt, reflection geometry, energy = 8.04 keV. Bottom, SR µ-XRD: area (h × v) = 290 × 100 μm^2, step size (h × v) = 1 × 1 μm^2, exposure time = 1 s/pt, transmission geometry, energy = 21 keV

disease", and for this reason, the equations below have been proposed to describe the degradation pathway (Eqs. 4, 5) [442]

$$Cu + Cl^- \rightarrow CuCl + e^-, \tag{4}$$

$$4CuCl + O_2 + 4H_2O \rightleftarrows 2Cu_2(OH)_3Cl + 2H^+ + 2Cl^-. \tag{5}$$

Even though metallic copper is usually not present in paints, Eq. 4 does illustrate how nantokite can be formed as a secondary reaction product. In particular, the latter can occur when an anion exchange takes place between the copper carbonate and copper acetate-based pigments with chloride anions, which are potentially supplied by environmental contaminants. Equation 5 shows how in a subsequent step, the formation of copper hydroxychlorides can be expected.

Similarly, Svarcová et al. [434] studied the transformation of copper carbonates in contact with sodium chloride solutions, noting the formation of paratacamite from azurite and malachite after 20 months of exposure. This research also highlighted the effect of oxalic acid, which can catalyze the reaction by increasing the amount of

paratacamite formed, even at low concentrations, as suggested by Eq. 6

$$2Cu_2CO_3(OH)_2 + 2NaCl + H_2C_2O_4 \rightleftarrows 2Cu_2Cl(OH)_3 + Na_2C_2O_4 + 2CO_2. \quad (6)$$

6.3.2 Verdigris and copper resinate

Verdigris, a term used for various blue–green copper (II) acetates, is formed by the reaction of copper with vinegar. Some variants of the historical recipes for verdigris include the addition of honey, common salt, or an ammonium salt mixed with urine (NH_4Cl) [443]. The specific type of copper acetate formed, whether neutral or basic, is influenced by the recipe and environmental conditions, which overall determine the pigment's chemical and physical properties: hydration, basicity, color, morphology, and grain size. All the copper acetate forms can be expressed by the general formula: $xCu(CH_3COO_2)\cdot yCu(OH)_2\cdot zH_2O$, with copper (II) hydroxide acetate pentahydrate [$2Cu(CH_3COO)_2\cdot Cu(OH)_2\cdot 5H_2O$], copper (II) trihydroxide acetate dihydrate [$Cu(CH_3COO)_2\cdot 3Cu(OH)_2\cdot 2H_2O$], and copper (II) acetate monohydrate $Cu(CH_3COO)_2\cdot H_2O$ as some of the compounds that, so far, have been identified in the pigment, along with copper (II) oxalates and hydroxychlorides as byproducts [9, 412, 443, 444]. The molecular structure of neutral copper (II) acetate consists of two copper atoms bridged by four acetate ligands with two axial water ligands [167]. Basic forms of verdigris display both bridging bidentate and monodentate coordination of the Cu^{2+} ions [166, 445, 446].

The best-known recipe for copper resinate is from the manuscript by Théodore Turquet de Mayerne manuscript dating from the seventeenth century, although earlier occurrences have been noted in Italian and Northern oil paintings of the fifteenth and sixteenth centuries [9]. Copper resinate was obtained by dissolving verdigris in heated essence of turpentine. The treatment favors the extraction of copper ions by the formation of salts of resin acids (abietates); the resulting green substance could be applied fresh as a transparent green glaze to obtain a brilliant chromatic effect or as dried powder mixed as a pigment with the oil binder.

Experimental studies based on Cu K-edge SR XAS [42], FT-IR [447], and electrospray ionization mass spectrometry with the support of theoretical investigations by Density functional theory (DFT) calculations [448] allowed disclosing the molecular environment of copper ions in the amorphous matrix of copper resinate. These mostly retain the same configuration of the verdigris pigment, where the carboxylate ligands available from the resinous matrix complex the copper ions, in place of the acetate groups, in a bridging bidentate configuration. However, EPR spectroscopy evidenced that a fraction of copper (II) acetate dimers undergoes a partial dissociation during the substitution of acetate by abietate ligands, leading to the formation of monomeric copper (II) carboxylate complexes [41].

Distinguishing copper resinate from verdigris in historical paint proves challenging as both display a similar glaze-like appearance, due to general reactivity of verdigris in oleoresinous binders and other organic components (e.g., wax and protein [413, 449]). XRD, FT-IR, Raman spectroscopy, and GC–MS, combined with optical microscopy

observation, are analytical techniques suitable for recognizing these pigments [412, 425, 444, 450].

Despite their historical significance, verdigris and copper resinate have relatively low stability in paintings. Experimental studies by molecular spectroscopies have demonstrated that copper organo-metallic complex pigments generally show a more pronounced reactivity toward organic components than copper inorganic compounds [449, 451, 452]. This is explained by the higher propensity of copper ions complexed by organic ligands to the extraction into the organic matrix. Furthermore, it was demonstrated that copper ions participate in the oxidative processes of oil-based painting media [451, 453]. For these reasons, the presence of verdigris and copper resinate very often combines with the observation of alteration products of the paint materials, such as copper carboxylates, copper oxalates, basic copper chlorides, and, more sporadically, copper formates [454]. In some cases, the most impacting consequence of this decay is the progressive darkening of the green paint [9, 41, 448, 455], thus determining the disuse of these two pigments after the seventeenth century.

The intriguing chemistry of this class of copper-based pigments attracted the interest of many scientists, who attempted to understand the mechanism behind the change of the green color. This objective is made more difficult by the ambiguity in the detection of verdigris and copper resinate and in distinguishing them from the alteration products. Furthermore, the low crystalline or totally amorphous nature of some of these compounds inhibits the use of structural techniques, such as XRD. For these reasons, a complementary analytical approach is necessary to provide a comprehensive insight into the phenomenon. High lateral resolution and highly sensitive techniques, such as those based on SR, including FT-IR and XRD among others, are essential to resolve the occurrence of the different Cu pigments and relative degradation products at the micro-scale level in actual painting samples [43, 75]. These studies, combined with investigations carried out on naturally and artificially aged oil paint mock-ups in the presence of verdigris and copper resinate, highlighted the role of light exposure in combination with environmental O_2 in the darkening process [41, 178].

XANES and EXAFS spectroscopy at the Cu K-edge [42, 178] enabled the characterization of the valence states and the local chemical environment (coordination numbers and bond distances) of copper ions in degraded oil paints containing verdigris and copper resinate. The analyses excluded the formation of inorganic copper oxides in quantities sufficient to justify the discoloration of the pigments, while revealing a substantially unchanged local environment of copper ions [42]. Furthermore, the application of X-ray fluorescence yield (XFY) and TEY mode XAS measurements allowed the investigation of the copper environment at different depths (micrometers versus first hundreds of nanometers). No evident surface effect was observed, hinting toward a degradation process that, once triggered, rapidly involves the whole stratigraphy.

Recent studies, based on EPR combined with UV–VIS absorption and transmission spectroscopy [41, 178], proposed the formation of peroxo-bimetallic copper (II) complexes as an explanation for the darkening process. This is supposed to occur through a redox cycle of copper with the transient formation of copper (I) in the pigment/oil system in the presence of light and environmental oxygen. Nevertheless, unambiguous identification of these peroxo complexes still must be achieved and the formation

of EPR-silent copper (I) is difficult to prove, because it is rapidly reconverted to the oxidized copper (II) form.

6.4 Arsenic-based pigments

6.4.1 Emerald green

The green copper acetate arsenite, emerald green [$Cu(CH_3COO)_2.3Cu(AsO_2)_2$], also known as Paris green, Veronese green or Schweinfurt green, was synthesized at the beginning of the nineteenth century, as an attempt to improve the characteristics and color properties of its precursor, Scheele's green (copper arsenite). Due to its bright green shade, emerald green found place in most of the palettes of Impressionist and Post-Impressionist painters quite soon after its introduction on the market. It was also applied either as a dye for textiles and design objects or as insecticide or fungicide for agricultural purposes due to its toxicity. Two precipitation synthesis processes of emerald green were developed in the nineteenth century: the acetate and sulfate methods. In both processes, arsenic (3+) oxide (As_2O_3) was used as arsenic source, while either copper acetate [$Cu(CH_3COO)_2$] or copper sulfate ($CuSO_4$) was employed as copper-containing reagent. In the sulfate method, the further addition of acetic acid (CH_3COOH) was needed to obtain the desired product [456].

Elemental and morphological analytical techniques, including XRF and SEM–EDX, may provide a first clue for the possible identification of emerald green, via the simultaneous detection of copper and arsenic [184, 456–458]. Nevertheless, molecular and structural probing techniques are required to unequivocally assess its presence. In several cases, XRD [456, 459], Raman [458, 460–463], VIS, and mid-near IR spectroscopies [458, 459, 464, 465] allowed the identification of emerald green, via the detection of peculiar marker bands.

Emerald green, as the other pigments discussed so far, undergoes degradation in paintings, by losing their original brilliant color and by weakening the physical–mechanical stability of the paint film [45, 184, 189, 466, 467]. The application of laterally resolved SR μ-XRF/μ-XANES at the As K-edge on micro-samples obtained from altered emerald green-based paints of several artworks has significantly advanced our knowledge on the degradation process of such pigment [44, 45, 184, 189, 466, 467]. The sensitivity of As K-edge XANES spectroscopy to distinguish between As^{3+} and As^{5+} species revealed that the alteration of the pigment results from a transformation of original As^{3+} species into As^{5+} compounds [44, 184]. Keune et al. [44, 45], for example, observed such phenomenon by studying a micro-sample taken from a poorly preserved emerald green area of *The Descent of the Cattle* (ca. 1834–1835) by Théodore Rousseau (Fig. 22a-f). In this painting and in other case studies [189, 466, 467], μ-FT-IR, μ-Raman, and XRD investigations allowed the presence of arsenates of copper, lead, and/or calcium to be identified as As^{5+}-containing degradation products of emerald green. Moreover, outcomes from T. Rousseau's masterpiece highlighted the migration capacity of As-rich degradation products across the paint stratigraphy. As^{5+} was also present in pictorial layers not originally painted with emerald green, such as the protective varnish and the ground. Here, additional secondary compounds,

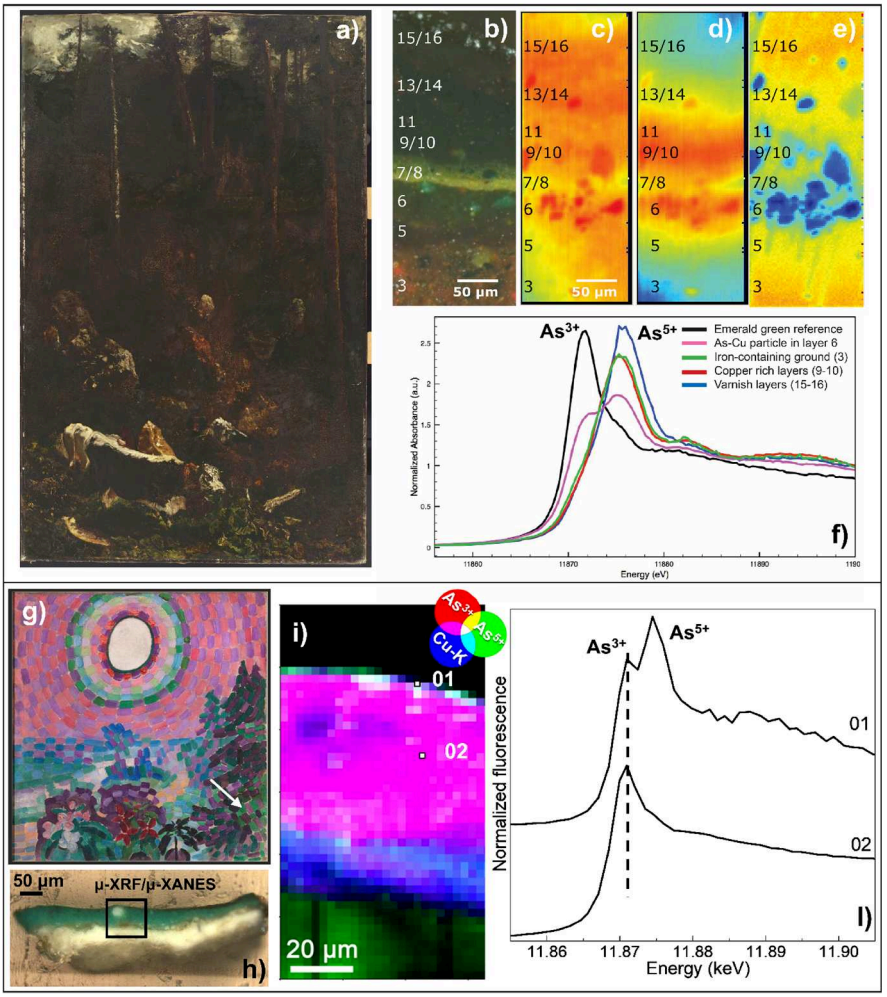

Fig. 22 **a** Photograph of the oil painting *The Descent of the Cattle* (ca. 1834–1835) by Théodore Rousseau (The Mesdag Collection, The Hague, NL; credit photograph: Van Gogh Museum, Amsterdam, NL) and **b** detail of a micrograph of the corresponding cross-section analyzed by SR µ-XRF and XANES at As K-edge (data collected at SSRL BL 2–3). SR µ-XRF maps of **c** As and **d** Cu and **e** As K-edge position map (blue pixels: mainly As^{3+}; orange/red pixels: mainly As^{5+} species). **f** Selection of As K-edge XANES spectra taken from emerald green reference (black) and different areas of the cross-section as highlighted in **b–e**). Adapted from [44]. **g** Photograph of the oil painting *Paysage au disque* (1905–1906) by Robert Delaunay (©Georges Meguerditchian—Centre Pompidou, MNAM-CCI /Dist. RMN-GP) and **h** micrograph of the corresponding cross-section obtained from the spot shown by the white arrow in (**g**). **i** RGB SR µ-XRF maps of As^{3+}/As^{5+}/Cu-K recorded from the area illustrated in (**h**). (**l**) selection of As K-edge µ-XANES spectra acquired on the spots displayed in (**i**) (data collected at ESRF-BM23)

namely copper soaps, were also detected. In line with laboratory experiments [44, 189], they represent the result of a reaction between Cu^{2+} species from emerald green with fatty acids from the oily binder.

Recent analyses carried out on a micro-sample taken from the twentieth century oil painting *Paysage au Disque* (1905–1906) by Robert Delaunay, even though revealing the oxidative alteration of emerald green, showed some differences in the As^{3+}/As^{5+} stratigraphic distribution (Fig. 22g–i) with respect to that occurring in the painting by T. Rousseau (Fig. 22e). As speciation maps combined with single-point As K-edge XANES measurements (Fig. 22i,l, pt 01) highlighted the presence of a thin As^{5+} and Cu^{2+}-rich layer (thickness of ~ 5–8 μm) at the paint surface exposed to the environment. The innermost green paint layer underneath (Fig. 22i,l, pt 02) is instead mainly composed of As^{3+} species, due to the original unaltered emerald green. The stratification of alteration compounds in a superficial thin layer resembles the one earlier noticed for other photosensitive pigments [52]. Thus, it cannot be excluded that an oxidative degradation process of emerald green induced by light exposure took place in the painting by Delaunay.

Considering the described variability, a systematic study on laboratory prepared mock-up samples is required to shed light on unsolved issues, such as the mechanism of mobility on paints and the sensitivity to environmental factors, and to draw a complete picture of the reactivity of emerald green in paintings.

6.4.2 Arsenic sulfides

Due to their vibrant yellow, orange, and red tones, arsenic sulfide pigments have been widely used in various kinds of heritage objects since Antiquity, including mural and easel paintings [31, 71, 456, 468, 469], manuscripts [268, 470–472], and works on paper [456, 469, 473].

The mineralogical phases, occurring naturally and more commonly reported in cultural heritage objects, are the monoclinic arsenic trisulfide yellow orpiment (α-As_2S_3) and the monoclinic tetraarsenic tetrasulfide orange–red realgar (α-As_4S_4). Starting in the fifteenth century, the discovery of the synthesis of arsenic sulfide pigments stimulated the quick incorporation of such materials into the artists' palettes across the world [383, 456, 469, 474–477]. Two kinds of synthesis methods were described in the literature [478–480]: the dry and wet processes. The former method leads to the production of amorphous arsenic sulfide pigments through heating, roasting, and sublimation of the naturally occurring minerals or the fusion of arsenolite (As_2O_3) and sulfur in various ratios. From the nineteenth century onwards, the wet process is described, where a hydrochloric solution of arsenic trioxide is treated with a stream of hydrogen sulfide or thioacetamide. The mineral pyrite (FeS) is an example that was used as a source of hydrogen sulfide [481].

XRF and SEM–EDX usually represent the first step in the characterization of arsenic sulfides, asserting their presence based on the presence of arsenic and sulfur, morphology of pigment particles (foliated or not, Fig. 23a,b), and approximative estimations of arsenic/sulfur molar ratio [31, 482, 483]. Nevertheless, specific molecular and structural information are obtainable by Raman spectroscopy and XRD. While XRD, as Raman spectroscopy, enables the distinction among crystalline arsenic sulfides through

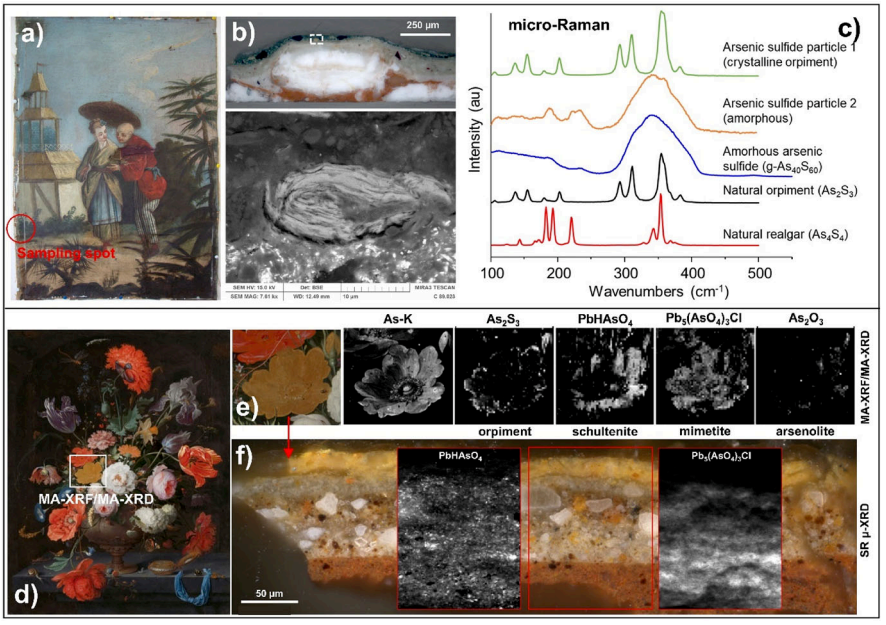

Fig. 23 **a** Photograph of the oil painting *Couple in a Garden* (eighteenth century French Chinoiserie, unknown painter; private collection, FR). **b** Micrograph of extracted cross-section from the green border shown in (**a**) by the red circle and SEM–EDX analysis of a yellow particle presenting foliated structure often associated with natural orpiment. **c** Raman spectra for natural orpiment, natural realgar and amorphous arsenic sulfide and two arsenic sulfide particles from cross-section presented in (**b**). Adapted with permission from [31]. **d** Photograph of the oil painting *Still Life with Flowers and a Watch* (ca. 1660–1679) by Abraham Mignon (Rijksmuseum, Amsterdam, NL). **e** MA-XRF maps of arsenic and MA-XRD maps recorded from the area indicated in (**d**) and showing the distribution of different As-containing crystalline phases. **f** Micrograph of the cross-section taken from a degraded paint in the yellow rose showing the corresponding SR µ-XRD maps of schultenite and mimetite (data collected from the region indicated with a red square at P06-PETRA III, DESY). Adapted from [32]

specific marker peaks, Raman also allows to identify amorphous arsenic sulfides and to assess the extent of crystallinity of the compound based on the bands' shape (i.e., sharp for crystalline pigments; broad and featureless for glass arsenic sulfides) (Fig. 23c) [475, 480, 484]. Different types of arsenic sulfides were identified in several seventeenth–nineteenth century paintings; in some cases, it was also possible to differentiate the natural types from artificial one, based on a series of characteristic Raman sharp and well-defined peaks (associated to crystalline starting reagent materials) compared to a broad, featureless band centered at 340 cm^{-1} (ascribable to amorphous compounds resulting from the heating, roasting or sublimation processes) [31, 127, 383, 475, 479, 480, 482–484].

Technically, both Raman and XRD are also sensitive to the detection of other As phases, including pararealgar (a polymorph and degradation product of realgar), the χ-phase (intermediate degradation product of realgar), and arsenolite (degradation product of orpiment, realgar, and other arsenic sulfide compounds). However, in practice, when these compounds are crystalline and present together, XRD is a much

more sensitive technique than Raman in distinguishing them. Pararealgar, χ-phase, and arsenolite have all been identified as in situ formed secondary compounds of realgar under exposure to different white lights and wavelengths of the visible light [485–490]. Pararealgar, as a degradation product, in combination with some remnants of realgar, was found in several paintings by artists of sixteenth century, including those by Paolo Veronese [491], Sebastiano del Piombo [492] and Tiziano [493], and of late nineteenth century, like Henrique Pousão [494]. In other artworks, however, since pararealgar was found without remnants of realgar, it was suggested that this material was used as a pigment rather than being a secondary product of realgar [127, 484, 495–497].

The sensitivity to light has been documented also for orpiment, which, like realgar, tends to convert into As_2O_3 and sulfur species in paintings, often identified as sulfates [46, 72, 99, 183, 456, 469]. As established by SR μ-XRD and As K-edge μ-XANES spectroscopy investigations of cross-sections from altered areas of a series of seventeenth century oil paintings and thirteenth–fourteenth century tempera artworks, As^{5+} species were found as further secondary degradation compound of orpiment [31–33, 46, 65, 72, 183]. In selected cases [33, 46, 65, 498], including the *Still Life with Flowers and a Watch* by Abram Mignon (Fig. 23d,f) [32], these species were found widespread across the paint stratigraphy as crystalline lead arsenates [i.e., schultenite: ($PbHAsO_4$) and/or mimetite ($Pb_5(AsO_4)_2Cl$)]. Non-invasive MA-XRD mapping of selected areas of the painting by A. Mignon complemented the SR μ-XRD results visualizing the presence of the same compounds at the macro-scale length (Fig. 23e). Even if less frequently, As K-edge XANES spectroscopy analysis also suggested the possible formation of calcium arsenate, as described by Keune et al. [65] and Vermeulen et al. [31].

Based on complementary XANES studies on artificially aged orpiment paint mock-ups, a pathway of degradation has been recently proposed by Broers, 2023 et al. [183] in painting systems with a medium in the presence and absence of light (Fig. 24, reactions A and B, respectively).

In an aerobic and moist environment, either As_2S_3 (reaction B) or As_2O_3 (reaction C, i.e., the primary photo-alteration product of As_2S_3) may partially dissolve within the paint matrix, thus giving rise to other intermediate arsenic (3+) compounds (H_3AsO_3, $H_2AsO_3^-$, $HAsO_3^{2-}$, and AsO_3^{3-}) and then oxidize to arsenic (5+) species (reaction E). The hydrated arsenate species can further react with the other cations (e.g., Pb^{2+}

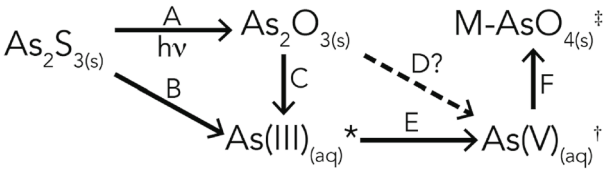

Fig. 24 Overall degradation pathways of orpiment in paintings. *As(III): arsenites in various species in solution (e.g., $AsO_3^{3-}{}_{(aq)}$, $HAsO_3^{2-}{}_{(aq)}$, $H_2AsO_3^-{}_{(aq)}$, or $H_3AsO_{3(aq)}$). † As(V): arsenates with different forms in solution ($H_3AsO_{4(aq)}$, $H_2AsO_4^-{}_{(aq)}$, $HAsO_4^{2-}{}_{(aq)}$, or $AsO_4^{3-}{}_{(aq)}$). ‡ Metal arsenates. Adapted from [183]

or Ca^{2+}) associated with other pigments/components of the paint that can act as counterion forming lead arsenates or calcium arsenates (reaction F). Whether As^{5+} species can form directly from $As_2O_{3(s)}$ (reaction D), or it needs to be dissolved first (reaction D, then E), needs to be studied further. The mobility of arsenates can explain why such compounds were often encountered widespread across the paint stratigraphy (cf. Figure 23f).

Black Cu-, Pb- and Ag-sulfides were identified by SR μ-XRD in a series of paint mock-ups and thirteenth–fourteenth century Italian tempera paintings, in which either Cu-/Pb-containing pigments (e.g., verdigris, red lead) or metallic silver were found either in mixture or in close contact with orpiment [46, 71, 72]. The formation of reactive sulfur species (e.g., polysulfides, S-radicals, and H_2S) arising from the degradation of arsenic sulfide paint was exploited to explain the formation of such compounds.

Further systematic research on paint mock-ups is ongoing to understand how other local conditions (e.g., pH, nature of the binding medium, and matrix composition) must have an influence on the complex degradation pathways of arsenic sulfide pigments.

6.5 Red mercury sulfide pigments

6.5.1 Discoloration issues

Red α-HgS, used as a pigment both in its natural and synthetic forms, has received multiple denominations across different historical periods. Since 1962, according to the US Department of Standards, the naturally occurring pigment is called cinnabar, whereas the term vermilion is applied to the artificially prepared pigment [6]. The application of the mineral ore of cinnabar as a pigment is attested since at least the sixth century BCE in Greece, Asia Minor, and Egypt, among other territories [499, 500]. Despite its attractive red color, this pigment suffers from discoloration, and its appearance ranges from whitish, gray or purple to black.

Its discoloration has been noted since Antiquity [1, 501] and its results can be observed in many Roman mural paintings [502, 503]. Medieval case studies in which α-HgS has discolored are the plasterworks of the Hall of the Kings of the Alhambra (Granada) and the mural paintings of the Gothic church of the Monastery of Pedralbes (Barcelona) [12, 382, 504]. Regarding easel paintings, darkened vermilion has been observed in several fourteenth–seventeenth century artworks from the National Gallery of London and the Courtauld Gallery [10]. The examples range from egg tempera to oil paintings (either on panel or canvas), such are those by Nardo di Cione (ca.1365), Paolo Uccello (1450–1460), and Jacob Jordaens (1620–1625). Discolored vermilion was also noticed in a tempera work by Francescuccio di Cecco Ghisi (1375, North Carolina Museum of Art) [505] and in the following oil paintings: *Triptych of Saint Wilgefortis* by Hieronymus Bosch (ca.1497, Gallerie dell'Accademia di Venezia, Italy) [506], *Minerva and Hercules Opening the Doors for Victory* by Christiaan van Couwenberg (1651, Oranjezaal Huis ten Bosch Palace, The Hague, The Netherlands) [11], *Portrait of a Lady* (ca. 1625, Mauritshuis, The Hague) [11], and *The Adoration of the Magi* (1624–1625 Royal Museum of Fine Arts of Antwerp, Belgium) [12] both by Peter Paul Rubens.

6.5.2 Chemical analyses of degraded α-HgS

Historical paintings. Over the years, there has been a plethora of different hypotheses trying to disclose the nature of discoloration of α-HgS. As summarized in Table 3, several laboratory and SR-based techniques have been used (being with X-rays or not) to detect the main degradation compounds associated to the transformation of this pigment.

Until the twenty-first century, many researchers associated the darkening of red α-HgS to the formation of black metacinnabar (β-HgS). This was proved by Istudor et al. [507] by XRD investigations of mural paintings of a northern Moldavian church. β-HgS was also detected via pump-probe microscopy in a fourteenth century tempera painting attributed to Francescuccio di Cecco Ghissi [505].

Besides metacinnabar, many other degradation products were identified in altered α-HgS painted areas. Spring et al. [10] were among the first to point out the possible key-role played by chlorine in the degradation of α-HgS. Notably, the study of cross-sections from fourteenth to seventeenth century artworks, via a combination of SEM–EDS and Raman spectroscopy, revealed the presence of chloride in the outer, deteriorated dirt crust of the paint stratigraphy, in some cases associated with the

Table 3 Degradation compounds found on degraded α-HgS paintings/samples and analytical techniques used for their detection

Compound	Color	Analytical techniques
β-HgS	Black	XRD [507, 508], pump-probe microscopy [505, 508]
Amorphous phase	Black	XRD [509, 510]
Hg(0)	Black	SEM–EDS [11], linear sweep voltammetry [511], XPS [512], FESEM [513], pump-probe microscopy [505, 508]
Hg_2Cl_2	White	Raman spectroscopy [8, 10], TOF–SIMS [506], XRD [517], μ-XRD/SR μ-XRD [12, 146, 234]
$HgCl_2$	White	SIMS [11]
α-$Hg_3S_2Cl_2$	Purplish-gray [12], light orange–pink (turns grayish black when exposed to light) [146], yellow [234]	μ-XRD/SR μ-XRD [12, 146, 234]
γ-$Hg_3S_2Cl_2$	Yellow (turns grayish black when exposed to light) [12]	SR μ-XRD [12, 234]
β-$Hg_3S_2Cl_2$	Yellow [515]	SR-μ-XRD [234]
$HgSO_4 \cdot H_2O$	White	XRD [513]
$Hg_3(SO_4)O_2$	Yellow	XRD [513]
$CaSO_4 \cdot 2H_2O$	White, but detected in black layers	μ-XANES at the S K-edge [7, 12, 382], Raman spectroscopy [8]

presence of white calomel (Hg_2Cl_2). The latter compound, which does not explain the grayish aspect of degraded α-HgS painted areas, was suggested to be present along with sulfur and black undetected forms of HgS, such as either metacinnabar or an amorphous phase. The combination of α-HgS with other pigments, including red lead, was also suggested to preclude the formation of sulfochlorides, such as corderoite (α-$Hg_3S_2Cl_2$) (a potential precursor of calomel) [10, 510].

Few years later, other authors [7, 8, 11, 12, 516] have also reported the influence of chlorine (even at trace levels) in the darkening of cinnabar, especially in humid areas and/or with direct sunlight exposure. Keune et al. [11] demonstrated that chloride ions, identified as mercuric chloride ($HgCl_2$) in the analyzed samples by SIMS and EDX, even if present in small quantities in the native pigment, may catalyze a photo-electrochemical process in which cinnabar decomposes in gray metallic mercury (nanoparticles) and sulfur (possibly volatilized via oxidation to sulfur oxide). In this case, neither calomel nor metacinnabar was identified.

The study of Cotte et al. [7] of blackened samples from Roman wall paintings of the Vesuvian area (Fig. 25a) was pioneering in demonstrating the usefulness of SR-based X-ray techniques to characterize the degradation state of α-HgS. SR μ-XRF mapping and S/Cl K-edges μ-XANES measurements allowed the local chemical speciation of S- and Cl-bearing degradation products of cinnabar to be determined in gray and black areas. μ-XANES spectra acquired at the Cl K-edge on gray degraded areas were very similar to a series of mercury chloride compounds [i.e., corderoite, calomel, and terlinguaite (Hg_2OCl)] and at the S K-edge to that of corderoite. In the black Pompeian degraded samples, S K-edge μ-XANES spectroscopy revealed also the presence of high amount of sulfates, with spectra similar to that of gypsum (Fig. 25b). In S K-edge XANES spectra, the position of the white line shifts toward higher energies with increasing oxidation number of sulfur (i.e., sulfides, E_1: 2.471 keV; sulfate, E_2:

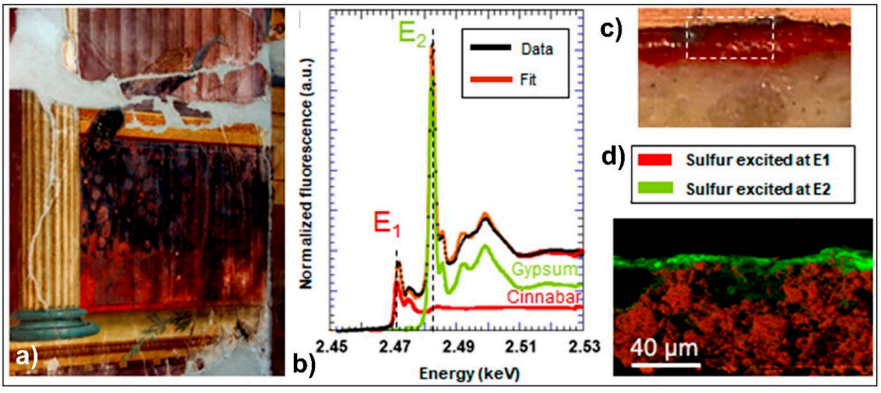

Fig. 25 **a** Blackened cinnabar on a wall painting ("Villa Sora" in Torre del Greco, near Pompeii, Italy). **b** S K-edge μ-XANES spectra acquired on a black area: fit (orange) of the experimental data (black) by combination of cinnabar (red) and gypsum (green) spectra. **c** Cross-section of a sample of a blackened cinnabar wall painting. The dotted rectangle indicates the area analyzed by μ-XRF/μ-XANES. **d** RG SR μ-XRF maps of S^{2-}/S^{6+} species (data collected at ESRF-ID21; photo credits: Mario Pagano, Soprintendenza per i Beni Archeologici del Molise). Adapted with permission from [7]

2.482 keV). As explained in Sect. 2, this property can be exploited to semi-qualitatively map sulfides and sulfates, by recording the same μ-XRF map at the two corresponding energies over the paint cross-section (Fig. 25c,d). The result shows that sulfates form a continuous blackened layer of about 5 μm at the surface of an intact sulfide paint.

Later, Radepont et al. [12] illustrated the necessity of integrating SR μ-XRD with SR μ-XRF/μ-XANES to more specifically characterize the chemical nature of crystalline secondary compounds and to visualize their distribution across the paint stratigraphy. Notably, the study of original painting samples taken from different artworks, including the Gothic wall paintings of the Monastery of Pedralbes in Spain (Fig. 26a,b) identified, besides to the presence of calomel and corderoite, two rare and relatively unknown polymorph phases: γ-$Hg_3S_2Cl_2$ (kenhsuite) and β-Hg_3S_2Cl [12, 234]. SR μ-XRD maps (Fig. 26c,d) revealed that the β-form, present as a relatively thick layer (~ 20 μm) in close contact to α-HgS, is covered by a thinner layer made up of γ- and α- forms (~ 2–5 μm) and of an uppermost layer of Hg_2Cl_2. Such distribution suggests a progressing conversion of one phase into another, until the complete substitution of sulfides by chlorides [234].

More recently, Pérez-Diez et al. resumed the study of cinnabar-decorated mural paintings from the Vesuvian area [8, 516] by combining in situ studies of blackened paintings using portable instruments and the investigation of affected samples in the

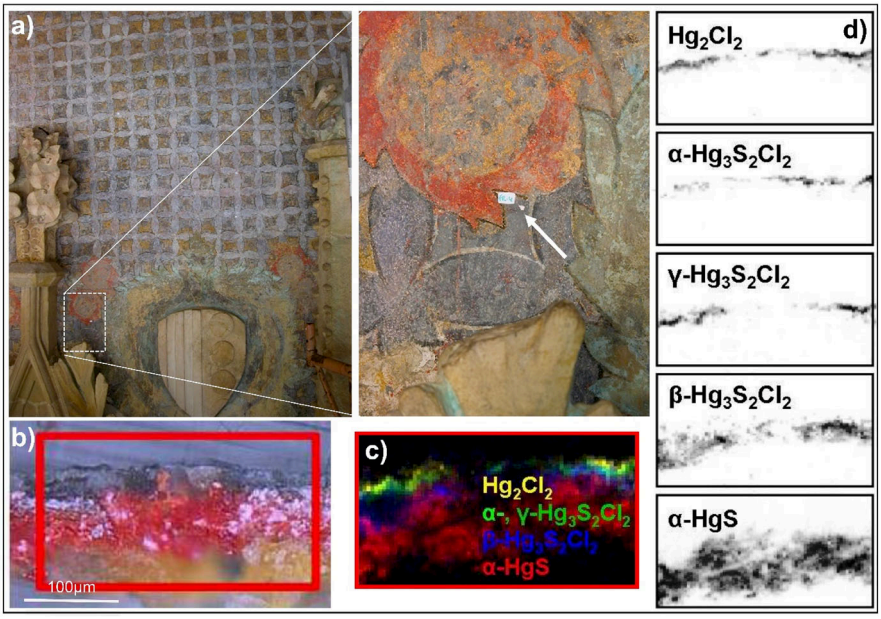

Fig. 26 a Darkened cinnabar on the wall paintings of the Monastery of Pedralbes (Photo credits: Javier Chillida, Chillida Conservación-Restauración Art S.L.U.). The white arrow points to the area in which a sample was taken. **b** Cross-section of a degraded sample taken in a gray region. SR μ-XRD maps of cinnabar and four Hg degradation compounds: **c** composite map and **d** distributions of each crystalline phase (data collected at P06-PETRA III, DESY). Adapted with permission from [234]

laboratory. SEM–EDS, micro-Raman spectroscopy, and XRD measurements allowed the possible presence of mercury perchlorate hemihydrate [$Hg(ClO_4)_2{\cdot}2H_2O$] along with calomel and gypsum to be identified. In near future, SR μ-XRD mapping analysis will be performed to assess the presence of additional Hg–S, Hg–Cl, or Hg–S–Cl degradation compounds.

Paint mock-ups. In addition to the study of historical paintings, many experiments have been carried out on paint mock-ups. A series of studies have evaluated the effect of light on α-HgS degradation [19, 28, 517]. Elert et al. [512] used XRD to investigate outdoor exposed cinnabar-based mock-ups, but without observing any changes, possibly due to the formation of black amorphous metallic mercury. In a subsequent study by the same authors [513], XRD and XPS investigations of cinnabar pigments and tempera mock-ups attributed the blackening due to UV-C light exposure to the oxidation of HgS to mercury sulfates [i.e., $HgSO_4{\cdot}H_2O$ and $Hg_3(SO_4)O_2$] and their reduction to Hg(0) by photo-induced electron transfer. The sensitivity of pump-probe microscopy to distinguish among α-HgS, β-HgS, and metallic mercury was also recently exploited for studying UV-degraded samples, revealing the formation of both metallic mercury and β-HgS [505, 508].

Further experiments and calculations have been dedicated to assessing the formation of metacinnabar under the effect of temperature. Ballirano et al. [333] evaluated the possibility of the thermal transformation of cinnabar to metacinnabar in Pompeian wall paintings and its persistence over a span of 2 millennia, attributing this to the reported slow kinetics of transformation [518, 519]. More recently, thermodiffractometric experiments in an open system have excluded the possibility that metacinnabar can be formed in cinnabar-decorated fresco paintings because of the thermal impact that took place in Pompeii due to the 79 CE eruption [509]. However, thermal experiments in a closed system allowed the formation of metacinnabar to be detected.

Studies aimed at tracking the combined effect of light and chlorides on the degradation of α-HgS have also been performed over the last two decades. Neiman et al. [514] infused cinnabar fresco mock-ups with NaCl and exposed them to sunlight, next to powdered pigments affected by 5 M NaCl solutions and they studied the aged samples using XRF, SEM–EDS, and XRD. Including also in their methodology thermodynamic modeling, the authors concluded that both chlorides and light were fundamental to induce discoloration, although calomel could already occur in the absence of light.

Radepont et al. [146] reproduced the alteration process of α-HgS by preparing synthetic pellets of the pigment and by exposing them to Cl-solutions and ClO(g) either under UV–VIS radiation or in the dark. SR μ-XRF, μ-XANES, and μ-XRD were crucial to detect calomel, corderoite, and sulfates from the reaction of α-HgS with ClO(g) formed from the exposure to light and NaOCl solution. The distribution of layers of mercury chloride compounds atop red mercury sulfide layers, and sulfates present at the surface, mimic the one observed in historical paintings, as shown in Fig. 26 [12]. In the case of a two-layered pellet composed of $CaSO_4{\cdot}2H_2O$/α-HgS aged with NaOCl solution, the formation of Hg_2SO_4 was also observed.

In summary, the degradation of red α-HgS is a very complex phenomenon where light, temperature, humidity, and external agents, such as chloride species, can play a role. These parameters can act separately or combined and lead to the formation of various species, including metacinnabar, metallic mercury, different sulfates (mercury

sulfates but also gypsum when a source of calcium is available), and a series of Hg–S–Cl and Hg–Cl compounds.

From the analytical point of view, the combined use of SR-based XRF, XRD, and XANES techniques was found to be particularly efficient for gaining complementary information on the nature and stratigraphic distribution of most of secondary compounds in both degraded mock-ups and historical samples. The development of HERFD-XAS seems extremely promising to further study Hg speciation (through Hg L_3-edge μ-XANES), in particular to detect the presence of Hg(0).

6.6 Cadmium sulfide-based pigments

6.6.1 Properties and alteration phenomena

Cadmium yellows and reds are II–VI semiconductor materials based on cadmium sulfide (CdS), which have found extensive use among artists of mid-nineteenth–twentieth century because of their vibrant colors and excellent tinting and covering power [520].

Different dry and wet synthetic routes were developed to achieve various pigment hues by modifying the crystal morphology (i.e., grain shape and size) and the optical and optoelectronic properties [i.e., hue, band-gap energy (E_g)] of these classes of pigments [521–523]. A wide range of materials, with shades spanning from the lemon-yellow to the purple-red ones corresponding to E_g values between ~ 2.65 eV (~ 470 nm) and ~ 1.95 eV (~ 635 nm), were synthesized by introducing variable quantities of either zinc or selenium into the structure of CdS as solid solutions described by the formula $Cd_{1-x}Zn_xS$ and $CdS_{1-x}Se_x$. Yellow-orange and orange hues were obtained, instead, by changing the crystalline structure of CdS from the hexagonal (E_g: 2.44 eV/508 nm) to the cubic one (E_g: 2.36 eV/525 nm) [524, 525].

As direct semiconductors, $Cd_{1-x}Zn_xS$ and $CdS_{1-x}Se_x$ solid solutions exhibit direct radiative recombination with green–orange emissions in the 490–630 nm range (known as near band edge emission, NBE) and radiative deactivation from intragap trapping states due to crystal defects, which give rise to peculiar red and near infrared emissions in the 680–1110 nm range (known as deep level emissions, DLEs). The positions of the NBE and DLE maxima and that of the inflection point of the visible diffuse reflectance spectra depend on the zinc and selenium content of $Cd_{1-x}Zn_xS$ and $CdS_{1-x}Se_x$ as well as on the grain sizes of the pigment, when these are in the nanometric scale range. Therefore, photoluminescence and VIS–NIR reflectance spectroscopy have been profitably used for the non-invasive characterization of different cadmium yellow and red formulations in paintings and historical pigments [149, 526–531].

X-ray methods, namely XRD (employing SR and traditional sources) and SR μ-XANES at the S K-/Cd L_3-edges, and SR deep-UV excited micro-photoluminescence allowed researchers to successfully study some of the causes of the discoloration phenomenon observed in a series of late nineteenth–early twentieth century masterpieces (Fig. 27). These methods provided insights down to the submicrometric scale length and were also applied to artificially aged paint mock-ups [34, 36, 87, 97, 101, 102, 124, 125, 135, 532].

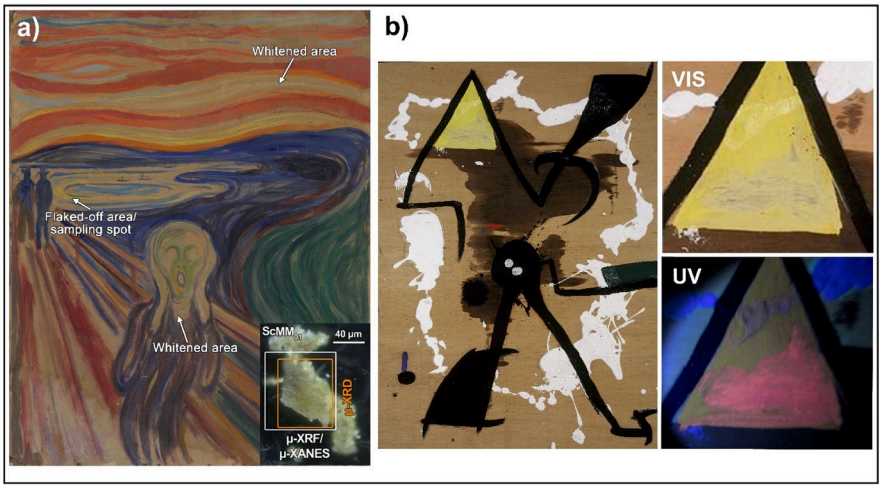

Fig. 27 **a** Photograph of *The Scream (ca. 1910)* by Edvard Munch (MUNCH collection, Oslo, catalog nr. Woll.M.896) showing the altered cadmium yellow areas (Photo credits: Irina Crina Anca Sandu and Eva Storevik Tveit, MUNCH collection) along with the micrograph of the micro-flakes sampled from the flaked-off yellow area of the lake and analyzed by µ-XRD and µ-XANES. Adapted from [102]. **b** Photographs of an untitled painting by Joan Miró (1977, Fundació Miró Mallorca, Spain, catalog nr. FPJM 00135), with close-up pictures of the cadmium yellow passage under VIS and UV light showing the pink/orange luminescence emitted by the altered cadmium yellow paint. Adapted from [135]

These studies have established that, under high moisture conditions and illumination with supra-band-gap light ($h\nu > E_g$), the CdS pigment undergoes oxidation of sulfides (S^{2-}) to white cadmium sulfates ($CdSO_4$/$CdSO_4 \cdot H_2O$). The process is related to the chemical composition, morphology, and degree of crystallinity of cadmium yellow, all properties depending on the manufacturing process of the pigment itself. Notably, $Cd_{1-x}Zn_xS$ solid solutions [125, 532] and nanocrystalline and/or poorly crystalline CdS [87, 135] exhibit the highest sensitivity toward photo-corrosion. The in situ $S^{2-} \rightarrow S^{6+}$ oxidation may take place also in the dark by exposing the paint to high moisture conditions and in the presence of chloride species, which are often residues of the starting reagents of certain CdS formulation synthesized by wet processes [102, 124, 521]. Exposure to humidity can also trigger secondary reactions that occur via dissolution, migration, and recrystallization of water-soluble/-partial soluble phases [such as Na_2SO_4, Cd(OH)Cl, and magnesium carbonates], thus favoring the formation of further $CdSO_4$, sodium/cadmium chlorides, and/or hydrated magnesium sulfate by ion exchange [102, 533].

Additional secondary products, resulting from the oxidative degradation of the oily binder or its interaction with $Cd_{1-x}Zn_xS$/CdS (i.e., cadmium oxalate, zinc oxalate, and long-chain fatty acids), were also revealed by TOF–SIMS imaging [534] and mid-FT-IR spectroscopy (with both SR and traditional sources) [98, 101, 125]. Pump-probe measurements allowed the achievement of information about the early stage detection of CdS degradation on the micrometer scale, that mainly affects small particles and the surface of larger particles [535], and the formation of a defective phase, compatible

with Cd vacancies and the formation of both CdO and $CdSO_4$ superficial clusters [536]. The interpretation of most of these experimental data is consistent with ab initio simulations on the subject [124, 537–539].

Alteration phenomena of cadmium red paints have been less frequently investigated to date. Rayner et al. [540] observed the discoloration of orangish $CdS_{1-x}Se_x$ in an ancient Greek terracotta krater (ca. 430–420 BCE), where the paint was applied for restoration purpose. The application of SEM–EDS, pyrolysis-GC–MS, XRF, and vibrational spectroscopy investigations of the retouched areas of the krater, combined with the study of treated terracotta mock-ups, led authors to conclude that light and chlorine species were two key factors prompting the fading of the orange paint. In addition, the possible formation of a series of alteration products, including selenium-rich compounds as well as cadmium sulfate, cadmium oxalate, and/or cadmium carbonate, was suggested. The alteration of $CdS_{1-x}Se_x$ has been also identified in a selection of twentieth century artworks by Monico et al. [149]. XRD, VIS–NIR, and FT-IR spectroscopy investigations of paintings and of a set of $CdS_{1-x}Se_x$ paint mock-ups established that, under the exposure to light and moisture, the alteration is due to the oxidation of original sulfides to white cadmium sulfates and is favored for the pigments containing the lowest amount of Se.

In what follows, a selection of cadmium yellow degradation studies published during the past decade on early twentieth century masterpieces by Edvard Munch, Pablo Picasso, and Joan Miró and related artificially aged paint mock-ups will be detailed. They will highlight how SR-based X-ray methods and SR deep-UV excited micro-photoluminescence significantly contributed to unveil the nature of secondary compounds in altered cadmium yellow paints at the (sub)micrometric-scale length and to inform on some of key factors prompting the overall degradation process.

6.6.2 Moisture and chlorides as key factors for the alteration

The version of *The Scream (ca. 1910)*, belonging to the MUNCH Collection in Oslo (Norway), displays clear signs of discoloration of cadmium yellow brushstrokes of the sunset cloudy sky and the neck area of the central figure, while flaking and paint loss are visible in the lake water, where a thick cadmium yellow paint was applied (Fig. 27a).

SR-based X-ray methods, namely μ-XRD, μ-XRF, and μ-XANES spectroscopy at the S K-, Cl K- and Cd L_3-edges were performed on minute flakes taken off from the surface of the yellow lake to obtain speciation information on the S, Cd, and Cl compounds present [102, 124]. SR μ-XRD and S oxidation state maps (Fig. 28a,b) reveal that poorly crystalline hexagonal CdS and $CdCO_3$ are the main components of the yellow paint, with sulfate compounds present as micrometric agglomerates (with diameter of ~ 3 to 12 μm). As shown by S K-edge μ-XANES spectroscopy measurements (Fig. 28d), the sulfate agglomerates consist of Na_2SO_4 (i.e., a residue of the CdS synthesis) along with a variable amount of $CdSO_4$ [also detected by SR μ-XRD (Fig. 28a)] and minor abundances of sulfite (S^{4+}) compounds (Na_2SO_3). Sulfates are often associated with Cd(OH)Cl, as revealed by SR μ-XRD and Cl K-edge μ-XANES spectroscopy (Fig. 28a,c,e).

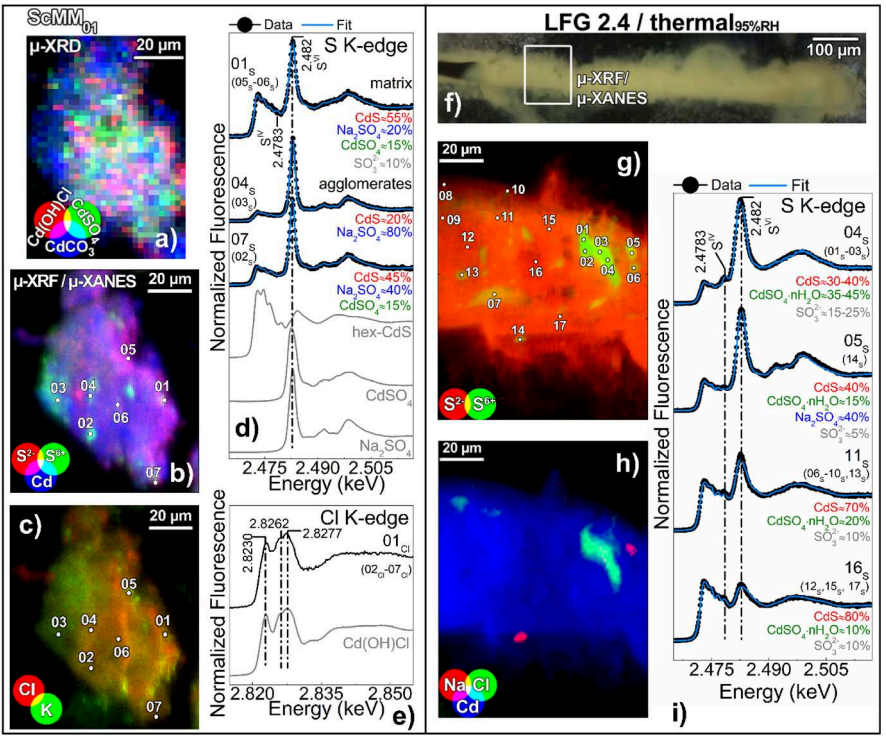

Fig. 28 SR X-ray-based analysis of **a**–**e** a micro-flake obtained from *The Scream (ca. 1910)* and **f**–**i** thermally aged Munch's cadmium yellow lemon oil paint tube (LFG 2.4) (RH ≥ 95%, T = 40 °C, 90 days). **b** RGB composite SR μ-XRD maps of $Cd(OH)Cl/CdSO_4/CdCO_3$ and SR μ-XRF maps of **b**,**g** S^{2-}/S^{6+}/Cd, **c** Cl/K, **h** Na/Cl/Cd. Selection of **d**, **i**) S K-edge and **e** Cl K-edge XANES spectra (black) and result of the linear combination fitting (LCF) (cyan) of different S-based compounds. In gray, the spectra of selected reference compounds are reported for comparison. Numbers in brackets refer to the spectra showing similar features to those reported (data were collected at ESRF-ID21). Adapted from [102]

The in situ $S^{2-} \rightarrow S^{6+}$ oxidation, with recrystallization of cadmium sulfates in the Cd-/Cl-rich areas, was observed after exposure to high moisture conditions in the dark of a series of oil paint mock-ups, with composition equivalent to that of the flaked yellow area of the lake of *The Scream (ca. 1910)* (Fig. 28f–i).

The results from the micro-flakes of the painting, integrated with those arising from artificially aged paint mock-ups, led to the conclusion that sulfates and sulfites can be interpreted as degradation products of the cadmium yellow paint, with their formation prompted by a highly moist environment and chlorine species. The fact that the formation of $CdSO_4$ was not observed in Cl-free CdS oil paint mock-ups aged under similar circumstances [125], points out that, under high-humidity levels, the close contact of Cd(OH)Cl [and possibly other (Cd,Cl) compounds] with CdS grains trigger the alteration of CdS oil paints. DFT method investigations allowed the presence of a built-in dipole in Cd(OH)Cl to be highlighted [124], thus explaining the role of Cd(OH)Cl as oxidative catalyst for CdS in an aqueous environment: Cd(OH)Cl

facilitates the transfer of electrons from S^{2-} species in the vicinity of its anodic surface (CdS/Cd(OH)Cl interface) to either OH radicals or H_3O^+ ions on its cathodic side, thereby prompting the oxidation of CdS to $CdSO_4$.

6.6.3 Extent of crystallinity and photoluminescence properties

Cadmium yellow oil paint discoloration was reported also on Pablo Picasso's painting *Femme* (1907, Foundation Beyeler, Riehen/Basel, Switzerland) [87, 529] and in 26 paintings by Joan Miró (dated around 1970s) belonging to Fundació Miró Mallorca Collection [135].

All the altered areas of these artworks, when analyzed under UV light, show a very intense, reddish or pinkish luminescence (Fig. 27b). Micro-photoluminescence measurements of corresponding cross-sections provided equivalent stratigraphic information at the micro-scale length (Fig. 29a): degraded paints exhibited intense red luminescence (650–700 nm) primarily on the surface, while "intact" paint samples showed only the typical NIR emission (800–870 nm) of CdS, uniformly distributed throughout the paint layer. Based on SR μ-XRD results, such different photoluminescence behavior was ascribed to the extent of crystallinity of CdS: poorly crystalline or nanocrystalline CdS particles (characterized by a high density of surface defects) was found in altered cadmium yellow paints, while highly crystalline CdS phases (hexagonal, cubic, or a mixture of both) were identified in "intact" paints.

A combination of SR μ-XRD and μ-XRF/μ-XANES spectroscopy at the S K-edge from altered cross-sections permitted the presence of a cadmium sulfate hydrate-rich alteration layer at the paint surface to be detected (Fig. 29b, c). In contrast, only compounds resulting from oil/pigment interaction (e.g., oxalates and carboxylates) were found in "intact" paints.

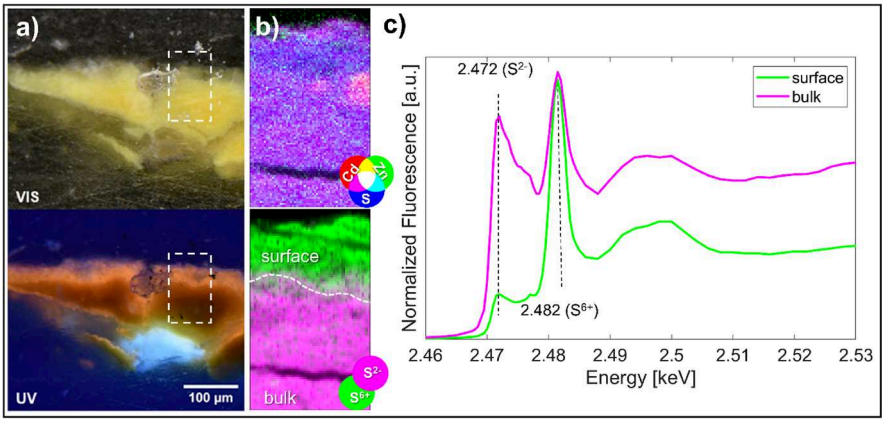

Fig. 29 **a** Visible and UV light micrographs of a cross-section taken from an untitled painting by Joan Mirò. The surface of the paint layer shows the orangish emission sometimes observed in altered cadmium yellow paints. **b** RGB composite SR μ-XRF maps of Cd/Zn/S (top) and S^{2-}/S^{6+}. **c** Average S K-edge XANES spectra extracted from S^{2-} and S^{6+} rich areas of (**b**) (data collected at ESRF-ID21). Adapted from [135]

In the painting by Picasso [87], chlorides, present as Cd(OH)Cl and amorphous Cd–Cl compounds, were also identified in the altered sulfate-rich areas characterized by intense reddish emission, thus highlighting again the influence of such species on the oxidative alteration of cadmium yellow paint and in the luminescence properties of CdS.

Overall, the results from the historical case studies above discussed, supported by those arising from mock-ups, show that three primary factors are linked to the degradation process of cadmium yellow paints: (i) exposure to high-humidity conditions (especially when also light is present); (ii) extent of crystallinity of the CdS pigment; (iii) presence of chlorine compounds.

6.7 Chrome yellow pigments

6.7.1 Properties, manufacturing processes, and analytical characterization

Chrome yellows is a family of pigments that exists in different chemical varieties, either as lead chromate ($PbCrO_4$, found in nature as the mineral crocoite) or as solid solutions of lead chromate and lead sulfate ($PbCr_{1-x}S_xO_4$, with $0 \leq x \leq 0.8$). The shade of these pigments can be gradually tuned from the yellow–orange to pale-yellow by increasing the sulfate content. In addition, when x increases beyond ~ 0.4–0.5, the crystalline structure of $PbCr_{1-x}S_xO_4$ changes from the monoclinic to the orthorhombic system [233, 520, 541].

The brilliant and forceful hues of chrome yellows offered new ways of artistic expression to late nineteenth–early twentieth century artists, such as Vincent van Gogh, thus becoming part of the pigment palette as soon as they were introduced in the market. In several letters of the period 1888–1890 (e.g., letters nr. 593, 595, 674, 687, 689, 720, 758, 806, 863) and annotated sketches (e.g., F-/JH1463, F-/JH1428 in letter nr. 622 and F-/JH1472 in letter nr. 628), Vincent mentions his use of three varieties of chrome yellow, called as chrome yellow types 1, 2, and 3, which correspond to the 'lemon', 'yellow', and 'orange' shades, respectively [5].

The most used method of preparation of chrome yellows is based on a co-precipitation reaction between a neutral solution or a suspension of a soluble lead salt (acetate, nitrate, chloride, etc.) and an aqueous solution containing different ratios of chromate/dichromate and sulfate salts (usually of potassium or sodium) [541–543]. Since the manufacturing process affects the chemical stability of chrome yellows, their synthesis process has evolved over the years. In this respect, literature describes the chrome yellow production records belonging to the nineteenth century archive database of Winsor & Newton™. Pigments synthesized via these historical methods were employed to prepare paint mock-ups and investigated to gather information on the possible relationship between manufacturing method and the stability of chrome yellow paint films from the chemical and mechanical point view [144, 151, 544, 545].

Chrome yellows have been assigned to the class of photosensitive pigments, considering their tendency to darken under the influence of light [63, 520, 542, 546–548]. Van Gogh, like other artists of his day, was aware of this inconvenience (see letter nr. 595) [5], even though he continued to prefer the use of these pigments up until

his death in July 1890, due to the incomparable effects they gave. The darkening of chrome yellows is a phenomenon visible nowadays in a few iconic paintings, including *the Sunflowers* series by Van Gogh, thus raising questions about which are the safest conditions for their long-term conservation [38, 39, 108, 549].

Since the development of the first synthesis processes during the nineteenth century, it has been suggested that not only specific environmental conditions, but also intrinsic properties of chrome yellows, including the relative abundance of chromium and sulfur, the crystalline structure, the size distribution, and crystal shapes of $PbCr_{1-x}S_xO_4$, are factors affecting their stability [542, 543, 546, 547].

A wide range of laboratory techniques (employing bench-top and portable devices), including XRD, FT-IR, Raman [63, 109, 151, 233, 354, 544], EPR [106, 107, 143], and EELS [103], in combination with SR-based X-ray methods, such as μ-XRF, XANES spectroscopy at the Cr K-edge, and μ-XRD [63, 106–108, 123, 142–145, 548, 550], have been successfully exploited to understand the origin of darkening of chrome yellows and some of the factors triggering this phenomenon. Such a multi-technique approach has been employed to study photochemically aged paint mock-ups as well as a series of late nineteenth century masterpieces and related paint cross-sections obtained from darkened chrome yellow paints. Specifically, XRD, FT-IR, and Raman spectroscopy allowed different types of chrome yellows to be distinguished by identifying specific spectral markers depending on the sulfate content and crystalline structure [109, 233, 354, 541], whereas EPR, EELS, μ-XRF, and XANES spectroscopy at the Cr K-edge revealed the presence of chromium in different oxidation states (i.e., Cr^{6+}, Cr^{5+}, and Cr^{3+}) and its stratigraphic distribution within the samples down to the nanometric length scale [63, 103, 106, 107, 143, 144, 548].

The relationship between the structure and electronic properties of different $PbCrO_4$ and $PbCr_{1-x}S_xO_4$ varieties have been also examined by DFT methods, thus providing a more in-depth explanation on the role played by sulfur content [551], solubility [552], and p-type semiconductive and optical absorption properties [553] on the lightfastness of each chrome yellow variety.

These aspects will be discussed below, describing selected X-ray results obtained from an integrated approach involving non-invasive MA-XRD investigations of chrome yellow-based paint areas of the Amsterdam *Sunflowers* by Van Gogh (Van Gogh Museum, Amsterdam) (Fig. 30a) and advanced SR-based X-ray micro-analytical studies of paint micro-samples and photochemically aged chrome yellow oil paint mock-ups.

6.7.2 Differentiating chrome yellow types

As described above, it is known that Van Gogh made use of different varieties of chrome yellows, each with their own hue and synthesis pathway. By replacing CrO_4^{2-} with increasing amounts of SO_4^{2-} ions within $PbCrO_4$, the color shifts from a bright yellow–orange to a pale yellow. From a crystallographic perspective, both solid solution end members, $PbCrO_4$ and $PbSO_4$, are characterized, respectively, by stable monoclinic and orthorhombic crystal structures [233, 520, 541]. Depending on the amount of sulfate substitution, different effects are apparent within the crystal structure. With a substitution rate of $x \sim 0.5$, the crystal structure transforms from a monoclinic into an

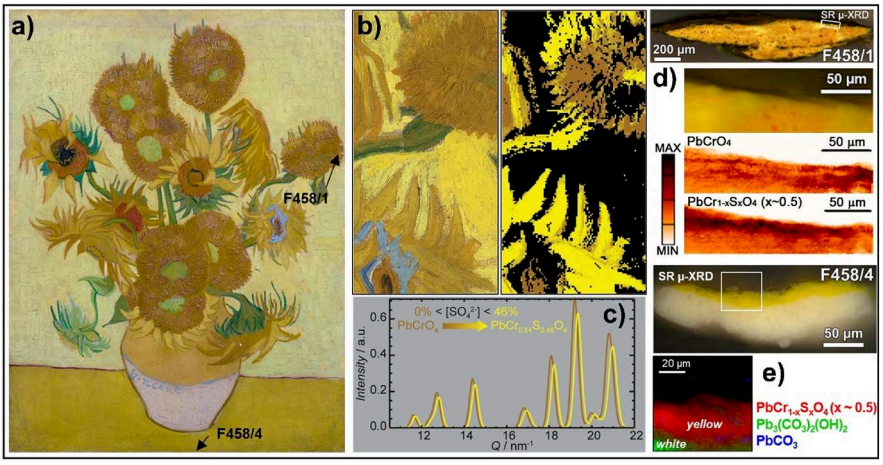

Fig. 30 **a** Photograph of *Sunflowers* (1889) by Vincent van Gogh (Van Gogh Museum, Amsterdam, NL; F458) with arrows pointing to the sampling positions [photo credits: Van Gogh Museum, Amsterdam (Vincent van Gogh Foundation)]. **b** Detail of the painting analyzed by MA-XRD and false color image showing $PbCrO_4$ (brown) and $PbCr_{1-x}S_xO_4$ (x ~ 0.5) (yellow). **c** Diffractogram showing the small shift in diffraction peak position between $PbCrO_4$ and $PbCr_{1-x}S_xO_4$ (x ~ 0.5). $PbCrO_4$ and $PbCr_{1-x}S_xO_4$ (x ~ 0.5) distributions obtained by SR µ-XRD for **d** sample F458/1 and **e** sample F458/4 (data acquired at P06-PETRA III, DESY). Adapted with permission from [108, 109]

orthorhombic unit cell. Additionally, since SO_4^{2-} ions are smaller than CrO_4^{2-} ions, the lattice parameters for both monoclinic and orthorhombic $PbCr_{1-x}S_xO_4$ decrease with increasing x [541].

XRD is a highly specific technique to see the change in crystal structure as well as the contraction of the lattice both at the micro- and macro-scale lengths. Indeed, the positions of the diffraction signals progressively shift to higher scattering vector values (Q) with increasing sulfur content [109, 233], as shown in Fig. 30c. Complementary information on the chemical composition and crystalline structure of $PbCrO_4$/$PbCr_{1-x}S_xO_4$ can be obtained also using FT-IR and Raman spectroscopy, as evidenced by the shifts and changes in the shape of bands assigned to the bending and stretching modes [233, 354].

In the Amsterdam *Sunflowers*, three areas (each around 10 × 20 cm^2) were non-invasively mapped using MA-XRD in transmission mode (Fig. 30b), which revealed two distinct types of the monoclinic chrome yellow: $PbCrO_4$ and $PbCr_{1-x}S_xO_4$ (x ~ 0.5) [109]. No evidence of the orthorhombic $PbCr_{1-x}S_xO_4$ (x > 0.5) was found. The two identified varieties of chrome yellows, namely $PbCrO_4$ and $PbCr_{1-x}S_xO_4$ (x ~ 0.5), could be associated with the chrome yellow types 1 and 2, respectively, as mentioned by Van Gogh in his letters [5]. Sulfur-free $PbCrO_4$, with a deeper yellow color, was found to be primarily present in the yellow–orange and darker yellow hues of the flower corollas and petals, while the paler yellow sulfur-rich $PbCr_{1-x}S_xO_4$ (x ~ 0.5) mostly occurs in the light-yellow tones of the petals. In the light- and dark-green stems and the green flower hearts emerald green was sometimes mixed with $PbCr_{1-x}S_xO_4$ (x ~ 0.5); in the orange flower hearts, $PbCrO_4$ is present

together with emerald green and chrome orange ($PbCrO_4 \cdot PbO$). The latter was identified in multiple orangish brushstrokes. Smaller amounts of $PbCr_{1-x}S_xO_4$ (x ~ 0.5) were also found in mixture with zinc white in the pale-yellow background.

In line with findings of non-invasive MA-XRD studies of the painting, SR μ-XRD mapping and vibrational micro-spectroscopy analysis of cross-sections revealed the presence of a mixture of $PbCrO_4$ and $PbCr_{1-x}S_xO_4$ (x ~ 0.5) in a sample taken from a yellow–orange petal (Fig. 30d), while only $PbCr_{1-x}S_xO_4$ (x ~ 0.5) was detected in the light-yellow table (Fig. 30e) and in the background, where the yellow pigment is finely mixed with zinc white and viridian (a green Cr^{3+}-based pigment: $Cr_2O_3 \cdot 2H_2O$) [38, 108]. The latter was identified by non-invasive VIS reflectance spectroscopy measurements [38, 554].

Based on both the non-invasive MA-XRD investigation and the micro-scale analysis of a limited number of samples, it becomes clear that a major part of the chromium containing yellow regions in the painting are made up of $PbCr_{1-x}S_xO_4$ (x ~ 0.5). Sulfur-rich varieties of chrome yellow were also identified in other artworks by Van Gogh and in oil paintings and palettes of other nineteenth–twentieth century artists, such as Paul Cézanne, Paul Gauguin, Séraphine Louis, and Gerardo Dottori [142, 233, 354, 555–557].

The possibility to experimentally distinguish among different chrome yellow types is highly significant, since the susceptibility to darkening of this class of pigments also depends on the sulfate content and crystalline structure [548], as explained in the next paragraph.

6.7.3 Causes of darkening

To understand what mechanism of reaction is driving the darkening and how both the environment and the intrinsic properties of chrome yellow paints may influence the extent of color change, studies have been carried out during the past decade on a series of photochemically aged paint mock-ups. Samples were prepared using either historical, commercial, or self-synthesized powders of $PbCr_{1-x}S_xO_4$ with different crystalline structures and different *x* values (Fig. 31a) [63, 106, 107, 143, 548] sometimes in mixture with different additives/fillers [151, 544, 545].

High lateral resolution Cr K-edge μ-XRF/μ-XANES investigations in XFY detection mode on thin-sectioned samples allowed establishing that the greenish-brown thin layer at the paint surface results from a photo-reduction reaction of the original tetrahedrally coordinated chromate to octahedrally coordinated Cr^{3+} compounds (Fig. 31c). In the XANES spectra the occurrence of this reaction is highlighted by the red-shift of the absorption edge energy and the decreasing of the pre-edge peak intensity at 5.993 keV, assigned to a dipole-forbidden transition from the Cr 1s orbital into orbitals with Cr 3d character (t_2 symmetry) and quantitatively proportional to the Cr^{6+}-to-total Cr content ratio (Fig. 31d) [63, 548]. Selective and specific Cr speciation information were also more recently obtained by analyzing directly the paint surface of darkened chrome yellow paints by means of Cr K-edge XANES spectroscopy in TEY detection mode (see Sect. 2 for details) [145]. SR μ-XRD mapping has revealed the amorphous nature of the secondary Cr compounds [106].

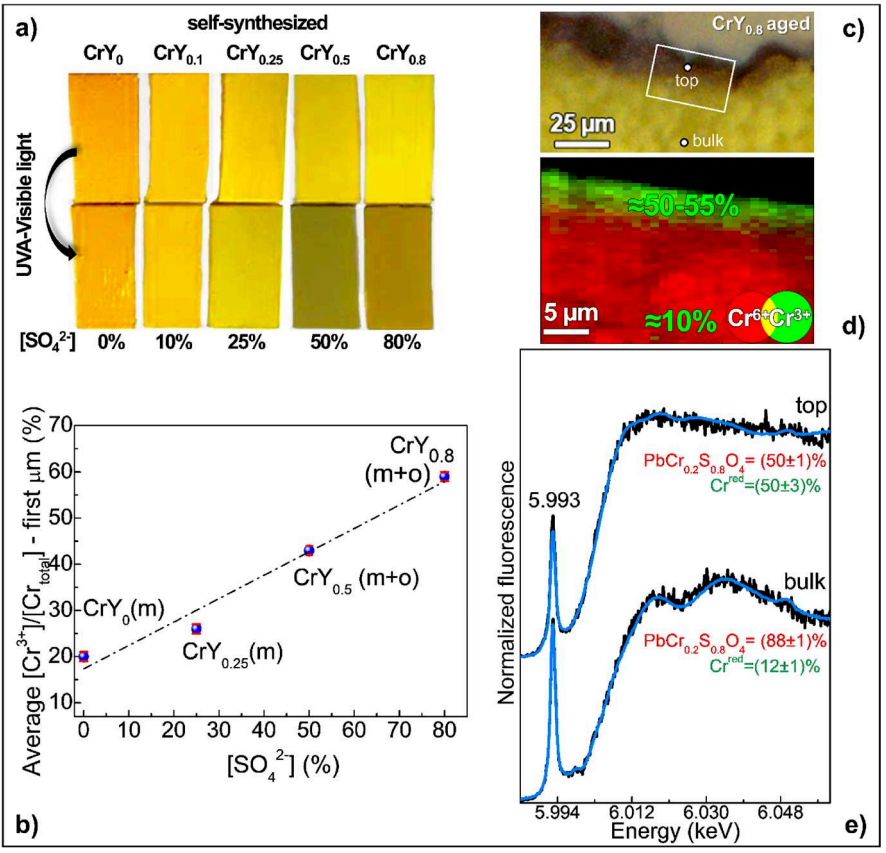

Fig. 31 **a** Photographs of oil mock-up paints made up of self-synthesized chrome yellow powders differing in sulfate content (CrY_x denotes $PbCr_{1-x}S_xO_4$ with $0 \leq x \leq 0.8$) and crystalline structure [monoclinic (m) and/or orthorhombic (o)] before (top) and after (bottom) exposure to UVA–VIS light. **b** Cr^{3+}-abundance percentage (averaged at the uppermost micrometer of the paint surface) *vs*. sulfate amount percentage obtained from the light-exposed mock-up paints. Dashed line shows the linear trend. **c** Photomicrograph of a thin section obtained from the self-synthesized $CrY_{0.8}$ paints aged by UVA–VIS light (top) and **d** corresponding RG composite Cr^{6+}/ Cr^{3+} maps. **e** Result of the linear combination fit (cyan) of the µ-XANES spectra of $PbCr_{0.2}S_{0.8}O_4$ and one/two Cr^{3+}-references [namely: $Cr(OH)_3/Cr_2O_3$ and Cr^{3+}-acetate/Cr^{3+}-acetylacetonate] to the ones recorded from the surface of the uppermost alteration layer and the bulk paint of the $CrY_{0.8}$ thin section (black) shown in (**c**) (data of (**c**–**e**) were collected at ESRF-ID21). Adapted with permission from [38, 145, 548]

Sulfate content, crystalline structure, and solubility are among the intrinsic factors prompting the formation of Cr^{3+} compounds in chrome yellows oil paints [63, 107, 548]. The amount of reduced chromium increases with increasing sulfur content, and thus, more soluble sulfur-rich orthorhombic $PbCr_{1-x}S_xO_4$ (with $x > 0.4$) compounds show a higher tendency toward reduction than the less soluble monoclinic sulfur-free $PbCrO_4$, that is the most lightfast of these materials (Fig. 31b).

The type of binding medium also influences the photo-reduction process of chrome yellows, being more pronounced in the oily medium than in the acrylic one [107]. In the

presence of additives, like $CaCO_3$, the photo-degradation of the oil paint may lead to the formation of calcium oxalate, while the $Cr^{6+} \rightarrow Cr^{3+}$ conversion takes place [144]. In the presence of specific admixture pigments, such as zinc white, emerald green, and red lead, the rate of light-induced darkening of chrome yellow decreases, possibly as result of the competitive absorption of specific wavelengths between the chrome yellow pigment and the added one, chemical interactions between pigments, and/or electron/positive holes released during light excitation of semiconductor pigments [38].

The darkening of oil paints also depends on the environmental conditions to which the pigment is exposed to. Experiments performed using different wavelengths of the UV–VIS spectrum and commercial WLED systems have established that the reduction of chrome yellow is activated not only by the violet–blue light (i.e., energy range where the pigment shows its maximum of absorption) but also by the green-one [143, 558]. The efficiency of the latter to induce the alteration process could be explained via identification of Cr^{5+} species by EPR spectroscopy. These species, whose formation is favored by the exposure of the paint to humidity and interaction with the oil binder, may absorb radiation in this spectral range, thus may play a key role in driving the photo-reduction toward the formation of different Cr^{3+} compounds [143].

Knowledge acquired from paint mock-ups was exploited for achieving a more comprehensive interpretation of the Cr speciation results of chrome yellow cross-sections, sampled from darkened paints of a series of artworks by Van Gogh [38, 123, 142, 550], such as the Amsterdam *Sunflowers* and *Falling leaves (Les Alyscamps)* (Kröller-Müller Museum, Otterlo, NL) (Fig. 32a,b). XFY-mode XANES investigations at the Cr K-edge (both in point analysis and imaging mode) allowed revealing the presence of Cr^{3+} species either in the form of superficial thin alteration layers or micrometric particles at the interface between the yellow paint and the superficial restoration varnish layer (Fig. 32c,e). The fit of the XANES dataset permitted the presence of different Cr^{3+} compounds to be identified, namely sulfates and oxides. Since the stratigraphic distribution of Cr^{3+} compounds in paintings was found to be often very similar to that observed in more light-sensitive paint mock-up [$PbCr_{1-x}S_xO_4$ (with $x > 0.4$); cf. Figure 30d], the darkening of chrome yellow paints was reasonably ascribed to a chemical degradation of the original pigment driven by a gradual conversion of Cr^{6+} to Cr^{3+} compounds.

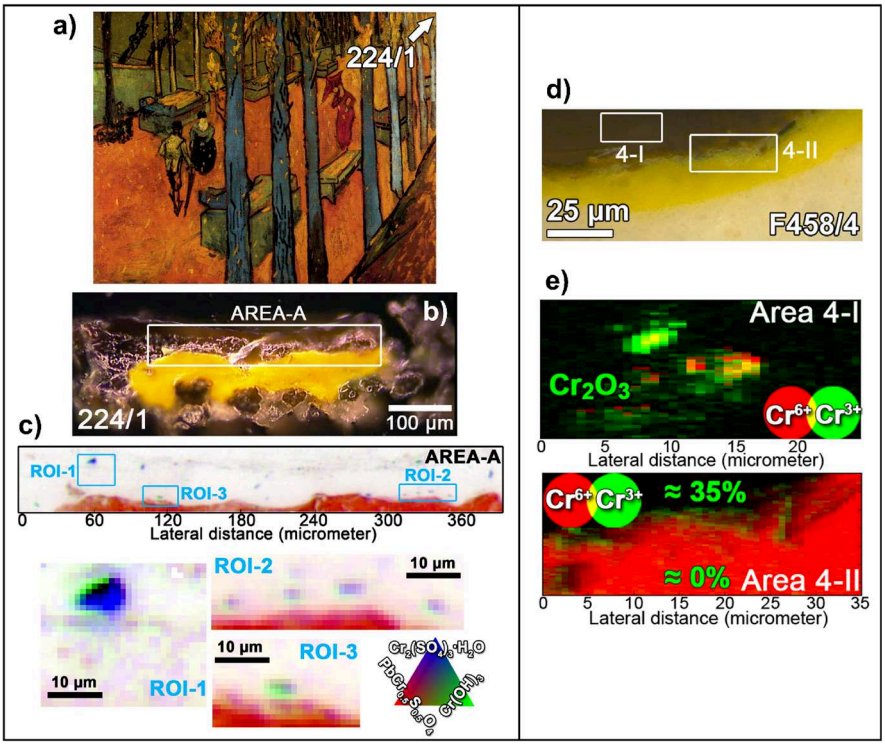

Fig. 32 **a** Photograph of the painting *Falling leaves (Les Alyscamps)* (1888) by Vincent van Gogh (Kröller-Müller Museum, Otterlo; Inv. nr. KM 108.668) (photo credits: Kröller-Müller Museum). **b** Photomicrograph of the cross-section 224/1 obtained from a sample taken off from the area shown by the arrow in (**a**). **c** Quantitative Cr phase maps and corresponding magnification of the regions of interest obtained from the linear combination fitting of the XANES stack collected at the XFM beamline (Australian synchrotron) using the spectra of $PbCr_{0.5}S_{0.5}O_4$ (red), $Cr(OH)_3$ (green), and $Cr_2(SO_4)_3{\cdot}H_2O$ (blue) as references. **d** Photomicrograph of sample F458/4, obtained from the light-yellow table of the Amsterdam *Sunflowers* (see Fig. 30a, e for the sampling spots and further results) and relative **e** RG composite Cr^{6+}/Cr^{3+} maps acquired at ESRF-ID21. In (**e**), the relative amounts percentage of Cr^{3+} found via Cr K-edge µ-XANES spectroscopy are also reported. Adapted with permission from [108, 123]

7 Conclusions and perspectives

In this review, we have described the current state-of-the-art of advanced X-ray methods for the study of alteration of pigments in paintings.

The combination of different X-ray methods (employing conventional sources and synchrotron radiation), often integrated with a wide range of other microscopy and spectroscopic techniques, is a successful strategy to elucidate the complex degradation pathways of certain classes of pigments in paint, from the macro down to the nanometric length scale.

The selected case studies here presented have highlighted that chemical alterations of pigments are due to irreversible reactions, that depend on several factors, including some intrinsic properties of the pigment itself, its manufacturing process, and/or

different environmental parameters (e.g., light, humidity, and air pollutants) to which the painting is exposed to.

From the hundreds of papers here quoted, one can conclude that the heritage science community has shown an increasing interest toward the exploitation of X-ray methods to study paintings degradation phenomena. The interest in SR-based techniques is confirmed by the implementation of new dedicated access modes at some synchrotrons [called block allocation group (BAG)], as it occurred at ESRF [55] and PETRA III-DESY (experiment nr. BAG-20230002 EC) during the last 5 years. Through BAG, experiments are scheduled every 6 months, they facilitate access to beamlines dedicated to structural investigations of materials and favor the development of activities and interactions of heritage researchers.

Next to the X-rays methods described in this review (namely XRF, XAS, and XRD) other state-of-the-art SR-based X-ray techniques are expected to find application for the study of the alteration processes of pigments in the future, namely: X-ray Raman scattering (XRS) and X-ray excited optical luminescence (XEOL). So far, such methods were already used for the characterization of organic components in archaeological/paleontological objects [559–561] and for the investigation of structural and optical properties of semiconducting phases [562, 563]. In particular, the development of new XEOL set-ups for lifetime measurements, full-field multispectral imaging (PUMA beamline, SOLEIL; Paris, France), and hyperspectral mapping (Carnaúba beamline, Sirius; São Paulo, Brazil) are opening new possibilities for probing crystal defects and impurities associated with the manufacturing process of artists' pigments and their potential reactivity within historical paint layers down to the submicrometer length scale [174, 564].

Further, the latest instrumental developments allow acquiring today massive amounts of datasets in a short time, thus calling upon smart statistical data evaluation, and analysis. Particularly promising perspectives concern the systematic integration of a wide range of available software with new algorithms/tools based on machine learning methods.

Still, due to the complexity of oil paints and current challenges associated both with object- and sample-based macro/micro-analysis, a lot of efforts are regularly ongoing to optimize the preparation of reliable mock-ups, whose study is fundamental for a deeper understanding of data recorded on historical paintings.

From the point of view of preventive conservation, the outcomes here described are providing important bases for the development of effective monitoring strategies for the safeguard of artworks at risk of degradation. In addition, they form a significant contribution toward the development of models for the virtual reconstruction of the original appearance of altered artworks and for the prediction of their evolution over time, when adequate safeguard measures are not implemented.

Acknowledgements The authors acknowledge the following Editors for the permission to reprint/adapt the following Figures: RSC for Figures 1a,b, 18, 23a-c, 32a-c; Springer Nature for Figures 8, 22a-f, 27b, 29; ACS for Figures 6, 20b,c, 24, 25, 31; Wiley for Figures 6, 10, 16, 30, 32d,e; Elsevier for Figures 9,19, 31; MDPI for Figures 11,14; De Gruyter for Figure 15; Science Advances for Figures 1c, 23d-f, 27a, 28; APS for Figure 26; Amsterdam University Press-Van Gogh Museum for Figure 31. The authors warmly thank also all the collaborators, institutes, museums, and heritage sites involved in the different research projects presented here.

Author contributions All authors contributed to the conception and design of the manuscript. Material preparation, data collection, and analysis were performed by all authors. The first draft of the manuscript was written by all authors and all authors commented on previous versions of the manuscript. All authors read and approved the final version of the manuscript.

Funding The research was financially supported by: Horizon 2020 project IPERION-HS (H2020-INFRAIA-2019–1, GA nr. 871034); the Horizon Europe project PERCEIVE (HORIZON-CL2-2021-HERITAGE-01, GA nr. 101061157); the project PE 0000020 CHANGES—CUP: B53C22003890006, NRP Mission 4 Component 2 Investment 1.3, funded by the European Union—NextGenerationEU, under the Italian Ministry of University and Research (MUR); Interreg "Vlaanderen-Nederland" project SmartLight 2.0; the BeAM (Belgian Avant Garde Modernism) project of BELSPO (Brussels, Belgium); the NanoLight Center of Excellence (Research Council, University of Antwerp, Belgium); the grant TED2021-129299A-I00 funded by MCIN/AEI/10.13039/501100011033; the Research Foundation Flanders (FWO) through its program on PhD Fellowships in Fundamental Research (application nr. 1181221N, 1181223N, 1183123N, and 1183125N). Koen Janssens and Geert Van der Snickt are indebted to the UAntwerp BOF DOCPRO project on lead-white speciation (project ID 44608). This research was also part of the activities of the Chair on Advanced Imaging Techniques for the Arts, established by the Baillet Latour fund. Koen Janssens, Ermanno Avranovich Clerici, and Steven De Meyer acknowledge financial support from the Fund for Scientific Research, Brussels, via project AutomatED (FN 7022, contract S000121N). Laura Cartechini, Francesca Rosi, and Aldo Romani thank the European Union—NextGenerationEU, Mission 4, Component 2, under the Italian Ministry of University and Research (MUR) National Innovation Ecosystem grant ECS00000041—VITALITY—CUP B43C22000470005. Katrien Keune, Fréderique T. H. Broers, and Nouchka De Keyser acknowledge the support by the Netherlands Institute for Conservation + Art + Science + (NICAS) and the Dutch Research Council (NWO) (3D2P Project, Project Nr. 628.007.031). Marine Cotte thanks the Royal Netherlands Academy of Arts and Sciences, KNAW (Descartes Huygens price 2018), and the PHC Van Gogh granted by the French Ministries of European and Foreign Affairs, and of Higher Education, Research and Innovation.

Data availability The datasets generated during and/or analyzed during the current study are available from the corresponding authors on reasonable request.

Declarations

Conflict of interest The authors have no financial or non-financial interests to disclose.

References

1. Plinio, Storia Naturale - V (Einaudi, Torino, 1988)
2. C. Cennini, F. Frezzato, Il libro dell'arte (Neri Pozza, Milano, 2003)
3. G. P. Lomazzo, Chapters 5–7, in: Trattato Dell'Arte Della Pittura, Scultura Ed Architettura - Volume 1, ed. By S. Del Monte (Roma, 1844), pp. 328–333
4. C. Pissarro, Eragny [May 31st, 1887], in: Letters to His Son Lucien, ed. By J. Rewald 2nd ed., (Pantheon Books Inc., New York, 1943), pp. 113–114
5. L. Jansen, H. Luijten, N. Bakker, Vincent van Gogh – The Letters (Thames & Hudson Ltd., London and Amsterdam, 2009). http://vangoghletters.org/vg/letters.html. Accessed June 2025

6. R. Nöller, Cinnabar reviewed: characterization of the red pigment and its reactions. Stud. Conserv. **60**, 79–87 (2015). https://doi.org/10.1179/2047058413Y.0000000089
7. M. Cotte, J. Susini, N. Metrich, A. Moscato, C. Gratziu, A. Bertagnini, M. Pagano, Blackening of Pompeian cinnabar paintings: X-ray microspectroscopy analysis. Anal. Chem. **78**, 7484–7492 (2006). https://doi.org/10.1021/ac0612224
8. S. Pérez-Diez, A. Pitarch Martí, A. Giakoumaki, N. Prieto-Taboada, S. Fdez-Ortiz de Vallejuelo, A. Martellone, B. De Nigris, M. Osanna, J. M. Madariaga, M. Maguregui, When Red Turns Black: Influence of the 79 AD Volcanic Eruption and Burial Environment on the Blackening/Darkening of Pompeian Cinnabar. Anal. Chem. **93**, 15870–15877 (2021). https://doi.org/10.1021/acs.analchem.1c02420
9. A. Roy, Artists' pigments. A handbook of their history and characteristics-Volume 2 (National Gallery of Art and Oxford University Press, Washington and Oxford, 1993)
10. M. Spring, R. Grout, The blackening of vermilion: an analytical study of the process in paintings. Natl. Gallery Tech. Bull. **23**, 50–61 (2002)
11. K. Keune, J.J. Boon, Analytical imaging studies clarifying the process of the darkening of vermilion in paintings. Anal. Chem. **77**, 4742–4750 (2005). https://doi.org/10.1021/ac048158f
12. M. Radepont, W. De Nolf, K. Janssens, G. Van Der Snickt, Y. Coquinot, L. Klaassen, M. Cotte, The use of microscopic X-ray diffraction for the study of HgS and its degradation products corderoite (α-$Hg_3S_2Cl_2$), kenhsuite (γ-$Hg_3S_2Cl_2$) and calomel (Hg_2Cl_2) in historical paintings. J. Anal. At. Spectrom. **26**, 959–968 (2011). https://doi.org/10.1039/c0ja00260g
13. M. Vagnini, R. Vivani, E. Viscuso, M. Favazza, B.G. Brunetti, A. Sgamellotti, C. Miliani, Investigation on the process of lead white blackening by Raman spectroscopy, XRD and other methods: study of Cimabue's paintings in Assisi. Vib. Spectrosc. **98**, 41–49 (2018). https://doi.org/10.1016/j.vibspec.2018.07.006
14. E. Avranovich Clerici, S. de Meyer, F. Vanmeert, S. Legrand, L. Monico, C. Miliani, K. Janssens, Multi-scale X-ray imaging of the pigment discoloration processes triggered by chlorine compounds in the upper Basilica of Saint Francis of Assisi. Molecules **28**, 6106 (2023). https://doi.org/10.3390/molecules28166106
15. A. Mignosi Tantillo, Restauri alla basilica inferiore di Assisi. Bollettino d'Arte **5**, 217–223 (1975)
16. F. Corsini, A. De Marchi, V. Picchiarelli, G. Verdiani, E. Zappasodi, Un esercizio di anastilosi digitale nella basilica inferiore di San Francesco ad Assisi, in: Il Maestro Di San Francesco e Lo Stil Novo Del Duecento Umbro, eds. By A. De Marchi, V. Picchiarelli, E. Zappasodi (Silvana Editoriale, Milano, 2024), pp. 193–211
17. V. Gonzalez, I. Fazlic, M. Cotte, F. Vanmeert, A. Gestels, S. De Meyer, F. Broers, J. Hermans, A. van Loon, K. Janssens, P. Noble, K. Keune, Lead(II) formate in Rembrandt's Night Watch: detection and distribution from the macro- to the micro-scale. Angewandte Chemie – Int. Ed. **62**, e202216478 (2023). https://doi.org/10.1002/anie.202216478
18. S. De Meyer, F. Vanmeert, R. Vertongen, A. van Loon, V. Gonzalez, G. van der Snickt, A. Vandivere, K. Janssens, Imaging secondary reaction products at the surface of Vermeer's Girl with the Pearl Earring by means of macroscopic X-ray powder diffraction scanning. Herit. Sci. **7**, 67 (2019). https://doi.org/10.1186/s40494-019-0309-3
19. F. Vanmeert, G. Van der Snickt, K. Janssens, Plumbonacrite identified by X-ray powder diffraction tomography as a missing link during degradation of red lead in a Van Gogh painting. Angewandte Chemie – Int. Ed. **54**, 3607–3610 (2015). https://doi.org/10.1002/anie.201411691
20. M. Spring, New insights into the materials of fifteenth- and sixteenth-century Netherlandish paintings in the National Gallery, London. Herit. Sci. **5**, 40 (2017). https://doi.org/10.1186/s40494-017-0152-3
21. K. Schnetz, A.A. Gambardella, R. van Elsas, J. Rosier, E.E. Steenwinkel, A. Wallert, P.D. Iedema, K. Keune, Evidence for the catalytic properties of ultramarine pigment. J. Cult. Herit. **45**, 25–32 (2020). https://doi.org/10.1016/j.culher.2020.04.002
22. A. van Loon, A.A. Gambardella, V. Gonzalez, M. Cotte, W. De Nolf, K. Keune, E. Leonhardt, S. de Groot, A.N. Proaño Gaibor, A. Vandivere, Out of the blue: Vermeer's use of ultramarine in Girl with a Pearl Earring. Herit. Sci. **8**, 25 (2020). https://doi.org/10.1186/s40494-020-00364-5
23. E. Cato, C. Borca, T. Huthwelker, E.S.B. Ferreira, Aluminium X-ray absorption near-edge spectroscopy analysis of discoloured ultramarine blue in 20th century oil paintings. Microchem. J. **126**, 18–24 (2016). https://doi.org/10.1016/j.microc.2015.11.021
24. J.S. Ferrer, I.C.A. Sandu, T. Syversen, A.M. Cardoso, A. Candeias, C.N. Borca, Investigating Colour Changes in Red and Blue Paints - A Preliminary Study of Art Materials and Techniques in Edvard

Munch's Old Man in Warnemünde (1907), in: Conservation of Modern Oil Paintings (Springer International Publishing, 2020), pp. 209–218. https://doi.org/10.1007/978-3-030-19254-9_15
25. P. Noble, A. van Loon, J. Bikker, Rembrandt's The Standard Bearer: New Findings from Imaging Analyses. Rijksmuseum Bulletin **71**, 170–179 (2023). https://doi.org/10.52476/trb.15070
26. P. Santopadre, M. Verità, A study of smalt and its conservation problems in two sixteenth-century wall paintings in Rome. Stud. Conserv. **51**, 29–40 (2006). https://doi.org/10.1179/sic.2006.51.1.29
27. C. de Mecquenem, M. Eveno, M. Alfeld, R. Pillay, E. Laval, E. Ravaud, I. Reiche, A multimodal study of smalt preservation and degradation on the painting "Woman doing a Libation or Artemisia" from an anonymous painter of the Fontainebleau School. Eur. Phys. J. Plus **138**, 185 (2023). https://doi.org/10.1140/epjp/s13360-023-03799-4
28. C. de Mecquenem, M. Eveno, D. Zurbach, K. Mösl, M. Cotte, I. Reiche, Influence of the painting medium on the alteration process of smalt in oil paintings studied using combined K and Co K-edge XANES. Appl. Phys. A Mater. Sci. Process. **130**, 781 (2024). https://doi.org/10.1007/s00339-024-07943-4
29. M. Spring, C. Higgitt, D. Saunders, Investigation of pigment-medium interaction processes in oil paint containing degraded smalt. Natl. Gallery Tech. Bull. **26**, 56–70 (2005)
30. A. Vila, K. Monrad, T. Filtenborg, J. Wadum, As Time Passed by Came Sunset. Christen Købke's View of Lake Sortedam, its Genesis and Colour Changes, in: Science and Art: The Painted Surface, eds. By A. Sgamellotti, B.G. Brunetti, C. Miliani (Royal Society of Chemistry, 2014), pp. 354–372. https://doi.org/10.1039/9781839161957-00354
31. M. Vermeulen, G. Nuyts, J. Sanyova, A. Vila, D. Buti, J.P. Suuronen, K. Janssens, Visualization of As(III) and As(V) distributions in degraded paint micro-samples from Baroque- and Rococo-era paintings. J. Anal. At. Spectrom. **31**, 1913–1921 (2016). https://doi.org/10.1039/c6ja00134c
32. N. De Keyser, F. Broers, F. Vanmeert, S. De Meyer, F. Gabrieli, E. Hermens, G. Van der Snickt, K. Janssens, K. Keune, Reviving degraded colors of yellow flowers in 17th century still life paintings with macro- and microscale chemical imaging. Sci. Adv. **8**, eabn6344 (2022). https://doi.org/10.1126/sciadv.abn6344
33. J. Simoen, S. De Meyer, F. Vanmeert, N. de Keyser, E. Avranovich, G. Van der Snickt, A. Van Loon, K. Keune, K. Janssens, Combined Micro- and Macro scale X-ray powder diffraction mapping of degraded Orpiment paint in a 17th century still life painting by Martinus Nellius. Herit. Sci. **7**, 83 (2019). https://doi.org/10.1186/s40494-019-0324-4
34. G. Van Der Snickt, J. Dik, M. Cotte, K. Janssens, J. Jaroszewicz, W. De Nolf, J. Groenewegen, L. Van Der Loeff, Characterization of a degraded cadmium yellow (CdS) pigment in an oil painting by means of synchrotron radiation based X-ray techniques. Anal. Chem. **81**, 2600–2610 (2009). https://doi.org/10.1021/ac802518z
35. T. Froysaker, N. Streeton, H. Kutzke, F. Hanssen-Bauer, B. Topalova-Casadiego, Public Paintings by Edvard Munch and His Contemporaries: Change and Conservation Challenges (Archetype Publications Ltd, London, 2015)
36. J.L. Mass, R. Opila, B. Buckley, M. Cotte, J. Church, A. Mehta, The photodegradation of cadmium yellow paints in Henri Matisse's le Bonheur de vivre (1905–1906). Appl. Phys. A Mater. Sci. Process. **111**, 59–68 (2013). https://doi.org/10.1007/s00339-012-7418-0
37. F. Casadio, S. Xie, S.C. Rukes, B. Myers, K.A. Gray, R. Warta, I. Fiedler, Electron energy loss spectroscopy elucidates the elusive darkening of zinc potassium chromate in Georges Seurat's A Sunday on la Grande Jatte-1884. Anal. Bioanal. Chem. **399**, 2909–2920 (2011). https://doi.org/10.1007/s00216-010-4264-9
38. L. Monico, E. Hendriks, M. Geldof, C. Miliani, K. Janssens, B. G. Brunetti, M. Cotte, F. Vanmeert, A. Chieli, G. Van der Snickt, A. Romani, M. J. Melo, Chemical Alteration and Colour Changes in the Amsterdam Sunflowers, in: Van Gogh's Sunflowers Illuminated, eds. By E. Hendriks, M. Vellekoop, M. van Bommel, M. Geldof (Amsterdam University Press and Van Gogh Museum, Amsterdam, 2019), pp. 125–157. https://doi.org/10.1515/9789048550531-006
39. C. Higgitt, G. Macaro, M. Spring, Methods, materials and condition of the London Sunflowers, in: Van Gogh's Sunflowers Illuminated, eds. By E. Hendriks, M. Vellekoop, M. van Bommel, M. Geldof (Amsterdam University Press and Van Gogh Museum, Amsterdam, 2019), pp. 49–84. https://doi.org/10.1017/9789048550531.004
40. L. van Tilborgh, E. Hendriks, Vincent Van Gogh Paintings: Antwerp and Paris, 1885–1888, vol. 2 (Waanders Publishers and Van Gogh Museum, Zwolle and Amsterdam, 2011)

41. M. Alter, L. Binet, N. Touati, N. Lubin-Germain, A.S. Le Hô, F. Mirambet, D. Gourier, Photochemical origin of the darkening of copper acetate and resinate pigments in historical paintings. Inorg. Chem. **58**, 13115–13128 (2019). https://doi.org/10.1021/acs.inorgchem.9b02007
42. L. Cartechini, C. Miliani, B.G. Brunetti, A. Sgamellotti, C. Altavilla, E. Ciliberto, F. D'Acapito, X-ray absorption investigations of copper resinate blackening in a XV century Italian painting. Appl. Phys. A Mater. Sci. Process. **92**, 243–250 (2008). https://doi.org/10.1007/s00339-008-4498-y
43. N. Salvadó, S. Butí, M. Cotte, G. Cinque, T. Pradell, Shades of green in 15th century paintings: combined microanalysis of the materials using synchrotron radiation XRD, FTIR and XRF. Appl. Phys. A Mater. Sci. Process. **111**, 47–57 (2013). https://doi.org/10.1007/s00339-012-7483-4
44. K. Keune, J. Mass, A. Mehta, J. Church, F. Meirer, Analytical imaging studies of the migration of degraded orpiment, realgar, and emerald green pigments in historic paintings and related conservation issues. Herit. Sci. **4**, 10 (2016). https://doi.org/10.1186/s40494-016-0078-1
45. K. Keune, J.J. Boon, R. Boitelle, Y. Shimadzu, Degradation of emerald green in oil paint and its contribution to the rapid change in colour of the Descente des vaches (1834–1835) painted by Théodore Rousseau. Stud. Conserv. **58**, 199–210 (2013). https://doi.org/10.1179/2047058412Y.0000000063
46. L. Monico, S. Prati, G. Sciutto, E. Catelli, A. Romani, D.Q. Balbas, Z. Li, S. De Meyer, G. Nuyts, K. Janssens, M. Cotte, J. Garrevoet, G. Falkenberg, V.I. Tardillo Suarez, R. Tucoulou, R. Mazzeo, Development of a multi-method analytical approach based on the combination of synchrotron radiation X-ray micro-analytical techniques and vibrational micro-spectroscopy methods to unveil the causes and mechanism of darkening of "fake-gilded" decorations in a Cimabue painting. J. Anal. At. Spectrom. **37**, 114–129 (2022). https://doi.org/10.1039/d1ja00271f
47. F. Casadio, K. Keune, P. Noble, A. Van Loon, E. Hendriks, S.A. Centeno, G. Osmond, Metal Soaps in Art: Conservation and Research (Springer International Publishing, Switzerland, 2019)
48. F.C. Izzo, M. Kratter, A. Nevin, E. Zendri, A Critical review on the analysis of metal soaps in oil paintings. ChemistryOpen **10**, 904–921 (2021). https://doi.org/10.1002/open.202100166
49. S. Russo, L. Brambilla, J.B. Thomas, E. Joseph, But aren't all soaps metal soaps? A review of applications, physico-chemical properties of metal soaps and their occurrence in cultural heritage studies. Herit. Sci. **11**, 172 (2023). https://doi.org/10.1186/s40494-023-00988-3
50. K. Janssens, M. Alfeld, G. Van Der Snickt, W. De Nolf, F. Vanmeert, M. Radepont, L. Monico, J. Dik, M. Cotte, G. Falkenberg, C. Miliani, B.G. Brunetti, The use of synchrotron radiation for the characterization of artists' pigments and paintings. Annu. Rev. Anal. Chem. **6**, 399–425 (2013). https://doi.org/10.1146/annurev-anchem-062012-092702
51. K. Janssens, G. Van der Snickt, F. Vanmeert, S. Legrand, G. Nuyts, M. Alfeld, L. Monico, W. Anaf, W. De Nolf, M. Vermeulen, J. Verbeeck, K. De Wael, Non-invasive and non-destructive examination of artistic pigments, paints, and paintings by means of X-ray methods. Top. Curr. Chem. **374**, 81 (2016). https://doi.org/10.1007/s41061-016-0079-2
52. C. Miliani, L. Monico, M.J. Melo, S. Fantacci, E.M. Angelin, A. Romani, K. Janssens, Photochemistry of artists' dyes and pigments: towards better understanding and prevention of colour change in works of art. Angewandte Chemie – Int. Ed. **57**, 7324–7334 (2018). https://doi.org/10.1002/anie.201802801
53. K. Janssens, M. Cotte, Using synchrotron radiation for characterization of cultural heritage materials, in: Synchrotron Light Sources and Free-Electron Lasers: Accelerator Physics, Instrumentation and Science Applications (2020), pp. 2457–2483. https://doi.org/10.1007/978-3-030-23201-6_78
54. L. Bertrand, L. Robinet, M. Thoury, K. Janssens, S.X. Cohen, S. Schöder, Cultural heritage and archaeology materials studied by synchrotron spectroscopy and imaging. Appl. Phys. A Mater. Sci. Process. **106**, 377–396 (2012). https://doi.org/10.1007/s00339-011-6686-4
55. M. Cotte, V. Gonzalez, F. Vanmeert, L. Monico, C. Dejoie, M. Burghammer, L. Huder, W. De Nolf, S. Fisher, I. Fazlic, C. Chauffeton, G. Wallez, N. Jiménez, F. Albert-Tortosa, N. Salvadó, E. Possenti, C. Colombo, M. Ghirardello, D. Comelli, E. Avranovich Clerici, R. Vivani, A. Romani, C. Costantino, K. Janssens, Y. Taniguchi, J. McCarthy, H. Reichert, J. Susini, The "Historical Materials BAG": a new facilitated access to synchrotron X-ray diffraction analyses for cultural heritage materials at the european synchrotron radiation facility. Molecules **27**, 1997 (2022). https://doi.org/10.3390/molecules27061997
56. A. Gianoncelli, S. Schöder, J.R. Plaisier, M. Fugazzotto, G. Barone, A. Russo, P. Mazzoleni, S. Raneri, X-ray synchrotron radiation to look at pigments in antiquities: overview and examples. Heritage **7**, 2118–2137 (2024). https://doi.org/10.3390/heritage7040100

57. P. Sedigh Rahimabadi, M. Khodaei, K.R. Koswattage, Review on applications of synchrotron-based X-ray techniques in materials characterization. X-Ray Spectrom. **49**, 348–373 (2020). https://doi.org/10.1002/xrs.3141
58. Y. Liu, X. Su, J. Ding, J. Zhou, Z. Liu, X. Wei, H. Yang, B. Liu, Progress and challenges in structural, in situ and operando characterization of single-atom catalysts by X-ray based synchrotron radiation techniques. Chem. Soc. Rev. **53**, 11850–11887 (2024). https://doi.org/10.1039/D3CS00967J
59. F. Meirer, B.M. Weckhuysen, Spatial and temporal exploration of heterogeneous catalysts with synchrotron radiation. Nat. Rev. Mater. **3**, 324–340 (2018). https://doi.org/10.1038/s41578-018-0044-5
60. C. Cao, M.F. Toney, T.K. Sham, R. Harder, P.R. Shearing, X. Xiao, J. Wang, Emerging X-ray imaging technologies for energy materials. Mater. Today **34**, 132–147 (2020). https://doi.org/10.1016/j.mattod.2019.08.011
61. H. Hu, J. Zhao, L. Wang, L. Shang, L. Cui, Y. Gao, B. Li, Y.F. Li, Synchrotron-based techniques for studying the environmental health effects of heavy metals: current status and future perspectives. Trends Anal. Chem. **122**, 115721 (2020). https://doi.org/10.1016/j.trac.2019.115721
62. C. Sanchez-Cano, R.A. Alvarez-Puebla, J.M. Abendroth, T. Beck et al., X-ray-based techniques to study the nano–bio interface. ACS Nano **15**, 3754–3807 (2021). https://doi.org/10.1021/acsnano.0c09563
63. L. Monico, G. Van Der Snickt, K. Janssens, W. De Nolf, C. Miliani, J. Verbeeck, H. Tian, H. Tan, J. Dik, M. Radepont, M. Cotte, Degradation process of lead chromate in paintings by Vincent van Gogh studied by means of synchrotron X-ray spectromicroscopy and related methods. 1. Artificially aged model samples. Anal. Chem. **83**, 1214–1223 (2011). https://doi.org/10.1021/ac102424h
64. L. Zanella, F. Casadio, K.A. Gray, R. Warta, Q. Ma, J.F. Gaillard, The darkening of zinc yellow: XANES speciation of chromium in artist's paints after light and chemical exposures. J. Anal. At. Spectrom. **26**, 1090–1097 (2011). https://doi.org/10.1039/c0ja00151a
65. K. Keune, J. Mass, F. Meirer, C. Pottasch, A. Van Loon, A. Hull, J. Church, E. Pouyet, M. Cotte, A. Mehta, Tracking the transformation and transport of arsenic sulfide pigments in paints: synchrotron-based X-ray micro-analyses. J. Anal. At. Spectrom. **30**, 813–827 (2015). https://doi.org/10.1039/c4ja00424h
66. L. Robinet, M. Spring, S. Pagès-Camagna, D. Vantelon, N. Trcera, Investigation of the discoloration of smalt pigment in historic paintings by micro-X-ray absorption spectroscopy at the Co K-edge. Anal. Chem. **83**, 5145–5152 (2011). https://doi.org/10.1021/ac200184f
67. I. Cianchetta, I. Colantoni, F. Talarico, F. D'Acapito, A. Trapananti, C. Maurizio, S. Fantacci, I. Davoli, Discoloration of the smalt pigment: experimental studies and ab initio calculations. J. Anal. At. Spectrom. **27**, 1941–1948 (2012). https://doi.org/10.1039/c2ja30132f
68. L. Samain, G. Silversmit, J. Sanyova, B. Vekemans, H. Salomon, B. Gilbert, F. Grandjean, G.J. Long, R.P. Hermann, L. Vincze, D. Strivay, Fading of modern Prussian blue pigments in linseed oil medium. J. Anal. At. Spectrom. **26**, 930–941 (2011). https://doi.org/10.1039/c0ja00234h
69. L. Samain, F. Grandjean, G.J. Long, P. Martinetto, P. Bordet, J. Sanyova, D. Strivay, Synthesis and fading of eighteenth-century Prussian blue pigments: a combined study by spectroscopic and diffractive techniques using laboratory and synchrotron radiation sources. J. Synchrotron Radiat. **20**, 460–473 (2013). https://doi.org/10.1107/S0909049513004585
70. F. Grandjean, L. Samain, G.J. Long, Characterization and utilization of Prussian blue and its pigments. Dalton Trans. **45**, 18018–18044 (2016). https://doi.org/10.1039/c6dt03351b
71. M. Vermeulen, J. Sanyova, K. Janssens, G. Nuyts, S. De Meyer, K. De Wael, The darkening of copper- or lead-based pigments explained by a structural modification of natural orpiment: a spectroscopic and electrochemical study. J. Anal. At. Spectrom. **32**, 1331–1341 (2017). https://doi.org/10.1039/c7ja00047b
72. H. Howard, J. Najorka, P.F. Schofield, K. Geraki, Degradation of fourteenth-century mordant gilding layers: synchrotron-based microfocus XRF, XRD, and XANES analyses of two paintings by Pietro Lorenzetti. Stud. Conserv. **69**, 193–208 (2024). https://doi.org/10.1080/00393630.2023.2201094
73. V. Gonzalez, A. Van Loon, S. Wt Price, P. Noble, K. Keune, Synchrotron micro-XRD and micro-XRD-CT reveal newly formed lead-sulfur compounds in Old Master paintings. J. Anal. At. Spectrom. **35**, 2267–2273 (2020). https://doi.org/10.1039/d0ja00169d
74. N. Salvadó, T. Pradell, E. Pantos, M.Z. Papiz, J. Molera, M. Seco, M. Vendrell-Saz, Identification of copper-based green pigments in Jaume Huguet's Gothic altarpieces by Fourier transform infrared microspectroscopy and synchrotron radiation X-ray diffraction. J. Synchrotron Radiat. **9**, 215–222 (2002). https://doi.org/10.1107/S0909049502007859

75. N. Salvadó, S. Butí, J. Nicholson, H. Emerich, A. Labrador, T. Pradell, Identification of reaction compounds in micrometric layers from gothic paintings using combined SR-XRD and SR-FTIR. Talanta **79**, 419–428 (2009). https://doi.org/10.1016/j.talanta.2009.04.005
76. N. Salvadó, S. Butí, A. Labrador, G. Cinque, H. Emerich, T. Pradell, SR-XRD and SR-FTIR study of the alteration of silver foils in medieval paintings. Anal. Bioanal. Chem. **399**, 3041–3052 (2011). https://doi.org/10.1007/s00216-010-4365-5
77. E. Welcomme, P. Walter, P. Bleuet, J.L. Hodeau, E. Dooryhee, P. Martinetto, M. Menu, Classification of lead white pigments using synchrotron radiation micro X-ray diffraction. Appl. Phys. A Mater. Sci. Process. **89**, 825–832 (2007). https://doi.org/10.1007/s00339-007-4217-0
78. V. Gonzalez, G. Wallez, T. Calligaro, M. Cotte, W. De Nolf, M. Eveno, E. Ravaud, M. Menu, Synchrotron-based high angle resolution and high lateral resolution X-ray diffraction: revealing lead white pigment qualities in old masters paintings. Anal. Chem. **89**, 13203–13211 (2017). https://doi.org/10.1021/acs.analchem.7b02949
79. V. Gonzalez, T. Calligaro, G. Wallez, M. Eveno, K. Toussaint, M. Menu, Composition and microstructure of the lead white pigment in Masters paintings using HR Synchrotron XRD. Microchem. J. **125**, 43–49 (2016). https://doi.org/10.1016/j.microc.2015.11.005
80. N. Palladino, M. Occelli, G. Wallez, Y. Coquinot, Q. Lemasson, L. Pichon, S. Stankic, V. Etgens, J. Salvant, An analytical survey of zinc white historical and modern artists' materials. Herit. Sci. **12**, 47 (2024). https://doi.org/10.1186/s40494-023-01082-4
81. C.I. Hiley, G. Hansford, N. Eastaugh, High-resolution non-invasive X-ray diffraction analysis of artists' paints. J. Cult. Herit. **53**, 1–13 (2022). https://doi.org/10.1016/j.culher.2021.10.008
82. L. Dalecky, I. Bonaduce, É. Anheim, J. La Nasa, M. L'Héronde, C. Morel, E. Catelli, S. Prati, Z. Li, L. Beck, I. Caffy, E. Delqué-Količ, A. Chevalier, L. Bertrand, A typical postwar workshop: Insights into Simon Hantaï's oil paint palette. J. Cult. Herit. **66**, 511–522 (2024). https://doi.org/10.1016/j.culher.2023.11.019
83. C. Costantino, L. Monico, F. Rosi, R. Vivani, A. Romani, L.C. Colocho Hurtarte, E. Villalobos-Portillo, C.J. Sahle, T. Huthwelker, C. Dejoie, M. Burghammer, M. Cotte, Non-destructive and non-invasive approaches for the identification of hydroxy lead-calcium phosphate solid solutions ($(Pb_xCa_{1-x})_5(PO_4)_3OH$) in cultural heritage materials. Appl. Spectrosc. **78**, 1231–1244 (2024). https://doi.org/10.1177/00037028241243375
84. L. Dalecky, F. Sottile, L. Hung, L. Cazals, A. Desolneux, A. Chevalier, J.P. Rueff, L. Bertrand, Non-resonant inelastic X-ray scattering for discrimination of pigments. Phys. Chem. Chem. Phys. **26**, 4363–4371 (2023). https://doi.org/10.1039/d3cp04753a
85. M. Thoury, J.P. Echard, M. Réfrégiers, B. Berrie, A. Nevin, F. Jamme, L. Bertrand, Synchrotron UV-visible multispectral luminescence microimaging of historical samples. Anal. Chem. **83**, 1737–1745 (2011). https://doi.org/10.1021/ac102986h
86. S. Hageraats, K. Keune, M. Thoury, R. Hoppe, A Synchrotron Photoluminescence Microscopy Study into the Use and Degradation of Zinc White in 'The Woodcutters' by Bart van der Leck, in: Conservation of Modern Oil Paintings, ed. By K. J. van den Berg, I. Bonaduce, A. Burnstock, B. Ormsby, M. Scharff, L. Carlyle, G. Heydenreich, K. Keune (Springer, Cham., 2020), pp. 275–288. https://doi.org/10.1007/978-3-030-19254-9_21
87. M. Ghirardello, V. Gonzalez, L. Monico, A. Nevin, D. MacLennan, C.S. Patterson, M. Burghammer, M. Réfrégiers, D. Comelli, M. Cotte, Application of synchrotron radiation-based micro-analysis on cadmium Yellows in Pablo Picasso's Femme. Microsc. Microanal. **28**, 1504–1513 (2022). https://doi.org/10.1017/S1431927622000873
88. A. Rogalev, J. Goulon, X-ray Excited Optical Luminescence Spectroscopies, in: Chemical Applications of Synchrotron Radiation. Part II: X-Ray Applications, ed. By T. K. Sham (World Scientific, 2002), pp. 707–760. https://doi.org/10.1142/9789812775757_0015
89. T.K. Sham, Photon-in/photon-out spectroscopic techniques for materials analysis: some recent developments. Adv. Mater. **26**, 7896–7901 (2014). https://doi.org/10.1002/adma.201304349
90. L. Liu, X. Sun, X-ray Excited Optical Luminescence and Its Applications, in: Synchrotron Radiation Applications, ed. By X. Zhang (World Scientific, 2018), pp. 493–534. https://doi.org/10.1142/9789813227675_0012
91. S. Hageraats, K. Keune, S. Stanescu, J.M. Laurent, W. Fresquet, M. Thoury, Combining X-ray excited optical luminescence and X-ray absorption spectroscopy for correlative imaging on the nanoscale. J. Synchrotron Radiat. **28**, 1858–1864 (2021). https://doi.org/10.1107/S1600577521009450

92. P. Reischig, L. Helfen, A. Wallert, T. Baumbach, J. Dik, High-resolution non-invasive 3D imaging of paint microstructure by synchrotron-based X-ray laminography. Appl. Phys. A Mater. Sci. Process. **111**, 983–995 (2013). https://doi.org/10.1007/s00339-013-7687-2
93. C. Gervais, J.J. Boon, F. Marone, E.S.B. Ferreira, Characterization of porosity in a 19th century painting ground by synchrotron radiation X-ray tomography. Appl. Phys. A Mater. Sci. Process. **111**, 31–38 (2013). https://doi.org/10.1007/s00339-012-7533-y
94. K. Krug, L. Porra, P. Coan, A. Wallert, J. Dik, A. Coerdt, A. Bravin, M. Elyyan, P. Reischig, L. Helfen, T. Baumbach, Relics in medieval altarpieces? Combining X-ray tomographic, laminographic and phase-contrast imaging to visualize thin organic objects in paintings. J. Synchrotron Radiat. **15**, 55–61 (2007). https://doi.org/10.1107/S0909049507045438
95. F.T.H. Broers, I. Verslype, K.W. Bossers, F. Vanmeert, V. Gonzalez, J. Garrevoet, A. van Loon, E. van Duijn, A. Krekeler, N. De Keyser, I. Steeman, P. Noble, K. Janssens, F. Meirer, K. Keune, Correlated X-ray fluorescence and ptychographic nanotomography on Rembrandt's The Night Watch reveals unknown lead "layer." Sci. Adv. **9**, eadj9394 (2023). https://doi.org/10.1126/sciadv.adj9394
96. M. Cotte, A. Genty-Vincent, K. Janssens, J. Susini, Applications of synchrotron X-ray nano-probes in the field of cultural heritage. C. R. Phys. **19**, 575–588 (2018). https://doi.org/10.1016/j.crhy.2018.07.002
97. E. Pouyet, M. Cotte, B. Fayard, M. Salomé, F. Meirer, A. Mehta, E.S. Uffelman, A. Hull, F. Vanmeert, J. Kieffer, M. Burghammer, K. Janssens, F. Sette, J. Mass, 2D X-ray and FTIR micro-analysis of the degradation of cadmium yellow pigment in paintings of Henri Matisse. Appl. Phys. A Mater. Sci. Process. **121**, 967–980 (2015). https://doi.org/10.1007/s00339-015-9239-4
98. J. Mass, J. Sedlmair, C.S. Patterson, D. Carson, B. Buckley, C. Hirschmugl, SR-FTIR imaging of the altered cadmium sulfide yellow paints in Henri Matisse's le Bonheur de vivre (1905–6)-examination of visually distinct degradation regions. Analyst **138**, 6032–6043 (2013). https://doi.org/10.1039/c3an00892d
99. M. Vermeulen, K. Janssens, J. Sanyova, V. Rahemi, C. McGlinchey, K. De Wael, Assessing the stability of arsenic sulfide pigments and influence of the binding media on their degradation by means of spectroscopic and electrochemical techniques. Microchem. J. **138**, 82–91 (2018). https://doi.org/10.1016/j.microc.2018.01.004
100. J.J. Hermans, K. Keune, A. Van Loon, R.W. Corkery, P.D. Iedema, Ionomer-like structure in mature oil paint binding media. RSC Adv. **6**, 93363–93369 (2016). https://doi.org/10.1039/c6ra18267d
101. G. Van Der Snickt, K. Janssens, J. Dik, W. De Nolf, F. Vanmeert, J. Jaroszewicz, M. Cotte, G. Falkenberg, L. Van Der Loeff, Combined use of synchrotron radiation based micro-X-ray fluorescence, micro-X-ray diffraction, micro-X-ray absorption near-edge, and micro-fourier transform infrared spectroscopies for revealing an alternative degradation pathway of the pigment Cadmium Yellow in a Painting by Van Gogh. Anal. Chem. **84**, 10221–10228 (2012). https://doi.org/10.1021/ac3015627
102. L. Monico, L. Cartechini, F. Rosi, A. Chieli, C. Grazia, S. de Meyer, G. Nuyts, F. Vanmeert, K. Janssens, M. Cotte, W. de Nolf, G. Falkenberg, I.C.A. Sandu, E.S. Tveit, J. Mass, R.P. de Freitas, A. Romani, C. Miliani, Probing the chemistry of CdS paints in the Scream by in situ noninvasive spectroscopies and synchrotron radiation x-ray techniques. Sci. Adv. **6**, eaay3514 (2020). https://doi.org/10.1126/sciadv.aay3514
103. H. Tan, H. Tian, J. Verbeeck, L. Monico, K. Janssens, G. Van Tendeloo, Nanoscale investigation of the degradation mechanism of a historical chrome yellow paint by quantitative electron energy loss spectroscopy mapping of chromium species. Angewandte Chemie – Int. Ed. **52**, 11360–11363 (2013). https://doi.org/10.1002/anie.201305753
104. R. Punis, M. Veronese, M. Meneghetti, A. Zoleo, Copper soaps formation in verdigris-linseed oil painting mixtures: a multispectroscopic characterization. Inorg. Chem. **63**, 4108–4119 (2024). https://doi.org/10.1021/acs.inorgchem.3c03794
105. R. Punis, A. Zoleo, Cu(II)-binder complexes in azurite and malachite pictorial mixtures: an EPR study. Microchem. J. **200**, 110303 (2024). https://doi.org/10.1016/j.microc.2024.110303
106. L. Monico, K. Janssens, M. Cotte, L. Sorace, F. Vanmeert, B.G. Brunetti, C. Miliani, Chromium speciation methods and infrared spectroscopy for studying the chemical reactivity of lead chromate-based pigments in oil medium. Microchem. J. **124**, 272–282 (2016). https://doi.org/10.1016/j.microc.2015.08.028
107. L. Monico, L. Sorace, M. Cotte, W. De Nolf, K. Janssens, A. Romani, C. Miliani, Disclosing the binding medium effects and the pigment solubility in the (photo)reduction process of chrome yellows

($PbCrO_4$/$PbCr_{1-x}S_xO_4$). ACS Omega **4**, 6607–6619 (2019). https://doi.org/10.1021/acsomega.8b03669
108. L. Monico, K. Janssens, E. Hendriks, F. Vanmeert, G. Van der Snickt, M. Cotte, G. Falkenberg, B.G. Brunetti, C. Miliani, Evidence for degradation of the chrome yellows in Van Gogh's Sunflowers: a study using noninvasive in situ methods and synchrotron-radiation-based X-ray techniques. Angewandte Chemie – Int. Ed. **54**, 13923–13927 (2015). https://doi.org/10.1002/anie.201505840
109. F. Vanmeert, E. Hendriks, G. Van der Snickt, L. Monico, J. Dik, K. Janssens, Chemical mapping by macroscopic X-ray powder diffraction (MA-XRPD) of Van Gogh's Sunflowers: identification of areas with higher degradation risk. Angewandte Chemie – Int. Ed. **57**, 7418–7422 (2018). https://doi.org/10.1002/anie.201713293
110. C. Cucci, J.K. Delaney, M. Picollo, Reflectance hyperspectral imaging for investigation of works of art: old master paintings and illuminated manuscripts. Acc. Chem. Res. **49**, 2070–2079 (2016). https://doi.org/10.1021/acs.accounts.6b00048
111. M. Picollo, C. Cucci, A. Casini, L. Stefani, Hyper-spectral imaging technique in the cultural heritage field: new possible scenarios. Sensors **20**, 2843 (2020). https://doi.org/10.3390/s20102843
112. F. Vanmeert, S. De Meyer, A. Gestels, E.A. Clerici, N. Deleu, S. Legrand, P. Van Espen, G. Van der Snickt, M. Alfeld, J. Dik, L. Monico, W. De Nolf, M. Cotte, V. Gonzalez, S. Saverwyns, L. Depuydt-Elbaum, K. Janssens, Non-invasive and Non-destructive Examination of Artists' Pigments, Paints and Paintings by Means of X-Ray Imaging Methods, in: Analytical Chemistry for the Study of Paintings and the Detection of Forgeries. Cultural Heritage Science, eds. By M.P. Colombini, I. Degano, A. Nevin (Springer, Cham., 2022), pp. 317–357. https://doi.org/10.1007/978-3-030-86865-9_11
113. B. Brunetti, C. Miliani, F. Rosi, B. Doherty, L. Monico, A. Romani, A. Sgamellotti, Non-invasive investigations of paintings by portable instrumentation: the MOLAB experience. Top. Curr. Chem. **374**, 10 (2016). https://doi.org/10.1007/s41061-015-0008-9
114. F. Rosi, L. Cartechini, D. Sali, C. Miliani, Recent trends in the application of Fourier Transform Infrared (FT-IR) spectroscopy in heritage science: from micro- to non-invasive FT-IR. Phys. Sci. Rev. **4**, 20180006 (2019). https://doi.org/10.1515/psr-2018-0006
115. S. Legrand, F. Vanmeert, G. Van der Snickt, M. Alfeld, W. De Nolf, J. Dik, K. Janssens, Examination of historical paintings by state-of-the-art hyperspectral imaging methods: from scanning infrared spectroscopy to computed X-ray laminography. Herit. Sci. **2**, 13 (2014). https://doi.org/10.1186/2050-7445-2-13
116. M. Alfeld, L. de Viguerie, Recent developments in spectroscopic imaging techniques for historical paintings—a review. Spectrochim. Acta Part B At. Spectrosc. **136**, 81–105 (2017). https://doi.org/10.1016/j.sab.2017.08.003
117. S. Mosca, C. Conti, N. Stone, P. Matousek, Spatially offset Raman spectroscopy. Nat. Rev. Methods Primers **1**, 21 (2021). https://doi.org/10.1038/s43586-021-00019-0
118. J. Striova, A.D. Fovo, R. Fontana, Reflectance imaging spectroscopy in heritage science. Rivista Del Nuovo Cimento **43**, 515–566 (2020). https://doi.org/10.1007/s40766-020-00011-6
119. P. Matousek, C. Conti, M. Realini, C. Colombo, Micro-scale spatially offset Raman spectroscopy for non-invasive subsurface analysis of turbid materials. Analyst **141**, 731–739 (2016). https://doi.org/10.1039/c5an02129d
120. L. Bertrand, S. Schöeder, D. Anglos, M.B.H. Breese, K. Janssens, M. Moini, A. Simon, Mitigation strategies for radiation damage in the analysis of ancient materials. TrAC - Trends Anal. Chem. **66**, 128–145 (2015). https://doi.org/10.1016/j.trac.2014.10.005
121. L. Bertrand, S. Schöder, I. Joosten, S.M. Webb, M. Thoury, T. Calligaro, É. Anheim, A. Simon, Practical advances towards safer analysis of heritage samples and objects. TrAC - Trends Anal. Chem. **164**, 117078 (2023). https://doi.org/10.1016/j.trac.2023.117078
122. C.G. Schroer, P. Boye, J.M. Feldkamp, J. Patommel, D. Samberg, A. Schropp, A. Schwab, S. Stephan, G. Falkenberg, G. Wellenreuther, N. Reimers, Hard X-ray nanoprobe at beamline P06 at PETRA III. Nucl. Instrum. Methods Phys. Res. A **616**, 93–97 (2010). https://doi.org/10.1016/j.nima.2009.10.094
123. L. Monico, K. Janssens, M. Alfeld, M. Cotte, F. Vanmeert, C.G. Ryan, G. Falkenberg, D.L. Howard, B.G. Brunetti, C. Miliani, Full spectral XANES imaging using the Maia detector array as a new tool for the study of the alteration process of chrome yellow pigments in paintings by Vincent van Gogh. J. Anal. At. Spectrom. **30**, 613–626 (2015). https://doi.org/10.1039/c4ja00419a
124. S. Mayda, L. Monico, D. Krishnan, S. De Meyer, M. Cotte, J. Garrevoet, G. Falkenberg, I.C. Sandu, B. Partoens, D. Lamoen, A. Romani, C. Miliani, J. Verbeeck, K. Janssens, A combined experimental and

computational approach to understanding CdS pigment oxidation in a renowned early 20th century painting. Chem. Mater. **35**, 10403–10415 (2023). https://doi.org/10.1021/acs.chemmater.3c01470
125. L. Monico, A. Chieli, S. De Meyer, M. Cotte, W. de Nolf, G. Falkenberg, K. Janssens, A. Romani, C. Miliani, Role of the relative humidity and the Cd/Zn stoichiometry in the photooxidation process of cadmium yellows ($CdS/Cd_{1-x}Zn_xS$) in oil paintings. Chem. Eur. J. **24**, 11584–11593 (2018). https://doi.org/10.1002/chem.201801503
126. J. Salvant, J. Williams, M. Ganio, F. Casadio, C. Daher, K. Sutherland, L. Monico, F. Vanmeert, S. De Meyer, K. Janssens, C. Cartwright, M. Walton, A roman egyptian painting workshop: technical investigation of the portraits from tebtunis, Egypt. Archaeometry **60**, 815–833 (2018). https://doi.org/10.1111/arcm.12351
127. N. De Keyser, F.T.H. Broers, F. Vanmeert, A. van Loon, F. Gabrieli, S. De Meyer, A. Gestels, V. Gonzalez, E. Hermens, P. Noble, F. Meirer, K. Keune, K. Janssens, Discovery of pararealgar and semi-amorphous pararealgar in Rembrandt's The Night Watch: analytical study and historical contextualization. Herit Sci **12**, 237 (2024). https://doi.org/10.1186/s40494-024-01350-x
128. S. De Meyer, F. Vanmeert, R. Vertongen, A. Van Loon, V. Gonzalez, J. Delaney, K. Dooley, J. Dik, G. Van der Snickt, A. Vandivere, K. Janssens, Macroscopic X-ray powder diffraction imaging reveals Vermeer's discriminating use of lead white pigments in Girl with a Pearl Earring. Sci. Adv. **5**, eaax1975 (2019). https://doi.org/10.1126/sciadv.aax1975
129. A. van Loon, A. Vandivere, J.K. Delaney, K.A. Dooley, S. De Meyer, F. Vanmeert, V. Gonzalez, K. Janssens, E. Leonhardt, R. Haswell, S. de Groot, P. D'Imporzano, G.R. Davies, Beauty is skin deep: the skin tones of Vermeer's Girl with a Pearl Earring. Herit. Sci. **7**, 102 (2019). https://doi.org/10.1186/s40494-019-0344-0
130. K. Janssens, S. Legrand, G. Van Der Snickt, F. Vanmeert, Virtual archaeology of altered paintings: multiscale chemical imaging tools. Elements **12**, 39–44 (2016). https://doi.org/10.2113/gselements.12.1.39
131. W. De Nolf, F. Vanmeert, K. Janssens, XRDUA: Crystalline phase distribution maps by two-dimensional scanning and tomographic (micro) X-ray powder diffraction. J. Appl. Crystallogr. **47**, 1107–1117 (2014). https://doi.org/10.1107/S1600576714008218
132. L. Monico, M. Cotte, F. Vanmeert, L. Amidani, K. Janssens, G. Nuyts, J. Garrevoet, G. Falkenberg, P. Glatzel, A. Romani, C. Miliani, Damages induced by synchrotron radiation-based X-ray microanalysis in chrome yellow paints and related Cr-compounds: assessment, quantification, and mitigation strategies. Anal. Chem. **92**, 14164–14173 (2020). https://doi.org/10.1021/acs.analchem.0c03251
133. C. Riekel, M. Burghammer, R. Davies, Progress in micro- and nano-diffraction at the ESRF ID13 beamline. IOP Conf. Ser. Mater. Sci. Eng. **14**, 012013 (2010). https://doi.org/10.1088/1757-899x/14/1/012013
134. G. Pastorelli, A.S.O. Miranda, E.A. Clerici, P. d'Imporzano, B.V. Hansen, K. Janssens, G.R. Davies, N. Borring, Darkening of lead white in old master drawings and historic prints: a multi-analytical investigation. Microchem. J. **199**, 109912 (2024). https://doi.org/10.1016/j.microc.2024.109912
135. M. Gomez Lobon, M. Ghirardello, E. Juncosa Darder, C. Palomino Cabello, M. Bauza, M. Cotte, A. Burnstock, A. Nevin, S.R. Amato, F.C. Izzo, D. Comelli, A study of cadmium yellow paints from Joan Miró's paintings and studio materials preserved at the Fundació Miró Mallorca. Herit. Sci. **11**, 145 (2023). https://doi.org/10.1186/s40494-023-00987-4
136. A. Suzuki, C.S. Cheung, Y. Li, A. Hogg, P.S. Atkinson, C. Riminesi, C. Miliani, H. Liang, Time and spatially resolved vis-NIR hyperspectral imaging as a novel monitoring tool for laser-based spectroscopy to mitigate radiation damage on paintings. Analyst **149**, 2338–2350 (2024). https://doi.org/10.1039/d3an02041j
137. M. Cotte, E. Checroun, W. De Nolf, Y. Taniguchi, L. De Viguerie, M. Burghammer, P. Walter, C. Rivard, M. Salomé, K. Janssens, J. Susini, Lead soaps in paintings: friends or foes? Stud. Conserv. **62**, 2–23 (2017). https://doi.org/10.1080/00393630.2016.1232529
138. E.H. Purdy, S. Critchley, C. Holé, M. Cotte, A. Kirkham, M. Casford, Characterisation of rouaite, an unusual copper-containing pigment in early modern English wall paintings, by synchrotron micro X-Ray diffraction and micro X-Ray absorption spectroscopy. Appl. Phys. A Mater. Sci. Process. **130**, 817 (2024). https://doi.org/10.1007/s00339-024-07954-1
139. V. Gonzalez, G. Wallez, E. Ravaud, M. Eveno, I. Fazlic, T. Fabris, A. Nevin, T. Calligaro, M. Menu, V. Delieuvin, M. Cotte, X-ray and infrared microanalyses of Mona Lisa's ground layer and significance regarding Leonardo da Vinci's Palette. J. Am. Chem. Soc. **145**, 23205–23213 (2023). https://doi.org/10.1021/jacs.3c07000

140. V. Gonzalez, M. Cotte, G. Wallez, A. van Loon, W. de Nolf, M. Eveno, K. Keune, P. Noble, J. Dik, Unraveling the Composition of Rembrandt's Impasto through the Identification of Unusual Plumbonacrite by Multimodal X-ray Diffraction Analysis. Angewandte Chemie – Int. Ed. **58**, 5619–5622 (2019). https://doi.org/10.1002/anie.201813105
141. M. Cotte, E. Pouyet, M. Salomé, C. Rivard, W. De Nolf, H. Castillo-Michel, T. Fabris, L. Monico, K. Janssens, T. Wang, P. Sciau, L. Verger, L. Cormier, O. Dargaud, E. Brun, D. Bugnazet, B. Fayard, B. Hesse, A.E. Pradas Del Real, G. Veronesi, J. Langlois, N. Balcar, Y. Vandenberghe, V.A. Solé, J. Kieffer, R. Barrett, C. Cohen, C. Cornu, R. Baker, E. Gagliardini, E. Papillon, J. Susini, The ID21 X-ray and infrared microscopy beamline at the ESRF: Status and recent applications to artistic materials. J. Anal. At. Spectrom. **32**, 477–493 (2017). https://doi.org/10.1039/c6ja00356g
142. L. Monico, K. Janssens, F. Vanmeert, M. Cotte, B.G. Brunetti, G. Van Der Snickt, M. Leeuwestein, J. Salvant Plisson, M. Menu, C. Miliani, Degradation process of lead chromate in paintings by Vincent van Gogh studied by means of spectromicroscopic methods. Part 5. Effects of nonoriginal surface coatings into the nature and distribution of chromium and sulfur species in chrome yellow paints. Anal. Chem. **86**, 10804–10811 (2014). https://doi.org/10.1021/ac502841g
143. L. Monico, K. Janssens, M. Cotte, A. Romani, L. Sorace, C. Grazia, B.G. Brunetti, C. Miliani, Synchrotron-based X-ray spectromicroscopy and electron paramagnetic resonance spectroscopy to investigate the redox properties of lead chromate pigments under the effect of visible light. J. Anal. At. Spectrom. **30**, 1500–1510 (2015). https://doi.org/10.1039/c5ja00091b
144. V. Otero, M. Vilarigues, L. Carlyle, M. Cotte, W. De Nolf, M.J. Melo, A: Little key to oxalate formation in oil paints: protective patina or chemical reactor? Photochem. Photobiol. Sci. **17**, 266–270 (2018). https://doi.org/10.1039/c7pp00307b
145. L. Monico, F. d'Acapito, M. Cotte, K. Janssens, A. Romani, G. Ricci, C. Miliani, L. Cartechini, Total electron yield (TEY) detection mode Cr K-edge XANES spectroscopy as a direct method to probe the composition of the surface of darkened chrome yellow ($PbCr_{1-x}S_xO_4$) and potassium chromate paints. Nucl. Instrum. Methods Phys. Res. B **539**, 141–147 (2023). https://doi.org/10.1016/j.nimb.2023.03.040
146. M. Radepont, Y. Coquinot, K. Janssens, J.J. Ezrati, W. De Nolf, M. Cotte, Thermodynamic and experimental study of the degradation of the red pigment mercury sulfide. J. Anal. At. Spectrom. **30**, 599–612 (2015). https://doi.org/10.1039/c4ja00372a
147. A.A. Gambardella, C.M. Schmidt Patterson, S.M. Webb, M.S. Walton, Sulfur K-edge XANES of lazurite: toward determining the provenance of lapis lazuli. Microchem. J. **125**, 299–307 (2016). https://doi.org/10.1016/j.microc.2015.11.030
148. A.A. Gambardella, M. Cotte, W. de Nolf, K. Schnetz, R. Erdmann, R. van Elsas, V. Gonzalez, A. Wallert, P.D. Iedema, M. Eveno, K. Keune, Sulfur K-edge micro- and full-field XANES identify marker for preparation method of ultramarine pigment from lapis lazuli in historical paints. Sci. Adv. **6**, eaay8782 (2020). https://doi.org/10.1126/sciadv.aay8782
149. L. Monico, F. Rosi, R. Vivani, L. Cartechini, K. Janssens, N. Gauquelin, D. Chezganov, J. Verbeeck, M. Cotte, F. d'Acapito, L. Barni, C. Grazia, L. Pensabene Buemi, J.L. Andral, C. Miliani, A. Romani, Deeper insights into the photoluminescence properties and (photo)chemical reactivity of cadmium red ($CdS_{1-x}Se_x$) paints in renowned twentieth century paintings by state-of-the-art investigations at multiple length scales. Eur Phys J Plus **137**, 311 (2022). https://doi.org/10.1140/epjp/s13360-022-02447-7
150. A. Kostomitsopoulou Marketou, F. Giannici, S. Handberg, W. De Nolf, M. Cotte, F. Caruso, Synchrotron radiation-based micro-XANES and Micro-XRF study of unsuccessfully produced egyptian blue from the late hellenistic production site of Kos (Dodecanese, Greece). Anal. Chem. **93**, 11557–11567 (2021). https://doi.org/10.1021/acs.analchem.1c02063
151. V. Otero, J.V. Pinto, L. Carlyle, M. Vilarigues, M. Cotte, M.J. Melo, Nineteenth century chrome yellow and chrome deep from Winsor & NewtonTM. Stud. Conserv. **62**, 123–149 (2017). https://doi.org/10.1080/00393630.2015.1131478
152. G. Martinez-Criado, J. Villanova, R. Tucoulou, D. Salomon, J.P. Suuronen, S. Laboure, C. Guilloud, V. Valls, R. Barrett, E. Gagliardini, Y. Dabin, R. Baker, S. Bohic, C. Cohen, J. Morse, ID16B: A hard X-ray nanoprobe beamline at the ESRF for nano-analysis. J. Synchrotron Radiat. **23**, 344–352 (2016). https://doi.org/10.1107/S1600577515019839
153. E. Avranovich Clerici, S. De Meyer, G. Van der Snickt, K. Janssens, Synchrotron X-ray powder diffraction study of lead white oxidation by sodium hypochlorite, in: Acta Artis Academica, eds. By J. Hradilová, D. Hradil (Academy of Fine Arts Prague, Prague, 2017), pp. 13–20.

154. N. Salvadó, S. Butí, M.A.G. Aranda, T. Pradell, New insights on blue pigments used in 15th century paintings by synchrotron radiation-based micro-FTIR and XRD. Anal. Methods **6**, 3610–3621 (2014). https://doi.org/10.1039/c4ay00424h
155. A. Fitch, C. Dejoie, E. Covacci, G. Confalonieri, O. Grendal, L. Claustre, P. Guillou, J. Kieffer, W. De Nolf, S. Petitdemange, M. Ruat, Y. Watier, ID22 - the high-resolution powder-diffraction beamline at ESRF. J. Synchrotron Radiat. **30**, 1003–1012 (2023). https://doi.org/10.1107/S1600577523004915
156. V. Gonzalez, D. Gourier, T. Calligaro, K. Toussaint, G. Wallez, M. Menu, Revealing the origin and history of lead-white pigments by their photoluminescence properties. Anal. Chem. **89**, 2909–2918 (2017). https://doi.org/10.1021/acs.analchem.6b04195
157. A. Fanost, A. Gimat, L. de Viguerie, P. Martinetto, A.C. Giot, M. Clémancey, G. Blondin, F. Gaslain, H. Glanville, P. Walter, G. Mériguet, A.L. Rollet, M. Jaber, Revisiting the identification of commercial and historical green earth pigments. Colloids. Surf. A Physicochem. Eng. Asp. **584**, 124035 (2020). https://doi.org/10.1016/j.colsurfa.2019.124035
158. V. Gonzalez, G. Wallez, T. Calligaro, D. Gourier, M. Menu, Synthesizing lead white pigments by lead corrosion: new insights into the ancient manufacturing processes. Corros. Sci. **146**, 10–17 (2019). https://doi.org/10.1016/j.corsci.2018.10.033
159. G.A. Chahine, N. Blanc, S. Arnaud, F. De Geuser, R. Guinebretière, N. Boudet, Advanced non-destructive in situ characterization of metals with the French collaborating research group D2AM/BM02 beamline at the European synchrotron radiation facility. Metals (Basel) **9**, 352 (2019). https://doi.org/10.3390/met9030352
160. M. Sánchez del Río, J. García-Rivas, M. Suárez, E. García-Romero, Crystal–chemical and diffraction analyses of Maya blue suggesting a different provenance of the palygorskite found in Aztec pigments*. Archaeometry **63**, 738–752 (2021). https://doi.org/10.1111/arcm.12644
161. F.J. Martínez-Casado, M. Ramos-Riesco, J.A. Rodríguez-Cheda, M.I. Redondo-Yélamos, L. Garrido, A. Fernández-Martínez, J. García-Barriocanal, I. Da Silva, M. Durán-Olivencia, A. Poulain, Lead(II) soaps: Crystal structures, polymorphism, and solid and liquid mesophases. Phys. Chem. Chem. Phys. **19**, 17009–17018 (2017). https://doi.org/10.1039/c7cp02351k
162. F. D'Acapito, G.O. Lepore, A. Puri, A. Laloni, F. La Manna, E. Dettona, A. De Luisa, A. Martin, The LISA beamline at ESRF. J. Synchrotron Radiat. **26**, 551–558 (2019). https://doi.org/10.1107/S1600577518018434
163. J.F.W. Mosselmans, P.D. Quinn, A.J. Dent, S.A. Cavill, S.D. Moreno, A. Peach, P.J. Leicester, S.J. Keylock, S.R. Gregory, K.D. Atkinson, J.R. Rosell, I18—The microfocus spectroscopy beamline at the Diamond Light Source. J. Synchrotron Radiat. **16**, 818–824 (2009). https://doi.org/10.1107/S0909049509032282
164. S.W.T. Price, A. Van Loon, K. Keune, A.D. Parsons, C. Murray, A.M. Beale, J.F.W. Mosselmans, Unravelling the spatial dependency of the complex solid-state chemistry of Pb in a paint micro-sample from Rembrandt's Homer using XRD-CT. Chem. Commun. **55**, 1931–1934 (2019). https://doi.org/10.1039/c8cc09705d
165. S.P. Thompson, J.E. Parker, J. Potter, T.P. Hill, A. Birt, T.M. Cobb, F. Yuan, C.C. Tang, Beamline I11 at Diamond: a new instrument for high resolution powder diffraction. Rev. Sci. Instrum. **80**, 075107 (2009). https://doi.org/10.1063/1.3167217
166. S. Bette, R.K. Kremer, G. Eggert, C.C. Tang, R.E. Dinnebier, On verdigris, part I: synthesis, crystal structure solution and characterisation of the 1–2-0 phase ($Cu_3(CH_3COO)_2(OH)_4$). Dalton Trans. **46**, 14847–14858 (2017). https://doi.org/10.1039/c7dt03288a
167. S. Bette, A. Costes, R.K. Kremer, G. Eggert, C.C. Tang, R.E. Dinnebier, On verdigris, part III: crystal structure, magnetic and spectral properties of anhydrous copper(II) acetate, a paddle wheel Chain. Z. Anorg. Allg. Chem. **645**, 988–997 (2019). https://doi.org/10.1002/zaac.201900125
168. A.J. Dent, G. Cibin, S. Ramos, S.A. Parry, D. Gianolio, A.D. Smith, S.M. Scott, L. Varandas, S. Patel, M.R. Pearson, L. Hudson, N.A. Krumpa, A.S. Marsch, P.E. Robbins, Performance of B18, the core EXAFS bending magnet beamline at diamond. J. Phys. Conf. Ser. **430**, 012023 (2013). https://doi.org/10.1088/1742-6596/430/1/012023
169. J. Juanhuix, F. Gil-Ortiz, G. Cuní, C. Colldelram, J. Nicolás, J. Lidón, E. Boter, C. Ruget, S. Ferrer, J. Benach, Developments in optics and performance at BL13-XALOC, the macromolecular crystallography beamline at the Alba Synchrotron. J. Synchrotron Radiat. **21**, 679–689 (2014). https://doi.org/10.1107/S160057751400825X

170. N. Salvadó, S. Butí, C. Clemente, V. Beltran, G. Cinque, J. Juanhuix, T. Pradell, Microanalytical study of luster glazed gilding and silvering from Baroque altarpieces. Pure Appl. Chem. **90**, 477–492 (2018). https://doi.org/10.1515/pac-2017-0602
171. L. Rebuffi, J.R. Plaisier, M. Abdellatief, A. Lausi, A.P. Scardi, Mcx: a synchrotron radiation beamline for X-ray diffraction line profile analysis. Z. Anorg. Allg. Chem. **640**, 3100–3106 (2014). https://doi.org/10.1002/zaac.201400163
172. E. Possenti, C. Colombo, C. Conti, L. Gigli, M. Merlini, J.R. Plaisier, M. Realini, G.D. Gatta, What's underneath? A non-destructive depth profile of painted stratigraphies by synchrotron grazing incidence X-ray diffraction. Analyst **143**, 4290–4297 (2018). https://doi.org/10.1039/c8an00901e
173. L. Bertrand, M.A. Languille, S.X. Cohen, L. Robinet, C. Gervais, S. Leroy, D. Bernard, E. Le Pennec, W. Josse, J. Doucet, S. Schöder, European research platform IPANEMA at the SOLEIL synchrotron for ancient and historical materials. J. Synchrotron Radiat. **18**, 765–772 (2011). https://doi.org/10.1107/S090904951102334X
174. S. Schöder, K. Müller, L. Tranchant, A. Rouquié, P. Gueriau, M. Thoury, E. Bérard, T. Okbinoglu, F. Berenguer, C. Iacconi, L. Robbiola, T. Moreno, S.X. Cohen, L. Bertrand, Heritage research at the PUMA beamline. Appl. Phys. A Mater. Sci. Process. **130**, 848 (2024). https://doi.org/10.1007/s00339-024-08026-0
175. M. Eveno, E. Ravaud, Early occurrences of the use of smalt and shell gold in the Madonna of Humility by Jacopo Bellini at the beginning of the fifteenth century. Eur. Phys. J. Plus **136**, 685 (2021). https://doi.org/10.1140/epjp/s13360-021-01650-2
176. M. Godet, L. Binet, S. Schöder, L. Brunel-Duverger, M. Thoury, L. Bertrand, X-ray irradiation effects on Egyptian blue and green pigments. J. Anal. At. Spectrom. **37**, 1265–1272 (2022). https://doi.org/10.1039/d2ja00020b
177. C. Barata, F. Rocha, A.J. Cruz, S. Andrejkovičová, S. Reguer, Synchrotron X-ray diffraction of bole layers from Portuguese gilded baroque retables. Appl. Clay Sci. **116–117**, 39–45 (2015). https://doi.org/10.1016/j.clay.2015.08.012
178. C. Santoro, K. Zarkout, A.S. Le Hô, F. Mirambet, D. Gourier, L. Binet, S. Pagès-Camagna, S. Reguer, S. Mirabaud, Y. Le Du, P. Griesmar, N. Lubin-Germain, M. Menu, New highlights on degradation process of verdigris from easel paintings. Appl. Phys. A Mater. Sci. Process. **114**, 637–645 (2014). https://doi.org/10.1007/s00339-014-8253-2
179. C. Gervais, M. Thoury, S. Réguer, P. Gueriau, J. Mass, Radiation damages during synchrotron X-ray micro-analyses of Prussian blue and zinc white historic paintings: detection, mitigation and integration. Appl. Phys. A Mater. Sci. Process. **121**, 949–955 (2015). https://doi.org/10.1007/s00339-015-9462-z
180. F. Baudelet, Q. Kong, L. Nataf, J.D. Cafun, A. Congeduti, A. Monza, S. Chagnot, J.P. Itié, ODE: a new beam line for high-pressure XAS and XMCD studies at SOLEIL. High Press Res. **31**, 136–139 (2011). https://doi.org/10.1080/08957959.2010.532794
181. C. Gervais, M.A. Languille, G. Moretti, S. Réguer, X-ray photochemistry of prussian blue cellulosic materials: evidence for a substrate-mediated redox process. Langmuir **31**, 8168–8175 (2015). https://doi.org/10.1021/acs.langmuir.5b00770
182. N.P. Edwards, S.M. Webb, U. Bergmann, Photons, folios, and fossils: the X-ray imaging and spectroscopy program of ancient materials at SSRL. Synchrotron Radiat. News **32**, 22–28 (2019). https://doi.org/10.1080/08940886.2019.1680211
183. F.T.H. Broers, K. Janssens, J. Nelson Weker, S.M. Webb, A. Mehta, F. Meirer, K. Keune, Two pathways for the degradation of orpiment pigment (As_2S_3) found in paintings. J. Am. Chem. Soc. **145**, 8847–8859 (2023). https://doi.org/10.1021/jacs.2c12271
184. M. Vermeulen, S.M. Webb, S. Russick, A.C. McGeachy, K. Muratore, M.S. Walton, Identification, transformations and mobility of hazardous arsenic-based pigments on 19th century bookbindings in accessible library collections. J. Hazard. Mater. **454**, 131453 (2023). https://doi.org/10.1016/j.jhazmat.2023.131453
185. M. Ganio, E.S. Pouyet, S.M. Webb, C.M. Schmidt Patterson, M.S. Walton, From lapis lazuli to ultramarine blue: Investigating Cennino Cennini's recipe using sulfur K-edge XANES. Pure Appl. Chem. **90**, 463–475 (2018). https://doi.org/10.1515/pac-2017-0502
186. Y. Gao, A. Kiss, R. Tappero, B. Stripe, W. Yun, Y.S. Chu, Design optimization of a confocal X-ray fluorescence imaging capability for XFM and SRX at NSLS-II. Proceedings Volume 11112, Proc. SPIE 11112, X-Ray Nanoimaging: Instruments and Methods IV, 1111204 (9 September 2019). https://doi.org/10.1117/12.2528026

187. M. Porell, M. Cushman, J.S.T. Fischel, M.H.H. Fischel, D.L. Sparks, R. Grayburn, Scanning X-ray fluorescence spectroscopy and micro-X-ray absorption near-edge structure analysis as a guiding tool for the conservation treatment of two eighteenth-century Philadelphian portraits. X-Ray Spectrom. **53**, 232–241 (2024). https://doi.org/10.1002/xrs.3345
188. J. Zhu, Zhang, G. Chen, J. Du, W. Li, Y. Li, The application of confocal depth-resolved micro-X-ray absorption spectroscopy to study colorant copper in ancient lead-silica glassy system at the Beijing Synchrotron Radiation Facility. Optik **218**, 165239 (2020). https://doi.org/10.1016/j.ijleo.2020.165239
189. L. Shen, C. Wang, J. Zhang, B. Cui, S. Zhu, J. Mao, Cu and As containing pigments in Zhejiang architecture polychrome paintings: a case study of degradation products of emerald green. Herit. Sci. **11**, 9 (2023). https://doi.org/10.1186/s40494-022-00834-y
190. D.L. Howard, M.D.D. Jonge, N. Afshar, C.G. Ryan, R. Kirkham, J. Reinhardt, C.M. Kewish, J. McKinlay, A. Walsh, J. Divitcos, N. Basten, L. Adamson, T. Fiala, L. Sammut, D.J. Paterson, The XFM beamline at the Australian Synchrotron. J. Synchrotron Radiat. **27**, 1447–1458 (2020). https://doi.org/10.1107/S1600577520010152
191. M. Cotte, J. Susini, J. Dik, K. Janssens, Synchrotron-based X-ray absorption spectroscopy for art conservation: looking back and looking forward. Acc. Chem. Res. **43**, 705–714 (2010). https://doi.org/10.1021/ar900199m
192. F. D'Acapito, X-Ray Absorption Spectroscopy (XAS) Applied to Cultural Heritage, in: Handbook of Cultural Heritage Analysis (Springer, 2022), pp. 45–67. https://doi.org/10.1007/978-3-030-60016-7_4
193. K. Janssens, M. Cotte, The use of XAS and related methods in cultural heritage investigations. Int. Tables Crystallog. **1**, 1039–1046 (2024). https://doi.org/10.1107/S1574870720004802
194. M.E. Fleet, X. Liu, X-ray absorption spectroscopy of ultramarine pigments: a new analytical method for the polysulfide radical anion S_3^- chromophore. Spectrochim. Acta Part B At. Spectrosc. **65**, 75–79 (2010). https://doi.org/10.1016/j.sab.2009.11.008
195. S. Hageraats, M. Thoury, M. Cotte, L. Bertrand, K. Janssens, K. Keune, Microchemical Imaging of Oil Paint Composition and Degradation: State-of-the-Art and Future Prospects, in: Analytical Chemistry for the Study of Paintings and the Detection of Forgeries. Cultural Heritage Science, eds. By M.P. Colombini, I. Degano, A. Nevin (Springer, Cham., 2022), pp. 359–418. https://doi.org/10.1007/978-3-030-86865-9_12
196. M. Siegbahn, The Spectroscopy of X-rays, vol. 10 (Humphrey Milford, Oxford University Press, Oxford, 1925)
197. E. Prince, Mathematical, physical and chemical tables. Int. Tables Crystallogr. (2021). https://doi.org/10.1107/97809553602060000117
198. W.T. Elam, B.D. Ravel, J.R. Sieber, A new atomic database for X-ray spectroscopic calculations. Radiat. Phys. Chem. **63**, 121–128 (2002). https://doi.org/10.1016/S0969-806X(01)00227-4
199. T. Schoonjans, A. Brunetti, B. Golosio, M. Sanchez Del Rio, V.A. Solé, C. Ferrero, L. Vincze, The xraylib library for X-ray-matter interactions. Recent developments. Spectrochim. Acta Part B At. Spectrosc. **66**, 776–784 (2011). https://doi.org/10.1016/j.sab.2011.09.011
200. B. Ravel, ATOMS: Crystallography for the X-ray absorption spectroscopist. J. Synchrotron Radiat. **8**, 314–316 (2001). https://doi.org/10.1107/S090904950001493X
201. M. Newville, Larch: An analysis package for XAFS and related spectroscopies. J. Phys. Conf. Ser. **430**, 012007 (2013). https://doi.org/10.1088/1742-6596/430/1/012007
202. P.A. Lee, P.H. Citrin, P. Eisenberger, B.M. Kincaid, Extended X-ray absorption fine structure its strengths and limitations as a structural tool. Rev. Mod. Phys. **53**, 769–806 (1981). https://doi.org/10.1103/RevModPhys.53.769
203. J.J. Rehr, R.C. Albers, Theoretical approaches to X-ray absorption fine structure. Rev. Mod. Phys. **72**, 621–654 (2000). https://doi.org/10.1103/RevModPhys.72.621
204. C.A. Ashley, S. Doniach, Theory of extended X-ray absorption edge fine structure (EXAFS) in crystalline solids. Phys. Rev. B **11**, 1279–1288 (1975). https://doi.org/10.1103/PhysRevB.11.1279
205. C.R. Natoli, M. Benfatto, A unifying scheme of interpretation of X-ray absorption spectra based on the multiple scattering theory. Le Journal de Physique Colloques **47**, C8-11-C8-23 (1986). https://doi.org/10.1051/jphyscol:1986802
206. A. Pantelouris, H. Modrow, M. Pantelouris, J. Hormes, D. Reinen, The influence of coordination geometry and valency on the K-edge absorption near edge spectra of selected chromium compounds. Chem. Phys. **300**, 13–22 (2004). https://doi.org/10.1016/j.chemphys.2003.12.017

207. M. Wilke, F. Farges, P.E. Petit, G.E. Brown, F. Martin, Oxidation state and coordination of Fe in minerals: an Fe K-XANES spectroscopic study. Am. Miner. **86**, 714–730 (2001). https://doi.org/10.2138/am-2001-5-612
208. A. Snigirev, I. Snigireva, High energy X-ray micro-optics. C. R. Phys. **9**, 507–516 (2008). https://doi.org/10.1016/j.crhy.2008.02.003
209. P. Kirkpatrick, A.V. Baez, Formation of optical images by X-rays. J. Opt. Soc. Am. **38**, 766–774 (1948). https://doi.org/10.1364/JOSA.38.000766
210. D.X. Balaic, K.A. Nugent, Z. Barnea, R. Garrett, S.W. Wilkins, Focusing of X-rays by total external reflection from a paraboloidally tapered glass capillary. J. Synchrotron Radiat. **2**, 296–299 (1995). https://doi.org/10.1107/s0909049595010831
211. Y.S. Chu, J.M. Yi, F. De Carlo, Q. Shen, W.K. Lee, H.J. Wu, C.L. Wang, J.Y. Wang, C.J. Liu, C.H. Wang, S.R. Wu, C.C. Chien, Y. Hwu, A. Tkachuk, W. Yun, M. Feser, K.S. Liang, C.S. Yang, J.H. Je, G. Margaritondo, Hard-x-ray microscopy with Fresnel zone plates reaches 40 nm Rayleigh resolution. Appl. Phys. Lett. **92**, 103119 (2008). https://doi.org/10.1063/1.2857476
212. H.C. Kang, H. Yan, R.P. Winarski, M.V. Holt, J. Maser, C. Liu, R. Conley, S. Vogt, A.T. MacRander, G.B. Stephenson, Focusing of hard x-rays to 16 nanometers with a multilayer Laue lens. Appl. Phys. Lett. **92**, 221114 (2008). https://doi.org/10.1063/1.2912503
213. A. Snigirev, V. Kohn, I. Snigireva, B. Lengeler, A compound refractive lens for focusing high-energy X-rays. Nature **384**, 49–51 (1996). https://doi.org/10.1038/384049a0
214. S.R. Sutton, A. Lanzirotti, M. Newville, M.L. Rivers, P. Eng, L. Lefticariu, Spatially resolved elemental analysis, spectroscopy and diffraction at the GSECARS sector at the advanced photon source. J. Environ. Qual. **46**, 1158–1165 (2017). https://doi.org/10.2134/jeq2016.10.0401
215. T.K. Sham, Y.Z. Finfrock, Q. Xiao, R. Feng, S. Bassnett, Retrieving images from tarnished daguerreotypes using X-ray fluorescence imaging with an X-ray micro beam with tunable energy. J. Cult. Herit. **67**, 53–61 (2024). https://doi.org/10.1016/j.culher.2024.02.003
216. B. Fayard, E. Pouyet, G. Berruyer, D. Bugnazet, C. Cornu, M. Cotte, V. De Andrade, F. Di Chiaro, O. Hignette, J. Kieffer, T. Martin, E. Papillon, M. Salomé, V.A. Sole, The new ID21 XANES full-field end-station at ESRF. J. Phys. Conf. Ser. **425**, 192001 (2013). https://doi.org/10.1088/1742-6596/425/19/192001
217. E. Pouyet, L. Monico, P. Sciau, M. Cotte, Application of Full-field X-ray Absorption Spectroscopy Imaging in Transmission Mode to Study Cultural Heritage Samples, in: Synchrotron Radiation, Cultural Heritage, Biomineralization, eds. By C. Dejoie, P. Martinetto, N. Tamura (Wiley-ISTE, 2024), pp. 69–100. https://doi.org/10.1002/9781394332458.ch3
218. E. Pouyet, B. Fayard, M. Salomé, Y. Taniguchi, F. Sette, M. Cotte, Thin-sections of painting fragments: opportunities for combined synchrotron-based micro-spectroscopic techniques. Herit. Sci. **3**, 3 (2015). https://doi.org/10.1186/s40494-014-0030-1
219. F. Pfeiffer, X-ray ptychography. Nat. Photonics **12**, 9–17 (2018). https://doi.org/10.1038/s41566-017-0072-5
220. P. Lechner, A. Pahlke, H. Soltau, Novel high-resolution silicon drift detectors. X-Ray Spectrom. **33**, 256–261 (2004). https://doi.org/10.1002/xrs.717
221. S.A. Audet, J.J. Friel, T.P. Gagliardi, R.B. Mott, J.I. Patel, C.G. Waldman, High resolution energy dispersive spectroscopy with high purity germanium detectors and digital pulse processing, in: IEEE Nuclear Science Symposium & Medical Imaging Conference (1995), pp. 155–159. https://doi.org/10.1109/nssmic.1994.474369
222. G. Falkenberg, F. Seiboth, F. Koch, K.V. Falch, A. Schropp, D. Brückner, J. Garrevoet, CRL optics and silicon drift detector for P06 Microprobe experiments at 35 keV. Powder Diffr. **35**(S1), S34–S37 (2020). https://doi.org/10.1017/S0885715620000536
223. C.G. Ryan, R. Kirkham, M.D. de Jonge, D.P. Siddons, A. van der Ent, A. Pagés, U. Boesenberg, A.J. Kuczewski, P. Dunn, M. Jensen, W. Liu, H. Harris, G.F. Moorhead, D.J. Paterson, D.L. Howard, N. Afshar, J. Garrevoet, K. Spiers, G. Falkenberg, A.R. Woll, G. De Geronimo, G.A. Carini, S.A. James, M.W.M. Jones, L.A. Fisher, M. Pearce, The Maia detector and event mode. Synchrotron Radiat. News **31**, 21–27 (2018). https://doi.org/10.1080/08940886.2018.1528430
224. U. Boesenberg, C.G. Ryan, R. Kirkham, D.P. Siddons, M. Alfeld, J. Garrevoet, T. Núñez, T. Claussen, T. Kracht, G. Falkenberg, Fast X-ray microfluorescence imaging with submicrometer-resolution integrating a Maia detector at beamline P06 at PETRA III. J. Synchrotron Radiat. **23**, 1550–1560 (2016). https://doi.org/10.1107/S1600577516015289

225. W. Chen, D. Elliott, G. Giacomini, A. Kuczewski, D. Pinelli, A.K. Rumaiz, D.P. Siddons, G. Smith, Improvement of SDD-Maia Detector for X-ray Fluorescence Detection, in: 2017 IEEE Nuclear Science Symposium and Medical Imaging Conference, NSS/MIC 2017 - Conference Proceedings (2018). https://doi.org/10.1109/NSSMIC.2017.8532602
226. O. Proux, E. Lahera, W. Del Net, I. Kieffer, M. Rovezzi, D. Testemale, M. Irar, S. Thomas, A. Aguilar-Tapia, E.F. Bazarkina, A. Prat, M. Tella, M. Auffan, J. Rose, J. Hazemann, High-energy resolution fluorescence detected X-ray absorption spectroscopy: a powerful new structural tool in environmental biogeochemistry sciences. J. Environ. Qual. **46**, 1146–1157 (2017). https://doi.org/10.2134/jeq2017.01.0023
227. W.T. Elam, J.P. Kirkland, R.A. Neiser, P.D. Wolf, Depth dependence for extended X-ray-absorption fine-structure spectroscopy detected via electron yield in He and in vacuum. Phys. Rev. B **38**, 26–30 (1988). https://doi.org/10.1103/PhysRevB.38.26
228. S. Padovani, I. Borgia, B. Brunetti, A. Sgamellotti, A. Giulivi, F. D'Acapito, P. Mazzoldi, C. Sada, G. Battaglin, Silver and copper nanoclusters in the lustre decoration of Italian Renaissance pottery: an EXAFS study. Appl. Phys. A Mater. Sci. Process. **79**, 229–233 (2004). https://doi.org/10.1007/s00339-004-2516-2
229. G. Artioli, Science for the cultural heritage: the contribution of X-ray diffraction. Rend. Lincei. **24**(Suppl 1), 55–62 (2013). https://doi.org/10.1007/s12210-012-0207-z
230. F. Vanmeert, K. De Wael, K. Janssens, G. Falkenberg, M. Cotte, Using synchrotron radiation for understanding the spontaneous degradation of artists' pigments. Synchrotron Radiat. News **32**, 41–47 (2019). https://doi.org/10.1080/08940886.2019.1680214
231. V. Gonzalez, M. Cotte, F. Vanmeert, W. de Nolf, K. Janssens, X-ray diffraction mapping for cultural heritage science: a review of experimental configurations and applications. Chem. Eur. J. **26**, 1703–1719 (2020). https://doi.org/10.1002/chem.201903284
232. C. Dejoie, P. Martinetto, N. Tamura, M. Kunz, F. Porcher, P. Bordat, R. Brown, E. Dooryhée, M. Anne, L.B. McCusker, Crystal structure of an indigo@silicalite hybrid related to the ancient maya blue pigment. J. Phys. Chem. C **118**, 28032–28042 (2014). https://doi.org/10.1021/jp509969z
233. L. Monico, K. Janssens, C. Miliani, B.G. Brunetti, M. Vagnini, F. Vanmeert, G. Falkenberg, A. Abakumov, Y. Lu, H. Tian, J. Verbeeck, M. Radepont, M. Cotte, E. Hendriks, M. Geldof, L. Van Der Loeff, J. Salvant, M. Menu, Degradation process of lead chromate in paintings by Vincent van Gogh studied by means of spectromicroscopic methods. 3. Synthesis, characterization, and detection of different crystal forms of the chrome yellow pigment. Anal. Chem. **85**, 851–859 (2013). https://doi.org/10.1021/ac302158b
234. F. Da Pieve, C. Hogan, D. Lamoen, J. Verbeeck, F. Vanmeert, M. Radepont, M. Cotte, K. Janssens, X. Gonze, G. Van Tendeloo, Casting light on the darkening of colors in historical paintings. Phys. Rev. Lett. **111**, 208302 (2013). https://doi.org/10.1103/PhysRevLett.111.208302
235. L.M. Smieska, J. Twilley, A.R. Woll, M. Schafer, A. Marcereau DeGalan, Energy-optimized synchrotron XRF mapping of an obscured painting beneath Exit from the Theater, attributed to Honoré Daumier. Microchem. J. **146**, 679–691 (2019). https://doi.org/10.1016/j.microc.2019.01.058
236. F. Vanmeert, W. De Nolf, J. Dik, K. Janssens, Macroscopic X-ray powder diffraction scanning: possibilities for quantitative and depth-selective parchment analysis. Anal. Chem. **90**, 6445–6452 (2018). https://doi.org/10.1021/acs.analchem.8b00241
237. G. Chiari, P. Sarrazin, A. Heginbotham, Non-conventional applications of a noninvasive portable X-ray diffraction/fluorescence instrument. Appl. Phys. A Mater. Sci. Process. **122**, 990 (2016). https://doi.org/10.1007/s00339-016-0521-x
238. P. Bleuet, E. Welcomme, E. Dooryhée, J. Susini, J.L. Hodeau, P. Walter, Probing the structure of heterogeneous diluted materials by diffraction tomography. Nat. Mater. **7**, 468–472 (2008). https://doi.org/10.1038/nmat2168
239. W. De Nolf, K. Janssens, Micro X-ray diffraction and fluorescence tomography for the study of multilayered automotive paints. Surf. Interface Anal. **42**, 411–418 (2010). https://doi.org/10.1002/sia.3125
240. E. Possenti, C. Conti, G.D. Gatta, N. Marinoni, M. Merlini, M. Realini, G.B.M. Vaughan, C. Colombo, Synchrotron X-ray diffraction computed tomography to non-destructively study inorganic treatments for stone conservation. IScience **25**, 105112 (2022). https://doi.org/10.1016/j.isci.2022.105112
241. P. Bordet, F. Kergourlay, A. Pinto, N. Blanc, P. Martinetto, Applying multivariate analysis to X-ray diffraction computed tomography: the study of medieval applied brocades. J. Anal. At. Spectrom. **36**, 1724–1734 (2021). https://doi.org/10.1039/d1ja00143d

242. M. Alfeld, K. Janssens, J. Dik, W. De Nolf, G. Van Der Snickt, Optimization of mobile scanning macro-XRF systems for the in situ investigation of historical paintings. J. Anal. At. Spectrom. **26**, 899–909 (2011). https://doi.org/10.1039/c0ja00257g
243. M. Alfeld, J.V. Pedroso, M. Van Eikema Hommes, G. Van Der Snickt, G. Tauber, J. Blaas, M. Haschke, K. Erler, J. Dik, K. Janssens, A mobile instrument for in situ scanning macro-XRF investigation of historical paintings. J. Anal. At. Spectrom. **28**, 760–767 (2013). https://doi.org/10.1039/c3ja30341a
244. M. Alfeld, W. De Nolf, S. Cagno, K. Appel, D.P. Siddons, A. Kuczewski, K. Janssens, J. Dik, K. Trentelman, M. Walton, A. Sartorius, Revealing hidden paint layers in oil paintings by means of scanning macro-XRF: A mock-up study based on Rembrandt's "An old man in military costume". J. Anal. At. Spectrom. **28**, 40–51 (2013). https://doi.org/10.1039/c2ja30119a
245. J. Dik, K. Janssens, G. Van Der Snickt, L. Van Der Loeff, K. Rickers, M. Cotte, Visualization of a lost painting by Vincent van Gogh using synchrotron radiation based X-ray fluorescence elemental mapping. Anal. Chem. **80**, 6436–6442 (2008). https://doi.org/10.1021/ac800965g
246. D. Thurrowgood, D. Paterson, M.D. De Jonge, R. Kirkham, S. Thurrowgood, D.L. Howard, A hidden portrait by Edgar Degas. Sci. Rep. **6**, 29594 (2016). https://doi.org/10.1038/srep29594
247. L. Struick van der Loeff, M. Alfeld, T. Meedendorp, J. Dik, E. Hendriks, G. van der Snickt, J. Koen, C. Meta, Rehabilitation of a flower still life, in the Kröller-Müller Museum and a lost Antwerp painting by Van Gogh, in: Van Gogh: New Findings. Van Gogh Studies, 4th edn., ed. by L. van Tilborgh (Waanders BV, Zwolle, 2012), pp. 33–53
248. M. Alfeld, K. Janssens, K. Appel, B. Thijsse, J. Blaas, J. Dik, A portrait by Philipp Otto Runge: visualizing modifications to the painting using synchrotron-based X-ray fluorescence elemental scanning. Zeitschrift Für Kunsttechnologie Und Konservierung **25**, 157–163 (2011)
249. D.L. Howard, M.D. De Jonge, D. Lau, D. Hay, M. Varcoe-Cocks, C.G. Ryan, R. Kirkham, G. Moorhead, D. Paterson, D. Thurrowgood, High-definition X-ray fluorescence elemental mapping of paintings. Anal. Chem. **84**, 3278–3286 (2012). https://doi.org/10.1021/ac203462h
250. M. Alfeld, D.P. Siddons, K. Janssens, J. Dik, A. Woll, R. Kirkham, E. Van De Wetering, Visualizing the 17th century underpainting in Portrait of an Old Man by Rembrandt van Rijn using synchrotron-based scanning macro-XRF. Appl. Phys. A Mater. Sci. Process. **111**, 157–164 (2013). https://doi.org/10.1007/s00339-012-7490-5
251. M. Alfeld, K. Janssens, Strategies for processing mega-pixel X-ray fluorescence hyperspectral data: a case study on a version of Caravaggio's painting Supper at Emmaus. J. Anal. At. Spectrom. **30**, 777–789 (2015). https://doi.org/10.1039/c4ja00387j
252. K. Janssens, J. Dik, M. Cotte, J. Susini, Photon-based techniques for nondestructive subsurface analysis of painted cultural heritage artifacts. Acc. Chem. Res. **43**, 814–825 (2010). https://doi.org/10.1021/ar900248e
253. K. Stonor, C. Richardson, S.R. Amato, A. Nevin, A. Burnstock, Rubens's Death of Hippolytus (1610–12): How scanning XRF shed new light on old questions, in: Lasers in the Conservation of Artworks XIII - Proceedings of the International Conference on Lasers in the Conservation of Artworks XII, LACONA 2022 (2024), pp. 3–11. https://doi.org/10.1201/9781003386872-1
254. K. Trentelman, K. Janssens, G. van der Snickt, Y. Szafran, A.T. Woollett, J. Dik, Rembrandt's An Old Man in Military Costume: the underlying image re-examined. Appl. Phys. A Mater. Sci. Process. **121**, 801–811 (2015). https://doi.org/10.1007/s00339-015-9426-3
255. K. Janssens, G. Van Der Snickt, M. Alfeld, P. Noble, A. van Loon, J. Delaney, D. Conover, J. Zeibel, J. Dik, Rembrandt's "Saul and David" (c. 1652): use of multiple types of smalt evidenced by means of non-destructive imaging. Microchem. J. **126**, 515–523 (2016). https://doi.org/10.1016/j.microc.2016.01.013
256. P. Noble, A. van Loon, M. Alfeld, K. Janssens, J. Dik, Rembrandt and/or studio, Saul and David, c. 1655: visualising the curtain using cross-section analyses and X-ray fluorescence imaging. Techne **35**, 36–45 (2012)
257. I. Verslype, The restoration of woman in blue reading a letter by Johannes Vermeer. Rijksmuseum Bull. **60**, 3–18 (2012). https://doi.org/10.52476/trb.9694
258. D. Bull, A. Krekeler, M. Alfeld, J. Dik, K. Janssens, An intrusive portrait by Goya. Burlington Magazine **153**, 668–672 (2011)
259. S.R. Amato, A. Burnstock, Scanning X-ray fluorescence for the re-examination of the composition underneath Paul Gauguin's Nevermore in the Courtauld Gallery. Stud. Conserv. (2024). https://doi.org/10.1080/00393630.2024.2350276

260. K.A. Dooley, A. Chieli, A. Romani, S. Legrand, C. Miliani, K. Janssens, J.K. Delaney, Molecular fluorescence imaging spectroscopy for mapping low concentrations of red lake pigments: Van Gogh's painting The olive orchard. Angewandte Chemie – Int. Ed. **59**, 6046–6053 (2020). https://doi.org/10.1002/anie.201915490
261. G. Van Der Snickt, A. Martins, J. Delaney, K. Janssens, J. Zeibel, M. Duffy, C. McGlinchey, B. Van Driel, J. Dik, Exploring a hidden painting below the surface of René Magritte's Le portrait. Appl. Spectrosc. **70**, 57–67 (2016). https://doi.org/10.1177/0003702815617123
262. A.T. da Silva, S. Legrand, G. van der Snickt, R. Featherstone, K. Janssens, G. Bottinelli, MA-XRF imaging on René Magritte's La condition humaine: Insights into the artist's palette and technique and the discovery of a third quarter of La pose enchantée. Herit. Sci. **5**, 37 (2017). https://doi.org/10.1186/s40494-017-0150-5
263. E. Derzelle, D. Strivay, A. Defeyt, S.J. Klein, F. Vandepitte, C. Defeyt, Paul Delvaux: the study of nine paintings by non-invasive methods. Heritage **6**, 7181–7201 (2023). https://doi.org/10.3390/heritage6110376
264. A. Martins, C. Albertson, C. McGlinchey, J. Dik, Piet Mondrian's Broadway Boogie Woogie: non invasive analysis using macro X-ray fluorescence mapping (MA-XRF) and multivariate curve resolution-alternating least square (MCR-ALS). Herit. Sci. **4**, 22 (2016). https://doi.org/10.1186/s40494-016-0091-4
265. A. Martins, J. Coddington, G. Snickt, B. Driel, C. McGlinchey, D. Dahlberg, K. Janssens, J. Dik, Jackson Pollock's Number 1A, 1948: A non-invasive study using macro-X-ray fluorescence mapping (MA-XRF) and multivariate curve resolution-alternating least squares (MCR-ALS) analysis. Herit Sci **4**, 33 (2016). https://doi.org/10.1186/s40494-016-0105-2
266. M. Cotte, L. Monico, K. Janssens, W. De Nolf, M. Salomé, J. Langlois, Synchrotron-based micro-analyses of artistic materials at ID21, ESRF. Acta Crystallogr. A Found. Adv. **73**, C1344–C1344 (2017). https://doi.org/10.1107/s2053273317082316
267. S. Legrand, P. Ricciardi, L. Nodari, K. Janssens, Non-invasive analysis of a 15th century illuminated manuscript fragment: point-based vs imaging spectroscopy. Microchem. J. **138**, 162–172 (2018). https://doi.org/10.1016/j.microc.2018.01.001
268. P. Ricciardi, S. Legrand, G. Bertolotti, K. Janssens, Macro X-ray fluorescence (MA-XRF) scanning of illuminated manuscript fragments: potentialities and challenges. Microchem. J. **124**, 785–791 (2016). https://doi.org/10.1016/j.microc.2015.10.020
269. M. Perino, L. Pronti, C. Moffa, M. Rosellini, A.C. Felici, New frontiers in the digital restoration of hidden texts in manuscripts: a review of the technical approaches. Heritage **7**, 683–696 (2024). https://doi.org/10.3390/heritage7020034
270. G. Bartolozzi, A. Casini, L. Castelli, C. Cucci, F. Grazzi, A. Mazzinghi, I. Pieralli, C. Ruberto, R. Sarfati, A. Sidoti, L. Stefani, M. Picollo, The non-invasive spectroscopic study of a parchment object from the national central library of florence: the hebrew scroll. Heritage **7**, 206–224 (2024). https://doi.org/10.3390/heritage7010011
271. F. Fiorillo, E. Cheese, S. Öberg Strådal, S. Reynolds, The extraordinary universe of Peter Apian: technical investigation of five copies of a 16th-century astronomical book. Herit. Sci. **12**, 190 (2024). https://doi.org/10.1186/s40494-024-01306-1
272. A. Piccirillo, P. Buscaglia, C. Caliri, F.P. Romano, D.P. Pavone, E.L. Ravan, M. Botticelli, C. Conti, C.M. Maria Catrambone, I. Degano, F.N. Alessia Andreotti, M. Samadelli, A. Paladin, R. Genta, M. Cardinali, F. Pozzi, D. Picchi, Unraveling the mummy's shroud: a multi-analytical study of a rare painted textile from Roman Egypt. J. Cult. Herit. **68**, 107–121 (2024). https://doi.org/10.1016/j.culher.2024.05.006
273. S. Cagno, G. Van der Snickt, S. Legrand, J. Caen, M. Patin, W. Meulebroeck, Y. Dirkx, M. Hillen, G. Steenackers, A. Rousaki, P. Vandenabeele, K. Janssens, Comparison of four mobile, non-invasive diagnostic techniques for differentiating glass types in historical leaded windows: MA-XRF, UV–Vis–NIR, Raman spectroscopy and IRT. X-Ray Spectrom. **50**, 293–309 (2021). https://doi.org/10.1002/xrs.3185
274. S. Legrand, G. Van der Snickt, S. Cagno, J. Caen, K. Janssens, MA-XRF imaging as a tool to characterize the 16th century heraldic stained-glass panels in Ghent Saint Bavo Cathedral. J. Cult. Herit. **40**, 163–168 (2019). https://doi.org/10.1016/j.culher.2019.06.003
275. M. Vadrucci, M. Chiari, A. Mazzinghi, A. Rufoloni, C. Cicero, "Hearts of gold" (Cuori d'oro): the case study of the leather corami of Palazzo Chigi in Ariccia. J. Cult. Herit. **68**, 184–194 (2024). https://doi.org/10.1016/j.culher.2024.05.017

276. I. Vanden Berghe, M. Van Bos, M. Vandorpe, A. Coudray, Non-invasive analysis of heritage textiles with MA-XRF mapping—exploring the possibilities. The study of Bishop Jacques de Vitry's mitres and fragile medieval reliquary purses from Namur (Belgium). Herit Sci **11**, 183 (2023). https://doi.org/10.1186/s40494-023-00977-6
277. W. Liu, P.Y. Zhang, N. Wu, The spectroscopic analysis of corrosion products on gold-painted copper-based bodhisattva (Guanyin) in half lotus position from national museum of China. Guang Pu Xue Yu Guang Pu Fen Xi/Spectroscopy and Spectral Analysis **43**, 3832–3839 (2023). https://doi.org/10.3964/j.issn.1000-0593(2023)12-3832-08
278. J. Brocchieri, R. Vitale, C. Sabbarese, MA-XRF analysis of ancient silver coins minted in southern Italy. X-Ray Spectrom. **53**, 452–463 (2023). https://doi.org/10.1002/xrs.3395
279. K.A. Dooley, D.M. Conover, L.D. Glinsman, J.K. Delaney, Complementary standoff chemical imaging to map and identify artist materials in an early Italian renaissance panel painting. Angewandte Chemie – Int. Ed. **53**, 13775–13779 (2014). https://doi.org/10.1002/anie.201407893
280. E. Ravaud, L. Pichon, E. Laval, V. Gonzalez, M. Eveno, T. Calligaro, Development of a versatile XRF scanner for the elemental imaging of paintworks. Appl. Phys. A Mater. Sci. Process. **122**, 17 (2016). https://doi.org/10.1007/s00339-015-9522-4
281. F.P. Romano, C. Caliri, P. Nicotra, S. Di Martino, L. Pappalardo, F. Rizzo, H.C. Santos, Real-time elemental imaging of large dimension paintings with a novel mobile macro X-ray fluorescence (MA-XRF) scanning technique. J. Anal. At. Spectrom. **32**, 773–781 (2017). https://doi.org/10.1039/c6ja00439c
282. R. Alberti, T. Frizzi, L. Bombelli, M. Gironda, N. Aresi, F. Rosi, C. Miliani, G. Tranquilli, F. Talarico, L. Cartechini, CRONO: a fast and reconfigurable macro X-ray fluorescence scanner for in-situ investigations of polychrome surfaces. X-Ray Spectrom. **46**, 297–302 (2017). https://doi.org/10.1002/xrs.2741
283. F.P. Romano, K. Janssens, Preface to the special issue on: MA-XRF "developments and applications of macro-XRF in conservation, art, and archeology" (Trieste, Italy, 24 and 25 September 2017). X-Ray Spectrom. **48**, 249–250 (2019). https://doi.org/10.1002/xrs.3047
284. F.P. Romano, ed., Special Issue: MA-XRF. X-Ray Spectrometry **50**, 243–412 (2021)
285. J.K. Delaney, K.A. Dooley, K. Janssens, A collection of papers from the 2024 Macro X-ray Fluorescence and Reflectance Imaging Spectroscopy Meeting. https://www.springeropen.com/collections/MAXRF. Accessed June 2025
286. M. Alfeld, J.A.C. Broekaert, Mobile depth profiling and sub-surface imaging techniques for historical paintings—a review. Spectrochim. Acta Part B At. Spectrosc. **88**, 211–230 (2013). https://doi.org/10.1016/j.sab.2013.07.009
287. L. Musílek, T. Čechák, T. Trojek, X-ray fluorescence analysis in the study of paintings – an overview. Radiat. Eff. Defects Solids **179**, 1218–1232 (2024). https://doi.org/10.1080/10420150.2024.2332215
288. A. Harth, X-ray fluorescence (XRF) on painted heritage objects: a review using topic modeling. Herit. Sci. **12**, 17 (2024). https://doi.org/10.1186/s40494-024-01135-2
289. A. Gestels, F. Gabrieli, T. De Kerf, F. Vanmeert, H. García, J. Delaney, K. Janssens, G. Steenackers, S. Vanlanduit, High-resolution compound-specific mapping in works of art via data fusion of MA-XRPD with hyperspectral data (part 1: Method evaluation). Talanta **280**, 126731 (2024). https://doi.org/10.1016/j.talanta.2024.126731
290. S. Yan, J.J. Huang, H. Verinaz-Jadan, N. Daly, C. Higgitt, P.L. Dragotti, A fast automatic method for deconvoluting macro X-ray fluorescence data collected from easel paintings. IEEE Trans. Comput. Imaging **9**, 649–664 (2023). https://doi.org/10.1109/TCI.2023.3288343
291. G. Pastorelli, A.S. Ortiz Miranda, A.H. Christensen, Interpretation of X-ray spectral data using self-organising maps and hierarchical clustering: a study of Vilhelm Hammershøi's use of painting materials. X-Ray Spectrom. **53**, 392–404 (2024). https://doi.org/10.1002/xrs.3388
292. T. Gerodimos, I. Patakiouta, V. Papadakis, D. Exarchos, A. Asvestas, G. Kenanakis, D. Matikas, T. Anagnostopoulos, Scanning micro X-ray fluorescence and multispectral imaging fusion: a case study on postage stamps. J Imaging **10**, 95 (2024). https://doi.org/10.3390/jimaging10040095
293. M. Vermeulen, A. McGeachy, B. Xu, H. Chopp, A. Katsaggelos, R. Meyers, M. Alfeld, M. Walton, XRFast a new software package for processing of MA-XRF datasets using machine learning. J. Anal. At. Spectrom. **37**, 2130–2143 (2022). https://doi.org/10.1039/d2ja00114d
294. E. Pouyet, S. Devine, T. Grafakos, R. Kieckhefer, J. Salvant, L. Smieska, A. Woll, A. Katsaggelos, O. Cossairt, M. Walton, Revealing the biography of a hidden medieval manuscript using synchrotron

and conventional imaging techniques. Anal. Chim. Acta **982**, 20–30 (2017). https://doi.org/10.1016/j.aca.2017.06.016
295. Z. Preisler, R. Andolina, A. Busacca, C. Caliri, C. Miliani, F.P. Romano, Deep learning for enhanced spectral analysis of MA-XRF datasets of paintings. Sci. Adv. **10**, eadp6234 (2024). https://doi.org/10.1126/sciadv.adp6234
296. T. Trojek, R. Prokeš, R. Šefců, H. Bilavčíková, T. Čechák, Confocal X-ray fluorescence spectrometer for in-situ analyses of paintings. Radiat. Phys. Chem. **137**, 238–242 (2017). https://doi.org/10.1016/j.radphyschem.2016.02.031
297. C. Seim, C. Laurenze-Landsberg, B. Schröder-Smeibidl, I. Mantouvalou, C. De Boer, B. Kanngießer, Old traces, read anew-','The Reading Hermit' painting in the light of X-ray fluorescence. J. Anal. At. Spectrom. **29**, 1354–1360 (2014). https://doi.org/10.1039/c3ja50301a
298. T. Lachmann, G. Van Der Snickt, M. Haschke, I. Mantouvalou, Combined 1D, 2D and 3D micro-XRF techniques for the analysis of illuminated manuscripts. J. Anal. At. Spectrom. **31**, 1989–1997 (2016). https://doi.org/10.1039/c6ja00220j
299. J. Tapia, M. Eveno, E. Laval, I. Reiche, Depth-resolved historical painting study with minimal microsampling, illustrated with a newly discovered Botticelli workshop painting. X-Ray Spectrom. (2024). https://doi.org/10.1002/xrs.3430
300. V.A. Solé, E. Papillon, M. Cotte, P. Walter, J. Susini, A multiplatform code for the analysis of energy-dispersive X-ray fluorescence spectra. Spectrochim. Acta Part B At. Spectrosc. **62**, 63–68 (2007). https://doi.org/10.1016/j.sab.2006.12.002
301. M. Cotte, T. Fabris, G. Agostini, D. Motta Meira, L. De Viguerie, V.A. Solé, Watching kinetic studies as chemical maps using open-source software. Anal. Chem. **88**, 6154–6160 (2016). https://doi.org/10.1021/acs.analchem.5b04819
302. S.M. Webb, The microAnalysis toolkit: X-ray fluorescence image processing software. AIP Conf. Proc. **1365**, 196–199 (2010). https://doi.org/10.1063/1.3625338
303. A.P. Hitchcock, Analysis of X-ray images and spectra (aXis2000): A toolkit for the analysis of X-ray spectromicroscopy data. J. Electron. Spectros. Relat. Phenomena **266**, 147360 (2023). https://doi.org/10.1016/j.elspec.2023.147360
304. Y. Liu, F. Meirer, P.A. Williams, J. Wang, J.C. Andrews, P. Pianetta, TXM-Wizard: A program for advanced data collection and evaluation in full-field transmission X-ray microscopy. J. Synchrotron Radiat. **19**, 281–287 (2012). https://doi.org/10.1107/S0909049511049144
305. B. Ravel, M. Newville, ATHENA, ARTEMIS, HEPHAESTUS: Data analysis for X-ray absorption spectroscopy using IFEFFIT. J. Synchrotron Radiat. **12**, 537–541 (2005). https://doi.org/10.1107/S0909049505012719
306. S.M. Webb, SIXpack: A graphical user interface for XAS analysis using IFEFFIT. Phys. Scr. T. **T115**, 1011–1014 (2005). https://doi.org/10.1238/Physica.Topical.115a01011
307. J.J. Rehr, J.J. Kas, F.D. Vila, M.P. Prange, K. Jorissen, Parameter-free calculations of X-ray spectra with FEFF9. Phys. Chem. Chem. Phys. **12**, 5503–5513 (2010). https://doi.org/10.1039/b926434e
308. S. Tomic, B.G. Searle, A. Wander, N.M. Harrison, A.J. Dent, J.F.W. Mosselmans, J.E. Inglesfield, New tools for the analysis of EXAFS: the DL EXCURV package. Council for the Central Laboratory of the Research Councils (2005)
309. A. Filipponi, A. Di Cicco, X-ray-absorption spectroscopy and n-body distribution functions in condensed matter. II. Data analysis and applications. Phys. Rev. B **52**, 15135–15149 (1995). https://doi.org/10.1103/PhysRevB.52.15135
310. M. Ippoliti, F. Guzzi, A. Gianoncelli, F. Billè, G. Kourousias, XRFitProc: a novel web-based X-ray fluorescence fitting system. X-Ray Spectrom. **52**, 371–377 (2023). https://doi.org/10.1002/xrs.3341
311. L.L. Van Loon, N.S. McIntyre, M. Bauer, N.S.A. Sherry, N.R. Banerjee, Peakaboo: Advanced software for the interpretation of X-ray fluorescence spectra from synchrotrons and other intense X-ray sources. Software Impacts **2**, 100010 (2019). https://doi.org/10.1016/j.simpa.2019.100010
312. H. Yan, W. Xu, D. Yu, A. Heroux, W.-K. Lee, L. Li, S. Campbell, Y. Chu, PyXRF: Python-based X-ray fluorescence analysis package, in: X-Ray Nanoimaging: Instruments and Methods III. SPIE (2017), pp. 38–45. https://doi.org/10.1117/12.2272585
313. S. Vogt, MAPS: A set of software tools for analysis and visualization of 3D X-ray fluorescence data sets. J. Phys. IV France **104**, 635–638 (2003). https://doi.org/10.1051/jp4:20030160
314. C.G. Ryan, B.E. Etschmann, S. Vogt, J. Maser, C.L. Harland, E. Van Achterbergh, D. Legnini, Nuclear microprobe–synchrotron synergy: Towards integrated quantitative real-time elemental imaging using

PIXE and SXRF. Nucl Instrum Methods Phys Res B **231**, 183–188 (2005). https://doi.org/10.1016/j.nimb.2005.01.054
315. C.G. Ryan, J.S. Laird, L.A. Fisher, R. Kirkham, G.F. Moorhead, Improved dynamic analysis method for quantitative PIXE and SXRF element imaging of complex materials. Nucl. Instrum. Methods Phys. Res. B **363**, 42–47 (2015). https://doi.org/10.1016/j.nimb.2015.08.021
316. O. Bunău, Y. Joly, Self-consistent aspects of X-ray absorption calculations. J. Phys. Condens. Matter **21**, 345501 (2009). https://doi.org/10.1088/0953-8984/21/34/345501
317. C.T. Chantler, F. Boscherini, B. Bunker, X-ray absorption spectroscopy and related techniques. Int. Tables Crystallogr. (2020). https://doi.org/10.1107/97809553602060000116
318. J. Kieffer, V. Valls, N. Blanc, C. Hennig, New tools for calibrating diffraction setups. J. Synchrotron Radiat. **27**, 558–566 (2020). https://doi.org/10.1107/S1600577520000776
319. S. Gates-Rector, T. Blanton, The Powder Diffraction File: a quality materials characterization database. Powder Diffr. **34**, 352–360 (2019). https://doi.org/10.1017/S0885715619000812
320. D. Zagorac, H. Muller, S. Ruehl, J. Zagorac, S. Rehme, Recent developments in the Inorganic Crystal Structure Database: Theoretical crystal structure data and related features. J. Appl. Crystallogr. **52**, 918–925 (2019). https://doi.org/10.1107/S160057671900997X
321. C.R. Groom, I.J. Bruno, M.P. Lightfoot, S.C. Ward, The Cambridge structural database. Acta Crystallogr B Struct. Sci. Cryst. Eng. Mater. **72**, 171–179 (2016). https://doi.org/10.1107/S2052520616003954
322. R.T. Downs, M. Hall-Wallace, The American Mineralogist crystal structure database. Am. Miner. **88**, 247–250 (2003). https://doi.org/10.5860/choice.43sup-0302
323. S. Gražulis, A. Merkys, A. Vaitkus, Crystallography Open Database (COD), in: Handbook of Materials Modeling, eds. By W. Andreoni, S. Yip (Springer, Cham, 2020), pp. 1863–1881. https://doi.org/10.1007/978-3-319-44677-6_66
324. H. Putz, K. Brandenburg GbR, Match! Phase Analysis using Powder Diffraction, Crystal Impact. (n.d.). https://www.crystalimpact.de/match (Accessed November 2024)
325. A. Altomare, N. Corriero, C. Cuocci, A. Falcicchio, A. Moliterni, R. Rizzi, QUALX2.0: a qualitative phase analysis software using the freely available database POW_COD. J. Appl. Crystallogr. **48**, 598–603 (2015). https://doi.org/10.1107/S1600576715002319
326. B.H. Toby, R.B. Von Dreele, GSAS-II: the genesis of a modern open-source all purpose crystallography software package. J. Appl. Crystallogr. **46**, 544–549 (2013). https://doi.org/10.1107/S0021889813003531
327. H.M. Rietveld, A profile refinement method for nuclear and magnetic structures. J. Appl. Crystallogr. **2**, 65–71 (1969). https://doi.org/10.1107/s0021889869006558
328. C.J. Gilmore, J.A. Kaduk, H. Schenk, Powder diffraction. Int. Tables Crystallogr. (2019). https://doi.org/10.1107/97809553602060000115
329. B.M. Weckhuysen, Z. Öztürk, R.P. Brand, J.M. Boereboom, F. Meirer, Vibrational fingerprinting of defects sites in thin films of zeolitic imidazolate frameworks. Chem. Eur. J. **25**, 8070–8084 (2019). https://doi.org/10.1002/chem.201806414
330. I.K. Van Ravenhorst, A.S. Hoffman, C. Vogt, A. Boubnov, N. Patra, R. Oord, C. Akatay, F. Meirer, S.R. Bare, B.M. Weckhuysen, On the cobalt carbide formation in a Co/TiO_2 fischer-tropsch synthesis catalyst as studied by high-pressure, long-term operando X-ray absorption and diffraction. ACS Catal. **11**, 2956–2967 (2021). https://doi.org/10.1021/acscatal.0c04695
331. F. Meirer, Y. Liu, E. Pouyet, B. Fayard, M. Cotte, C. Sanchez, J.C. Andrews, A. Mehta, P. Sciau, Full-field XANES analysis of Roman ceramics to estimate firing conditions - A novel probe to study hierarchical heterogeneous materials. J. Anal. At. Spectrom. **28**, 1870–1883 (2013). https://doi.org/10.1039/c3ja50226k
332. L. Monico, L. Cartechini, F. Rosi, W. De Nolf, M. Cotte, R. Vivani, C. Maurich, C. Miliani, Synchrotron radiation Ca K-edge 2D-XANES spectroscopy for studying the stratigraphic distribution of calcium-based consolidants applied in limestones. Sci. Rep. **10**, 14337 (2020). https://doi.org/10.1038/s41598-020-71105-8
333. P. Ballirano, M. Botticelli, A. Maras, Thermal behaviour of cinnabar, α-HgS, and the kinetics of the β-HgS (metacinnabar) - α-HgS conversion at room temperature. Eur. J. Mineral. **25**, 957–965 (2014). https://doi.org/10.1127/0935-1221/2013/0025-2341
334. A. Kyono, M. Kimata, T. Hatta, Light-induced degradation dynamics in realgar: In situ structural investigation using single-crystal X-ray diffraction study and X-ray photoelectron spectroscopy. Am. Miner. **90**, 1563–1570 (2005). https://doi.org/10.2138/am.2005.1785

335. P. Ballirano, A. Maras, In-situ X-ray transmission powder diffraction study of the kinetics of the light induced alteration of realgar (α-As_4S_4). Eur. J. Mineral. **18**, 589–599 (2006). https://doi.org/10.1127/0935-1221/2006/0018-0589
336. W. De Nolf, H. Payno, O. Svensson, G. Koumoutsos, ewoks (0.5.0). Zenodo (2024). https://doi.org/10.5281/zenodo.12704398
337. J. Demšar, T. Curk, A. Erjavec, Č Gorup, T. Hočevar, M. Milutinovič, M. Možina, M. Polajnar, M. Toplak, A. Starič, M. Štajdohar, L. Umek, L. Žagar, J. Žbontar, M. Žitnik, B. Zupan, Orange: Data mining toolbox in python. J. Mach. Learn. Res. **14**, 2349–2353 (2013)
338. A. Gotz, J. F. Perrin, H. Fangohr, D. Salvat, F. Gliksohn, A. Markvardsen, A. McBirnie, A. Gonzalez-Beltran, J. Taylor, B. Matthews. PaNOSC FAIR Research Data Policy framework (1.1). Zenodo (2020). https://doi.org/10.5281/zenodo.3862701
339. T. Wang, T.Q. Zhu, Z.Y. Feng, B. Fayard, E. Pouyet, M. Cotte, W. De Nolf, M. Salomé, P. Sciau, Synchrotron radiation-based multi-analytical approach for studying underglaze color: the microstructure of Chinese Qinghua blue decors (Ming dynasty). Anal. Chim. Acta **928**, 20–31 (2016). https://doi.org/10.1016/j.aca.2016.04.053
340. P. Sciau, C. Sanchez, E. Gliozzo, Ceramic technology: how to characterize terra sigillata ware. Archaeol. Anthropol. Sci. **12**, 211 (2020). https://doi.org/10.1007/s12520-020-01137-8
341. G. Massinelli, N. Marinoni, C. Colombo, G.D. Gatta, M. Realini, M. Burghammer, E. Possenti, Advanced mapping of inorganic treatments on porous carbonate stones by combined synchrotron radiation high lateral μ-XRPD and μ-XRF. Sci. Rep. **14**, 9108 (2024). https://doi.org/10.1038/s41598-024-58718-z
342. E. Pouyet, A. Lluveras-Tenorio, A. Nevin, D. Saviello, F. Sette, M. Cotte, Preparation of thin-sections of painting fragments: classical and innovative strategies. Anal. Chim. Acta **822**, 51–59 (2014). https://doi.org/10.1016/j.aca.2014.03.025
343. A. Gianoncelli, L. Vaccari, G. Kourousias, D. Cassese, D.E. Bedolla, S. Kenig, P. Storici, M. Lazzarino, M. Kiskinova, Soft X-ray microscopy radiation damage on fixed cells investigated with synchrotron. Sci. Reports **5**, 10250 (2015). https://doi.org/10.1038/srep10250
344. E.F. Garmana, M. Weik, Radiation damage to biological samples: still a pertinent issue. Synchrotron Radiat. **28**, 1278–1283 (2021). https://doi.org/10.1107/S1600577521008845
345. R.A. Wogelius, P.L. Manning, H.E. Barden, N.P. Edwards, S.M. Webb, W.I. Sellers, K.G. Taylor, P.L. Larson, P. Dodson, H. You, L. Da-qing, U. Bergmann, Trace metals as biomarkers for eumelanin pigment in the fossil record. Science **1979**(333), 1622–1626 (2011). https://doi.org/10.1126/science.1205748
346. S.R. Stock, M.K. Stock, J.D. Almer, Combined computed tomography and position-resolved X-ray diffraction of an intact Roman-era Egyptian portrait mummy: Combined computed tomography and position-resolved X-ray diffraction of an intact Roman-era Egyptian portrait mummy. J. R. Soc. Interface. **17**, 20200686 (2020). https://doi.org/10.1098/rsif.2020.0686
347. C. Gervais, M.A. Lanquille, G. Moretti, S. Réguer, Time resolved XANES illustrates a substrate-mediated redox process in Prussian blue cultural heritage materials. J. Phys. Conf. Ser. **712**, 012139 (2016). https://doi.org/10.1088/1742-6596/712/1/012139
348. Z. Zhang, Z. Liu, Y. Jiang, H. Zhu, T. Ji, J. Wang, M. Chen, W. Peng, L. Wang, X. Wei, In situ investigation of synchrotron radiation damage effect of ancient paintings by time-resolved ED-XAS and IR combined techniques. X-Ray Spectrom. **51**, 394–402 (2022). https://doi.org/10.1002/xrs.3289
349. Y. Li, A. Suzuki, C.S. Cheung, Y. Gu, S. Kogou, H. Liang, A study of potential laser-induced degradation in remote standoff Raman spectroscopy for wall paintings. Eur. Phys. J. Plus **137**, 1102 (2022). https://doi.org/10.1140/epjp/s13360-022-03305-2
350. L. Burgio, R.J.H. Clark, S. Firth, Raman spectroscopy as a means for the identification of plattnerite (PbO_2), of lead pigments and of their degradation products. Analyst **126**, 222–227 (2001). https://doi.org/10.1039/b008302j
351. I. Osticioli, A.A. Mencaglia, S. Siano, Temperature-controlled portable Raman spectroscopy of photothermally sensitive pigments. Sens Actuators B Chem. **238**, 772–778 (2017). https://doi.org/10.1016/j.snb.2016.07.104
352. A. Philippidis, A. Mikallou, D. Anglos, Determining optimum irradiation conditions for the analysis of vermilion by Raman spectroscopy. Eur. Phys. J. Plus **136**, 1194 (2021). https://doi.org/10.1140/epjp/s13360-021-02186-1
353. G. Moretti, C. Gervais, Raman spectroscopy of the photosensitive pigment Prussian blue. J. Raman Spectrosc. **49**, 1198–1204 (2018). https://doi.org/10.1002/jrs.5366

354. L. Monico, K. Janssens, E. Hendriks, B.G. Brunetti, C. Miliani, Raman study of different crystalline forms of $PbCrO_4$ and $PbCr_{1-x}S_xO_4$ solid solutions for the noninvasive identification of Chrome yellows in paintings: A focus on works by Vincent van Gogh. J. Raman Spectrosc. **45**, 1034–1045 (2014). https://doi.org/10.1002/jrs.4548
355. R. Clarke, J. Valentin, A history of the international commission on radiological protection. Health Phys. **88**, 407–422 (2005). https://doi.org/10.1097/01.HP.0000154049.41251.1e
356. IAEA - Internation Atomic Energy Agency, IAEA Annual Report 2017 (2018). https://www.iaea.org/opic/annual-report-2017. Accessed June 2025
357. I. Joosten, M. Stols-Witlox, Maartje Tromp, K. Keune, Irradiation Passport for Art (IPA), in: IAEA Workshop on Innovative Approaches of Accelerator Science and Technology for Sustainable Heritage Management (IAEA, Vienna, 2022), pp. 39–40. https://conferences.iaea.org/event/291/
358. L. Robinet, M.C. Corbeil, The characterization of metal soaps. Stud. Conserv. **48**, 23–40 (2003). https://doi.org/10.1179/sic.2003.48.1.23
359. V. Otero, D. Sanches, C. Montagner, M. Vilarigues, L. Carlyle, J.A. Lopes, M.J. Melo, Characterisation of metal carboxylates by Raman and infrared spectroscopy in works of art. J. Raman Spectrosc. **45**, 1197–1206 (2014). https://doi.org/10.1002/jrs.4520
360. F. Rosi, L. Cartechini, L. Monico, F. Gabrieli, M. Vagnini, D. Buti, B. Doherty, C. Anselmi, B.G. Brunetti, C. Miliani, Tracking Metal Oxalates and Carboxylates on Painting Surfaces by Non-invasive Reflection Mid-FTIR Spectroscopy, in: Metal Soaps in Art: Conservation and Research, eds. By F. Casadio, K. Keune, P. Noble, A. Van Loon, E. Hendriks, S.A. Centeno, G. Osmond (Springer International Publishing, Switzerland, 2019), pp. 173–193. https://doi.org/10.1007/978-3-319-90617-1_10
361. J. Catalano, V. Di Tullio, M. Wagner, N. Zumbulyadis, S.A. Centeno, C. Dybowski, Review of the use of NMR spectroscopy to investigate structure, reactivity, and dynamics of lead soap formation in paintings. Magn. Reson. Chem. **58**, 798–811 (2020). https://doi.org/10.1002/mrc.5025
362. K. Keune, A. Van Loon, J.J. Boon, SEM backscattered-electron images of paint cross-sections as information source for the presence of the lead white pigment and lead-related degradation and migration phenomena in oil paintings. Microsc. Microanal. **17**, 696–701 (2011). https://doi.org/10.1017/S1431927610094444
363. M. Cotte, E. Checroun, J. Susini, P. Walter, Micro-analytical study of interactions between oil and lead compounds in paintings. Appl. Phys. A Mater. Sci. Process. **89**, 841–848 (2007). https://doi.org/10.1007/s00339-007-4213-4
364. Y.C.K. Chen-Wiegart, J. Catalano, G.J. Williams, A. Murphy, Y. Yao, N. Zumbulyadis, S.A. Centeno, C. Dybowski, J. Thieme, Elemental and molecular segregation in oil paintings due to lead soap degradation. Sci. Rep. **7**, 11656 (2017). https://doi.org/10.1038/s41598-017-11525-1
365. M.C. Corbeil, L. Robinet, X-ray powder diffraction data for selected metal soaps. Powder Diffr. **17**, 52–60 (2002). https://doi.org/10.1154/1.1431950
366. E. Kočí, J. Rohlíček, L. Kobera, J. Plocek, S. Švarcová, P. Bezdička, Mixed lead carboxylates relevant to soap formation in oil and tempera paintings: The study of the crystal structure by complementary XRPD and ssNMR. Dalton Trans. **48**, 12531–12540 (2019). https://doi.org/10.1039/c9dt02040c
367. M. Cotte, E. Checroun, J. Susini, P. Dumas, P. Tchoreloff, M. Besnard, P. Walter, Kinetics of oil saponification by lead salts in ancient preparations of pharmaceutical lead plasters and painting lead mediums. Talanta **70**, 1136–1142 (2006). https://doi.org/10.1016/j.talanta.2006.03.007
368. R.J. Gettens, H. Kühn, W.T. Chase, 3. Lead White. Stud. Conserv. **12**, 125–139 (1967). https://doi.org/10.1179/sic.1967.013
369. P. Walter, P. Martinetto, G. Tsoucaris, R. Bréniaux, M.A. Lefebvre, G. Richard, J. Talabot, E. Dooryhee, Making make-up in Ancient Egypt. Nature **397**, 483–484 (1999). https://doi.org/10.1038/17240
370. P. Martinetto, M. Anne, E. Dooryhée, M. Drakopoulos, M. Dubus, J. Salomon, A. Simionovici, P. Walter, Synchrotron X-ray micro-beam studies of ancient Egyptian make-up. Nucl. Instrum. Methods Phys. Res. B **181**, 744–748 (2001). https://doi.org/10.1016/S0168-583X(01)00383-4
371. T. Christiansen, M. Cotte, W. de Nolf, E. Mouro, J. Reyes-Herrera, S. de Meyer, F. Vanmeert, N. Salvadó, V. Gonzalez, P.E. Lindelof, K. Mortensen, K. Ryholt, K. Janssens, S. Larsen, Insights into the composition of ancient Egyptian red and black inks on papyri achieved by synchrotron-based microanalyses. Proc. Natl. Acad. Sci. U S A **117**, 27825–27835 (2020). https://doi.org/10.1073/pnas.2004534117
372. K.J. van den Berg, P. Noble, J. Wadum, K. Groen, R. Heeren, Aspects of 17th century Binding Medium: inclusions in Rembrandt's Anatomy Lesson of Dr Nicolaes Tulp, in: Proceedings of the

International Congress on Contribution of Chemistry to the Works of Art, Art & Chimie, La Couleur, eds. By G. Jacques, M. Jean-Pierre (CNRS Editions, Paris, 2000), pp. 126–129
373. E. Kotulanová, P. Bezdička, D. Hradil, J. Hradilová, S. Švarcová, T. Grygar, Degradation of lead-based pigments by salt solutions. J. Cult. Herit. **10**, 367–378 (2009). https://doi.org/10.1016/j.culher.2008.11.001
374. M. Niknejad, A.H. Karimy, Lead White or Lead Whites? Reconsideration of Methods of sefidāb-i-sorb Production in Iran. Stud. Conserv. **64**, 1–9 (2019). https://doi.org/10.1080/00393630.2018.1457290
375. I. Tapsoba, S. Arbault, P. Walter, C. Amatore, Finding out Egyptian Gods' secret using analytical chemistry: biomedical properties of Egyptian black makeup revealed by amperometry at single cells. Anal. Chem. **82**, 457–460 (2010). https://doi.org/10.1021/ac902348g
376. I. Costantini, P.P. Lottici, D. Bersani, D. Pontiroli, A. Casoli, K. Castro, J.M. Madariaga, Darkening of lead- and iron-based pigments on late Gothic Italian wall paintings: Energy dispersive X-ray fluorescence, μ-Raman, and powder X-ray diffraction analyses for diagnosis: Presence of β-PbO_2 (plattnerite) and α-PbO_2 (scrutinyite). J. Raman Spectrosc. **51**, 680–692 (2020). https://doi.org/10.1002/jrs.5817
377. M. Vagnini, R. Vivani, A. Sgamellotti, C. Miliani, Blackening of lead white: study of model paintings. J. Raman Spectrosc. **51**, 1118–1126 (2020). https://doi.org/10.1002/jrs.5879
378. S.M. Lussier, G.D. Smith, A review of the phenomenon of lead white darkening and its conversion treatment. Stud. Conserv. **52**, 41–53 (2007). https://doi.org/10.1179/sic.2007.52.supplement-1.41
379. E. Gliozzo, C. Ionescu, Pigments—Lead-based whites, reds, yellows and oranges and their alteration phases. Archaeol. Anthropol. Sci. **14**, 17 (2022). https://doi.org/10.1007/s12520-021-01407-z
380. R. Přikryl, J. Svobodová, K. Zák, D. Hradil, Anthropogenic origin of salt crusts on sandstone sculptures of Prague's Charles Bridge (Czech Republic): Evidence of mineralogy and stable isotope geochemistry. Eur. J. Mineral. **16**, 609–617 (2004). https://doi.org/10.1127/0935-1221/2004/0016-0609
381. J. Sterpenich, Cristallochimie des produits d'altération des vitreaux médiévaux: application au vieillissement des déchets vitrifiés. Bull. Eng. Geol. Env. **61**, 179–193 (2002)
382. M. Cotte, J. Susini, V.A. Solé, Y. Taniguchi, J. Chillida, E. Checroun, P. Walter, Applications of synchrotron-based micro-imaging techniques to the chemical analysis of ancient paintings. J. Anal. At. Spectrom. **23**, 820–828 (2008). https://doi.org/10.1039/b801358f
383. A. van Loon, P. Noble, A. Krekeler, G. Snickt, K. Janssens, Y. Abe, I. Nakai, J. Dik, Artificial orpiment, a new pigment in Rembrandt's palette. Herit Sci **5**, 26 (2017). https://doi.org/10.1186/s40494-017-0138-1
384. F. Vanmeert, N. De Keyser, A. Van Loon, L. Klaassen, P. Noble, K. Janssens, Transmission and reflection mode macroscopic X-ray powder diffraction imaging for the noninvasive visualization of paint degradation in still life paintings by Jan Davidsz. de Heem. Anal. Chem. **91**, 7153–7161 (2019). https://doi.org/10.1021/acs.analchem.9b00328
385. A. Van Loon, P. Noble, J. Boon, White hazes and surface crusts in Rembrandt 's Homer and related paintings, in: ICOM Committee for Conservation 16th Triennial Meeting Lisbon Portugal 19–23 September 2011 (Critério Artes Gráficas, Lda. and ICOM Committee for Conservation, 2011), n. 416
386. A. van Loon, P. Noble, J.J. Boon, The formation of complex crusts in oil paints containing lead white and smalt, in *Historical Technology, Materials and Conservation: SEM and Microanalysis*. ed. by B.N. Meeks (Archetype Publications Ltd, London, 2012), pp. 207–209
387. G. Albertson, A. Krekeler, A. van Loon, A.P. Gaibor, P. Noble, The blues of Jan de Bray's Judith and Holofernes: A technical study of two blue pigments and its impact on treatment. J. Am. Inst. Conserv. **58**, 217–232 (2019). https://doi.org/10.1080/01971360.2019.1643628
388. J.J. Boon, E. Oberthaler, Mechanical weakness and chemical reactivity observed in the paint structure and surface of The Art of Painting by Vermeer, in: Vermeer, Die Malkunst – Spurensicherung an Einem Meisterwerk: Ausstellungskatalog Des Kunsthistorischen Museums Wien, eds. By S. Haag, E. Oberthaler, S. Penot (Residenz Verlag, Wien, 2010), pp. 235–253, 328–335
389. J.J. Boon, Chemistry Underneath the Painting Surface: Palmierite Formation in/on a Painting by Johannes Vermeer and by Jacob Jordaens using Laboratory- and Synchrotron-aided Spectroscopic Methods. Microsc. Microanal. **19**, 1408–1409 (2013). https://doi.org/10.1017/s1431927613009033
390. D. Hradil, T. Grygar, J. Hradilová, P. Bezdička, V. Grunwaldová, I. Fogaš, C. Miliani, Microanalytical identification of Pb-Sb-Sn yellow pigment in historical European paintings and its differentiation from lead tin and Naples yellows. J. Cult. Herit. **8**, 377–386 (2007). https://doi.org/10.1016/j.culher.2007.07.001

391. H. Stege, Out of the blue? Considerations on the early use of smalt as blue pigment in European easel painting. Zeitschrift Für Kunsttechnologie Und Konservierung: ZKK **18**, 121–142 (2004)
392. F. Delamare, Blue Pigments: 5000 Years of Art and Industry (Archetype Publications Ltd, London, 2013)
393. G. Cavallo, M.P. Riccardi, Glass-based pigments in painting: smalt blue and lead–tin yellow type II. Archaeol. Anthropol. Sci. **13**, 199 (2021). https://doi.org/10.1007/s12520-021-01453-7
394. J. Riederer, Die Smalte. Deutsche Farbenzeitschrift **22**, 386–395 (1968)
395. Z. Zlámalová Cílová, M. Gelnar, S. Randáková, Smalt production in the Ore Mountains: Characterization of samples related to the production of blue pigment in Bohemia. Archaeometry **62**, 1202–1215 (2020). https://doi.org/10.1111/arcm.12584
396. J. Molera, A. Climent-Font, G. Garcia, T. Pradell, O. Vallcorba, A. Zucchiatti, Experimental study of historical processing of cobalt arsenide ore for colouring glazes (15–16th century Europe). J. Archaeol. Sci. Rep. **36**, 102797 (2021). https://doi.org/10.1016/j.jasrep.2021.102797
397. M. Spring, V. Kugler, S. Bean, Quantitative energy dispersive X-ray analysis of the blue pigment smalt, in: Historical Technology, Materials and Conservation: SEM and Microanalysis, eds. By N. Meek, C. Cartwright, A. Meek, A. Mongiatti (Archetype Publications Ltd, London, 2012), pp. 114–122
398. S. Panighello, A. Kavčič, K. Vogel-Mikuš, N.H. Tennent, A. Wallert, S.B. Hočevar, J.T. van Elteren, Investigation of smalt in cross-sections of 17th century paintings using elemental mapping by laser ablation ICP-MS. Microchem. J. **125**, 105–115 (2016). https://doi.org/10.1016/j.microc.2015.11.015
399. D. Spring, M. Von Aderkas, N. Rukavina, F. Peggie, An astronomer by ferdinand bol: materials, colour change and conservation. Natl. Gallery Tech. Bull. **38**, 76–96 (2017)
400. A. van Loon, P. Noble, D. de Man, M. Alfeld, T. Callewaert, G. Van der Snickt, K. Janssens, J. Dik, The role of smalt in complex pigment mixtures in Rembrandt's Homer 1663: combining MA-XRF imaging, microanalysis, paint reconstructions and OCT. Herit. Sci. **8**, 90 (2020). https://doi.org/10.1186/s40494-020-00429-5
401. N. von Aderkas, N. Daly, R. Billinge, A. van Loon, J. Dik, Using macro-XRF to examine Rembrandt's Portrait of Frederik Rihel on Horseback: new insights on pigment distribution and a hidden portrait, in: Rembrandt Now, Technical Practice, Conservation and Research, eds. By M. Spring, A. Roy (The National Gallery, Archetype Publications Ltd, London, 2022), pp. 126–137
402. M. Alfeld, C. Laurenze-Landsberg, A. Denker, K. Janssens, P. Noble, Neutron activation autoradiography and scanning macro-XRF of Rembrandt van Rijn's Susanna and the Elders (Gemäldegalerie Berlin): a comparison of two methods for imaging of historical paintings with elemental contrast. Appl. Phys. A Mater. Sci. Process. **119**, 795–805 (2015). https://doi.org/10.1007/s00339-015-9081-8
403. C. Laurenze-Landsberg, The examination of paintings by rembrandt with neutron autoradiography and a comparison of neutron autoradiography with scanning macro-XRF. Restaurierung Und Archäologie **8**, 99–114 (2015). https://doi.org/10.11588/ra.2015.0.37028
404. J. Plesters, A preliminary note on the incidence of discolouration of smalt in oil media. Stud. Conserv. **14**, 62–74 (1969). https://doi.org/10.1179/sic.1969.006
405. M. Spring, N. Penny, R. White, M. Wyld, Colour change in" The Conversion of the Magdalen" attributed to Pedro Campaña. Natl. Gallery Tech. Bull. **22**, 54–63 (2001)
406. M. Spring, C. Higgitt, D. Saunders, Investigation of pigment-medium processes in oil paint containing degraded smalt. Natl. Gallery Tech. Bull. **26**, 56–70 (2005)
407. J. Carter, A. van Loon, K. Keune, E. Froment, From purple to brown: Using degradation products in reconstructions of a complex smalt paint mixture in The Night Watch to study color change, in Working towards a Sustainable Past: ICOM-CC 20th Triennial Conference Preprints, Valencia, 18–22 September 2023. ed. by B.J. Bridgland (International Council of Museums, Paris, 2023), pp.1–9
408. F. Abrahim, A. Vandivere, S. Meloni, A. van Loon, Purple with a purpose: Investigating and reconstructing the discoloured skirt in Frans Hals's Portrait of Aletta Hanemans, in: Bridging the Gap - Synergies between Art History and Conservation, eds. By B. Sauge, T. Ford, T. Froysaker, K. J. van den Berg (Archetype Publications, London, 2024)
409. J.J. Boon, K. Keune, J. Van Der Weerd, M. Geldof, J.R.J. Van Asperen De Boer, Imaging microspectroscopic, secondary ion mass spectrometric and electron microscopic studies on discoloured and partially discoloured smalt in cross-sections of 16th century paintings. Chimia (Aarau) **55**, 952–960 (2001). https://doi.org/10.2533/chimia.2001.952
410. L. Robinet, M. Spring, S. Pagès-Camagna, Vibrational spectroscopy correlated with elemental analysis for the investigation of smalt pigment and its alteration in paintings. Anal. Methods **5**, 4628–4638 (2013). https://doi.org/10.1039/c3ay40906f

411. N. Eastaugh, V. Walsh, T. Chaplin, R. Siddal, The pigment compendium: a dictionary of historical pigments (Elsevier Butterworth-Heinemann, Oxford and Burlington, 2004)
412. S. Švarcová, D. Hradil, J. Hradilová, Z. Čermáková, Pigments—copper-based greens and blues. Archaeol. Anthropol. Sci. **13**, 190 (2021). https://doi.org/10.1007/s12520-021-01406-0
413. D. A. Scott, Copper and Bronze in Art. Corrosion, Colorants, Conservation (The Getty Conservation Institute, Los Angeles, 2002)
414. S. Schiegl, K.L. Weiner, A. El Goresy, Discovery of copper chloride cancer in ancient Egyptian polychromic wall paintings and faience: a developing archaeological disaster. Naturwissenschaften **76**, 393–400 (1989). https://doi.org/10.1007/BF00366160
415. M. Nicola, R. Gobetto, A. Masic, Egyptian blue, Chinese blue, and related two-dimensional silicates: from antiquity to future technologies. Part A: general properties and historical uses. Rend. Lincei. **34**, 369–413 (2023). https://doi.org/10.1007/s12210-023-01153-5
416. S. Pagès-Camagna, I. Reiche, C. Brouder, D. Cabaret, S. Rossano, B. Kanngießer, A. Erko, New insights into the colour origin of archaeological Egyptian blue and green by XAFS at the Cu K-edge. X-Ray Spectrom. **35**, 141–145 (2006). https://doi.org/10.1002/xrs.885
417. D. Lau, P. Kappen, M. Strohschnieder, N. Brack, P.J. Pigram, Characterization of green copper phase pigments in Egyptian artifacts with X-ray absorption spectroscopy and principal components analysis. Spectrochim. Acta Part B At. Spectrosc. **63**, 1283–1289 (2008). https://doi.org/10.1016/j.sab.2008.09.013
418. A. Lluveras, A. Torrents, P. Giráldez, M. Vendrell-Saz, Evidence for the use of Egyptian Blue in an 11th century mural altarpiece by sem-eds, FTIR and SR XRD (Church Of Sant Pere, Terrassa, Spain). Archaeometry **52**, 308–319 (2010). https://doi.org/10.1111/j.1475-4754.2009.00481.x
419. C. Calza, M.J. Anjos, S.M.F. Mendonça De Souza, A. Brancaglion, R.T. Lopes, X-ray microfluorescence with synchrotron radiation applied in the analysis of pigments from ancient Egypt. Appl. Phys. A Mater. Sci. Process. **90**, 75–79 (2008). https://doi.org/10.1007/s00339-007-4234-z
420. T. Pradell, N. Salvado, G.D. Hatton, M.S. Tite, Physical processes involved in production of the ancient pigment, Egyptian blue. J. Am. Ceram. Soc. **89**, 1426–1431 (2006). https://doi.org/10.1111/j.1551-2916.2005.00904.x
421. J. Bredal-Jørgensen, J. Sanyova, V. Rask, M.L. Sargent, R.H. Therkildsen, Striking presence of Egyptian blue identified in a painting by Giovanni Battista Benvenuto from 1524. Anal. Bioanal. Chem. **401**, 1433–1439 (2011). https://doi.org/10.1007/s00216-011-5140-y
422. A. Sgamellotti, C. Anselmi, An evergreen blue. Spectroscopic properties of Egyptian blue from pyramids to Raphael, and beyond. Inorganica Chim Acta **530**, 120699 (2022). https://doi.org/10.1016/j.ica.2021.120699
423. C. Anselmi, M. Vagnini, C. Seccaroni, M. Azzarelli, T. Frizzi, R. Alberti, M. Falcioni, A. Sgamellotti, Imaging the antique: unexpected Egyptian blue in Raphael's Galatea by non-invasive mapping. Rendiconti Lincei **31**, 913–917 (2020). https://doi.org/10.1007/s12210-020-00960-4
424. S. Švarcová, Z. Čermáková, J. Hradilová, P. Bezdička, D. Hradil, Non-destructive micro-analytical differentiation of copper pigments in paint layers of works of art using laboratory-based techniques. Spectrochim Acta A Mol. Biomol. Spectrosc. **132**, 514–525 (2014). https://doi.org/10.1016/j.saa.2014.05.022
425. C. Conti, J. Striova, I. Aliatis, E. Possenti, G. Massonnet, C. Muehlethaler, T. Poli, M. Positano, The detection of copper resinate pigment in works of art: Contribution from Raman spectroscopy. J. Raman Spectrosc. **45**, 1186–1196 (2014). https://doi.org/10.1002/jrs.4455
426. C. Paz, L.R. Rodriguez-Simón, E. Manzano, Spectroscopic study of mixtures of green copper pigments in fresh and aged model samples. Case studies on masterpieces from the Spanish Golden Age. J. Cult. Herit. **59**, 217–230 (2023). https://doi.org/10.1016/j.culher.2022.12.004
427. J. Xu, Y. Kuang, B. Zhang, Y. Liu, D. Fan, W. Zhou, H. Xie, High-pressure study of azurite $Cu_3(CO_3)_2(OH)_2$ by synchrotron radiation X-ray diffraction and Raman spectroscopy. Phys. Chem. Miner. **42**, 805–816 (2015). https://doi.org/10.1007/s00269-015-0764-7
428. G. Van Der Snickt, C. Miliani, K. Janssens, B.G. Brunetti, A. Romani, F. Rosi, P. Walter, J. Castaing, W. De Nolf, L. Klaassen, I. Labarque, R. Wittermann, Material analyses of "Christ with singing and music-making Angels", a late 15th-C panel painting attributed to Hans Memling and assistants: Part I. non-invasive in situ investigations. J. Anal. At. Spectrom. **26**, 2216–2229 (2011). https://doi.org/10.1039/c1ja10073d

429. L.M. Smieska, R. Mullett, L. Ferri, A.R. Woll, Trace elements in natural azurite pigments found in illuminated manuscript leaves investigated by synchrotron X-ray fluorescence and diffraction mapping. Appl. Phys. A Mater. Sci. Process. **123**, 484 (2017). https://doi.org/10.1007/s00339-017-1093-0
430. E. Mattei, G. De Vivo, A. De Santis, C. Gaetani, C. Pelosi, U. Santamaria, Raman spectroscopic analysis of azurite blackening. J. Raman Spectrosc. **39**, 302–306 (2008). https://doi.org/10.1002/jrs.1845
431. Y. Cudennec, A. Lecerf, The transformation of $Cu(OH)_2$ into CuO, revisited. Solid State Sci. **5**, 1471–1474 (2003). https://doi.org/10.1016/j.solidstatesciences.2003.09.009
432. S. Rickerby, Heat alterations to pigments painted in the fresco technique. The Conservator **15**, 39–44 (1991). https://doi.org/10.1080/01410096.1991.9995063
433. A. Lluveras, S. Boularand, A. Andreotti, M. Vendrell-Saz, Degradation of azurite in mural paintings: Distribution of copper carbonate, chlorides and oxalates by SRFTIR. Appl. Phys. A Mater. Sci. Process. **99**, 363–375 (2010). https://doi.org/10.1007/s00339-010-5673-5
434. S. Švarcová, D. Hradil, J. Hradilová, E. Kočí, P. Bezdička, Micro-analytical evidence of origin and degradation of copper pigments found in Bohemian Gothic murals. Anal. Bioanal. Chem. **395**, 2037–2050 (2009). https://doi.org/10.1007/s00216-009-3144-7
435. E. Egel, S. Simon, Investigation of the painting materials in Zhongshan Grottoes (Shaanxi, China). Herit. Sci. **1**, 29 (2013). https://doi.org/10.1186/2050-7445-1-29
436. M.M. Naumova, S.A. Pisareva, A note on the use of blue and green copper compounds in paintings. Stud. Conserv. **39**, 277–283 (1994). https://doi.org/10.1179/sic.1994.39.4.277
437. B. Shui, Z. Yu, Q. Cui, Z. Wang, Z. Yin, M. Sun, B. Su, Blue pigments in Cave 256, Mogao Grottoes: a systematic analysis of murals and statues in Five dynasties, Song Dynasty and Qing Dynasty. Herit. Sci. **10**, 89 (2022). https://doi.org/10.1186/s40494-022-00722-5
438. Theophilus, On Divers Arts: The Foremost Medieval Treatise on Painting, Glassmaking, and Metalwork (Dover Publications, Incorporated, New York, 1979)
439. E. Bidaud, E. Halwax, E. Pantos, B. Sipek, Analyses of a green copper pigment used in a thirteenth-century wall painting. Stud. Conserv. **53**, 81–92 (2008). https://doi.org/10.1179/sic.2008.53.2.81
440. P. Richardin, V. Mazel, P. Walter, O. Laprévote, A. Brunelle, Identification of different copper green pigments in renaissance paintings by cluster-TOF-SIMS imaging analysis. J. Am. Soc. Mass Spectrom. **22**, 1729–1736 (2011). https://doi.org/10.1007/s13361-011-0171-3
441. S. Valadas, R.V. Freire, A. Cardoso, J. Mirão, C.B. Dias, P. Vandenabeele, A. Candeias, On the Use of the Unusual Green Pigment Brochantite ($Cu_4(SO_4)(OH)_6$) in the 16th-Century Portuguese-Flemish Paintings Attributed to the Master Frei Carlos Workshop. Microsc. Microanal. **21**, 518–525 (2015). https://doi.org/10.1017/S1431927615000094
442. R.J. Gettens, The corrosion products of an ancient chinese bronze. J. Chem. Educ. **28**, 67–71 (1951). https://doi.org/10.1021/ed028p67
443. J. Buse, V. Otero, M.J. Melo, New insights into synthetic copper greens: the search for specific signatures by Raman and infrared spectroscopy for their characterization in medieval artworks. Heritage **2**, 1614–1629 (2019). https://doi.org/10.3390/Heritage2020099
444. M. San Andrés, J.M. De La Roja, V.G. Baonza, N. Sancho, Verdigris pigment: a mixture of compounds. Input from Raman spectroscopy. J. Raman Spectrosc. **41**, 1178–1186 (2010). https://doi.org/10.1002/jrs.2786
445. S. Švarcová, M. Klementová, P. Bezdička, W. Śasocha, M. Dušek, D. Hradil, Synthesis and characterization of single crystals of the layered copper hydroxide acetate $Cu_2(OH)_3(CH_3COO)\cdot H_2O$. Cryst. Res. Technol. **46**, 1051–1057 (2011). https://doi.org/10.1002/crat.201100262
446. S. Bette, R.K. Kremer, G. Eggert, R.E. Dinnebier, On verdigris, Part II: Synthesis of the 2–1-5 phase, $Cu_3(CH_3COO)_4(OH)_2\cdot 5H_2O$, by long-term crystallisation from aqueous solution at room temperature. Dalton Trans. **47**, 8209–8220 (2018). https://doi.org/10.1039/c8dt01758a
447. C.C.R. Sutton, G. Da Silva, G.V. Franks, Modeling the IR spectra of aqueous metal carboxylate complexes: Correlation between bonding geometry and stretching mode wavenumber shifts. Chem. Eur. J. **21**, 6801–6805 (2015). https://doi.org/10.1002/chem.201406516
448. S.W.C. Horn, M. Lewis, M.R. Palmer, C.A. Bayse, Examination of the composition and mechanism of discoloration of the fugitive pigment copper resinate. Inorganica Chim Acta **504**, 119407 (2020). https://doi.org/10.1016/j.ica.2019.119407

449. M. Gunn, G. Chottard, E. Rivière, J.J. Girerd, J.C. Chottard, Chemical reactions between copper pigments and oleoresinous media. Stud. Conserv. **47**, 12–23 (2002). https://doi.org/10.1179/sic.2002.47.1.12
450. L. Osete-Cortina, M.T. Doménech-Carbó, Analytical characterization of diterpenoid resins present in pictorial varnishes using pyrolysis-gas chromatography-mass spectrometry with online trimethylsilylation. J. Chromatogr. A **1065**, 265–278 (2005). https://doi.org/10.1016/j.chroma.2004.12.078
451. E. Ioakimoglou, S. Boyatzis, P. Argitis, A. Fostiridou, K. Papapanagiotou, N. Yannovits, Thin-film study on the oxidation of linseed oil in the presence of selected copper pigments. Chem. Mater. **11**, 2013–2022 (1999). https://doi.org/10.1021/cm9806578
452. A. Zoppi, C. Lofrumento, N.F.C. Mendes, E.M. Castellucci, Metal oxalates in paints: A Raman investigation on the relative reactivities of different pigments to oxalic acid solutions. Anal. Bioanal. Chem. **397**, 841–849 (2010). https://doi.org/10.1007/s00216-010-3583-1
453. S. Boyatzis, E. Ioakimoglou, P. Argitis, UV exposure and temperature effects on curing mechanisms in thin linseed oil films: Spectroscopic and chromatographic studies. J. Appl. Polym. Sci. **84**, 936–949 (2002). https://doi.org/10.1002/app.10117
454. S. Prati, I. Bonacini, G. Sciutto, A. Genty-Vincent, M. Cotte, M. Eveno, M. Menu, R. Mazzeo, ATR-FTIR microscopy in mapping mode for the study of verdigris and its secondary products. Appl. Phys. A Mater. Sci. Process. **122**, 10 (2016). https://doi.org/10.1007/s00339-015-9519-z
455. K. J. van den Berg, M. H. van Eikema Hommes, K. M. Groen, J. J. Boon, B. H. Berrie, On copper green glazes in paintings, in: Proceedings of the International Congress on Contribution of Chemistry to the Works of Art, Art & Chimie, La Couleur, eds. By G. Jacques, M. Jean-Pierre (CNRS Editions, Paris, 2000), pp. 18–23
456. E. West Fitzhugh, Artists' Pigments: A Handbook of Their History & Characteristics-Volume 3 (National Gallery of Art Washington & Oxford University Pres, Washington and Oxford, 1997)
457. X. Cheng, Y. Xia, Y. Ma, Y. Lei, Three fabricated pigments (Han purple, indigo and emerald green) in ancient Chinese artifacts studied by Raman microscopy, energy-dispersive X-ray spectrometry and polarized light microscopy. J. Raman Spectrosc. **38**, 1274–1279 (2007). https://doi.org/10.1002/jrs.1766
458. C. Herm, Emerald Green versus Scheele's Green, in: Acta Artis Academia 2020: The Colour Theme, Proceedings of the 7th Interdisciplinary ALMA Conference 16th -18th October 2019 (Academy of Fine Arts in Prague -University Library Bratislava, Prague, 2020), pp. 189–202
459. L. Pantoja Munoz, Hidden in plain sight: revisiting the synthesis, characterisation, degradation and the intricate relationship between Scheele's green and Emerald green. Herit. Sci. **12**, 94 (2024). https://doi.org/10.1186/s40494-024-01192-7
460. F. Rosi, C. Miliani, I. Borgia, B. Brunetti, A. Sgamellotti, Identification of nineteenth century blue and green pigments by in situ X-ray fluorescence and micro-Raman spectroscopy. J. Raman Spectrosc. **35**, 610–615 (2004). https://doi.org/10.1002/jrs.1180
461. S. Bahfenne, R.L. Frost, A review of the vibrational spectroscopic studies of arsenite, antimonite, and antimonate minerals. Appl. Spectrosc. Rev. **45**, 101–129 (2010). https://doi.org/10.1080/05704920903435839
462. O. Petrova, D. Pankin, A. Povolotckaia, E. Borisov, T. Krivul'ko, N. Kurganov, A. Kurochkin, Pigment palette study of the XIX century plafond painting by Raman spectroscopy. J. Cult. Herit. **37**, 233–237 (2019). https://doi.org/10.1016/j.culher.2018.11.010
463. S. Valadas, P. Vandenabeele, M. Gil, J.C. Frade, E. Vermeersch, S. Lycke, L. Dias, A. Candeias, M. Costa, Analysis of green pigments: The case of Almada Negreiros maritime station murals in Lisbon (Portugal). J. Raman Spectrosc. (2024). https://doi.org/10.1002/jrs.6717
464. M.P. Gil, E. Henderson, J. Burdge, E. Kotze, W. McCarthy, Detecting emerald green in 19thC book bindings using vis-NIR spectroscopy. Anal. Methods **15**, 6603–6609 (2023). https://doi.org/10.1039/d3ay01329d
465. D. Buti, F. Rosi, B.G. Brunetti, C. Miliani, In-situ identification of copper-based green pigments on paintings and manuscripts by reflection FTIR. Anal. Bioanal. Chem. **405**, 2699–2711 (2013). https://doi.org/10.1007/s00216-013-6707-6
466. Z. Li, L. Wang, H. Chen, Q. Ma, Degradation of emerald green: scientific studies on multi-polychrome Vairocana Statue in Dazu Rock Carvings, Chongqing, China. Herit. Sci. **8**, 64 (2020). https://doi.org/10.1186/s40494-020-00410-2

467. P. Holakooei, A.H. Karimy, G. Nafisi, Lammerite as a Degradation Product of Emerald Green: Scientific Studies on a Rural Persian Wall Painting. Stud. Conserv. **63**, 391–402 (2018). https://doi.org/10.1080/00393630.2017.1419658
468. K.P. Smith, G. Ólafsson, All that glitters is not gold: Multi-instrumental identification of Viking Age orpiment (As_2S_3) from Surtshellir cave, Iceland. J. Archaeol. Sci. Rep. **47**, 103724 (2023). https://doi.org/10.1016/j.jasrep.2022.103724
469. E. Gliozzo, L. Burgio, Pigments—Arsenic-based yellows and reds. Archaeol. Anthropol. Sci. **14**, 4 (2022). https://doi.org/10.1007/s12520-021-01431-z
470. P. Knipe, K. Eremin, M. Walton, A. Babini, G. Rayner, Materials and techniques of Islamic manuscripts. Herit. Sci. **6**, 55 (2018). https://doi.org/10.1186/s40494-018-0217-y
471. V.S.F. Muralha, C. Miguel, M.J. Melo, Micro-Raman study of Medieval Cistercian 12–13th century manuscripts: Santa Maria de Alcobaça, Portugal. J. Raman Spectrosc. **43**, 1737–1746 (2012). https://doi.org/10.1002/jrs.4065
472. Y. Oubelkacem, T. Lamhasni, A. El Bakkali, S.A. Lyazidi, M. Haddad, A. Ben-Ncer, Parchments and coloring materials in two IXth century manuscripts: On-site non-invasive multi-techniques investigation. Spectrochim Acta A Mol. Biomol. Spectrosc. **247**, 119093 (2021). https://doi.org/10.1016/j.saa.2020.119093
473. M. Vermeulen, L. Burgio, N. Vandeperre, E. Driscoll, M. Viljoen, J. Woo, M. Leona, Beyond the connoisseurship approach: creating a chronology in Hokusai prints using non-invasive techniques and multivariate data analysis. Herit. Sci. **8**, 62 (2020). https://doi.org/10.1186/s40494-020-00406-y
474. M. Vermeulen, M. Leona, Evidence of early amorphous arsenic sulfide production and use in Edo period Japanese woodblock prints by Hokusai and Kunisada. Herit. Sci. **7**, 73 (2019). https://doi.org/10.1186/s40494-019-0318-2
475. M. Vermeulen, J. Sanyova, K. Janssens, Identification of artificial orpiment in the interior decorations of the Japanese tower in Laeken, Brussels, Belgium. Herit. Sci. **3**, 9 (2015). https://doi.org/10.1186/s40494-015-0040-7
476. Y. Luo, E. Basso, H.D. Smith, M. Leona, Synthetic arsenic sulfides in Japanese prints of the Meiji period. Herit. Sci. **4**, 17 (2016). https://doi.org/10.1186/s40494-016-0087-0
477. S. Zaleski, Y. Takahashi, M. Leona, Natural and synthetic arsenic sulfide pigments in Japanese woodblock prints of the late Edo period. Herit. Sci. **6**, 32 (2018). https://doi.org/10.1186/s40494-018-0195-0
478. G. Grundmann, M. Richter, Types of dry-process artificial arsenic sulphide pigments in cultural heritage. Fatto d'archimia: Los Pigmentos Artificiales En Las Técnicas Pictóricas, 119–144 (2012)
479. G. Grundmann, M. Richter, Current research on artificial arsenic sulphide pigments in artworks: A short review. Chimia (Aarau) **62**, 903–907 (2008). https://doi.org/10.2533/chimia.2008.903
480. M. Vermeulen, K. Palka, M. Vlček, J. Sanyova, Study of dry- and wet-process amorphous arsenic sulfides: Synthesis, Raman reference spectra, and identification in historical art materials. J. Raman Spectrosc. **50**, 396–406 (2019). https://doi.org/10.1002/jrs.5534
481. G. Grundmann, C. Rötter, Artificial orpiment: Microscopic, diffractometric and chemical characteristics of synthesis products in comparison to natural orpiment, in: Auripigment: Studien Zu Dem Mineral Und Den Künstlichen Produkten (Siegl, München, 2007), pp. 105–140
482. J. Pérez-Arantegui, E. Ribechini, M.P. Colombini, F. Escudero, Characterization of an ancient "chemical" preparation: Pigments and drugs in medieval Islamic Spain. J. Archaeol. Sci. **38**, 3350–3357 (2011). https://doi.org/10.1016/j.jas.2011.07.021
483. A.J. Cruz, H.P. Melo, S. Valadas, C. Miguel, A. Candeias, The Matter from Which an Orange Colour Is Made: On the Arsenic Pigment Used in a Portuguese Mannerist Painting. Heritage **5**, 2646–2660 (2022). https://doi.org/10.3390/heritage5030138
484. M. Vermeulen, S. Saverwyns, A. Coudray, K. Janssens, J. Sanyova, Identification by Raman spectroscopy of pararealgar as a starting material in the synthesis of amorphous arsenic sulfide pigments. Dyes Pigm. **149**, 290–297 (2018). https://doi.org/10.1016/j.dyepig.2017.10.009
485. D.L. Douglass, Chichang Shing, Ge Wang, The light-induced alteration of realgar to pararealgar. Am. Miner. **77**, 1266–1274 (1992)
486. K. Trentelman, L. Stodulski, M. Pavlosky, Characterization of pararealgar and other light-induced transformation products from realgar by Raman microspectroscopy. Anal. Chem. **68**, 1755–1761 (1996). https://doi.org/10.1021/ac951097o

487. P. Bonazzi, L. Bindi, A crystallographic review of arsenic sulfides: Effects of chemical variations and changes induced by exposure to light. Zeitschrift Fur Kristallographie **223**, 132–147 (2008). https://doi.org/10.1524/zkri.2008.0011
488. P. Bonazzi, S. Menchetti, G. Pratesi, M. Muniz-Miranda, G. Sbrana, Light-induced variations in realgar and β-As_4S_4: X-ray diffraction and Raman studies. Am. Miner. **81**, 874–880 (1996). https://doi.org/10.2138/am-1996-7-810
489. A. Macchia, S. Nunziante Cesaro, L. Campanella, A. Maras, M. Rocchia, G. Roscioli, Which light for cultural heritage: Comparison of light sources with respect to realgar photodegradation. J. Appl. Spectrosc. **80**, 637–643 (2013). https://doi.org/10.1007/s10812-013-9820-6
490. F. Wu, Y. Zhang, Y. Li, Y. Wang, J. Ma, F. Wang, Photoinduced effects of monochromatic visible light with different wavelengths on realgar. J. Raman Spectrosc. **53**, 1533–1539 (2022). https://doi.org/10.1002/jrs.6408
491. D. Mahon, S.A. Centeno, M.T. Wypyski, X.F. Salomon, A. Bayer, Technical Study of Three Allegorical Paintings by Paolo Veronese: The Choice Between Virtue and Vice, Wisdom and Strength, and Mars and Venus united by Love (The Metropolitan Museum of Art and Yale University Press, New York and New Haven, 2010)
492. J. Dunkerton, H. Howard, Sebastiano del Piombo's "Raising of Lazarus": A History of Change. National Gallery Technical Bulletin **30**, 26–51 (2009)
493. J. Dunkerton, M. Spring, R. Billinge, K. Kalinina, R. Morrison, G. Macaro, D. Peggie, A. Roy, Titian's Painting Technique to c1540. National Gallery Technical Bulletin **34**, 4–31 (2013). https://www.nationalgallery.org.uk/research/research-resources/technical-bulletin/technical-bulletin-volume-34
494. A.M. Correia, R.J.H. Clark, M.I.M. Ribeiro, M.L.T.S. Duarte, Pigment study by Raman microscopy of 23 paintings by the Portuguese artist Henrique Pousão (1859–1884). J. Raman Spectrosc. **38**, 1390–1405 (2007). https://doi.org/10.1002/jrs.1786
495. M.C. Corbeil, K. Helwig, An occurrence of pararealgar as an original or altered artists' pigment. Stud. Conserv. **40**, 133–138 (1995). https://doi.org/10.1179/sic.1995.40.2.133
496. L. Burgio, R.J.H. Clark, K. Theodoraki, Raman microscopy of Greek icons: Identification of unusual pigments. Spectrochim Acta A Mol. Biomol. Spectrosc. **59**, 2371–2389 (2003). https://doi.org/10.1016/S1386-1425(03)00079-9
497. N. Penny, A. Roy, M. Spring, Veronese's Paintings in the National Gallery, Techniques and Materials: Part II. Natl. Gallery Tech. Bull. **17**, 32–55 (1996)
498. D. Hradil, J. Hradilová, P. Bezdička, S. Švarcová, Z. Čermáková, V. Košařová, I. Němec, Crocoite $PbCrO_4$ and mimetite $Pb_5(AsO_4)_3Cl$: Rare minerals in highly degraded mediaeval murals in Northern Bohemia. J. Raman Spectrosc. **45**, 848–858 (2014). https://doi.org/10.1002/jrs.4556
499. R.J. Gettens, R.L. Feller, W.T. Chase, Vermilion and cinnabar. Stud. Conserv. **17**, 45–69 (1972). https://doi.org/10.1179/sic.1972.006
500. J. Martín-Gil, F.J. Martín-Gil, G. Delibes-de-Castro, P. Zapatero-Magdaleno, F.J. Sarabia-Herrero, The first known use of vermillion. Experientia **51**, 759–761 (1995). https://doi.org/10.1007/BF01922425
501. M. Vitruvius Pollio, The Architecture of Marcus Vitruvius Pollio, In Ten Books (Priestley and Weale, London, 1826)
502. R. Ling, Roman Painting (Cambridge University Press, Cambridge, 1991)
503. U. Pappalardo, The Splendor of Roman Wall Painting (Getty Publications, Los Angeles, 2009)
504. A. Dominguez-Vidal, M. Jose De La Torre-Lopez, R. Rubio-Domene, M.J. Ayora-Cañada, In situ noninvasive Raman microspectroscopic investigation of polychrome plasterworks in the Alhambra. Analyst **137**, 5763–5769 (2012). https://doi.org/10.1039/c2an36027f
505. J. Yu, W.S. Warren, M.C. Fischer, Visualization of vermilion degradation using pump-probe microscopy. Sci. Adv. **5**, eaaw3136 (2019). https://doi.org/10.1126/sciadv.aaw3136
506. A. Sodo, L. Tortora, P. Biocca, A. Casanova Municchia, E. Fiorin, M.A. Ricci, Raman and time of flight secondary ion mass spectrometry investigation answers specific conservation questions on Bosch painting Saint Wilgefortis Triptych. J. Raman Spectrosc. **50**, 150–160 (2019). https://doi.org/10.1002/jrs.5479
507. I. Istudor, A. Dina, G. Rosu, D. Seclaman, G. Niculescu, An Alteration Phenomenon of Cinnabar Red Pigment in the Mural Paintings from Sucevita. E-Conservation **2**, 24–33 (2007)
508. D. Chiriu, M. Pala, F.A. Pisu, G. Cappellini, P.C. Ricci, C.M. Carbonaro, Time through colors: a kinetic model of red vermilion darkening from Raman spectra. Dyes Pigm. **184**, 108866 (2021). https://doi.org/10.1016/j.dyepig.2020.108866

509. S. Pérez-Diez, A. Larrañaga, J.M. Madariaga, M. Maguregui, Unraveling the role of the thermal and laser impacts on the blackening of cinnabar in the mural paintings of Pompeii. Eur. Phys. J. Plus **137**, 1184 (2022). https://doi.org/10.1140/epjp/s13360-022-03392-1
510. J.K. McCormack, The darkening of cinnabar in sunlight. Miner. Depos. **35**, 796–798 (2000). https://doi.org/10.1007/s001260050281
511. W. Anaf, K. Janssens, K. De Wael, Formation of metallic mercury during photodegradation/photodarkening of α-HgS: electrochemical evidence. Angewandte Chemie – Int. Ed. **52**, 12568–12571 (2013). https://doi.org/10.1002/anie.201303977
512. K. Elert, C. Cardell, Weathering behavior of cinnabar-based tempera paints upon natural and accelerated aging. Spectrochim Acta A Mol. Biomol. Spectrosc. **216**, 236–248 (2019). https://doi.org/10.1016/j.saa.2019.03.027
513. K. Elert, M. Pérez Mendoza, C. Cardell, Direct evidence for metallic mercury causing photo-induced darkening of red cinnabar tempera paints. Commun Chem **4**, 174 (2021). https://doi.org/10.1038/s42004-021-00610-2
514. M.K. Neiman, M. Balonis, I. Kakoulli, Cinnabar alteration in archaeological wall paintings: an experimental and theoretical approach. Appl. Phys. A Mater. Sci. Process. **121**, 915–938 (2015). https://doi.org/10.1007/s00339-015-9456-x
515. A.C. Wibowo, C.D. Malliakas, H. Li, C.C. Stoumpos, D.Y. Chung, B.W. Wessels, A.J. Freeman, M.G. Kanatzidis, An unusual crystal growth method of the chalcohalide semiconductor, β-$Hg_3S_2Cl_2$: A new candidate for hard radiation detection. Cryst. Growth Des. **16**, 2678–2684 (2016). https://doi.org/10.1021/acs.cgd.5b01802
516. S. Pérez-Diez, Red Cinnabar Blackening in the Mural Paintings of Pompeii: Volcanic Impact, Burial Environment and Atmospheric Exposure, PhD Thesis, Universidad del País Vasco UPV/EHU, 2022
517. R.L. Feller, Studies on the darkening of vermilion by light. Report Stud. History Art **1**, 99–111 (1967)
518. F.W. Dickson, G. Tunell, The stability relations of cinnabar and metacinnabar. Am. Miner. **44**, 471–487 (1959)
519. A.M.T. Bell, R.A.D. Pattrick, D.J. Vaughan, Structural evolution of aqueous mercury sulphide precipitates: energy-dispersive X-ray diffraction studies. Mineral. Mag. **74**, 85–96 (2010). https://doi.org/10.1180/minmag.2010.074.1.85
520. R.L. Feller, Artist's Pigments: a Handbook of their History and Characteristics, vol. 1 (National Gallery of Art, Washington, 1986)
521. M. Ghirardello, V. Otero, D. Comelli, L. Toniolo, D. Dellasega, L. Nessi, M. Cantoni, G. Valentini, A. Nevin, M.J. Melo, An investigation into the synthesis of cadmium sulfide pigments for a better understanding of their reactivity in artworks. Dyes Pigm. **186**, 108998 (2021). https://doi.org/10.1016/j.dyepig.2020.108998
522. G. Pfaff, Cadmium sulfide / selenide pigments, in: Antraquinonoid Pigments - Color Fundamentals (De Gruyter, Berlin and Boston, 2022), pp. 37–42. https://doi.org/10.1515/9783110588071-006
523. V. Gonzalez, D. Gourier, G. Wallez, T. Calligaro, A. Artesani, F. Rosi, A. Romani, C. Grazia, C. Miliani, L. Monico, D. Comelli, M. Ghirardello, Luminescent Inorganic Pigments Used in Ancient and Modern Times, in: Springer Series on Fluorescence (Springer, Cham., 2023), pp. 1–45. https://doi.org/10.1007/4243_2022_43
524. F. Rosi, C. Grazia, F. Gabrieli, A. Romani, M. Paolantoni, R. Vivani, B.G. Brunetti, P. Colomban, C. Miliani, UV–Vis-NIR and micro Raman spectroscopies for the non destructive identification of $Cd_{1-x}Zn_xS$ solid solutions in cadmium yellow pigments. Microchem. J. **124**, 856–867 (2016). https://doi.org/10.1016/j.microc.2015.07.025
525. C. Grazia, F. Rosi, F. Gabrieli, A. Romani, M. Paolantoni, R. Vivani, B.G. Brunetti, P. Colomban, C. Miliani, UV-Vis-NIR and microRaman spectroscopies for investigating the composition of ternary $CdS_{1-x}Se_x$ solid solutions employed as artists' pigments. Microchem. J. **125**, 279–289 (2016). https://doi.org/10.1016/j.microc.2015.11.008
526. M. Thoury, J.K. Delaney, E.R. De La Rie, M. Palmer, K. Morales, J. Krueger, Near-infrared luminescence of cadmium pigments: In situ identification and mapping in paintings. Appl. Spectrosc. **65**, 939–951 (2011). https://doi.org/10.1366/11-06230
527. A. Cesaratto, C. D'Andrea, A. Nevin, G. Valentini, F. Tassone, R. Alberti, T. Frizzi, D. Comelli, Analysis of cadmium-based pigments with time-resolved photoluminescence. Anal. Methods **6**, 130–138 (2014). https://doi.org/10.1039/c3ay41585f

528. M. Ghirardello, S. Mosca, J. Marti-Rujas, L. Nardo, A. Burnstock, A. Nevin, M. Bondani, L. Toniolo, G. Valentini, D. Comelli, Time-resolved photoluminescence microscopy combined with X-ray analyses and raman spectroscopy sheds light on the imperfect synthesis of historical cadmium pigments. Anal. Chem. **90**, 10771–10779 (2018). https://doi.org/10.1021/acs.analchem.8b01666
529. D. Comelli, D. Maclennan, M. Ghirardello, A. Phenix, C. Schmidt Patterson, H. Khanjian, M. Gross, G. Valentini, K. Trentelman, A. Nevin, Degradation of cadmium yellow paint: new evidence from photoluminescence studies of trap states in Picasso's Femme (époque des "Demoiselles d'Avignon"). Anal. Chem. **91**, 3421–3428 (2019). https://doi.org/10.1021/acs.analchem.8b04914
530. C. Grazia, C. Sapienza, C. Miliani, A. Romani, Vis-NIR reflection and luminescence spectral imaging for the determination of CdS-based pigment stoichiometry, in: UV–Vis Luminescence Imaging Techniques. CONSERVATION 360°, eds. By M. Picollo, M. Stols-Witlox, L. F. López (Editorial Universitat Politècnica de València, 2019), pp. 181–200. https://doi.org/10.4995/360.2019.110002
531. M. Ghirardello, G. Valentini, L. Toniolo, R. Alberti, M. Gironda, D. Comelli, Photoluminescence imaging of modern paintings: there is plenty of information at the microsecond timescale. Microchem. J. **154**, 104618 (2020). https://doi.org/10.1016/j.microc.2020.104618
532. L. Bronwyn, A. Burnstock, C. Jones, P. Hallebeek, J. Boon, K. Keune, The deterioration of cadmium sulphide yellow artists' pigments, in: ICOM Committee for Conservation. Triennial Meeting, 14th, The Hague, Netherlands, 2005, Vol. 2 (James and James/Earthscan, London, 2005), pp. 803–813
533. J. Harrison, J. Lee, B. Ormsby, D.J. Payne, The influence of light and relative humidity on the formation of epsomite in cadmium yellow and French ultramarine modern oil paints. Herit Sci **9**, 107 (2021). https://doi.org/10.1186/s40494-021-00569-2
534. Z.E. Voras, K. de Ghetaldi, M.B. Wiggins, B. Buckley, B. Baade, J.L. Mass, T.P. Beebe, TOF–SIMS imaging of molecular-level alteration mechanisms in Le Bonheur de vivre by Henri Matisse. Appl. Phys. A Mater. Sci. Process. **121**, 1015–1030 (2015). https://doi.org/10.1007/s00339-015-9508-2
535. Y. Zhou, D. Grass, W.S. Warren, M.C. Fischer, Non-destructive three-dimensional imaging of artificially degraded CdS paints by pump-probe microscopy. JPhys Photonics **6**, 025013 (2024). https://doi.org/10.1088/2515-7647/ad3e65
536. F.A. Pisu, P.C. Ricci, S. Porcu, C.M. Carbonaro, D. Chiriu, Degradation of CdS yellow and orange pigments: a preventive characterization of the process through pump-probe, reflectance, X-ray diffraction, and raman spectroscopy. Materials **15**, 5533 (2022). https://doi.org/10.3390/ma15165533
537. L. Giacopetti, A. Satta, Reactivity of Cd-yellow pigments: role of surface defects. Microchem. J. **137**, 502–508 (2018). https://doi.org/10.1016/j.microc.2017.12.013
538. L. Giacopetti, A. Satta, Degradation of Cd-yellow paints: Ab initio study of native defects in 10.0 surface CdS. Microchem. J. **126**, 214–219 (2016). https://doi.org/10.1016/j.microc.2015.12.005
539. S. Fantacci, A. Satta, Modeling Luminescence in Cultural Heritage: Theoretical Insight into the Luminescence of Dyes and Pigments, in: Springer Series on Fluorescence (Springer, Cham., 2023), pp. 1–29. https://doi.org/10.1007/4243_2023_47
540. G. Rayner, S.D. Costello, A. McClelland, A. Akey, K. Eremin, Preliminary investigations into the alteration of cadmium orange restoration paint on an ancient greek terracotta krater. Heritage **4**, 1497–1510 (2021). https://doi.org/10.3390/heritage4030082
541. M.J. Crane, P. Leverett, L.R. Shaddick, P.A. Williams, J.T. Kloprogge, R.L. Frost, The $PbCrO_4$-$PbSO_4$ system and its mineralogical significance. N. Jb. Miner. Mh. **11**, 505–519 (2001)
542. A.C.D. Cowley, Lead chromate—that dazzling pigment. Rev. Prog. Color. Relat. Top. **16**, 16–24 (1986). https://doi.org/10.1111/j.1478-4408.1986.tb03740.x
543. L.J.H. Erkens, H. Hamers, R.J.M. Hermans, E. Claeys, M. Bijnens, Lead chromates: A review of the state of the art in 2000. Surf. Coatings Int. Part B: Coatings Int. **84**, 169–176 (2001). https://doi.org/10.1007/BF02700395
544. V. Otero, L. Carlyle, M. Vilarigues, M.J. Melo, Chrome yellow in nineteenth century art: Historic reconstructions of an artists' pigment. RSC Adv. **2**, 1798–1805 (2012). https://doi.org/10.1039/c1ra00614b
545. D. Sanches, A.M. Ramos, J.F.J. Coelho, C.S.M.F. Costa, M. Vilarigues, M.J. Melo, Correlating thermophysical properties with the molecular composition of 19th century chrome yellow oil paints. Polym. Degrad. Stab. **138**, 201–211 (2017). https://doi.org/10.1016/j.polymdegradstab.2017.02.010
546. V. Watson, H.F. Clay, The lightfastness of lead chrome pigments. J. Oil Colour Chem. Assoc. **38**, 167–177 (1955)
547. R.J. Cole, The darkening of lead chromes. Res. Assoc. Br. Paint Colour Varnish Manuf. **199**, 1–62 (1955)

548. L. Monico, K. Janssens, C. Miliani, G. Van Der Snickt, B.G. Brunetti, M. Cestelli Guidi, M. Radepont, M. Cotte, Degradation process of lead chromate in paintings by Vincent van Gogh studied by means of spectromicroscopic methods. 4. Artificial aging of model samples of Co-precipitates of lead chromate and lead sulfate. Anal. Chem. **85**, 860–867 (2013). https://doi.org/10.1021/ac3021592
549. A. Roy, E. Hendriks, Van Gogh's Sunflowers in London and Amsterdam. National Gallery Technical Bulletin **37**, 60–77 (2016)
550. L. Monico, G. Van Der Snickt, K. Janssens, W. De Nolf, C. Miliani, J. Dik, M. Radepont, E. Hendriks, M. Geldof, M. Cotte, Degradation process of lead chromate in paintings by Vincent van Gogh studied by means of synchrotron X-ray spectromicroscopy and related methods. 2. Original Paint Layer Samples. Anal. Chem. **83**, 1224–1231 (2011). https://doi.org/10.1021/ac1025122
551. A.B. Muñoz-García, A. Massaro, M. Pavone, Ab initio study of $PbCr_{(1-x)}S_xO_4$ solid solution: An inside look at Van Gogh Yellow degradation. Chem. Sci. **7**, 4197–4203 (2016). https://doi.org/10.1039/c5sc04362j
552. A. Amat, C. Miliani, S. Fantacci, Structural and electronic properties of the $PbCrO_4$ chrome yellow pigment and of its light sensitive sulfate-substituted compounds. RSC Adv. **6**, 36336–36344 (2016). https://doi.org/10.1039/c6ra01444e
553. V. Rahemi, N. Sarmadian, W. Anaf, K. Janssens, D. Lamoen, B. Partoens, K. De Wael, Unique optoelectronic structure and photoreduction properties of sulfur-doped lead chromates explaining their instability in paintings. Anal. Chem. **89**, 3326–3334 (2017). https://doi.org/10.1021/acs.analchem.6b03803
554. E. Hendriks, M. Geldof, L. Monico, D.H. Johnson, C. Miliani, A. Romani, C. Grazia, D. Buti, B.G. Brunetti, K. Janssens, G. Van der Snickt, F. Vanmeert, Methods and Materials of the Amsterdam Sunflowers, in: Van Gogh's Sunflowers Illuminated-Art Meets Science, eds. By E. Hendriks, M. Vellekoop, M. van Bommel, M. Geldof (Amsterdam University Press and Van Gogh Museum, Amsterdam, 2019), pp. 85–124. https://doi.org/10.1017/9789048550531.005
555. M. Geldof, I.D. van der Werf, R. Haswell, The examination of Van Gogh's chrome yellow pigments in 'Field with Irises near Arles' using quantitative SEM–WDX. Herit Sci **7**, 100 (2019). https://doi.org/10.1186/s40494-019-0341-3
556. A. Haddad, K. Sutherland, S.A. Centeno, G.M. Kavich, M. Kokkori, C. Hoover, D. Hartman-Drumm, N. Balcar, G. Barabant, Painting on the margins: investigating the pigments, media, and techniques of Séraphine Louis. Herit Sci **12**, 85 (2024). https://doi.org/10.1186/s40494-024-01190-9
557. F. Rosi, M. Patti, L. Cartechini, F. Gabrieli, L. Monico, A. Romani, C. Anselmi, C. Grazia, A. Daveri, A. Sgamellotti, C. Miliani, Designs and colors. Gerardo Dottori through non invasive investigations, in: Gerardo Dottori: The Futurist View (Cat. Estorick Collection, London, 9th July – 7th September 2014) (Fabbri, Perugia, 2014), pp. 33–45
558. M. Lunz, E. Talgorn, J. Baken, W. Wagemans, D. Veldman, Can LEDs help with art conservation?–Impact of different light spectra on paint pigment degradation. Stud. Conserv. **62**, 294–303 (2017). https://doi.org/10.1080/00393630.2016.1189997
559. R. Georgiou, R.S. Popelka-Filcoff, D. Sokaras, V. Beltran, I. Bonaduce, J. Spangler, S.X. Cohen, R. Lehmann, S. Bernard, J.P. Rueff, U. Bergmann, L. Bertrand, Disentangling the chemistry of Australian plant exudates from a unique historical collection. Proc. Natl. Acad. Sci. U.S.A. **119**, e2116021119 (2022). https://doi.org/10.1073/pnas.2116021119
560. R. Georgiou, P. Gueriau, C. J. Sahle, S. Bernard, A. Mirone, R. Garrouste, U. Bergmann, J. P. Rueff, L. Bertrand, Carbon speciation in organic fossils using 2D to 3DX-ray Raman multispectral imaging. Sci Adv **5**, eaaw5019 (2019). https://doi.org/10.1126/sciadv.aaw5019
561. R. Georgiou, C.J. Sahle, D. Sokaras, S. Bernard, U. Bergmann, J.P. Rueff, L. Bertrand, X-ray Raman scattering: a hard X-ray probe of complex organic systems. Chem. Rev. **122**, 12977–13005 (2022). https://doi.org/10.1021/acs.chemrev.1c00953
562. J. Li, L. Liu, T.K. Sham, 2D XANES-XEOL spectroscopy studies of morphology-dependent phase transformation and corresponding luminescence from hierarchical TiO_2 nanostructures. Chem. Mater. **27**, 3021–3029 (2015). https://doi.org/10.1021/acs.chemmater.5b00363
563. M.W. Murphy, Y.M. Yiu, M.J. Ward, L. Liu, Y. Hu, J.A. Zapien, Y. Liu, T.K. Sham, Electronic structure and optical properties of CdS_xSe_{1-x} solid solution nanostructures from X-ray absorption near edge structure, X-ray excited optical luminescence, and density functional theory investigations. J. Appl. Phys. **116**, 193709 (2014). https://doi.org/10.1063/1.4902390
564. V.C. Teixeira, J.C. Silva, F.C.M. Silva, R. Szostak, M.G.D. Guaita, L.M. Kofukuda, A.C. Piccino Neto, A.P.S. Sotero, I.T. Neckel, C.A. Pérez, D. Galante, H.C.N. Tolentino, X-ray excited optical

luminescence at Carnaúba, the Sirius X-ray nanoprobe beamline. Opt. Mate. X **20**, 100278 (2023). https://doi.org/10.1016/j.omx.2023.100278

Authors and Affiliations

Letizia Monico[1,2,3] · Koen Janssens[3,4,5] · Marine Cotte[6,7] · Samuel M. Webb[8] · Frederik Vanmeert[3,4] · Victor Gonzalez[9] · Geert Van der Snickt[3,5] · Katrien Keune[4,10] · Brunetto Giovanni Brunetti[1,2] · Gerald Falkenberg[11] · Jan Garrevoet[11] · Annelies van Loon[4,12] · Marc Vermeulen[13] · Maite Maguregui[14] · Steven De Meyer[3,15] · Ermanno Avranovich Clerici[3] · Fréderique T. H. Broers[3,4,10,16] · Laura Cartechini[1] · Nouchka De Keyser[3,4,5,10] · Francesco d'Acapito[17] · Florian Meirer[16] · Aldo Romani[1,2] · Francesca Rosi[1] · Sara Carboni Marri[1,2] · Daniela Comelli[18] · Nina Deleu[3,5] · Ida Fazlic[4,6,10] · Marta Ghirardello[18] · Clément Holé[6] · Silvia Pérez-Diez[19,20] · Mathieu Thoury[21] · Costanza Miliani[22]

✉ Letizia Monico
letizia.monico@cnr.it

✉ Koen Janssens
koen.janssens@uantwerpen.be

1 Istituto di Scienze e Tecnologie Chimiche "Giulio Natta" (SCITEC), CNR, Via Elce di Sotto 8, 06123 Perugia, Italy

2 Centre of Excellence SMAArt and Department of Chemistry, Biology and Biotechnology, University of Perugia, Via Elce di Sotto 8, 06123 Perugia, Italy

3 AXIS Research Group, Faculty of Science, University of Antwerp, Groenenborgerlaan 171, 2020 Antwerp, Belgium

4 Rijksmuseum, Conservation and Science, Hobbemastraat 22, 1071 ZC Amsterdam, The Netherlands

5 ARCHES Research Group, Faculty of Design Sciences, University of Antwerp, Mutsaardstraat 31, 2000 Antwerp, Belgium

6 ESRF, Avenue des Martyrs 71, 38000 Grenoble, France

7 LAMS, CNRS UMR 8220, Sorbonne Université, UPMC Univ Paris 06, Place Jussieu 4, 75005 Paris, France

8 Stanford Synchrotron Radiation Lightsource SLAC National Accelerator Laboratory, 2575 Sand Hill Road, Menlo Park, CA 94025, USA

9 Université Paris-Saclay, ENS Paris-Saclay, CNRS, PPSM, 4 Av. Des Sciences, 91190 Gif-sur-Yvette, France

10 University of Amsterdam, Van't Hoff Institute for Molecular Sciences, Science Park 904, 1098 XH Amsterdam, The Netherlands

11 DESY, Notkestraße 85, 22607 Hamburg, Germany

12 Mauritshuis, Collection and Science, Plein 29, 2511 CS The Hague, The Netherlands

13 Collection Care Department, The National Archives, Richmond TW9 4DU, UK

[14] Department of Analytical Chemistry, Faculty of Pharmacy, University of the Basque Country UPV/EHU, Paseo de la Universidad 7, 01006 Vitoria-Gasteiz, Spain

[15] Paintings Laboratory, Royal Institute for Cultural Heritage (KIK-IRPA), Jubelpark 1, 1000 Brussels, Belgium

[16] Inorganic Chemistry and Catalysis, Institute for Sustainable and Circular Chemistry, Utrecht University, Universiteitsweg 99, 3584CG Utrecht, The Netherlands

[17] CNR-IOM-OGG, c/o ESRF LISA CRG, Avenue des Martyrs 71, 38000 Grenoble, France

[18] Department of Physics, Politecnico di Milano, Piazza Leonardo da Vinci 32, 20133 Milan, Italy

[19] Department of Analytical Chemistry Faculty of Science, University of the Basque Country UPV/EHU Barrio Sarriena s/n, Patrimonio Nacional, Bailén S/N, 48940 Leioa, Spain

[20] Department of Restoration, Directorate of Royal Collections, Royal Palace of Madrid, Patrimonio Nacional, Bailén S/N, 28071 Madrid, Spain

[21] IPANEMA CNRS, ministère de la Culture UVSQ Université Paris-Saclay, UAR 3461, 91192 Gif-sur-Yvette, France

[22] Istituto di Scienze del Patrimonio Culturale (ISPC), CNR, Via Cardinale Guglielmo Sanfelice 8, 80134 Naples, Italy